

1. Report No. UMTA-MA-06-0025-84-1		2. Government Accession No.		3. Recipient's Catalog No.	
4. Title and Subtitle ANALYSIS OF RAIL TRANSIT VEHICLE DYNAMIC CURVING PERFORMANCE				5. Report Date June 1984	
				6. Performing Organization Code DTS-76	
7. Author(s) D.N. Wormley, J.K. Hedrick, M.L. Nagurka				8. Performing Organization Report No. DOT-TSC-UMTA-84-6	
9. Performing Organization Name and Address Massachusetts Institute of Technology* Department of Mechanical Engineering Cambridge MA 02139				10. Work Unit No. (TRAI) UM477/R4643	
				11. Contract or Grant No. DTRS 57-80C-00152	
12. Sponsoring Agency Name and Address U.S. Department of Transportation Urban Mass Transportation Administration Office of Technical Assistance Washington DC 20590				13. Type of Report and Period Covered Final Report Jan. 1981 - Dec. 1983	
				14. Sponsoring Agency Code URT-11	
15. Supplementary Notes U.S. Department of Transportation Research and Special Programs Administration *Under contract to: Transportation Systems Center Cambridge MA 02142					
16. Abstract An analytical model is developed for determining the dynamic curving performance of rail transit vehicles. The dynamic wheel/rail interaction forces, vehicle suspension and body motions and track displacement are computed, as well as wheel and rail wear indices. The model incorporates a nonlinear, multi-point contact wheel-rail geometry characterization and is directly applicable to conventional, self-steered radial and forced steered (linkages between the carbody-bolster-wheelsets) truck configurations. A limited set of parametric studies are conducted in which dynamic forces and wear indices for conventional, radial and forced steered tracks are determined for new AAR and Heumann wheel profiles. Available experimental dynamic curving field test data is reviewed in the context of the model.					
17. Key Words Rail Vehicles Rail Trucks Radial Trucks Forced Steering Trucks				18. Distribution Statement DOCUMENT IS AVAILABLE TO THE PUBLIC THROUGH THE NATIONAL TECHNICAL INFORMATION SERVICE, SPRINGFIELD, VIRGINIA 22161	
19. Security Classif. (of this report) UNCLASSIFIED		20. Security Classif. (of this page) UNCLASSIFIED		21. No. of Pages 232	22. Price

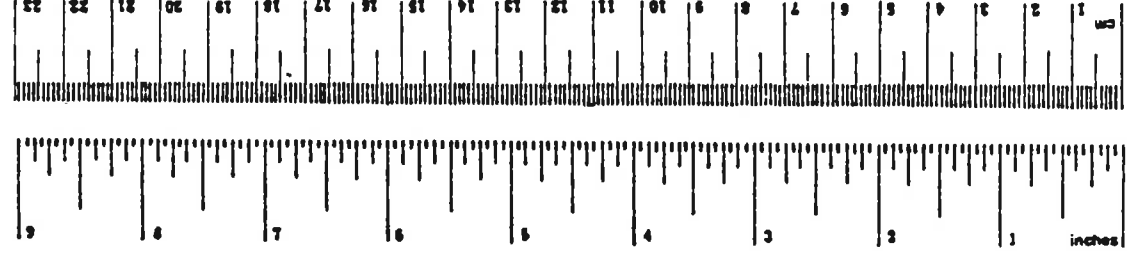
METRIC CONVERSION FACTORS

Approximate Conversions to Metric Measures

Symbol	When You Know	Multiply by	To Find	Symbol
LENGTH				
in	inches	2.5	centimeters	cm
ft	feet	30	centimeters	cm
yd	yards	0.9	meters	m
mi	miles	1.6	kilometers	km
AREA				
sq in	square inches	6.5	square centimeters	cm ²
sq ft	square feet	0.93	square meters	m ²
sq yd	square yards	0.8	square meters	m ²
sq mi	square miles	2.6	square kilometers	km ²
	acres	0.4	hectares	ha
MASS (weight)				
oz	ounces	28	grams	g
lb	pounds	0.45	kilograms	kg
	short tons (2000 lb)	0.9	tonnes	t
VOLUME				
teaspoon	teaspoons	5	milliliters	ml
tablespoon	tablespoons	15	milliliters	ml
fl oz	fluid ounces	30	milliliters	ml
c	cups	0.24	liters	l
pt	pints	0.47	liters	l
qt	quarts	0.95	liters	l
gal	gallons	3.8	liters	l
cu ft	cubic feet	0.028	cubic meters	m ³
cu yd	cubic yards	0.76	cubic meters	m ³
TEMPERATURE (exact)				
°F	Fahrenheit temperature	5/9 (after subtracting 32)	Celsius temperature	°C

Approximate Conversions from Metric Measures

Symbol	When You Know	Multiply by	To Find	Symbol
LENGTH				
mm	millimeters	0.04	inches	in
cm	centimeters	0.4	inches	in
m	meters	3.3	feet	ft
km	kilometers	1.1	yards	yd
		0.6	miles	mi
AREA				
cm ²	square centimeters	0.16	square inches	sq in
m ²	square meters	1.2	square yards	sq yd
km ²	square kilometers	0.4	square miles	sq mi
ha	hectares (10,000 m ²)	2.5	acres	ac
MASS (weight)				
g	grams	0.035	ounces	oz
kg	kilograms	2.2	pounds	lb
t	tonnes (1000 kg)	1.1	short tons	st
VOLUME				
ml	milliliters	0.03	fluid ounces	fl oz
l	liters	2.1	pints	pt
l	liters	1.06	quarts	qt
l	liters	0.26	gallons	gal
m ³	cubic meters	35	cubic feet	ft ³
m ³	cubic meters	1.3	cubic yards	yd ³
TEMPERATURE (exact)				
°C	Celsius temperature	9/5 (then add 32)	Fahrenheit temperature	°F



¹ 1 in = 2.54 exactly. For other exact conversions and more detailed tables, see NBS Misc. Publ. 226, *Units of Weights and Measures*, Price \$2.25, SI Catalog No. C1.3.10 286.

PREFACE

In support of the Office of Technical Assistance of the Urban Mass Transportation Administration (UMTA), the Transportation Systems Center is conducting analytical and experimental studies to relate transit truck design characteristics to wheel rail forces and wheel rail wear rates. The results of these studies are expected to provide rail transit systems with options for reducing the wheel rail wear rates experienced by transit properties while maintaining and improving equipment performance.

In the past decade there have been significant efforts towards developing steerable truck configurations which employ direct connections between axles and supplemental linkages connecting the axles to the car-body to aid in steering while maintaining the speed capacity of the truck design. Under contracts DOT-TSC-1739 and DOT-TSC-1740 with the Budd Company and with the Urban Transportation Development Corporation design studies have been conducted for the retrofit of existing trucks to linkage steered configurations.

Under an earlier contract with the U. S. Department of Transportation Office of University Research (DOT-OS-70052), the Department of Mechanical Engineering of the Massachusetts Institute of Technology conducted studies of the performance limits of conventional and self-steered trucks for intercity passenger application. This study used a curve negotiation criteria of preventing either flange contact or wheel slip which is inappropriate for the sharp curves typical of transit application.

The study described in this document extends the previous analyses to include regions of significant flange contact for sharper curve radii, to include a curving index which estimates wear rates under flange contact,

to include the dynamic curving problems associated with curve entry and exit and to consideration of the performance achievable with forced steering mechanizations which employ truck to carbody linkages.

The work was performed under contract to the Transportation Systems Center in support of the Urban Mass Transportation Administration. The authors would like to acknowledge Dr. Herbert Weinstock for many productive discussions on the work in progress and his careful review and comments on this report.

TABLE OF CONTENTS

<u>Section</u>	<u>Page</u>
1.0 INTRODUCTION.....	1-1
1.1 Background.....	1-1
1.2 Study Scope and Objectives.....	1-3
1.3 Previous Curving Studies.....	1-4
2.0 STUDY METHODOLOGY.....	2-1
2.1 Introduction.....	2-1
2.2 Performance Criteria.....	2-2
2.2.1 Curve Negotiation.....	2-2
2.2.2 Lateral Stability.....	2-3
2.3 Track Model.....	2-3
2.3.1 Flexible Rail Model.....	2-6
2.4 Wheelset Model.....	2-6
2.4.1 Coordinate Systems.....	2-10
2.4.2 Wheel/Rail Geometric Constraints.....	2-12
2.4.3 Wheel/Rail Contact Forces.....	2-19
2.5 Truck Model.....	2-19
2.5.1 Conventional Truck.....	2-21
2.5.2 Self-Steered Radial Truck.....	2-21
2.5.3 Forced-Steered Radial Truck.....	2-25
2.5.4 Generic Truck Model.....	2-31
2.6 Vehicle Model.....	2-33
2.6.1 Carbody/Bolster Model.....	2-33
2.7 Numerical Methods of Dynamic Curving Analysis.....	2-36
2.8 Baseline Rail and Vehicle Parameters.....	2-41
3.0 DYNAMIC CURVING STUDIES.....	3-1
3.1 Introduction.....	3-1
3.2 Curve Entry Performance of a Conventional Vehicle.....	3-3
3.2.1 Effect of Track Curvature on Curve Entry Performance of a Conventional Vehicle.....	3-7

3.2.2	Effect of Wheel/Rail Profile on Curve Entry Performance of a Conventional Vehicle.....	3-12
3.2.3	Effect of Spiral Length on Curve Entry Performance of a Conventional Vehicle.....	3-17
3.3	Curve Entry Performance of a Self-Steered Radial Vehicle.....	3-17
3.3.1	Effect of Wheel/Rail Profile on the Curve Entry Performance of a Self-Steered Radial Vehicle.....	3-23
3.4	Curve Entry Performance of a Forced-Steered Radial Vehicle.....	3-27
3.4.1	Effect of Wheel/Rail Profile on the Curve Entry Performance of a Forced-Steered Radial Vehicle.....	3-32
3.5	Comparative Curve Entry Performance of Conventional, Self-Steered, and Forced-Steered Radial Vehicles.....	3-35
3.6	Dynamic and Steady-State Model Comparisons.....	3-37
3.7	Review of Field Test Data.....	3-40
4.0	SUMMARY AND CONCLUSIONS.....	4-1
5.0	REFERENCES.....	5-1
APPENDIX A - DYNAMIC CURVING EQUATIONS OF MOTION OF A WHEELSET.....		
		A-1
A.1	Introduction.....	A-1
A.2	Coordinate Systems.....	A-2
A.3	Acceleration of Wheelset Center of Mass.....	A-7
A.4	Rate of Angular Momentum of Wheelset.....	A-8
A.5	Wheelset Forces and Moments.....	A-10
A.5.1	Normal Forces.....	A-11
A.5.2	Creep Forces and Moments.....	A-13
A.5.2.1	Heuristic Creep Model.....	A-15
A.5.2.2	Derivation of Creepages for Dynamic Curving.....	A-18
A.5.2.3	Definition of Contact Patch Work.....	A-22
A.6	Wheelset Equations of Motion.....	A-23
A.6.1	Single-Point Contact.....	A-26
A.6.2	Two-Point Contact.....	A-32

A.7	Wheelset Numerical Methods.....	A-41
A.7.1	Single-Point Contact.....	A-44
A.7.2	Two-Point Contact.....	A-47
APPENDIX B - DYNAMIC CURVING EQUATIONS OF MOTION OF A RAIL		
	VEHICLE MODEL.....	B-1
B.1	Introduction.....	B-1
B.2	Coordinate Systems.....	B-1
B.3	Acceleration of Center of Mass.....	B-9
B.3.2	Acceleration of Carbody Center of Mass.....	B-10
B.4	Rate of Angular Momentum.....	B-11
B.4.1	Rate of Angular Momentum of Truck Frame and Bolster.....	B-11
B.4.2	Rate of Angular Momentum of Carbody.....	B-12
B.5	Forces and Moments.....	B-13
B.5.1	Wheelset Suspension Forces and Moments.....	B-15
B.5.2	Truck Frame and Bolster Suspension Forces and Moments.....	B-22
B.5.3	Carbody Suspension Forces and Moments.....	B-30
B.6	Equations of Motion.....	B-33
B.6.1	Wheelset Equations of Motion.....	B-33
B.6.2	Truck Frame and Bolster Equations of Motion....	B-34
B.6.3	Carbody Equations of Motion.....	B-35
B.6.4	Modified Carbody Yaw Equation of Motion.....	B-36
B.7	Numerical Methods.....	B-40
B.7.1	Dynamic Curving Program.....	B-47

List of Figures

<u>Number</u>	<u>Title</u>	<u>Page</u>
2.1	Definition of (a) Degree Curve and (b) Superelevation Angle.....	2-5
2.2	Track Curvature and Superelevation as a Function of Distance.....	2-7
2.3	Lateral Track Model.....	2-8
2.4	Typical Wheelset Cross-Section.....	2-9
2.5	Track and Wheelset Coordinate Systems.....	2-11
2.6	Rolling Radii vs. Net Wheelset Lateral Excursion for (a) Heumann Wheel and (b) New Wheel on Worn Rails.....	2-13
2.7	Contact Angles vs. Net Wheelset Lateral Excursion for (a) Heumann Wheel and (b) New Wheel on Worn Rails.....	2-14
2.8	Wheelset Roll Angle vs. Net Wheelset Lateral Excursion for (a) Heumann and (b) New Wheel on Worn Rails.....	2-15
2.9	Left Wheel/Rail Contact.....	2-17
2.10	Contact Patch Creep Force vs. Creepage Relation.....	2-20
2.11	Schematic of Conventional Truck.....	2-22
2.12	Schematic of Self-Steering Radial Truck.....	2-23
2.13	Alternative Self-Steering Radial Truck Configurations.....	2-24
2.14	Schematic Diagram of "S" Forced-Steered Truck (Primary Suspension System Not Shown).....	2-27
2.15	Schematic Diagram of "L" Forced-Steered Truck (Primary Suspension System Not Shown).....	2-28
2.16	Schematic Diagram of "U" Forced-Steered Truck (Primary Suspension System Not Shown).....	2-29
2.17	Forced-Steering Truck Model.....	2-30
2.18	Generic Truck Model.....	2-32
2.19	Rail Vehicle Model, Side View.....	2-34
2.20	Rail Vehicle Model During Curving, Rear View.....	2-35

List of Figures (Continued)

<u>Number</u>	<u>Title</u>	<u>Page</u>
2.21	Physical Arrangement of the Secondary Yaw Suspension.....	2-37
2.22	Model of Secondary Yaw Suspension.....	2-38
2.23	Truck Frame/Bolster Yaw Suspension Characteristic.....	2-39
2.24	Wheel/Rail Contact Possibilities for Wheelsets of a Truck with New Wheels.....	2-42
3.1	History of (a) Wheelset Lateral Excursions and (b) Angles of Attack of a Baseline Conventional Vehicle with New Wheels Negotiating a 150 ft Curve Entry Spiral into a 10° Curve at a Balance Speed of 45 ft/sec.....	3-4
3.2	History of (a) Leading Outer (i.e., Flanging) Wheel Lateral Force and (b) Contact Work of a Baseline Conventional Vehicle with New Wheels, Negotiating a 150 ft Curve Entry Spiral into a 10° Curve at a Balance Speed of 45 ft/sec.....	3-5
3.3	History of (a) Wheelset Lateral Excursions and (b) Angles of Attack of a Baseline Conventional Vehicle with New Wheels Negotiating a 150 ft Curve Entry Spiral into a 2.5° Curve at a Balance Speed of 90 ft/sec.....	3-9
3.4	History of (a) Leading Outer (i.e., Flanging) Wheel Lateral Force and (b) Contact Work for a Baseline Conventional Vehicle with New Wheels Negotiating a 150 ft Curve Entry Spiral into a 2.5° Curve at a Balance Speed of 90 ft/sec.....	3-10
3.5	History of (a) Wheelset Lateral Excursions and (b) Angles of Attack of a Baseline Conventional Vehicle with Heumann Wheels Negotiating a 150 ft Curve Entry Spiral into a 10° Curve at a Balance Speed of 45 ft/sec.....	3-14
3.6	History of (a) Leading Outer (i.e., Flanging) Wheel Lateral Force and (b) Contact Work of a Baseline Conventional Vehicle with Heumann Wheels Negotiating a 150 ft Curve Entry Spiral into a 10° Curve at a Balance Speed of 45 ft/sec.....	3-15
3.7	Effect of Curve Entry Spiral Length on the Peak Lateral Wheel Force of a Baseline Conventional Vehicle with New Wheels Entering a 10° Curve at a Balance Speed of 45 ft/sec.....	3-18

List of Figures (Continued)

<u>Number</u>	<u>Title</u>	<u>Page</u>
3.8	History of (a) Wheelset Lateral Excursions and (b) Angles of Attack of a Self-Steered Radial Vehicle with New Wheels Negotiating a 150 ft Curve Entry Spiral into a 10° Curve at a Balance Speed of 45 ft/sec.....	3-19
3.9	History of (a) Leading Outer (i.e. Flanging) Wheel Lateral Force and (b) Contact Work of a Self-Steered Radial Vehicle with New Wheels Negotiating a 150 ft Curve Entry Spiral into a 10° Curve at a Balance Speed of 45 ft/sec.....	3-21
3.10	History of (a) Wheelset Lateral Excursions and (b) Angles of Attack of a Self-Steered Radial Vehicle with Heumann Wheels Negotiating a 150 ft Curve Entry Spiral into a 10° Curve at a Balance Speed of 45 ft/sec.....	3-24
3.11	History of (a) Leading Outer (i.e., Flanging) Wheel Lateral Force and (b) Contact Work of a Self-Steered Radial Vehicle with Heumann Wheels Negotiating a 150 ft Curve Entry Spiral into a 10° Curve at a Balance Speed of 45 ft/sec.....	3-25
3.12	History of (a) Wheelset Lateral Excursions and (b) Angles of Attack of a FSR I Forced-Steered Radial Vehicle with New Wheels Negotiating a 150 ft Curve Entry Spiral into a 10° Curve at a Balance Speed of 45 ft/sec.....	3-28
3.13	History of (a) Leading Outer (i.e., Flanging) Wheel Lateral Force and (b) Contact Work of a FSR I Forced-Steered Radial Vehicle with New Wheels Negotiating a 150 ft Curve Entry Spiral into a 10° Curve at a Balance Speed of 45 ft/sec.....	3-29
3.14	History of (a) Wheelset Lateral Excursions and (b) Angles of Attack of a FSR I Forced-Steered Radial Vehicle with Heumann Wheels Negotiating a 150 ft Curve Entry Spiral into a 10° Curve at a Balance Speed of 45 ft/sec.....	3-33
3.15	History of (a) Leading Outer (i.e., Flanging) Wheel Lateral Force and (b) Contact Work of a FSR I Forced-Steered Radial Vehicle with Heumann Wheels Negotiating a 150 ft Curve Entry Spiral into a 10° Curve at a Balance Speed of 45 ft/sec.....	3-34
3.16	Curve 37 Steady State Lateral Wheel Forces (adopted from [27]).....	3-41

List of Figures (Continued)

<u>Number</u>	<u>Title</u>	<u>Page</u>
3.17	Curve 37 Peak Lateral Wheel Forces (Adopted from [27]).....	3-42
3.18	Simulation of Curve 37 (7.6° Curve, 4° c.d., 40 mph, new wheel, spiral entry).....	3-45
3.19	Simulation of Curve 37 (7.6° curve, 4° c.d., 40 mph, Heumann wheel, spiral entry).....	3-46
3.20	Simulation of Curve 37 (7.6°, 4° c.d., 40 mph, Heumann Wheel, no spiral entry).....	3-47
A.1	Wheelset and Track Coordinate Systems.....	A-4
A.2	Definition of Wheelset and Track Coordinate System Orientations (Rotations Only) [The following notation is used: $s\alpha = \sin(\alpha)$, $c\alpha = \cos(\alpha)$].....	A-5
A.3	Wheel/Rail Geometry and Normal Forces Assuming Single-Point Contact.....	A-12
A.4	Contact Patch Coordinate Systems.....	A-14
A.5	Contact Patch Creep Force vs. Creepage Relation.....	A-19
A.6	Longitudinal Displacement of Contact Points Due to Wheelset Yaw.....	A-21
A.7	Lateral Track Model.....	A-25
A.8	Free-Body Diagram of Wheelset in Single-Point Contact.....	A-27
A.9	Left Wheel/Rail Contact.....	A-34
A.10	Wheel and Rail Forces for Two-Point Contact.....	A-36
A.11	Wheelset Dynamic Curving Analysis at One Time-Step.....	A-43
A.12	Wheel/Rail Force Calculation at One Time-Step.....	A-46
B.1	Rail Vehicle Model During Curving, Rear View.....	B-2
B.2	Rail Vehicle Model Coordinate Systems.....	B-3
B.3	Definition of Truck Frame Orientation (Rotation Only).....	B-5
B.4	Definition of Bolster Orientation (Rotation Only).....	B-6

List of Figures (Continued)

<u>Number</u>	<u>Title</u>	<u>Page</u>
B.5	Definition of Carbody Orientation (Rotation Only).....	B-7
B.6	Generic Truck Model.....	B-14
B.7	Suspension Forces and Moments Acting on Wheelset i.....	B-16
B.8	Lateral Suspension Forces and Yaw Suspension Moments Acting on Truck Frame.....	B-24
B.9	Truck Frame/Bolster Yaw Suspension Characteristic.....	B-28
B.10	Yaw Suspension Moments Acting on Bolsters.....	B-29
B.11	Suspension Forces and Moments Acting on Carbody.....	B-31
B.12	Truck Frame/Bolster Yaw Suspension Characteristic.....	B-38
B.13	Wheel/Rail Contact Possibilities for Wheelsets of a Truck with New Wheels.....	B-48
B.14	Flowchart of Dynamic Curving Program.....	B-50
B.15	Layout of Equation Subroutines.....	B-51

List of Tables

<u>Number</u>	<u>Title</u>	<u>Page</u>
2.1	Baseline Rail/Vehicle Parameters.....	2-43
3.1	Balanced Running Speeds Assuming 6 in Superelevation (i.e., $\phi_{SE} = 6.2^\circ$).....	3-2
3.2	Leading Outer Wheel Force and Work of a Baseline Conventional Vehicle with New Wheels Negotiating a 150 Ft Curve Entry Spiral into a 2.5°, 5°, and 10° Curve.....	3-13
3.3	Dynamic Curve Entry Performance in Terms of Flanging Wheel Lateral Force and Contact Work for Baseline Vehicles with New Wheels Negotiating a 150 Ft Spiral Into A 10° Curve at a Balance Speed of 45 Ft/Sec.....	3-36
3.4	Dynamic Curve Entry Performance in Terms of Flanging Wheel Lateral Force and Contact Work for Baseline Vehicles with Heumann Wheels Negotiating a 150 Ft Sprial Into a 10° Curve At A Balance Speed of 45 Ft/Sec.....	3-36
3.5	Flanging Wheel Lateral Force and Contact Work for Baseline Vehicles Running at Balance Speed in a Constant Radius 10° Curve.....	3-39
B.1	Coordinate Systems.....	B-4
B.2	States of the Rail Vehicle Model.....	B-45
B.3	Subroutine Descriptions for Dynamic Curving Program.....	B-52

EXECUTIVE SUMMARY

The dynamic stability and curve negotiation capability of rail transit vehicles have a strong influence on their operational performance and maintenance requirements. In this study computer simulation models have been developed to analyze the stability and curving performance of transit vehicles with conventional, radial and forced-steered trucks. In the initial phases of the study, a nonlinear steady-state curving model useful for evaluating the influence of different truck configurations and wheel profile geometries on steady-state wheel-rail interaction forces and wear indici was developed as well as a linear stability analysis for determining vehicle critical speeds. These analytical tools were used to generate extensive parametric data characterizing the steady-state curving stability performance tradeoffs offered by various truck and wheel profile designs.*

In this report, the steady-state curving analysis has been extended to develop a dynamic curving model for computing the time varying wheel-rail interaction forces and vehicle suspension and body forces and motions during curve entry and exit as well as due to changes in track geometry. The dynamic curving model includes nonlinear wheel/rail geometry, including multipoint wheel-rail contact, nonlinear vehicle suspension elements, and rail lateral flexibility.

Dynamic simulations of curve entry have been performed which have shown the influence of wheel profile and suspension design for conventional, self-steered and forced steered trucks on dynamic curving forces. In the parametric dynamic curving studies, a smooth 150 ft spiral entry to a 10° curve was considered with a vehicle operating at balance speed. In these

* Wormley, D. N., Hedrick, J. K., Nagurka, M. L., "Stability and Curving Performance of Conventional and Advanced Rail Transit Vehicles," DTRS-57-80C-00152, November, 1982.

simulations the peak dynamic forces for the baseline conventional, self-steered radial and forced steered radial vehicles were found to be a maximum of 35% greater than the equivalent steady-state curving forces for the baseline vehicle designs. For conditions in which the spiral length is reduced to 50 ft, the conventional baseline design dynamic to steady-state force ratio increased to a factor of 1.8. Also for the conventional truck baseline design the ratio of dynamic to steady-state forces increased to 3.8 for the 150 ft spiral entry as curve radius increased to a 2.5° curve, however, the overall steady-state force levels for the 2.5° curve are less than one third of those for the 10° curve and overall the maximum dynamic and steady-state force magnitudes occur for the small radius curves.

Data comparing truck designs negotiating a 150 ft transition spiral to a 10° curve have shown that significant decreases in both steady-state and peak dynamic forces may be achieved using forced steered trucks with Heumann wheel profiles. For the three baseline truck designs, both peak dynamic forces and steady-state forces are smaller with a Heumann than with a new AAR wheel profile with small reductions in peak forces of 5-6% for the baseline conventional and self-steered radial designs and a significant 58% reduction in peak forces for the forced-steered baseline design. The peak dynamic curving forces for baseline trucks with Heumann wheels are 4950 lbs for the conventional, 4800 lbs for the self-steered radial and 1820 lbs for the forced steered baseline trucks. The forced steered truck has peak forces 35% greater than the steady-state forces while the conventional and radial have peak forces 22% above steady-state forces. Thus, while the forced steered truck has a higher ratio of dynamic to steady-state curving forces than the other two baseline designs, its maximum dynamic force is less than one half the force in the other two

baseline designs. These simulation results have been limited to an evaluation of performance on smooth track with a 150 ft spiral transition into a constant radius curve.

Limited experimental data is available on dynamic curving forces. Field test data obtained on the Washington Metropolitan Area Transit Authority for a rapid transit vehicle with a conventional truck have been reviewed. The data for a truck employing new AAR wheels negotiating a 150 ft transition spiral into a 7.5° constant radius curve indicate dynamic to steady-state forces in ratios of two to one occurring in the constant radius section of the curve. The model simulation studies conducted representative of these field conditions have only achieved such force ratios for cases in which the vehicle undergoes significant transient motions from an initial state displaced significantly from the steady-state conditions. Such a state could occur due to local track conditions. Further effort is required to resolve the differences between field data and the analysis. Future effort is recommended with a coupled analytical and experimental study of dynamic curving to develop an experimentally verified dynamic curving model.

NOMENCLATURE

a	half of track gage
$\frac{\beta}{a}$	acceleration of point α in reference system β
a_e	longitudinal semi-axis of contact patch ellipse
b	half of wheelbase
b_e	lateral semi-axis of contact patch ellipse
c_o	secondary yaw viscous damping
c_{px}	primary longitudinal damping
c_{py}	primary lateral damping
c_{pz}	primary vertical damping
c_r	effective lateral rail viscous damping
c_{sy}	secondary lateral damping
c_{sz}	secondary vertical damping
$C_{\beta/\alpha}$	coordinate transformation matrix from α to β
d_p	half of lateral spacing between primary longitudinal springs
d_s	half of lateral spacing between secondary vertical springs
D	degree curve
f_{ij}^*	nominal creep coefficients ($ij = 11, 12, 22, 33$)
f_{11}	lateral creep coefficient
f_{12}	lateral/spin creep coefficient
f_{22}	spin creep coefficient
f_{33}	longitudinal creep coefficient
\bar{F}_{axle}	vector of wheelset axle forces
F_{buff}	lateral buff load
\bar{F}_c	creep force vector (with components F_{CPX} , F_{CPY} , and M_{CP} in longitudinal, lateral, and normal contact patch directions, respectively)
F_{CPX}, F_{CPY}	creep force in longitudinal, lateral contact patch direction
F'_{CPX}, F'_{CPY}	unlimited creep force in longitudinal, lateral contact patch direction
F_{CXi}	longitudinal track component of creep force at i -th contact patch; $i = L$ (left), R (right) for single-point; $i = LT$ (left tread), LF (left flange), R (right) for two-point

F_f	lateral flange force (i.e., leading outer wheel lateral force)
F_{lat}	wheelset lateral force (in lateral track direction) provided by suspension and body forces
F_N	normal force
F_N^*	nominal normal force
F_{Ni}	normal force at i-th contact patch; i = L (left), R (right) for single-point; i = LT (left tread), LF (left flange), R (right) for two-point
F_{NYi}	lateral track component of normal force at i-th contact patch; i = L (left), R (right) for single-point, i = LT (left tread), LF (left flange), R (right) for two-point
F_{NZi}	vertical track component of normal force at i-th contact patch; i = L (left), R (right) for single-point; i = LT (left tread), LF (left flange), R (right) for two-point
F_{rail_L}, F_{rail_R}	lateral rail reaction force at left, right rail
F'_R	unlimited resultant creep force
\bar{F}_{susp}	vector of suspension forces
F_t	wheelset longitudinal thrust or drawbar force
F_y	net lateral wheel force composed of creep and normal forces
g	acceleration of gravity
g'	actual rail gage
G	track curvature steering gain
G_{prl}	track curvature steering gain to follow pure rolling line
h_{cs}	vertical distance from secondary suspension to carbody center of mass
h_{tp}	vertical distance from primary suspension to truck center of mass
h_{ts}	vertical distance from truck center of mass to secondary suspension
H	cant deficiency steering gain
$\bar{H}^{\alpha/\beta}$	angular momentum of body α about point β
$\hat{i}, \hat{j}, \hat{k}$	unit vectors in longitudinal, lateral, vertical direction, respectively
I_{BZ}	yaw principal mass moment of inertia of bolster
I_{CX}	roll principal mass moment of inertia of carbody
I_{CZ}	yaw principal mass moment of inertia of carbody
I_{FX}	roll principal mass moment of inertia of truck frame

I_{FZ}	yaw principal mass moment of inertia of truck frame
I_{WY}	pitch principal mass moment of inertia of wheelset
I_{WZ}	yaw principal mass moment of inertia of wheelset
k_b	total bending stiffness of a truck
k_{b2}	interaxle bending stiffness
k_{px}	primary longitudinal suspension stiffness
k_{pxaux}	auxiliary primary longitudinal suspension stiffness
k_{py}	primary lateral suspension stiffness
k_{pz}	primary vertical suspension stiffness
k_r	effective lateral rail stiffness
k_s	total shear stiffness of a truck
k_{sy}	secondary lateral suspension stiffness
k_{sz}	secondary vertical suspension stiffness
k_{s2}	interaxle shear stiffness
$k_{s\psi}$	secondary yaw suspension stiffness
l_s	half of truck center pin spacing
(L/V)	lateral to vertical wheel force ratio
m_r	effective lateral rail mass
\bar{M}^α	vector sum of all external moments acting about the center of mass of point α
\bar{M}_{axle}	vector of wheelset axle moments
M_{CP}	creep moment normal to contact patch
M_{CYi}	lateral track frame component of creep moment at i-th contact patch; $i = L$ (left), R (right) for single-point; $i = LT$ (left tread), LF (left flange), R (right) for two-point
M_{CZi}	vertical track frame component of creep moment at i-th contact patch; $i = L$ (left), R (right) for single-point; $i = LT$ (left tread), LF (left flange), R (right) for two-point
\bar{M}_{susp}	vector of suspension moments
M_{yaw}	wheelset yaw moment (in vertical wheelset frame direction) provided by suspension forces
P	power dissipated at contact patch
P_{in}, P_{out}	input, output power
$\frac{-\beta}{r}$	position vector from point α to point β

r_i rolling radius measured from wheelset spin axis to i -th contact patch; $i = L$ (left), R (right) for single-point, $i = LT$ (Left tread), LF (left flange), R (right) for two-point
 r_o rolling radius for centered wheelset; nominal rolling radius
 R curve radius, often expressed in degree curve, D , where $D = \frac{360}{\pi} [\sin^{-1}(\frac{50}{R})] \approx \frac{5730}{R}$ deg with R in ft
 T_d wheelset drive/brake torque
 T_o secondary yaw suspension breakaway torque
 V vehicle speed
 V_{cr} critical speed of the vehicle
 V_L, V_R external vertical load acting on left, right wheel (in negative vertical track frame direction) provided by body and suspension forces
 W contact patch work per unit distance (in force units)
 $W = \bar{F}_c \cdot \bar{\xi}$
 W' contact patch work per unit distance (W) divided by contact patch area
 W_B bolster weight
 W_c carbody weight
 W_F truck frame weight
 W_V total vehicle weight
 W_W wheelset weight
 x longitudinal coordinate
 \bar{X} geometry state vector
 \bar{X}_m misaligned geometry state vector
 y lateral coordinate
 y_{fc} flange clearance
 y_{rail_L}, y_{rail_R} lateral displacement of left, right rail
 z vertical coordinate
 β normalized unlimited resultant creep force
 δ_i contact angle at i -th contact patch; $i = L$ (left), R (right) for single-point; $i = LT$ (left tread), LF (left flange), R (right) for two-point
 Δx_i longitudinal displacement of i -th contact patch from vertically below wheelset axis

Δy	track curvature steering offset
Δz	vertical distance between points of flange and tread contact
$\Delta\psi$	cant deficiency steering offset
ϵ	creep force saturation constant
$\dot{\theta}_w$	wheelset spin speed
λ	wheel conicity
μ	coefficient of friction
μ_f	coefficient of flange friction
$\vec{\xi}$	creepage vector (with components ξ_{Xi} , ξ_{Yi} , and ξ_{SPi} in longitudinal, lateral, and normal contact patch directions, respectively)
ξ_R	resultant creepage
ξ_{SPi}	spin creepage in normal contact patch direction at i-th contact patch
ξ_{Xi}	longitudinal creepage at i-th contact patch
ξ_{Yi}	lateral creepage at i-th contact patch
ϕ_d	cant deficiency (lateral unbalance load)
	$\phi_d = \frac{v^2}{Rg} - \phi_{SE}$
ϕ_{SE}	track superelevation (or bank) angle
ϕ_w	wheelset roll angle with respect to track plane
ψ	yaw angle
ψ_w	wheelset angle of attack, or yaw angle with respect to radial alignment
$\frac{\beta}{\omega} \alpha$	angular velocity of system α relative to system β

1.0 INTRODUCTION

1.1 Background

The service provided in an urban rail transportation system and the associated operating costs are strongly influenced by maintenance requirements of rolling stock and track. Components including wheels, axles, suspension elements and power and braking equipment, as well as rails, switching gear, ties and ballast sustain wear and experience forces directly related to wheel/rail interaction forces. The control and limitation of these forces can have a significant impact upon urban rail transit system maintenance requirements. These forces are associated directly with vehicle stability or hunting, vehicle curve negotiation capability and vehicle vertical and lateral suspension capability to accommodate track irregularities.

In the last decade an increasing interest in developing vehicles which control these interaction forces to reduce wheel and rail and vehicle and track deterioration has developed and led to proposals for:

- (1) Conventional suspension trucks employing rubber or mechanical components between the axle and truck frame which have reduced stiffness.
- (2) Self-steering radial trucks which employ direct links between truck axles to aid in aligning the axles radially in curves.
- (3) Forced steering trucks which employ direct links between carbody-truck-axle elements to force the axles into radial alignment on curves.

In addition, proposals for use of profiled wheels to reduce curving forces have been made. These developments have been motivated primarily by the desire to reduce wheel and rail wear associated with curve negotiation while maintaining adequate dynamic stability to avoid hunting and adequate suspension capability to accommodate forces developed due to

rail irregularities.

The evaluation of various types of conventional, self-steering radial and forced steering trucks represents a tradeoff between a potential for performance improvement and increased truck complexity. The selection of an appropriate type of truck and wheel profile for a specific urban system depends strongly on the system route characteristics - particularly, the prevalence and distribution of small radius curves. For example in systems with few small radius curves, conventional truck suspensions may provide a good compromise between performance and truck design complexity, while for older systems with many small radius curves, self-steering or forced-steering trucks may prove to provide the best overall performance. To facilitate the evaluation of truck design by urban rail operating authorities, analytical evaluation methods, design data and field test data are required. This study is directed to providing analytical models, performance data and evaluation methods for conventional and advanced urban rail truck designs.

A principal objective of this study is to develop performance data for evaluating the stability and curving performance of conventional, self steering radial and forced steering trucks designed for urban rail systems. The analytical basis for the study has been provided by developing a generic truck model which directly reduces to conventional, self-steering radial and forced steering truck designs.

In an effort described in an interim report [1], the model has been incorporated into a linear stability program which allows computation of the truck critical speed at which sustained hunting occurs and computation of the damping ratios associated with truck modes of oscillation. The model has also been incorporated into a nonlinear steady-state

curving program which computes wheelset, truck and carbody angles of attack and wheel/rail as well as suspension forces for negotiation of a constant radius curve at constant speed with a given superelevation. An indication of wheel/rail wear has been computed based upon the work performed at the wheel/rail interface.

An extensive parametric study has been conducted to determine the influence of suspension and wheel profile design parameters on stability and steady-state curving performance of conventional, self-steering radial and forced steering truck designs. These performance studies, which have provided tradeoff data necessary to identify truck designs for a given critical speed which result in reduced wear for a given radius curve based on steady-state analysis, are described in the interim report [1].

1.2 Study Scope and Objectives

The current study is directed to extending the steady-state analytical model of curving performance to include dynamic effects which may occur during curve entry and exit or due to track irregularities and misalignment. Specific effort is directed to development of a dynamic curving computer simulation model which can predict the transient forces resulting from wheel-rail interactions. The simulation is based upon the generalized rail vehicle model that represents conventional and innovative suspension designs, including self-steered and forced-steered vehicles and includes nonlinear wheel/rail profile geometry, wheel/rail friction force saturation, and nonlinear suspension components. The analysis considers two-point wheel/rail contact which occurs with many common wheel profiles during curving.

A limited set of parametric studies have been conducted in the study to evaluate the influence of track configuration and wheel profile on dynamic curving performance. Of particular concern in this study is the degree to which dynamic curving force magnitudes are different from steady-state curving forces.

The study has included a limited comparison of the dynamic curving model results with experimental data. The scope of this comparison did not permit a detailed assessment of the model and additional effort is required in this area to develop an experimentally validated dynamic curving model.

1.3 Previous Curving Studies

The majority of wheel-rail geometry representations in curving studies in the literature have assumed that each wheel of the vehicle contacts the rails at a single point. This is an acceptable approximation of tread contact, but for some profiles this represents a simplistic view of flange contact. Two-point tread and flange contact can occur for profiles with steep flanges, such as the new AAR 1 in 20 wheel profile. The vehicle curving studies of Marcotte, et. al. [2] considered two-point wheel/rail contact by using a wheel profile composed of a tread and flange segment of constant (but different) conicity. Using experimental data, Elkins and Weinstock [3] showed that significant errors result in predicting curving behavior based on analyses assuming single-point wheel/rail contact when in fact two-point contact occurs. Thus, formulation of a model which can represent many wheel profiles, requires consideration of the multi-point contact geometry.

An early investigator of dynamic curving was Mueller [4] who used the friction center method to study the performance of a rail truck during transition from tangent to curved track. The friction center method assumes that the wheel profiles are cylindrical, the primary suspension elements are rigid, and that one or more wheels are in flange contact. Mueller predicted that the magnitude of the impact force on the flange can become significant in comparison to the steady-state curving force.

During the last few years nonlinear dynamic analyses have been developed, relying heavily on large scale computer systems. Smith [5] formulated a dynamic curving analysis which considers nonlinear suspension, damping, and creep forces. The analysis is limited in that it assumes conical wheels and a carbody which does not yaw with respect to the local tangent to the track centerline. The study does not consider track super-elevation (banking), irregularities, or flexibility. Smith showed that as the length of spiral transition track (between tangent and constant radius track) decreased the forces during curve entry increased.

Law and Cooperrider [6, 7] have developed comprehensive steady-state and dynamic curving models that include nonlinear suspension elements, creep forces, and wheel/rail geometry but do not directly account for rail flexibility. System inputs are track curvature, super-elevation angle, and irregularities. Results of their models indicate that dynamic wheel/rail forces are large compared with steady-state forces in large radius curves, at balance speed (corresponding to zero lateral unbalance), and in situations where flange contact is not severe. A reduction in dynamic flange forces is demonstrated using self-steered radial trucks.

Clark, et al, [8] introduced a nonlinear dynamic curving analysis that predicts the transient response of two-axle vehicles. The analysis accounts for lateral truck flexibility and irregularities. Predictions made for a vehicle traversing a section of misaligned track agreed well with an experimental derailment.

Duffek and Jaschinski [9] formulated a detailed model of wheel/rail interaction to be used for dynamic curving studies. The model includes nonlinear creep force laws and accounts for the influence of wheelset yaw angle on wheel/rail contact geometry. Single-point wheel/rail contact is assumed.

Krolewski [10] developed a model for freight car dynamic curving simulations that includes nonlinear wheel/rail geometry, coulomb friction elements, and creep force saturation. With the model, dynamic wheel/rail forces exceeding steady-state values have been predicted.

The dynamic curving studies cited above do not account for the two-point wheel/rail contact.

2.0 STUDY METHODOLOGY

2.1 Introduction

This chapter describes the establishment of dynamic performance criteria, the formulation of track and vehicle models, and the development of computational tools. The wheel/rail contact work due to friction which is related to wheel and rail wear [11] is adopted as the principal curving performance index. The stability index is the maximum speed for stable operation, the critical speed.

A model of the track is adopted in which the track curvature and bank angle are assumed to be known functions of the distance along the track. In addition, the rails are assumed to have lateral flexibility.

A model of the wheelset is developed that accounts for nonlinear wheel/rail profile geometry and friction force saturation. The profile geometry is a principal parameter influencing the performance of the vehicle.

The nonlinear wheelset model is incorporated into a vehicle model which includes nonlinear suspension components and a generic truck model that can represent conventional as well as advanced design suspension configurations.

The performance of the rail vehicle is investigated using a dynamic curving analysis. In this analysis, the coupled, nonlinear, differential equations of motion are solved numerically using a fourth order Runge-Kutta integration scheme.

Baseline rail and vehicle parameters are used in the performance studies. The vehicle parameters have been selected to represent conventional and advanced-design urban transit vehicles. Two wheel profiles

have been identified to represent profiles characterized by single-point and two-point wheel/rail contact.

2.2 Performance Criteria

The curve negotiation and stability capabilities of a rail vehicle are measured in terms of performance criteria or indices.

2.2.1 Curve Negotiation

Several criteria have been developed to represent the curving performance of a rail vehicle. During curve negotiation, different performance objectives can be identified, including perfect steering, prevention of derailment, minimum wheel/rail forces, and minimum wheel/rail wear as described in [1].

A wear index which represents the work expended at the wheel/rail contact interface has been recommended by British Rail [11]. The index is the contact patch work, W , defined as the dot product of the resultant creep force and creepage vectors. When summed over all contact patches, this index represents the additional work per distance along the track required for the vehicle to negotiate the curve. This index has units of work per distance, or force.

Comprehensive verification of wear indices has been limited. Tests by British Rail [11] and I.I.T. [12] have shown potentially useful trends, including a positive relation between contact patch work (W) and experimentally-induced wear. Dry wear laboratory tests by British Rail [13] have suggested that the wear rate can be expressed in terms of creep force, creepage, and Hertzian contact area. Recent field data described in [14] has provided additional data indicating the usefulness of the contact patch work as an indicator of wear.

In this report the contact patch work, W, has been selected as the principal index of curving performance. The contact patch work is a comprehensive measure of the work expended (i.e., energy dissipated) due to friction at the wheel/rail interface. The work index includes the effect of wheel/rail creepage and, in particular, wheelset angle of attack.

Experience shows that the flanging wheel is responsible for the majority of wheel and track wear [14]. For a vehicle negotiating a curve, flanging usually occurs at the leading outer wheel. Significant wear occurs on the wheel flange and on the gage face of the outer rail. Therefore, the principal curving performance index used in this report is the contact work at the flanging wheel.

2.2.2 Lateral Stability

A useful index of vehicle stability is the critical speed. At the critical speed, the vehicle exhibits sustained oscillatory behavior called hunting, involving coupled lateral and yaw motions of the wheelsets, truck frames, and carbody. In general, the wheelset oscillations tend to diverge until they are limited by the wheel flanges. To avoid this behavior, a vehicle should be designed to achieve a critical speed significantly greater than the operating speed.

2.3 Track Model

The track is characterized by its curvature, superelevation, and irregularities. The track curvature is defined as $1/R$, where R is the curve radius. It is often expressed in terms of degree curve, D, corresponding to the degrees of arc subtended by a 100 ft chord at the track centerline. Mathematically,

$$D = \frac{360}{\pi} \sin^{-1} \left(\frac{50}{R} \right) \quad (2-1)$$

with R in ft. The track superelevation or bank angle, ϕ_{SE} , is the angle between the track and the horizon. It is usually expressed in degrees. Degree curve and superelevation are shown in Figure 2.1.

It is convenient to combine the track curvature, the superelevation angle, and the vehicle forward speed, V, into a parameter of net lateral unbalance called the cant deficiency, ϕ_d . Cant deficiency is defined by:

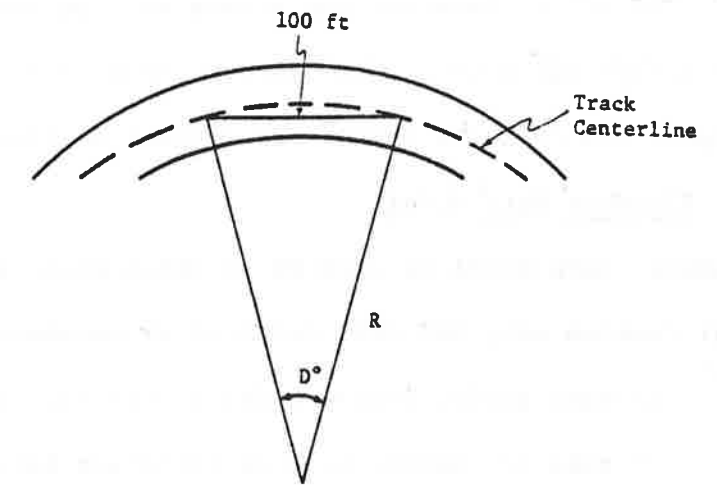
$$\phi_d = \frac{V^2}{Rg} - \phi_{SE} \quad (2-2)$$

and represents an angular measure of lateral unbalance between centrifugal and gravitational forces. When $\phi_d = 0$, a condition of balanced running is achieved for which the components of centrifugal force and weight parallel to the rail plane cancel each other. For comfort and safety, the cant deficiency is limited in the U. S. to 6° of inboard unbalance and 3° of outboard unbalance [1].

Track irregularities are due to a combination of installation error and gradual degradation. In the literature, four types of irregularities are defined: gage, cross-level, alignment, and vertical. Gage is the horizontal distance between two rails; cross-level is the difference between the elevations of the rails, alignment is the average of two rail lateral positions; and, vertical is the average of the two rail elevations. In this study track irregularities are neglected and the track is assumed to be smooth. Implementation of cross-level and alignment irregularities is possible by the addition of a random disturbance to the superelevation angle and the rail lateral excursion, respectively.

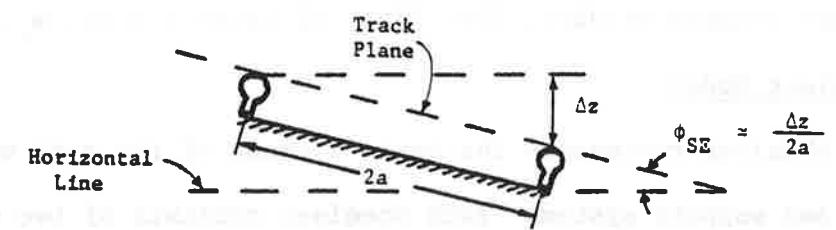
In this study a simple model of track curve geometry is adopted [1]. In tangent track, the track curvature and superelevation angle are zero. In constant radius curve track, the curvature and superelevation angle are

PLAN
VIEW:



(a) Degree Curve, D

CROSS-
SECTION:



(b) Superlevation Angle, ϕ_{SE}

Figure 2.1 Definition of (a) Degree Curve and (b) Superlevation Angle

constants (and maximum). In transition spiral sections, the track curvature and superelevation angle vary quadratically, as shown in Figure 2.2. The track curvature and superelevation angle of a spiral section are approximated by second order polynomial functions fitted between tangent and constant radius curve track sections.

2.3.1 Flexible Rail Model

A flexible track model is adopted in which each rail is assumed to have lateral freedom only and rail rollover or overturning motion is neglected.* The mass-spring-damper model of the rail is shown in Figure 2.3. The rail is assumed to have effective lateral mass, viscous damping, and linear stiffness, m_r , c_r , and k_r , respectively. The rail lateral displacement, y_{rail} , is related to the net lateral wheel force by the rail equation of motion presented in Appendix A.

Typical values of effective lateral stiffness are 1.0×10^5 lb/ft for soft rail and 1.0×10^7 lb/ft for stiff rail [15]. A representative value of effective lateral damping is 1.0×10^4 lb-sec/ft. In the curving performance studies, the effect of lateral mass, m_r , is neglected.

2.4 Wheelset Model

The wheelset represents the basic element of the rail vehicle steering and support system. Each wheelset consists of two steel wheels rigidly mounted to a solid axle. A typical wheelset cross-section is shown in Figure 2.4. Each wheel profile has a steep taper section at the inner edge known as the flange and a shallow taper (or sometimes cylindrical) section from the flange to the outer edge known as the tread.

* If rail rollover occurs, the wheel/rail profile data which assumes fixed gage must be modified. The implications of gage changes due to rail flexibility are discussed in Section 2.4.2.

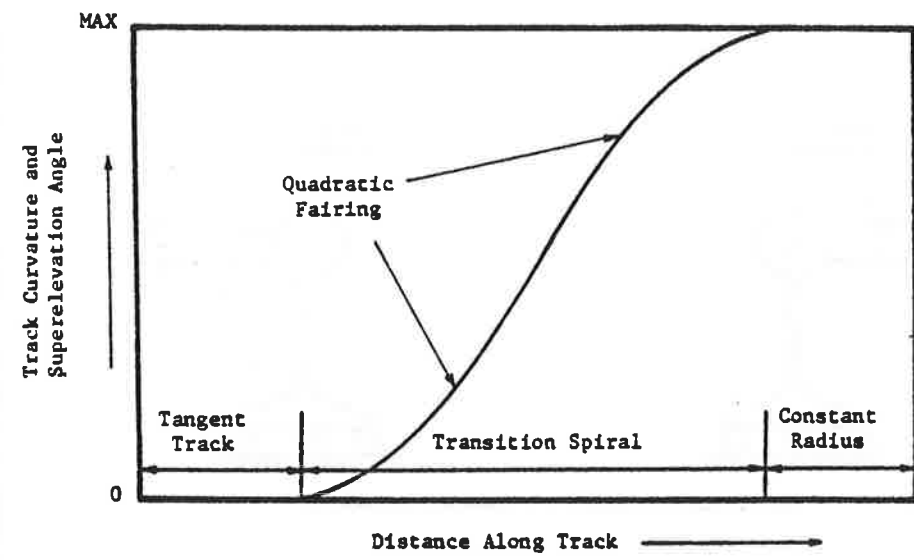


Figure 2.2 Track Curvature and Superelevation as a Function of Distance

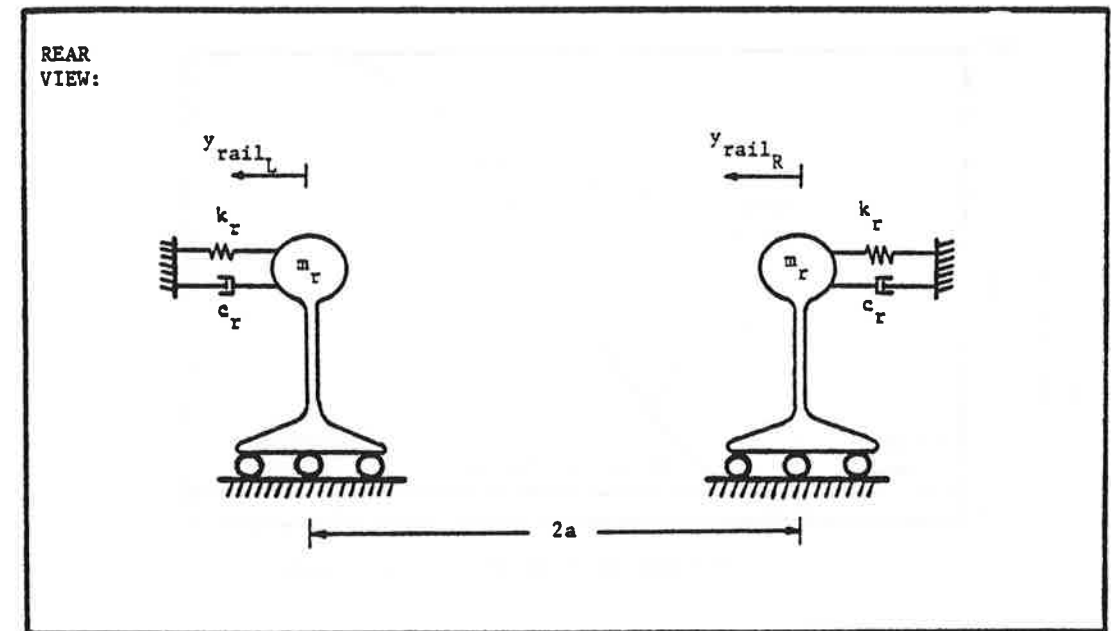


Figure 2.3 Lateral Track Model

REAR VIEW:

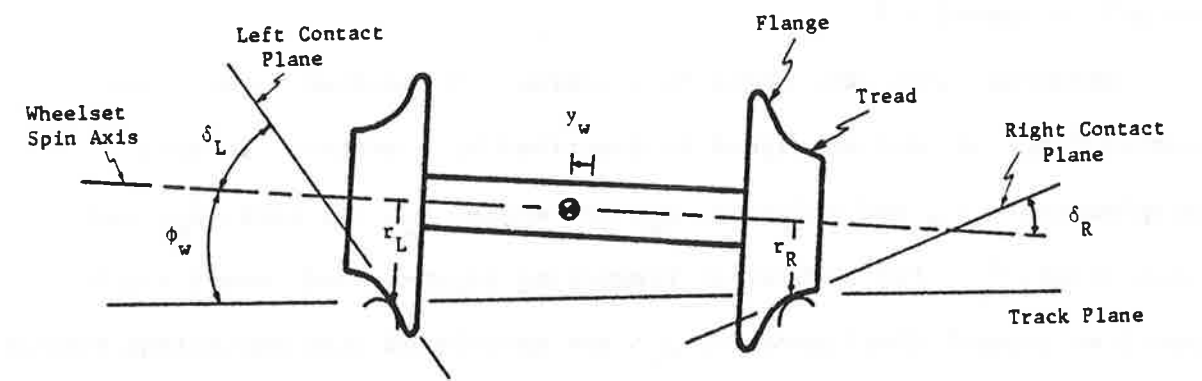


Figure 2.4 Typical Wheelset Cross-Section

A variety of wheel profile shapes are used by the transit industry.

A model has been developed to characterize wheelset dynamic curving behavior. The model accounts for nonlinear wheel/rail profile geometry and contact forces, and represents single-point and two-point contact at the flanging wheel.

2.4.1 Coordinate Systems

A free wheelset negotiating smooth, curved track is exposed to track curvature and inertial force inputs, including cant deficiency. The inertial force inputs are due to dynamic effects, and are discussed in detail in Appendix A.

Assuming continuous wheel/rail contact, a wheelset negotiating curved track at constant speed is described by 5 states: lateral displacement, y_W , and velocity, \dot{y}_W ; yaw angle, ψ_W , and rate, $\dot{\psi}_W$; and spin speed, $\dot{\theta}_W$. For a wheelset traversing right-handed curved track, positive lateral displacements, y_W , are associated with excursions toward the left rail (i.e., the outer or high rail). Thus, as the wheelset displaces laterally in the positive sense, flange contact occurs at the left wheel. In general, the spin speed, $\dot{\theta}_W$, differs from the pure rolling angular speed due to slippage (i.e., creepage) at the wheels.

Wheelset (W) and track (T) coordinate systems are introduced in Figure 2.5. The relation between the wheelset and track coordinate systems is

$$\begin{Bmatrix} x_W \\ y_W \\ z_W \end{Bmatrix} = \begin{bmatrix} 1 & \psi_W & 0 \\ -\psi_W & 1 & \phi_W \\ 0 & -\phi_W & 1 \end{bmatrix} \begin{Bmatrix} x_T \\ y_T \\ z_T \end{Bmatrix} \quad (2-3)$$

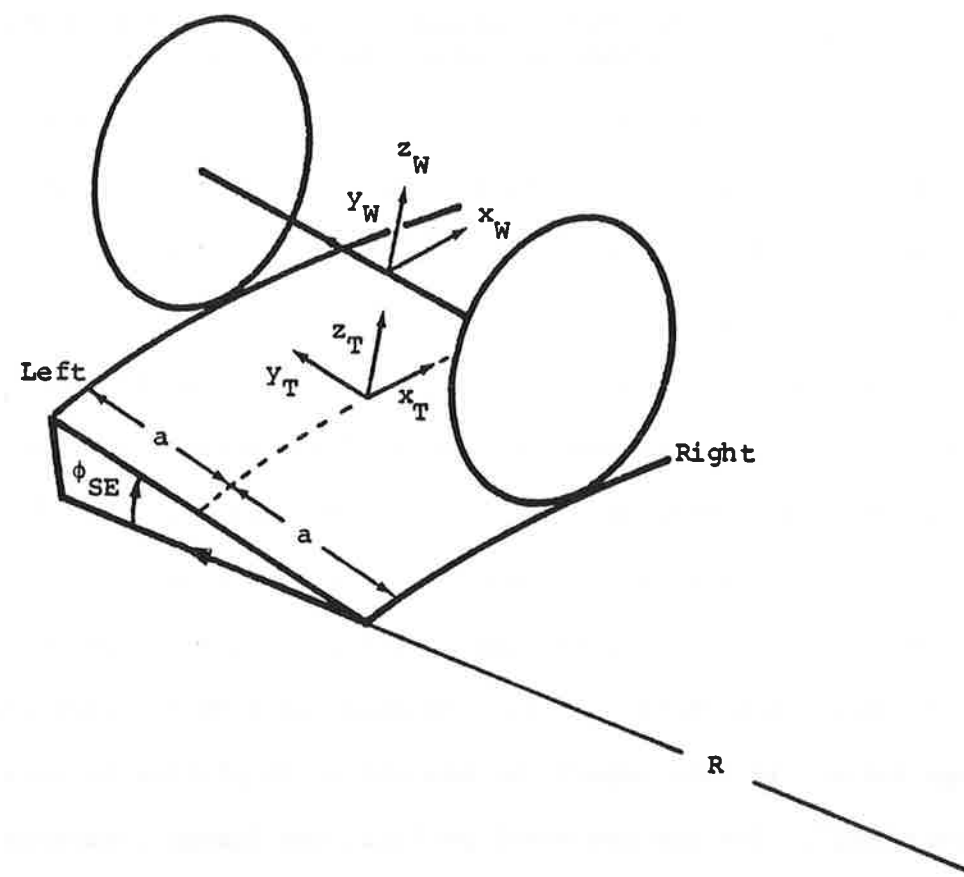


Figure 2.5 Track and Wheelset Coordinate Systems

where small yaw (ψ_W) and roll (ϕ_W) angles are assumed and pitch (θ_W) is neglected. Coordinate system transformation relations are derived in Appendix A (Section A.2).

2.4.2 Wheel/Rail Geometric Constraints

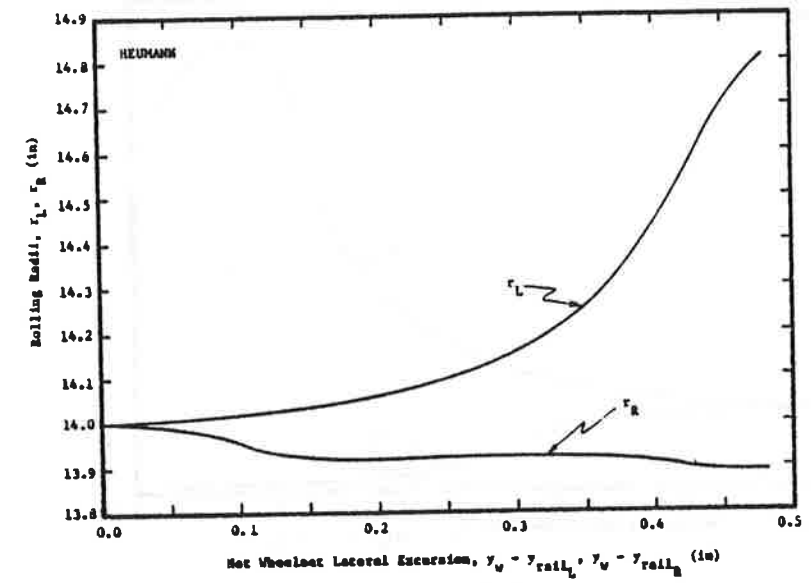
The following wheel/rail contact geometry parameters are defined:

- δ_L, δ_R left, right contact angle; i.e., angle of contact patch plane with respect to wheelset spin axis
- r_L, r_R left, right rolling radius, i.e., radial distance from wheelset spin axis to contact "point"
- ϕ_W wheelset roll angle relative to track plane.

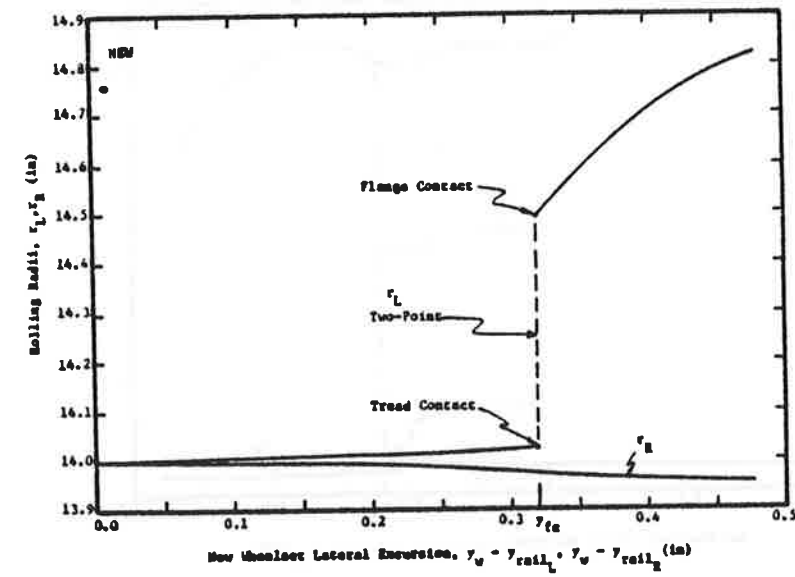
The contact angles, rolling radii, and wheelset roll angle are shown in Figure 2.4 for a wheelset in single-point contact at the left and right wheels.

For a wheelset which never loses contact with the rails, the rolling radii, contact angles, and wheelset roll angle are functions of the net wheelset-rail lateral excursion for a given wheel/rail profile. These functions are shown in Figures 2.6a, 2.7a, and 2.8a for a Heumann wheel on worn rail profile and in Figures 2.6b, 2.7b, and 2.8b for a new AAR 1 in 20 wheel on worn rail [1]. The data for both profiles assume standard gage rails. In this report the new AAR wheel profile is referred to as "new wheel". For the new wheel profile, the flange clearance is 0.32 in.

The rolling radii, contact angles, and roll angle are wheel/rail geometric constraint variables since they are functions of the net wheelset rail lateral displacement. If the rolling radii and contact angles are single-valued functions of the lateral excursion, single-point contact occurs at both wheels for all displacements. Continuous single-point contact occurs for the Heumann wheel profile. As the wheelset displaces laterally, the outer wheel shifts smoothly from tread to flange contact,

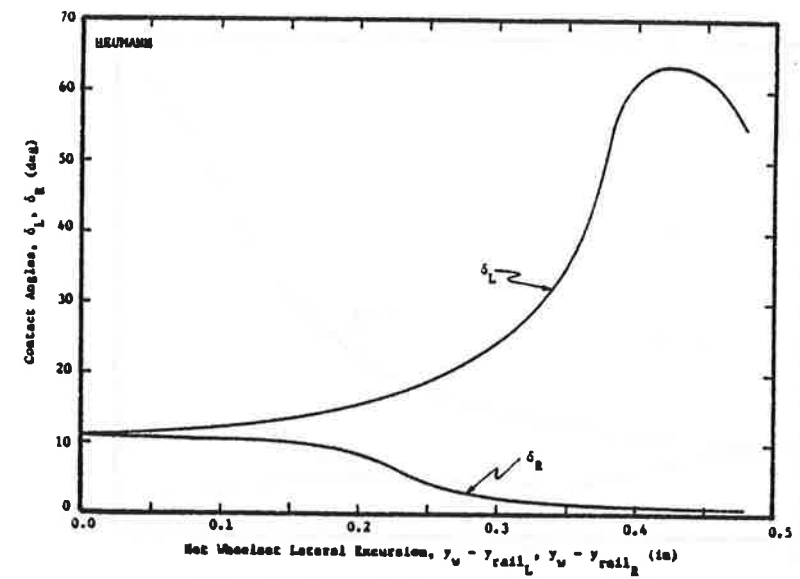


(a)

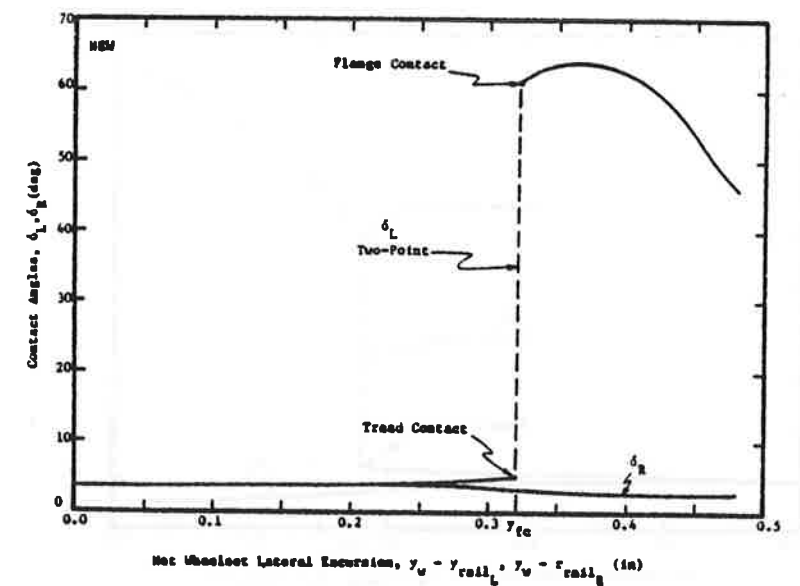


(b)

Figure 2.6 Rolling Radii vs. Net Wheelset Lateral Excursion for (a) Heumann Wheel and (b) New Wheel on Worn Rails

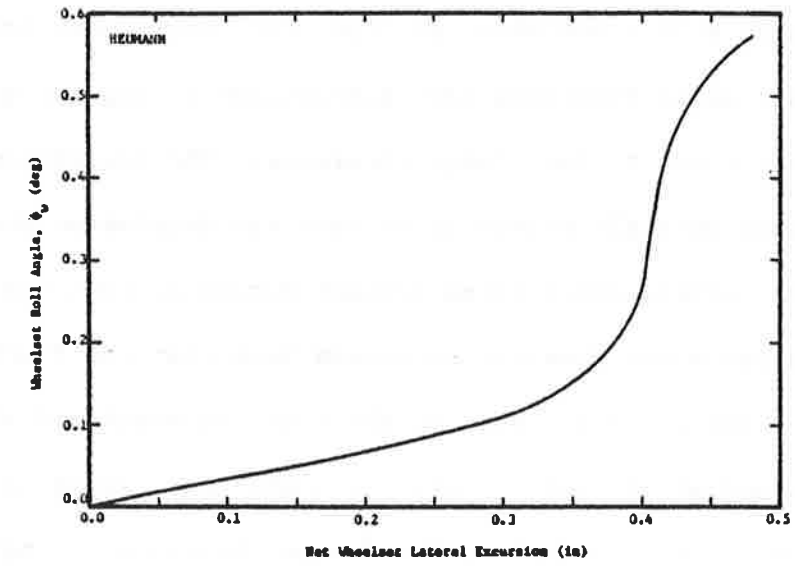


(a)

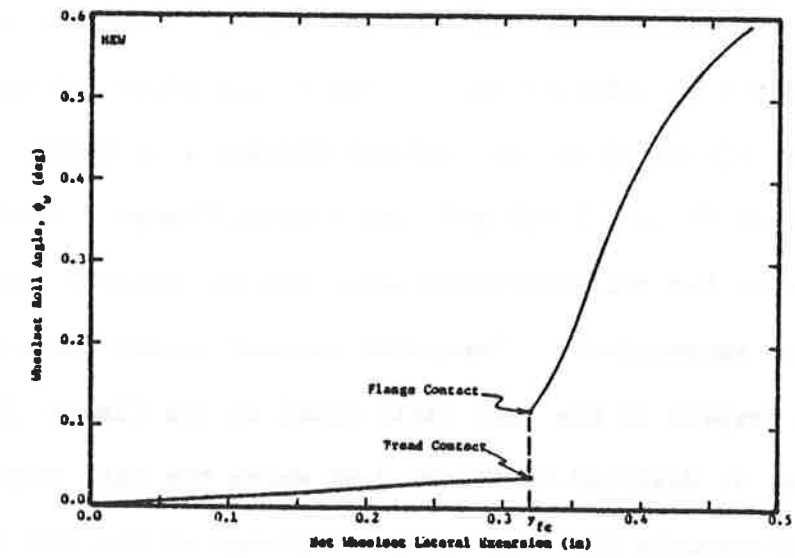


(b)

Figure 2.7 Contact Angles vs. Net Wheelset Lateral Excursion for (a) Heumann Wheel and (b) New Wheel on Worn Rails



(a)



(b)

Figure 2.8 Wheelset Roll Angle vs. Net Wheelset Lateral Excursion for (a) Heumann and (b) New Wheel on Worn Rails

while the inner wheel maintains tread contact. For other profiles with steep flanges, such as the new wheel profile, the outer wheel rolling radius and contact angle functions have discontinuous jumps at net lateral excursions equal to the flange clearance. The discontinuous jumps indicate that multiple points of contact can develop at the flanging wheel. As before, single-point tread contact occurs at both the inner and outer wheels for a net wheelset excursion less than the flange clearance. Two-point contact occurs at the flanging wheel and single-point contact occurs at the inner wheel for a wheelset excursion (relative to the flanging wheel rail) equal to the flange clearance. Single-point flange contact occurs at the flanging wheel for net excursions greater than the flange clearance.

For a wheelset negotiating right-handed curved track, the left wheel represents the outer or flanging wheel. Figure 2.9 shows the contact condition at the left wheel as the wheelset displaces laterally. Single-point tread contact (Figure 2.9a) and single-point flange contact (Figure 2.9c) occur for net excursions less than and greater than the flange clearance, respectively. Two-point contact occurs for a wheelset excursion (with respect to the left rail) equal to the flange clearance. Two-point contact is depicted in Figure 2.9b where the rail head is shown to contact simultaneously both the tread and flange of the left wheel.

For a wheelset in two-point contact,^{*} the displacement relative to the left rail is fixed at the flange clearance. Mathematically,

*The terminology assumes that the two points of contact occur at the flanging wheel. "A wheelset in two-point contact" actually has three points of wheel/rail contact, two at the flanging or outer wheel and one at the inner wheel.

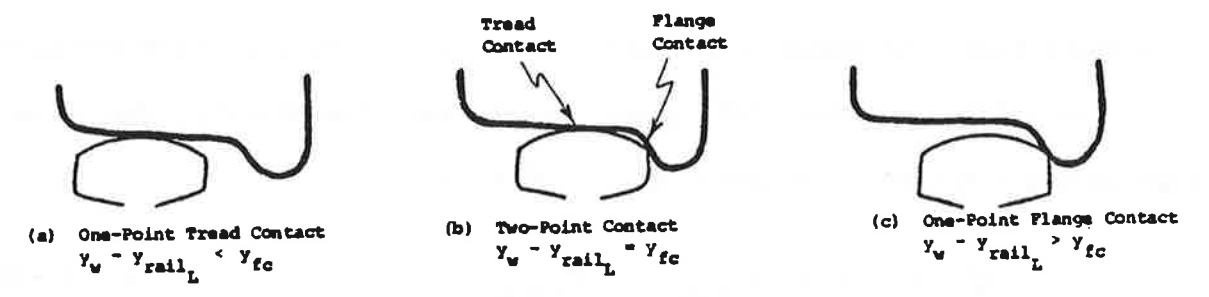


Figure 2.9 Left Wheel/Rail Contact

$$y_W - y_{\text{rail}_L} = y_{fc} \quad (2-4)$$

where y_W and y_{rail_L} are the lateral displacements of the wheelset and left rail, respectively, and y_{fc} is the flange clearance. Equation (2-4) represents a constraint relation between the wheelset and left rail lateral excursions for two-point contact. The constraint relation determines the contact geometry of the tread and flange contact points at the left wheel.

The contact geometry (rolling radius, contact angle) at each wheel is specified by the net lateral excursion according to the geometric constraint functions shown in Figures 2.6 and 2.7. These profile functions apply for a fixed standard rail gage. Due to rail flexibility, the actual gage is not constant. The gage, g' , is given by

$$g' = 2a + y_{\text{rail}_L} - y_{\text{rail}_R} \quad (2-5)$$

and differs only slightly from $2a$. Since gage changes occur, use of the fixed-gage wheel/rail profile data represents an approximation. In this work, it is assumed that (1) the flanging wheel contact geometry is correct, and (2) the nonflanging wheel contact geometry is in error but the error is small since the tread contact geometry is relatively constant.

In addition to rail flexibility, rail rollover alters the wheel/rail profile data. The effect of rail rollover which changes the rail cant angle, is not addressed.

In summary, some wheel/rail profiles, notably many European profiles including the Heumann wheel profile achieve single-point contact at all realistic displacements. Many new wheel profiles, including the standard

AAR 1 in 20 profile used commonly in the U. S. contact the rails at multiple points during normal use.

2.4.3 Wheel/Rail Contact Forces

For a wheelset negotiating a curve, slip or creepage may develop at the rails. Normal loads acting on the slipping wheelset result in the generation of friction-type forces known as creep forces. In general, the wheel/rail contact forces are separated into normal forces acting perpendicular to the contact plane and creep forces acting in the plane.

Each point of wheel/rail contact is a "patch" of finite area. At each patch, a state between pure-roll and pure-slip exists. During the last ten years there has been a significant improvement in the understanding of the friction mechanism which develops at the contact patch. Kalker [16] has developed linear, simplified nonlinear, and exact nonlinear theories and computational programs to predict contact patch creep forces. In this report a heuristic nonlinear creep force model is used which is computationally fast and reasonably accurate. This model predicts a resultant creep force which agrees with linear Kalker theory for small creepages and which saturates at the adhesion limit for larger creepages, as shown in Figure 2.10. In Appendix A, the creep force model is described in detail and expressions for the creepages are derived.

2.5 Truck Model

This section describes models of conventional and innovative truck configurations. All of the physical configurations discussed in Section 2.5.1 through 2.5.3 represent special cases of the generic model presented in section 2.5.4.

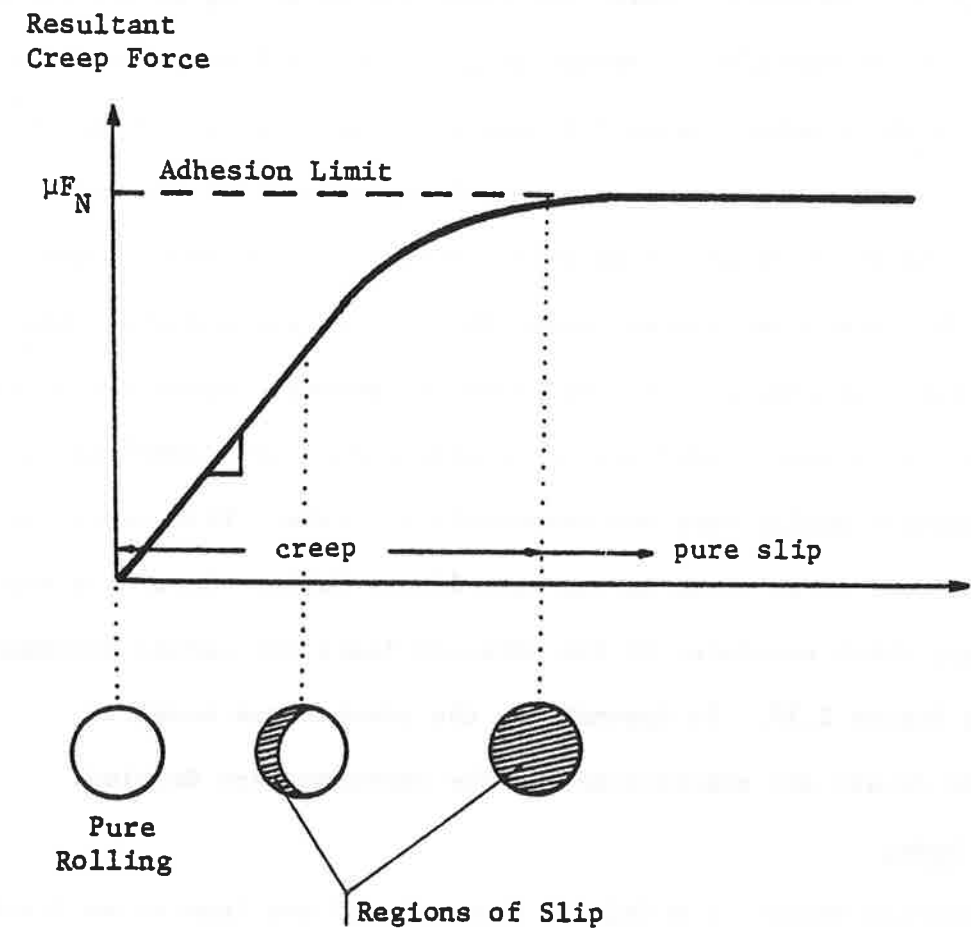


Figure 2.10 Contact Patch Creep Force vs. Creepage Relation

2.5.1 Conventional Truck

In a conventional truck, the wheelsets are connected to the truck frame by primary suspension elements. Typically, the primary suspension elements consist of coiled springs, rubber chevrons or rubber bushings between the bearing adapter and the truck frame. A conventional truck is shown schematically in Figure 2.11. The following notation is used: k_{px} is the primary longitudinal stiffness, k_{py} is the primary lateral stiffness, $2d_p$ is the distance between the longitudinal springs, and $2b$ is the truck wheelbase.

2.5.2 Self-Steered Radial Truck

A self-steered radial truck is a conventional truck with an additional direct connection between the two wheelsets by means of passive springs or structural members in shear and bending. A schematic representation of a self-steered truck is shown in Figure 2.12.

A self-steered truck has two additional stiffness parameters which connect the two wheelsets directly. These are defined as the direct interaxle bending stiffness, k_{b2} , and the direct interaxle shear stiffness, k_{s2} . The stiffnesses k_{b2} and k_{s2} are sufficient to model any direct elastic connection between the two wheelsets. Most often this connection takes the form of steering arms [17], cross-braces [18], or similar linkages as shown in Figure 2.13.

The term self-steered radial truck describes the steering action produced by direct interwheelset connections when the stiffness k_{b2} is low. With soft k_{b2} , a yaw motion of one wheelset causes the other wheelset to yaw in the opposite direction helping to align the wheelsets radially in a curve. The self-steered radial design has two essential differences

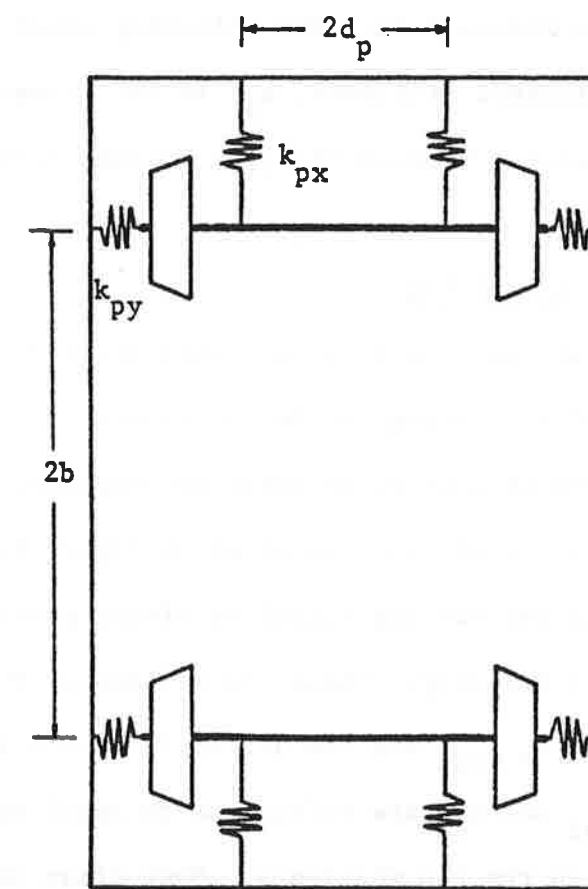


Figure 2.11 Schematic of Conventional Truck

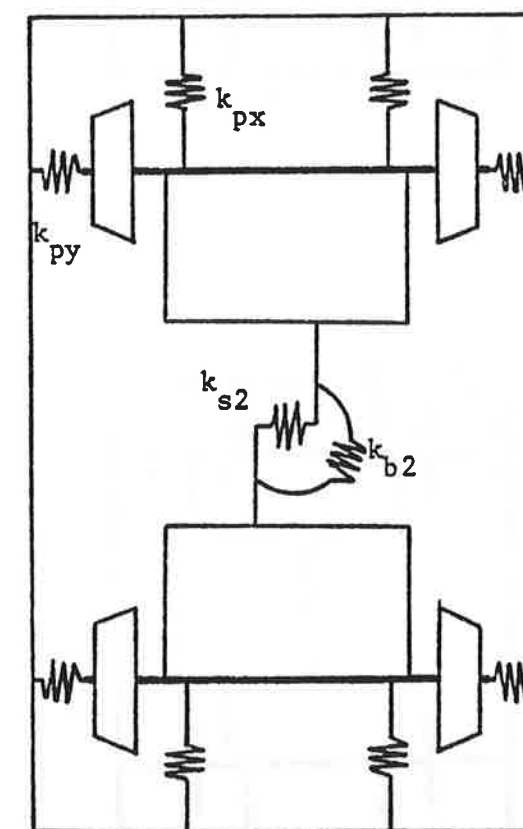
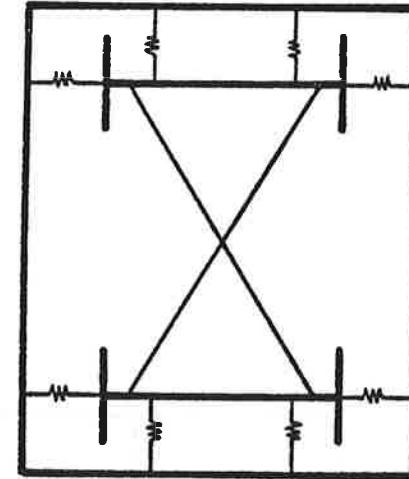
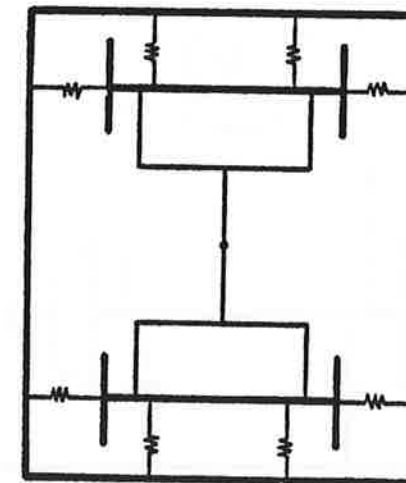


Figure 2.12 Schematic of Self-Steering Radial Truck



(a)
Cross-Braced



(b)
Steering Arm

Figure 2.13 Alternative Self-Steering Radial Truck Configurations

from the conventional design. First, forces are transmitted directly between the wheelsets, and second, the total truck shear stiffness is not limited as it is in the conventional design. The first property allows for a more stable design since the truck frame can become dynamically decoupled from hunting wheelsets [19]. The second property helps the truck reduce wheelset angles of attack during curve negotiation after flanging has occurred.

2.5.3 Forced-Steered Radial Truck

A forced-steered truck utilizes linkages between the carbody and the truck frame to force the wheelsets into near radial alignment when traversing curves. In particular, the yaw angle that develops between the carbody and the truck is related to the curve radius, and linkages between the carbody and the wheelsets can be used to force the wheelsets into a more radial alignment. Similarly, the lateral displacement between the carbody and truck is related to the cant deficiency, and linkages can be designed to produce forces on the wheelsets as a function of the cant deficiency. Thus, a forced-steered radial truck is a self-steered radial truck with additional linkages which impose forces on the wheelsets as a function of the relative yaw and lateral displacements between the carbody and truck.*

Several forced-steered truck configurations have been proposed with different linkage arrangements. The schematics of three configurations

*Typically, the forced-steering linkages are connected to the bolsters, rather than the carbody directly. However, since the bolsters are stiffly connected to the carbody, they essentially execute the same motions. Thus, in this discussion, the forced-steering linkages are assumed to be connected to the carbody. This differs from the development in Appendix B, which assumes that the linkages are connected to the bolster (in yaw).

that have forced steering action are shown in Figures 2.14, 2.15 and 2.16. In this study they are designated the S, L, and U trucks because configurationally they are similar to the Scales [20], List [17], and UTDC* [21] designs, respectively.

The bending and shear stiffnesses due to forced-steering linkages are equivalent to "effective" truck interaxle bending and shear stiffnesses, respectively. Typically, the L truck has high effective interaxle shear stiffness and the U truck has zero interaxle shear stiffness. The S truck has properties similar to the three piece freight truck because of its high interaxle bending stiffness and relatively low interaxle shear stiffness. For each prototype, expressions for the effective stiffnesses and the steering gains in terms of linkage stiffness and dimensions are included in Figures 2.14, 2.15 and 2.16 with detailed derivations [1].

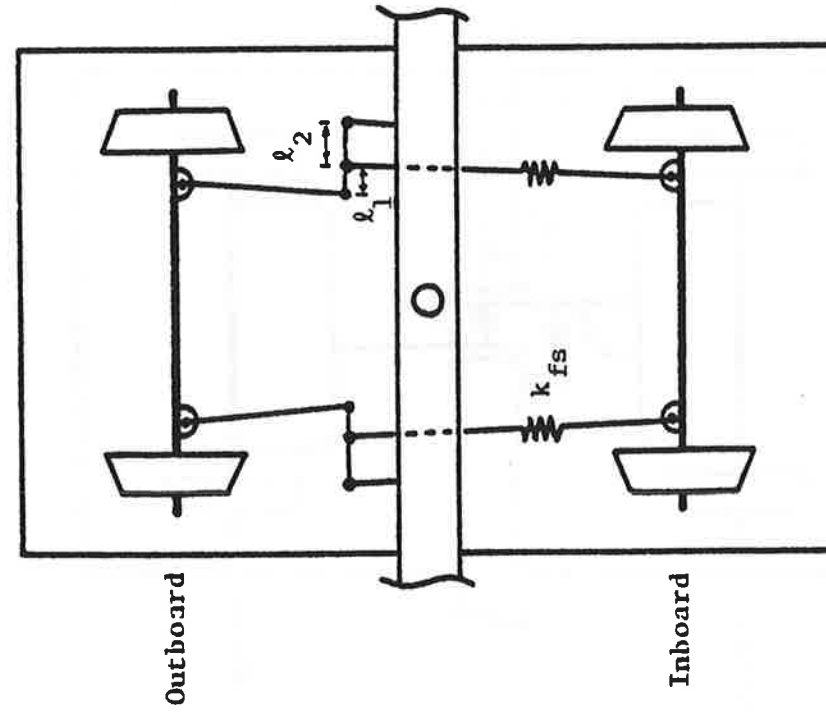
The actuation of the forced-steering linkages for the forced steered trucks can be represented by a geometric offset in series with a linkage bending and/or shear stiffness. The lateral and yaw offsets, Δy and $\Delta \psi$, as well as the linkage stiffnesses, k_{s2} and k_{b2} , are shown in Figure 2.17.

The curving performance of a forced-steered truck is a function of the steering gain G which is determined by the dimensions of the forced-steering linkages. The gain can be set by appropriate selection of linkage dimensions such that kinematically (i.e., with the assumption of rigid steering linkages and no flange forces) the wheelsets track the pure rolling line,** the track centerline or any line parallel to the track centerline. Theoretically, the gain which makes the wheelsets track

*Urban Transportation Development Corporation Ltd., Ontario, Canada

**The lateral displacement that produces pure kinematic rolling of a single wheelset.

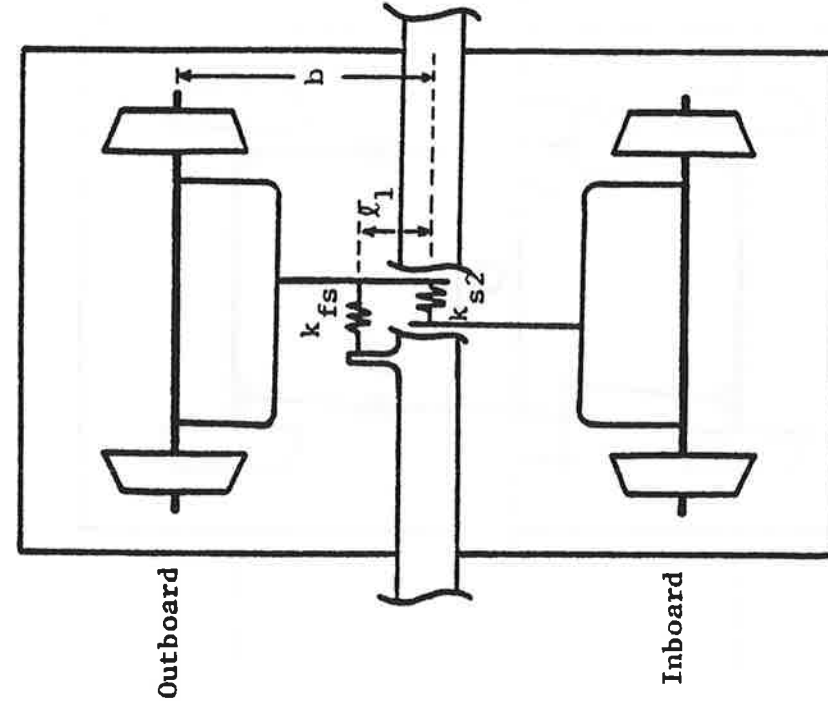
"S" Truck



$$\begin{aligned}
 k_b &= k_{b1} + k_{b2} \\
 k_{b1} &= d_{px}^2 k \\
 k_{b2} &= \frac{1}{2} d_{px}^2 k_{fs} \left(1 + \frac{l_2^2}{l_1 + l_2} \right)^2 \\
 k_s &= k_{s1} + k_{s2} \\
 k_{s1} &= \frac{d_{px}^2 k_{py}}{d_{px}^2 k_{px} + b^2 k_{py}} \\
 \Delta\psi_1 &= \pm 2G \left(\frac{\psi_{w1} + \psi_{w2}}{2} - \psi_c \right) \\
 \Delta\psi_2 &= 0 \\
 G &= \frac{1}{l_1 + 2l_2}
 \end{aligned}$$

Figure 2.14 Schematic Diagram of "S" Forced-Steered Truck
(Primary Suspension System Not Shown)

"L" Truck



$$k_b = k_{b1} + k_{b2}$$

$$k_{b1} = d_p^2 k_{px}$$

$$k_{b2} = \frac{(b-l_1)^2 k_{fs} k_{py}}{(4k_{py} + k_{fs})} *$$

$$k_s = k_{s1} + k_{s2} + \left(\frac{G_2}{b}\right) k_{b2} \quad \text{very small}$$

$$k_{s1} = \frac{d_p^2 k_{px} k_{py}}{d_p^2 k_{px} + b^2 k_{py}}$$

$$\Delta\psi_1 = + 2G \left(\frac{y_{w1} - y_{w2}}{2b} \right) - \psi_c$$

$$+ 2 \left(\frac{G+1}{b} \right) \left(\frac{y_{w1} + y_{w2}}{2} - y_f \right)$$

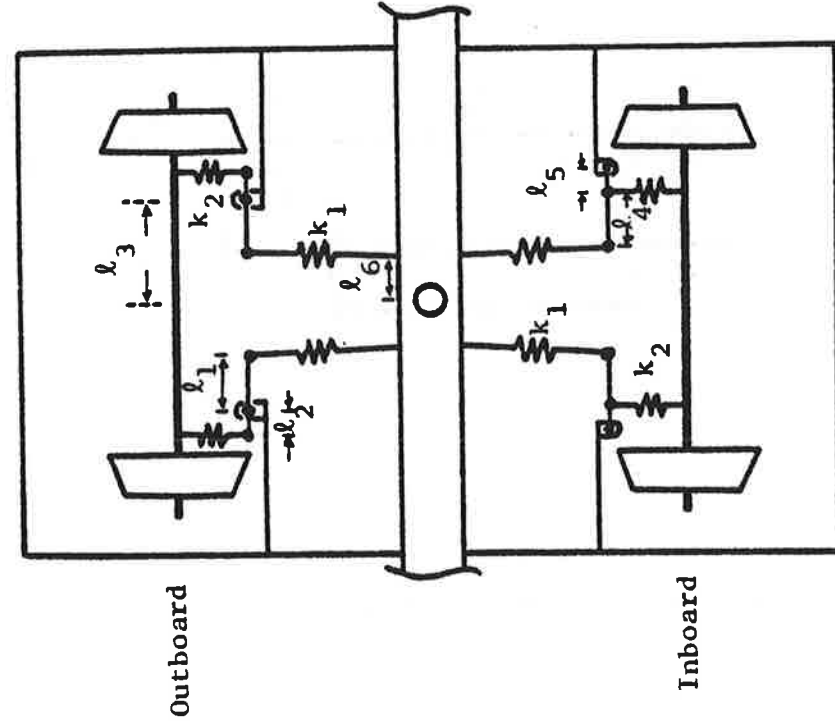
$$\Delta\psi_2 = 0$$

$$G = \frac{k_1}{b-l_1}$$

* Assumes stiff k_{s2} (for symmetry).

Figure 2.15 Schematic Diagram of "L" Forced-Steered Truck
(Primary Suspension System Not Shown)

"U" Truck



$$k_b = k_{b1} + k_{b3}$$

$$k_{b1} = d^2 k_{px}$$

$$k_{b3} = \frac{k_1 k_2 l_2^2 l_3^2}{(l_R^2 k_1 + k_2)}$$

$$l_R = \frac{l_1}{l_2} \text{ Outboard}$$

$$l_R = \frac{l_4 + l_5}{l_5} \text{ Inboard}$$

$$k_s = k_{s1} + k_{s3}$$

$$k_{s1}^* = \frac{(d^2 k_{px} + k_{b3}) k_{py}}{d^2 k_{px} + k_{b3} + b^2 k_{py}}$$

$$\Delta\psi_1 = 0$$

$$\Delta\psi_2 = \pm 2G(\psi_F - \psi_C)$$

$$G = \frac{l_6}{l_R l_3} \quad **$$

* Assumes stiff k_{s2} .

** Linearized.

Figure 2.16 Schematic Diagram of "U" Forced-Steered Truck
(Primary Suspension System Not Shown)

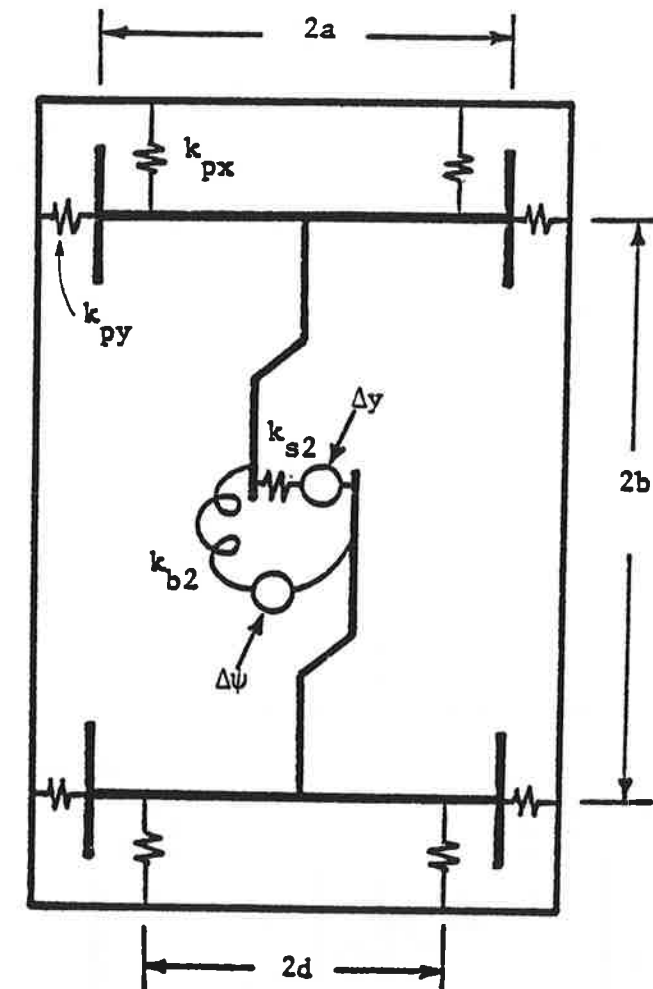


Figure 2.17 Forced-Steering Truck Model

the pure rolling line ensures perfect radial alignment (i.e., neutral steering) of the wheelsets.

In general, the pure rolling line gain is appropriate before flange contact occurs since it correctly aligns the wheelsets radially. However, after flange contact occurs the assumptions implicitly in the derivation of the pure rolling line gain are violated and as a result G_{pr} may not align the wheelsets appropriately. Other gains may have relative advantages. The pure rolling line gain is typically used in practice in prototype vehicles [22].

2.5.4 Generic Truck Model

A generic truck model that represents the different forced-steered truck prototypes as well as the conventional and self-steered radial trucks is shown in Figure 2.18. The generic truck model represents the suspension system of the conventional truck consisting of bearing connections between the wheelsets and truck frame. These primary suspension elements are modelled as parallel combinations of linear springs and viscous dampers between the wheelsets and truck frame in the longitudinal and lateral directions. In addition, the generic truck model includes the effect of steering linkages between the wheelsets, trucks, and carbody to represent a variety of forced-steered truck designs. The steering linkages of self and forced-steered trucks are also modelled as parallel linear spring/viscous damper combinations.

The generic truck model is reduced to particular truck configurations by appropriate assignment of stiffnesses and steering gain values [1].

The forced-steered truck studies in this report are based primarily on the L design. The L design has the inherent features of forced-steered trucks making it suitable for parametric study.

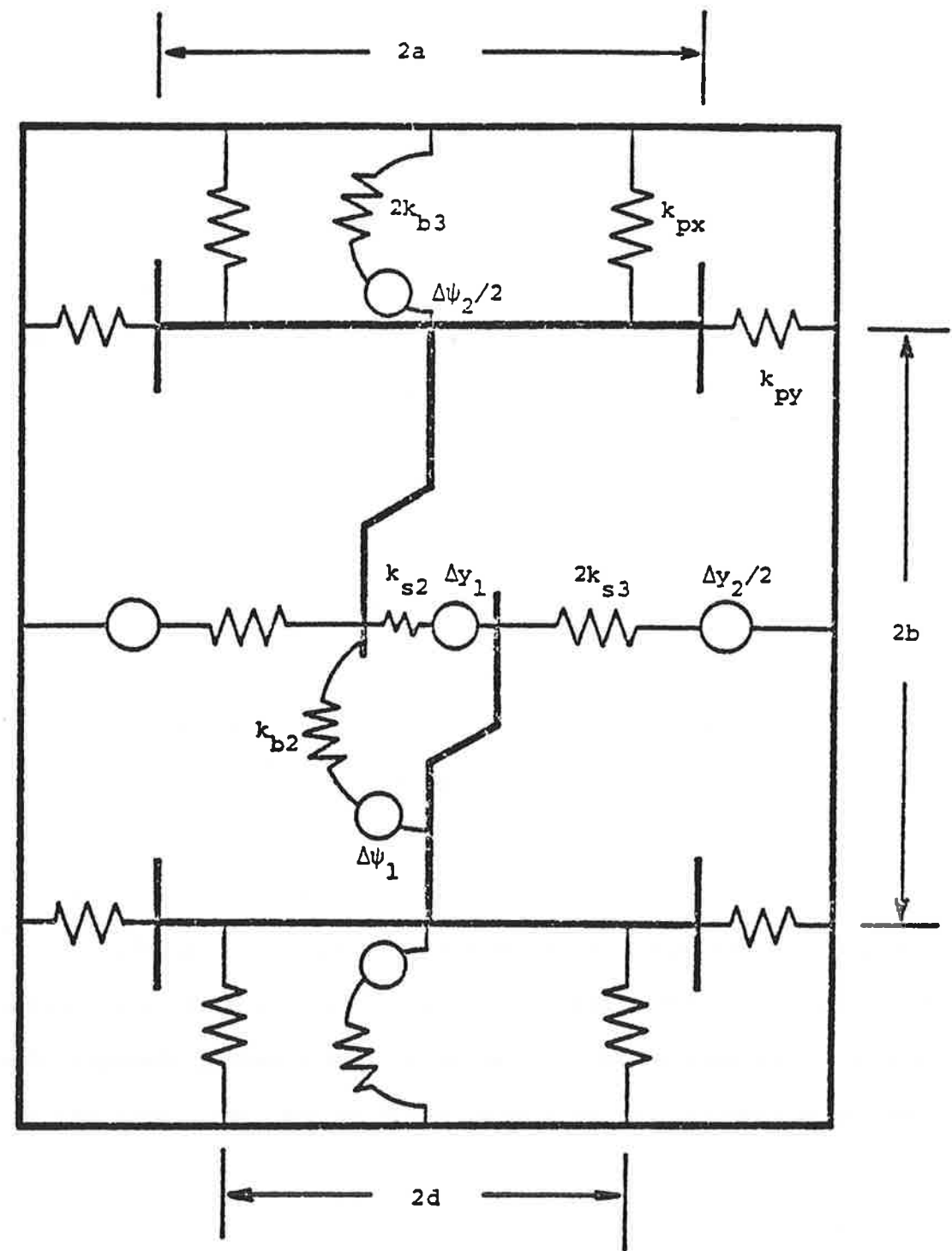


Figure 2.18 Generic Truck Model

(Important design parameters for forced-steered trucks include shear and bending stiffnesses and the steering gains.) In addition, the L truck was selected as one which has potential application to transit systems. Relative performance, design, and manufacturing benefits of specific forced-steered truck configurations are not addressed in this report.

2.6 Vehicle Model

A rail passenger vehicle consists of a carbody supported by four wheelsets, two truck frames, and two bolsters. The wheelsets are connected to the truck frame and is attached to the carbody via secondary suspension elements.

As a rail vehicle negotiates a curve, internal and external forces and moments act on the wheelsets, trucks, bolsters, and carbody. The internal forces and moments are due to the suspension components. The external forces and moments are due to (1) inertial forces, including weight and cant deficiency forces, (2) wheel/rail contact forces, and (3) drawbar or buff loads.

This section presents the rail vehicle model, shown schematically in Figures 2.19 and 2.20. The vehicle model incorporates the generic truck model described in the previous section. The dynamic curving equations of motion of the rail vehicle are developed in Appendix B.

2.6.1 Carbody/Bolster Model

The bolster is a structural member which rests on the truck and carries the load of the carbody from the secondary springs to the center-plate of the truck frame. During curve negotiation, the truck frame yaws relative to the bolster against the frictional resistance due to

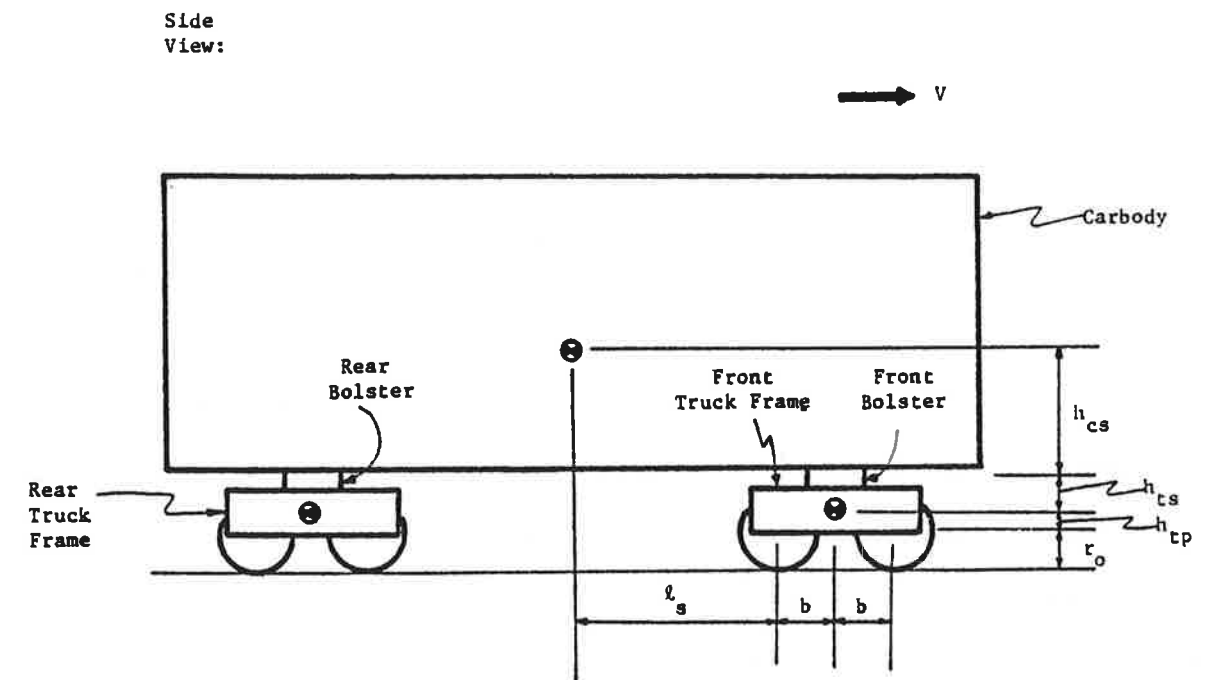


Figure 2.19 Rail Vehicle Model, Side View

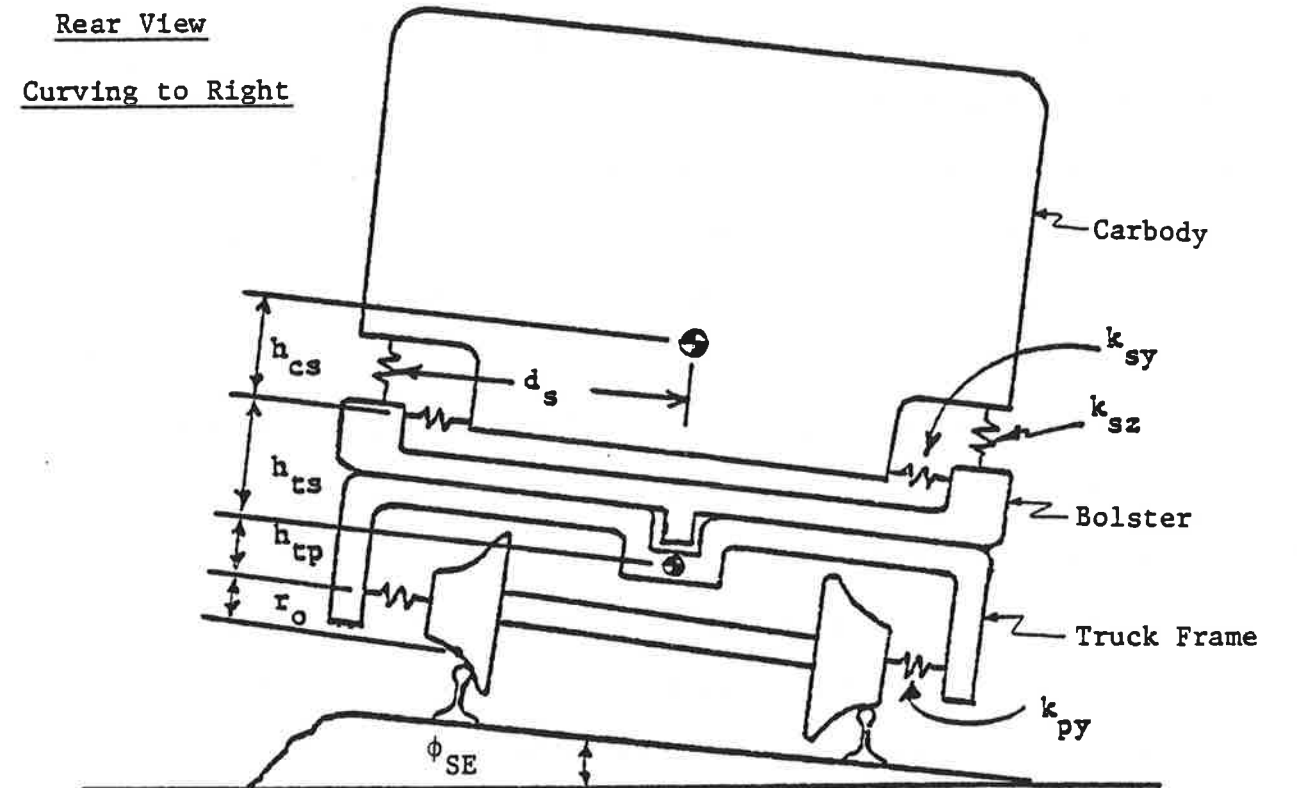


Figure 2.20 Rail Vehicle Model During Curving,
Rear View

pads at the centerplate. The physical arrangement and the model of the yaw suspension are shown in Figures 2.21 and 2.22 respectively. The bolster is connected to the carbody by anchor rods which provide torsional stiffness and damping. Typically, the torsional stiffness is quite high (i.e., $k_{s\psi} > 5.0 \times 10^6$ ft-lb/rad).

The secondary suspension system acting between the truck, bolster, and carbody is modelled as follows. The carbody is coupled to the bolster via (1) parallel spring/viscous friction elements in the lateral and vertical directions, as shown in Figure 2.22 and (2) a torsional spring/viscous damper combination in the yaw direction. The bolster is connected to the truck frame by a torsional coulomb damper which saturates at a breakaway torque. For computational reasons, the model of the coulomb damper is modified to include a linear viscous band at the origin, as shown in Figure 2.23.

In the performance studies, it is assumed that the anchor rods are rigid, i.e., $k_{s\psi} = \infty$. Thus, each bolster follows the carbody motion in yaw and the truck motion in the lateral direction.

2.7 Numerical Methods of Dynamic Curving Analysis

A dynamic curving analysis has been developed to predict dynamic behavior of the rail vehicle during curve negotiation. The behavior is described by coupled, nonlinear, differential equations of motion, which are developed in detail in Appendix B.

A total of 42 states (or 21 degrees of freedom) are used to characterize the full vehicle model: 20 states for the 4 wheelsets, 8 states for the 2 trucks, 6 states for the carbody, and 8 states for the rails. Each wheelset has a degree of freedom (i.e., 2 states) to

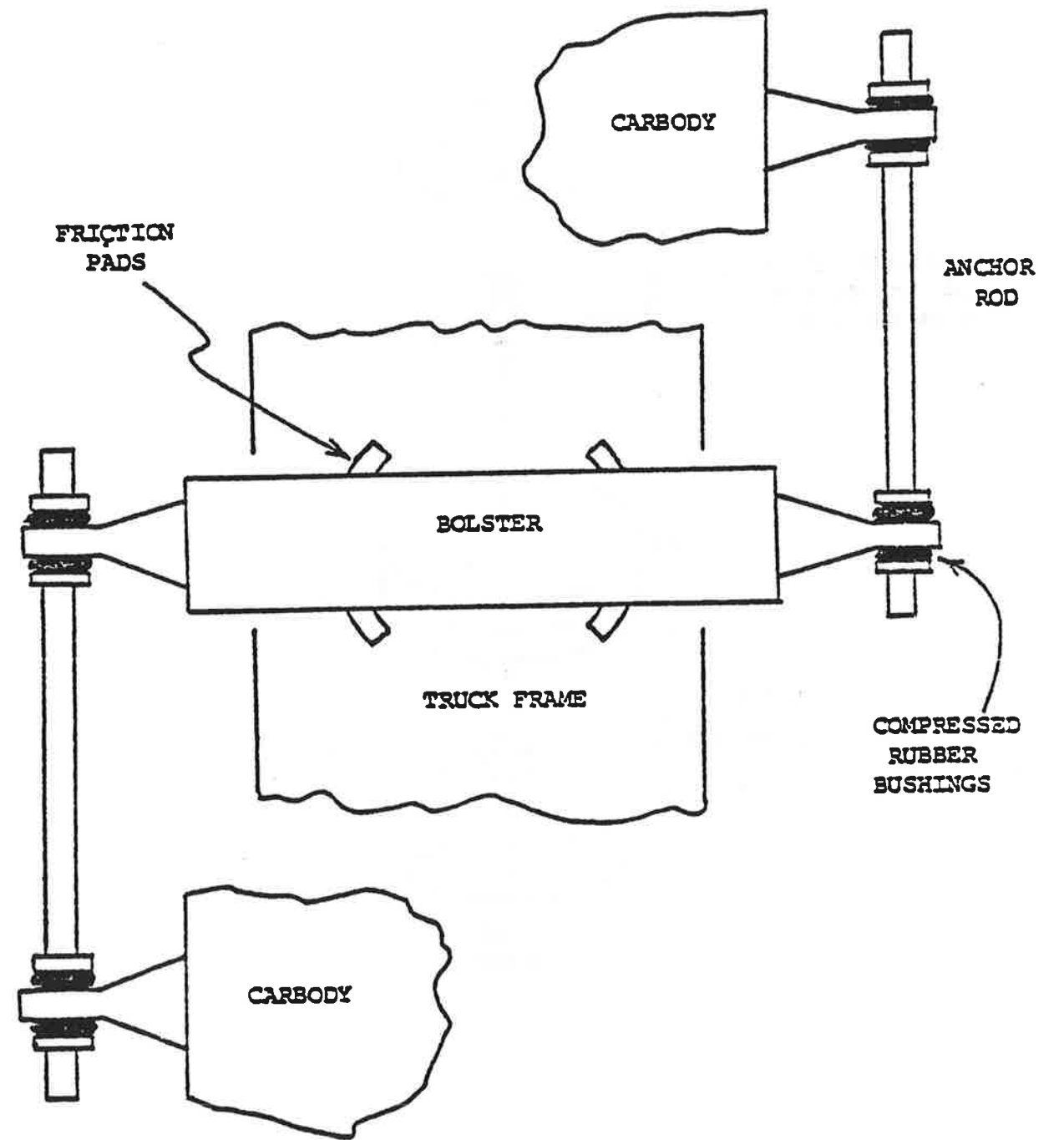


Figure 2.21 Physical Arrangement of the Secondary Yaw Suspension

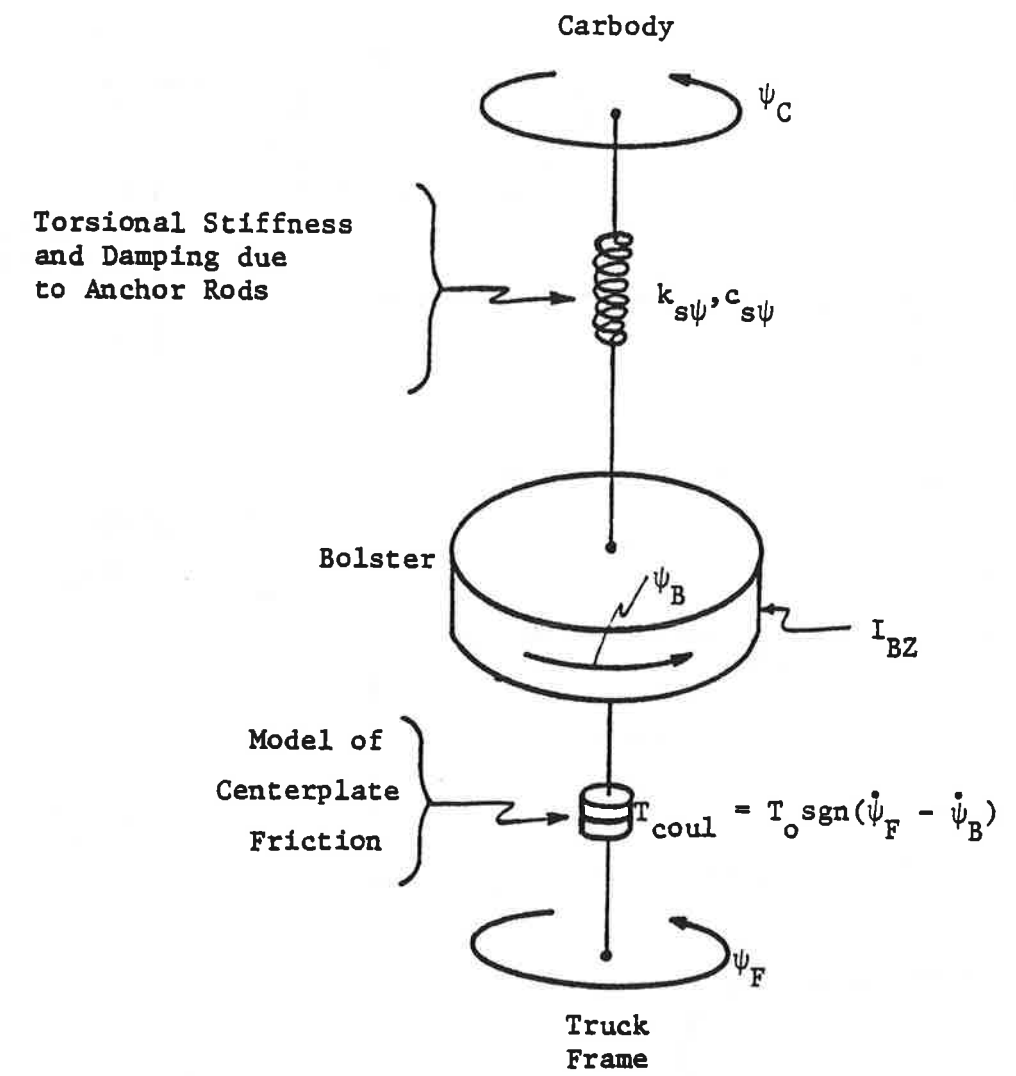


Figure 2.22 Model of Secondary Yaw Suspension

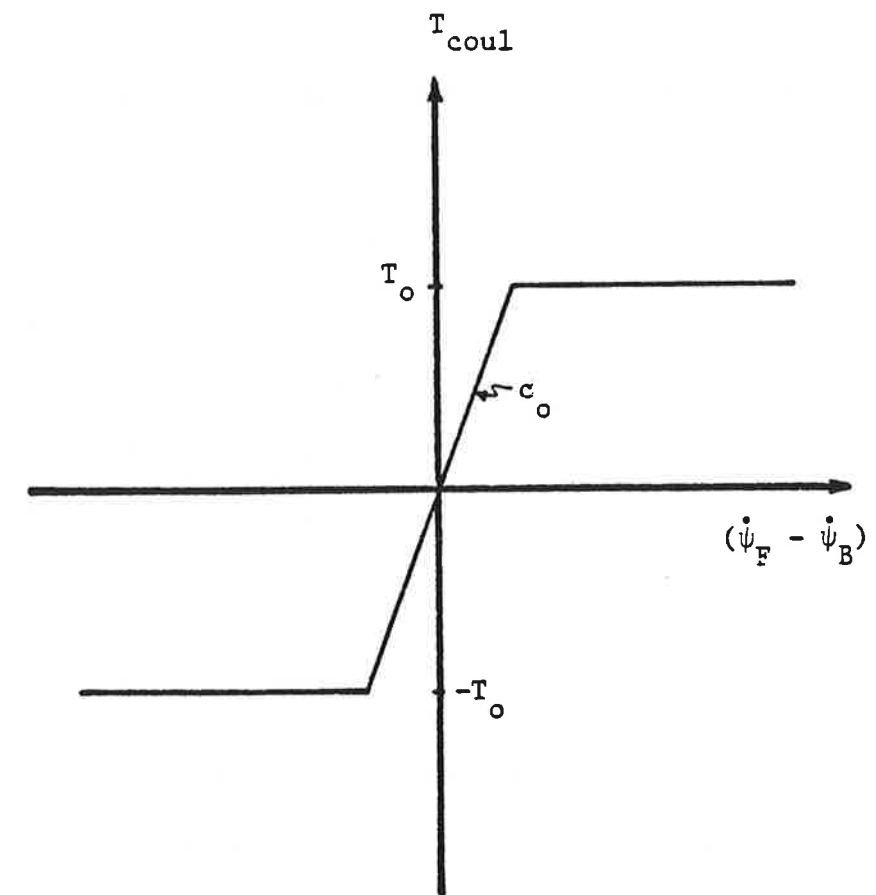


Figure 2.23 Truck Frame/Bolster Yaw Suspension Characteristic

describe its lateral and yaw motions, as well as a state to describe its spin speed. Each truck has a degree of freedom to describe its lateral and yaw motions. The carbody is characterized by lateral, yaw, and roll degrees of freedom. In addition, a simple model of the track is adopted in which the rail at each wheel has a state to describe its lateral motion.

In matrix notation, the dynamic curving equations of motion are written as:

$$[M] \ddot{\{\bar{X}\}} + [C(\bar{X}, \dot{\bar{X}})] \dot{\{\bar{X}\}} + [K(\bar{X}, \dot{\bar{X}})] \{\bar{X}\} = \{\bar{B}(\bar{X}, \dot{\bar{X}})\} \quad (2-6)$$

where $[M]$, $[C]$, and $[K]$ are mass, damping and stiffness matrices, $\{\bar{B}\}$ is a forcing function vector due to track curvature and cant deficiency, and $\{\bar{X}\}$ is a displacement state vector. The damping and stiffness matrices are functions of displacements and velocities due to nonlinear suspension components.

Equation (2-6) is a set of coupled, nonlinear differential equations. The equations are solved by digital integration using a variable time-step, fourth-order Runge-Kutta scheme, which requires that the equations be in first-order form. The transformation is obtained by letting

$$\dot{\{\bar{X}\}} = \{\bar{U}\} \quad (2-7)$$

where $\{\bar{U}\}$ is a velocity state vector. Substituting into equation (2-6) gives

$$\{\bar{U}\} = [M]^{-1} (\{\bar{B}(\bar{X}, \dot{\bar{X}})\} - [K(\bar{X}, \dot{\bar{X}})] \{\bar{X}\} - [C(\bar{X}, \dot{\bar{X}})] \{\bar{U}\}) \quad (2-8)$$

Equations (2-7) and (2-8) are numerically integrated to provide time histories of (1) all the state variables, i.e., $\{\bar{X}\}$ and $\{\bar{U}\}$, (2) the wheel/rail contact forces, and (3) the contact patch work.

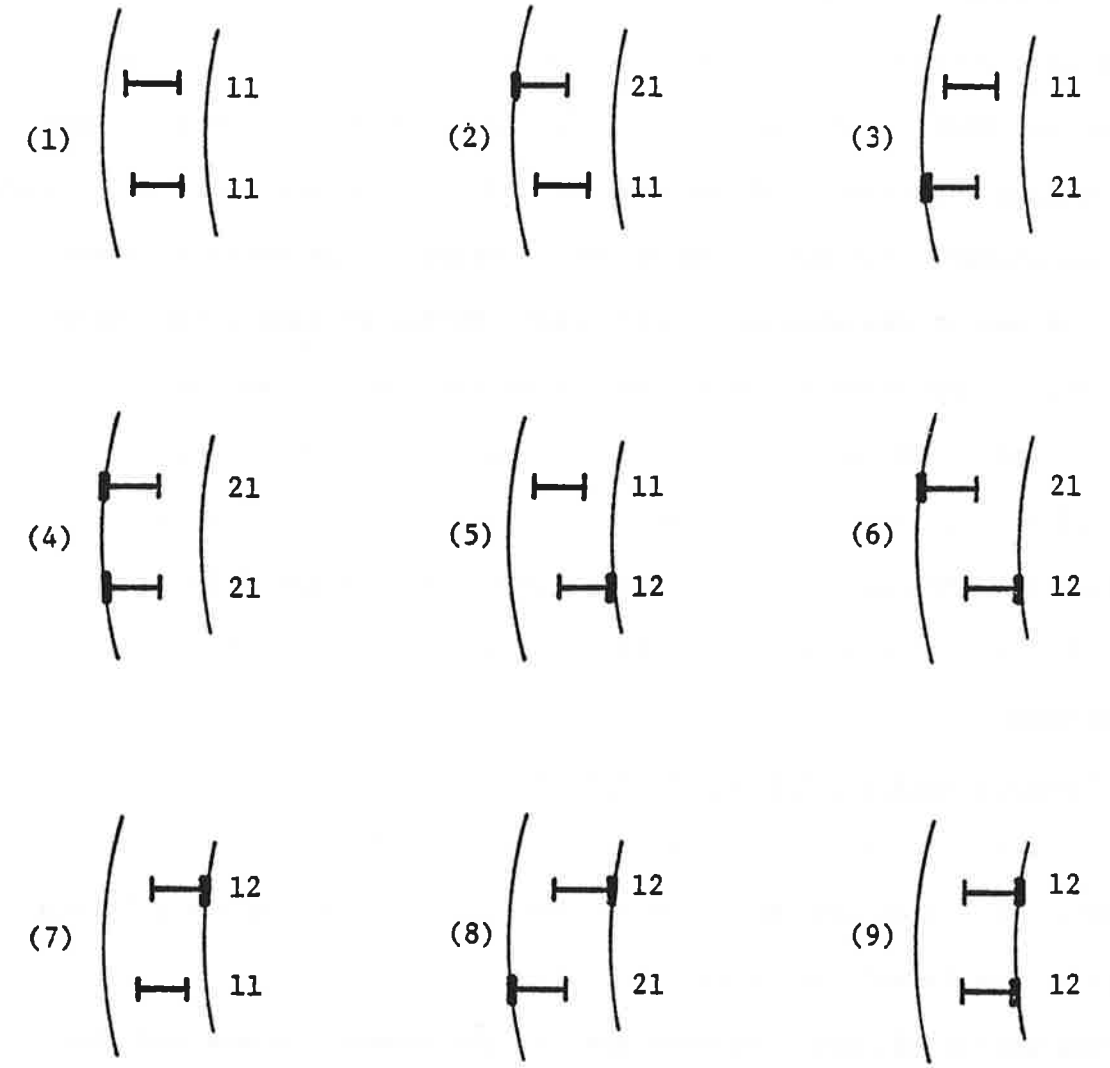
The dynamic curving analysis is coded in a FORTRAN program, entitled DYCURV (DYnamic CURVing). A flowchart of the program appears in Appendix B. The program automatically accounts for the possibility of two-point contact at any wheel of the vehicle. Figure 2.24 shows the possible wheel/rail contact conditions for the leading and trailing wheelsets of a truck with new wheels. Two-point contact can develop at the outer or inner wheels of any of the wheelsets, especially during violent curve entry and exit, during negotiation of reverse curves, and during hunting.

Program DYCURV has been used to simulate the dynamic response of the rail vehicle model as it enters and negotiates curved track. In general, the program requires a small time-step of digital integration (~ 0.0005 sec) for numerical stability, making it computationally time-consuming.

2.8 Baseline Rail and Vehicle Parameters

The baseline parameters used in the rail and vehicle models are listed in Table 2.1. They were selected to represent conventional and forced steered urban transit vehicles.

Two wheel/rail profiles were used in the studies: a new AAR wheel and a Heumann wheel both on worn rail of standard gage. Both profiles were obtained from tables in [23], smoothed, and modified to account for a centered rolling radius of 14.0 in. Geometric constraint functions for these two symmetric profiles are described in Section 2.4.2. The new AAR wheel represents a wheel with a 1/20 tread taper and a steep flange. Single-point contact occurs in the tread region. However, due to the steep flange of this profile, two-point tread and flange contact occurs at wheelset lateral excursions equal to the flange clearance.



Key: 11 Single-Point Contact Outer and Inner Wheels.
 21 Two-Point Contact Outer Wheel; Single-Point Contact Inner Wheel.
 12 Single-Point Contact Outer Wheel; Two-Point Contact Inner Wheel.

Figure 2.24 Wheel/Rail Contact Possibilities for Wheelsets of a Truck with New Wheels.

TABLE 2.1 BASELINE RAIL/VEHICLE PARAMETERS

<u>WHEEL/RAIL</u>	<u>New Wheel</u>	<u>Heumann Wheel</u>
f_{11T} [lb] [*]	1.09E6 ^{**}	1.01E6
f_{12T} [ft-lb]	8615.	9620.
f_{22T} (ft ² -lb)	82.	14.
f_{33T} [lb]	1.18E6	9.805E6
f_{11F} [lb]	7.34E5	5.755E5
f_{12F} [ft-lb]	6820.	4735.
f_{22F} [ft ² -lb]	2.	1.
f_{33F} [lb]	6.71E5	5.26E5
λ	0.05	0.20
μ	0.30	0.30

GEOMETRY

r_o [ft]	1.167	h_{ts} [ft]	1.48
a [ft]	2.32	h_{tp} [ft]	0.52
b [ft]	3.75	h_c [ft]	2.375
d_p [ft]	1.92	l_s [ft]	23.75
h_{cs} [ft]	2.90	d_s [ft]	3.71

* Creep coefficients are half-Kalker values with a nominal contact patch normal load of 15,000 lb.

** E represents to the power of 10, e.g., 1.0E6 = 1.0 x 10⁶

COMPONENT WEIGHTS AND MOMENTS OF INERTIA

<u>WHEELSET</u>	<u>Conventional Truck</u>	<u>Radial Trucks</u>
W_W [lb]	4054.	4854.
I_{WY} [slug-ft ²]	28.	28.
I_{WZ} [slug-ft ²]	547.	946.
 <u>TRUCK</u>		
W_F [lb]	4697.	4697.
I_{FX} [slug-ft ²]	1166.	1166.
I_{FZ} [slug-ft ²]	1251.	1251.
 <u>CARBODY</u>		
W_C [lb]		70,190.
I_{CX} [slug-ft ²]		4.40E4
I_{CZ} [slug-ft ²]		8.96E5
 <u>VEHICLE WEIGHT</u>		
W_V [lb]	<u>CONVENTIONAL</u> 95,800	<u>RADIAL</u> 99,000

BASELINE STIFFNESSES AND DAMPING

PRIMARY SUSPENSION

	<u>New Wheel</u>		<u>Heumann Wheel</u>	
	<u>Conventional</u>	<u>Radial</u>	<u>Conventional</u>	<u>Radial</u>
k_{px} [lb/ft]	1.35E5	1.20E5	6.50E5	5.00E5
C_{px} [lb-sec/ft]	574.	756.	2760.	3150.
-	-	-	-	-
k_{py} [lb/ft]	7.50E5		k_{pz} [lb/ft]	1.0E6
C_{py} [lb-sec/ft]	620.		C_{pz} [lb-sec/ft]	600.

INTERWHEELSET STIFFNESSES

	<u>Conventional</u>	<u>Radial</u>
k_{b2} [ft-lb/rad]	0.0	1.0E3
k_{s2} [lb/ft]	0.0	1.0E6

SECONDARY SUSPENSION

k_{sy} [lb/ft]	19,500.	k_{sz} [lb/ft]	20,400.
C_{sy} [lb-sec/ft]	1420.	C_{sz} [lb-sec/ft]	1630.
C_o [ft-lb-sec/rad]	1.E7	T_o [ft-lb]	7500.

FORCED STEERING PARAMETERS

$G_{prl} = 0.1579$

$H = 0.0$

The Heumann wheel profile was designed with the intention of maintaining single-point contact at all wheelset excursions to obtain a profile that would maintain its shape as it wears [24]. The new and Heumann wheel profiles are representative two-point contact and single-point contact profiles, respectively.

Linear creep coefficients typical of the tread and flange of the two wheel profiles were calculated using Hertzian contact theory. Rail and wheel radii of curvature were obtained from [23]. Flange creep coefficients are less than tread coefficients* (by about 30 percent for longitudinal and lateral coefficients). This decrease in flange creep coefficients is expected since the contact patch area decreases in the flange, and its effect outweighs the opposite effect of increased ellipticity.

The vehicle dimensions and weights are representative of urban transit trucks. Specifically, the geometry, weights, and inertias are based on those reported for the existing and modified PATCO** Pioneer III trucks described in [25]. The weight and inertia parameters reflect the fact that in yaw and roll the contribution of the traction motor must be included. In addition, for radial trucks the contribution of the steering arm is added. The weight and roll and pitch inertias of the truck include the side frames, braking equipment, and bolster. The bolster does not influence the truck yaw inertia.

The baseline primary, secondary, and interaxle suspension stiffnesses

*

The contact patch ellipse (a/b) ratio for the flange patch is limited to 10. This agrees with calculations by British Rail which show that the (a/b) ratio rarely exceeds 10 [26].

**

Port Authority Transit Corporation

3.0 DYNAMIC CURVING STUDIES

3.1 Introduction

The studies described in the Interim Report [1] have focused on the steady-state curving performance of rail vehicles. These studies have indicated the value of optimizing suspension design and wheel/rail profile to minimize wheelset angles and wheel/rail forces and thus reduce wheel and track wear. However, dynamic effects occur at track curve entry and exit sections and due to track irregularities. These dynamic effects resulting from prescribed changes in track curvature and banking are evaluated parametrically in this study.

In the curve entry simulations, the following assumptions are made:

- (1) The vehicles enter the transition spiral track at the initial time ($t = 0.0$ sec) from centered tangent track positions.
- (2) The vehicles operate at constant forward speed, determined by the balanced running speed for the constant radius curve track. (Table 3.1 lists the balance running speeds for different track curvatures used in the simulations.)
- (3) The baseline transition spiral is 150 ft, which represents a typical value for transit systems.
- (4) Laterally stiff rails are used, i.e., $k_{\text{rail}} = 1.0 \times 10^7$ lb/ft.
- (5) The wheelsets are powered with axle drive torques of 420 ft-lb, representing 5% of the slip torque for axles with 50 HP traction motors operating at 50 mph.

In the dynamic curving analysis, the following model of secondary yaw suspension is adopted. A coulomb damper which saturates at the breakaway torque acts between each truck and the carbody. For numerical convenience, the damper is represented with a linear viscous band at the origin. During dynamic conditions, the front and rear trucks display

TABLE 3.1
 BALANCED RUNNING SPEEDS
 ASSUMING 6 IN SUPERELEVATION
 (i.e., $\phi_{SE} = 6.2^\circ$)

DEGREE CURVE (deg)	CURVE RADIUS (ft)	BALANCED RUNNING SPEED	
		(ft/sec)	(mph)
2.5°	2290	90	60
5°	1146	60	45
10°	575	45	30
20°	288	30	20

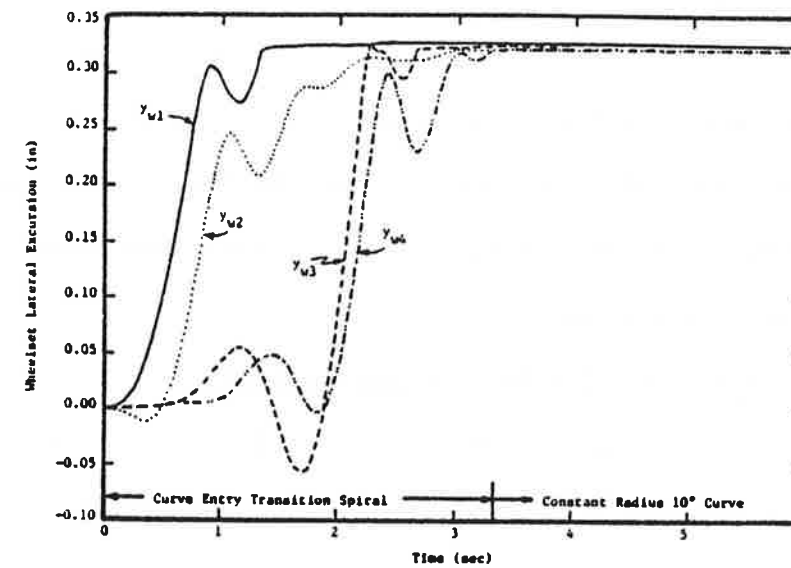
different behavior in general since truck and carbody yaw rates are present and thus yaw torques develop. Due to the linear viscous band, in steady-state the secondary yaw torques on the two trucks vanish since the truck and carbody yaw rates are zero. Thus, in the dynamic curving analysis, the two trucks behave identically in steady-state since no secondary yaw torques are imposed.

3.2 Curve Entry Performance of a Conventional Vehicle

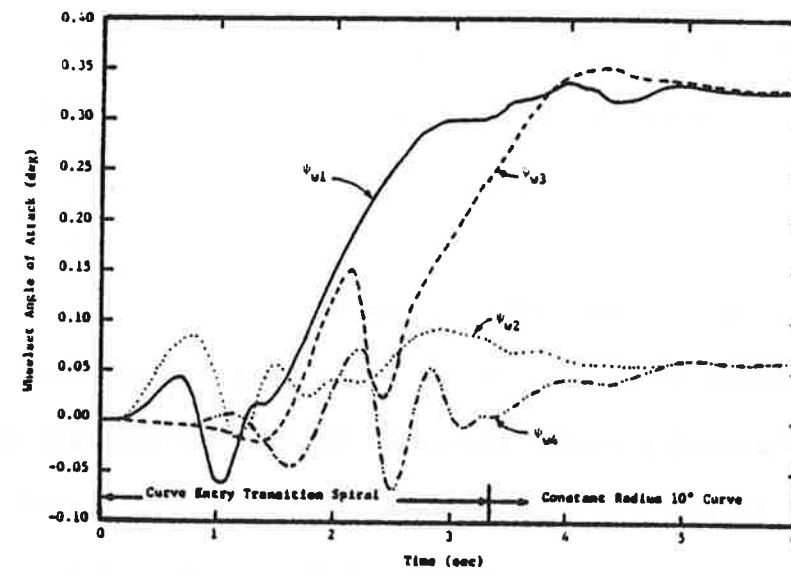
The effect of track curvature, wheel/rail profile, and transition spiral length on the transient behavior of baseline conventional vehicles has been determined.

Typical entry dynamics are shown in the response of a baseline conventional vehicle with new wheels (for which $k_{px} = 1.35 \times 10^5$ lb/ft) negotiating a 150 ft transition spiral into a 10° curve at a balance speed of 45 ft/sec. Figures 3.1a and b show the wheelset lateral excursions and angles of attack, respectively, as functions of time. Figures 3.2a and b show the leading outer (i.e., flanging) wheel lateral force and contact work, respectively, as functions of time.

As the front truck enters the spiral curve, the leading wheelset rapidly displaces laterally toward the outer rail. The wheelset overshoots its desired rolling radius difference and thus the lateral displacement decreases slightly and then grows again. The leading outer wheel approaches its flange, but maintains single-point tread contact until it encounters the flange at $t = 1.375$ sec (i.e., 62 ft into the spiral). Two-point contact occurs at the leading outer wheel for the remainder of the simulation. The trailing wheelset of the front truck shows similar but somewhat lagged behavior. It displaces laterally

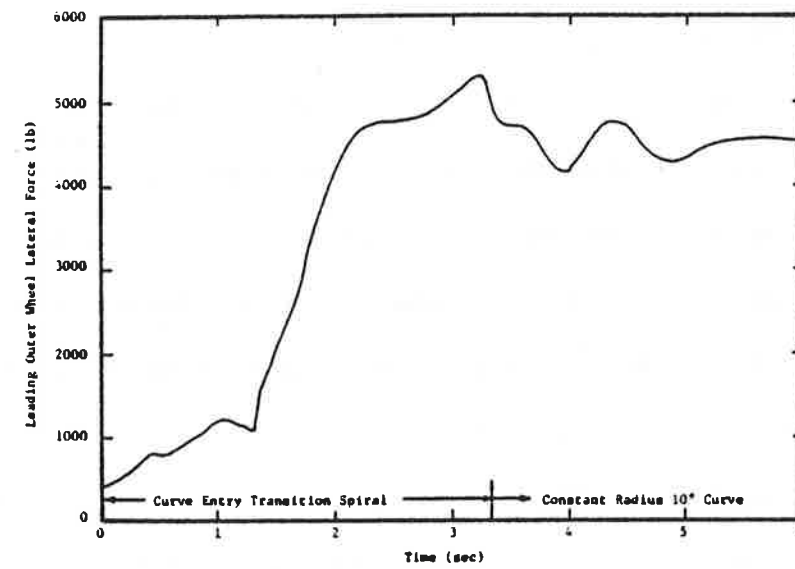


(a)

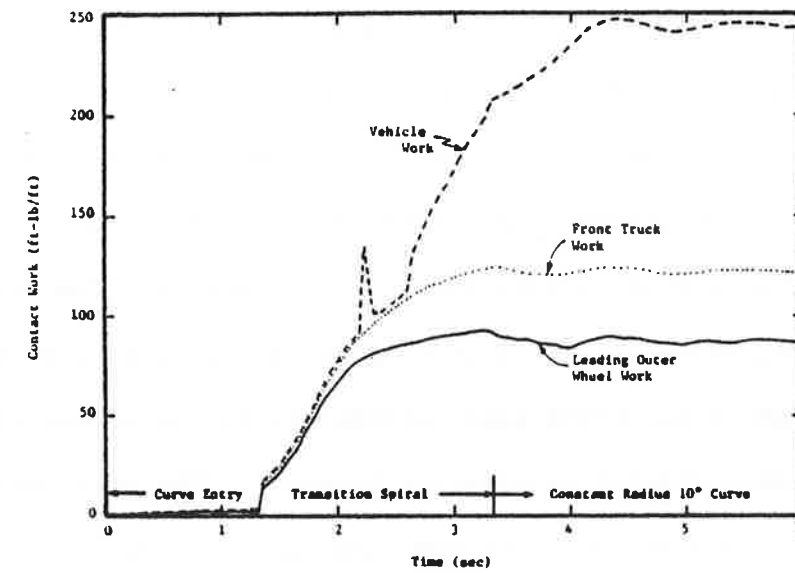


(b)

Figure 3.1: History of (a) Wheelset Lateral Excursions and (b) Angles of Attack of a Baseline Conventional Vehicle with New Wheels Negotiating a 150 ft Curve Entry Spiral into a 10° Curve at a Balance Speed of 45 ft/sec.



(a)



(b)

Figure 3.2 History of (a) Leading Outer (i.e., Flanging) Wheel Lateral Force and (b) Contact Work of a Baseline Conventional Vehicle with New Wheels, Negotiating a 150 ft Curve Entry Spiral into a 10° Curve at a Balance Speed of 45 ft/sec

maintaining single-point tread contact until the outer wheel impacts its flange at $t = 3.000$ sec (i.e., 135 ft into the spiral). It stays in two-point tread and flange contact for the remainder of the simulation.

The leading and trailing wheelsets of the rear truck displace rapidly toward the outer rail at $t \approx 2.0$ sec (i.e., ≈ 90 ft into the spiral). The leading outer wheel of the rear truck impacts its flange at $t = 2.250$ sec (i.e., 101 ft into the spiral) causing two-point contact to occur momentarily, and then bounces back into tread contact until $t = 2.750$ sec (i.e., 124 ft into the spiral). At all subsequent times two-point contact occurs at the leading outer wheel of the rear truck. The trailing wheelset of the rear truck maintains single-point tread contact during the entire transition spiral section. Two-point tread and flange contact occurs at the trailing outer wheel at $t = 3.375$ sec (i.e., 2 ft into the constant radius curve).

Figure 3.1b shows the angle of attack histories of the four wheelsets of the vehicle. As the vehicle enters the curve, the wheelsets of the front truck initially develop positive angles of attack. The wheelsets of the rear truck, which are still on tangent track, have zero angles. During negotiation of the transition spiral track, the angles of attack of all the wheelsets display oscillatory behavior. The oscillations decay as the vehicle negotiates the constant radius curve track. In steady-state conditions, the leading wheelsets of the front and rear trucks develop angles of attack of ~ 0.33 deg. and the trailing wheelsets develop angles of ~ 0.06 deg.

The lateral force at the leading outer wheel of the vehicle as a function of time is shown in Figure 3.2a. The force increases rapidly

at $t = 1.375$ sec when the leading outer wheel hits the flange and two-point contact develops. The force continues to increase, reaching a maximum of 5270 lb at $t = 3.250$ sec (i.e., 146 ft into the spiral) just before entering the constant radius curve. The peak force exceeds the steady-state force by 17%.

The leading outer wheel, front truck, and vehicle work as a function of time are shown in Figure 3.2b. The front truck work is the sum of the work expended at the contact patches at the four wheels of the front truck; similarly, the vehicle work is the sum of the work at all contact patches. At $t = 1.375$ sec, two-point contact develops at the leading outer wheel, and the work function increases significantly. As the vehicle continues through the curve, the contact work at the leading outer wheel and at the front truck continues to increase and each approaches a constant. The vehicle work increases rapidly at $t = 2.250$ sec when the leading outer wheel of the rear truck moves into the flange and two-point contact occurs. The work decreases since single-point tread contact is restored and then increases at $t = 2.750$ sec when two-point contact again develops. The vehicle work continues to increase and then reaches a constant as steady-state conditions are approached.

3.2.1 Effect of Track Curvature on Curve Entry Performance of a Conventional Vehicle

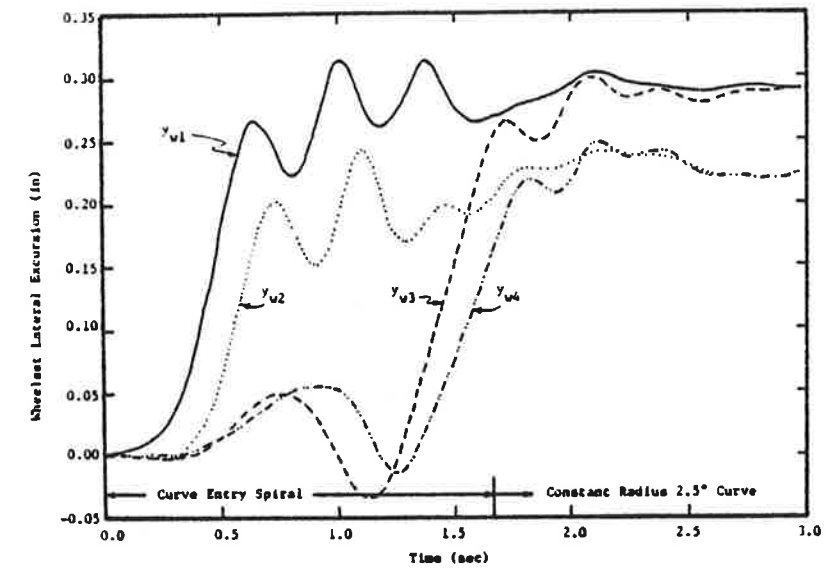
The track curvature is an important parameter influencing steady-state and dynamic curving performance. The steady-state results show that in general as tighter curves are negotiated, the flanging wheel contact work and lateral force increase. To determine the effect of track curvature on the transient behavior, a limited study of curve entry

performance of conventional vehicles with new wheels has been conducted.

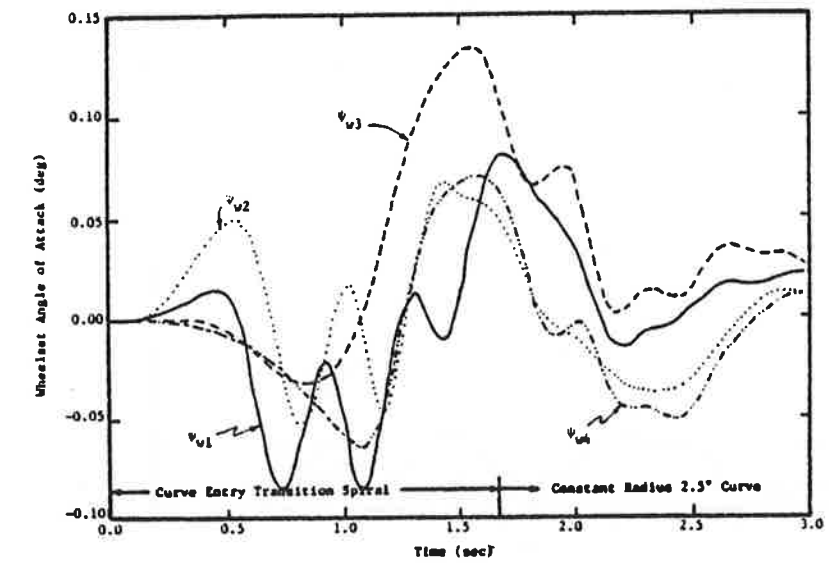
The response of a baseline conventional vehicle with new wheels negotiating a 150 ft curve entry spiral into a 2.5° curve at a balance speed of 90 ft/sec is shown in Figures 3.3 and 3.4. Figures 3.3a and 3.3b show the wheelset lateral excursion and angle of attack histories, respectively. Figures 3.4a and 3.4b show the flanging wheel lateral force and contact work histories, respectively. Single-point contact occurs at all wheels during the simulation. As the vehicle enters the transition spiral curve, the wheelsets of the front truck displace laterally toward the outer rail and oscillate, overshooting their desired positions (for the correct rolling radius difference). The wheelsets of the rear truck, which maintain their centered positions until they enter the curve, displace out and in slightly and then also displace laterally toward the outer rail and oscillate. In the constant radius curve section, the lateral excursions settle to the steady values: ~ 0.286 in for the leading wheelsets of the front and rear truck and ~ 0.221 in for the trailing wheelsets of the two trucks.

The wheelset angles of attack as a function of time, shown in Figure 3.3b exhibit sustained oscillatory behavior in the transition spiral curve. In the constant radius curve section, the oscillations slowly decrease. Steady-state conditions are reached at $t \sim 3.0$ sec (i.e., 120 ft into the constant radius curve).

Figure 3.4a shows the oscillatory behavior of the leading outer or flanging wheel lateral force as a function of time. The force increases as the vehicle enters the spiral curve, peaking at 1640 lb at $t = 0.751$ sec (i.e., 68 ft into the spiral). The force then decreases and

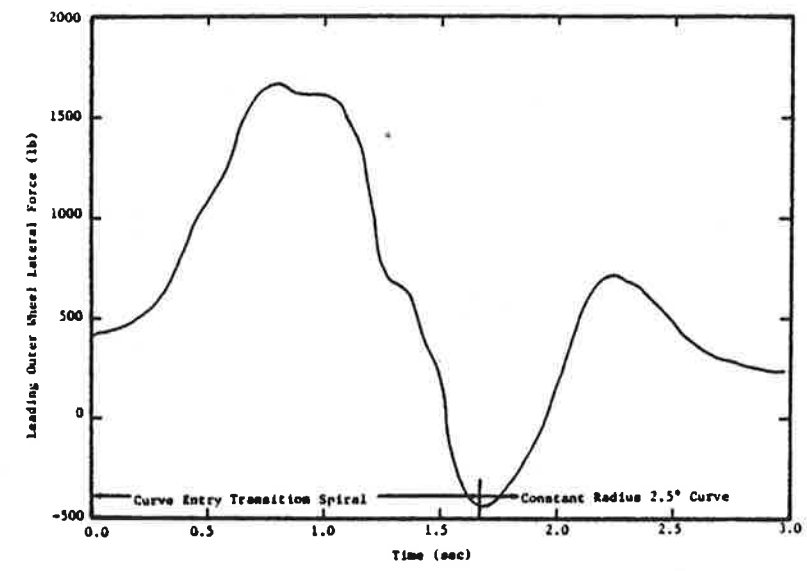


(a)

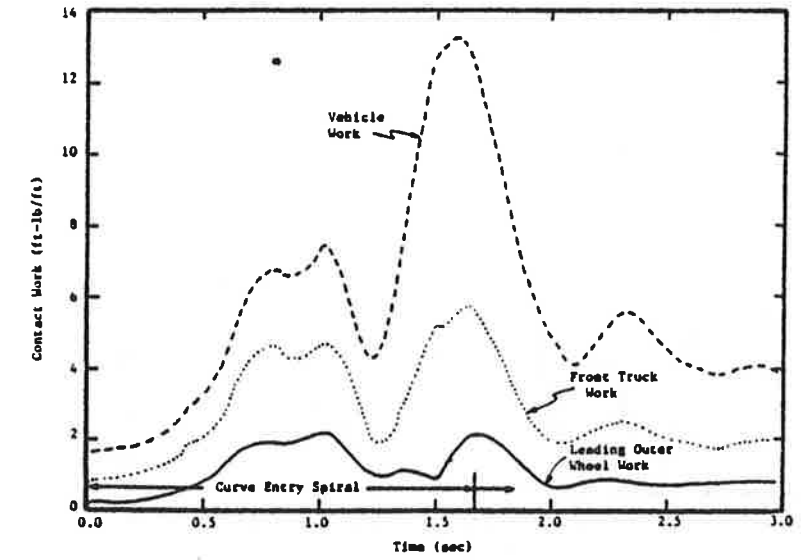


(b)

Figure 3.3 History of (a) Wheelset Lateral Excursions and (b) Angles of Attack of a Baseline Conventional Vehicle with New Wheels Negotiating a 150 ft Curve Entry Spiral into a 2.5° Curve at a Balance Speed of 90 ft/sec.



(a)



(b)

Figure 3.4 History of (a) Leading Outer (i.e., Flanging) Wheel Lateral Force and (b) Contact Work for a Baseline Conventional Vehicle with New Wheels Negotiating a 150 ft Curve Entry Spiral into a 2.5° Curve at a Balance Speed of 90 ft/sec.

eventually becomes negative. As the vehicle enters the constant radius curve section, the force reaches a minimum of -440 lb at $t = 1.688$ sec (i.e., 2 ft into the constant radius curve). The force increases and settles to its steady value of 340 lb by $t = 3.0$ sec (i.e., 120 ft into the constant radius curve).

The contact work expended as the leading outer wheel, at the front truck, and at the vehicle as a function of time is shown in Figure 3.4b. The work histories oscillate, until settling to their steady-state values: 1 ft-lb/ft for the leading outer wheel, 2 ft-lb/ft for the front truck, and 4 ft-lb/ft for the vehicle. The leading outer wheel work reaches a maximum of 2 ft-lb/ft at $t \approx 1.000$ sec (i.e., 146 ft into the spiral). The maximum values occur when the wheelset angles of attack are extreme, indicative of large lateral creepages.

In summary, important transient behavior develops for a conventional vehicle with new wheels negotiating a 150 ft transition spiral into a shallow 2.5° curve at balance speed. The wheelset excursions and angles, the leading outer wheel lateral force, and the contact work significantly exceed their steady-state values. The wheelsets show sustained lateral and yaw oscillations in the transition spiral curve. These oscillations dampen out in the constant radius curve, and eventually steady-state conditions are achieved.

In contrast, the response of the vehicle traversing a 150 ft spiral into a moderate 10° curve, shown in Figures 3.1 and 3.2 indicates that the peak flanging wheel force exceeds the steady-state force by 17% for the vehicle running into the 10° curve, whereas the peak force exceeds the steady-state force by 388% for the vehicle negotiating the 2.5° curve.

Table 3.2 summarizes the steady-state and peak flanging wheel force and contact work of a baseline conventional vehicle with new wheels entering a 2.5°, 5°, and 10° curve at balance speed. As tighter curves are traversed, the ratio of dynamic to steady-state forces decreases. The wheelsets displace to the flange clearance and remain there. In comparison, for negotiation of shallow curves, the wheelsets approach the flanges but always remain in tread contact. The wheelsets exhibit "hunting"-type oscillations along the transition spiral, which result in significant dynamic behavior.

3.2.2 Effect of Wheel/Rail Profile on Curve Entry Performance of a Conventional Vehicle

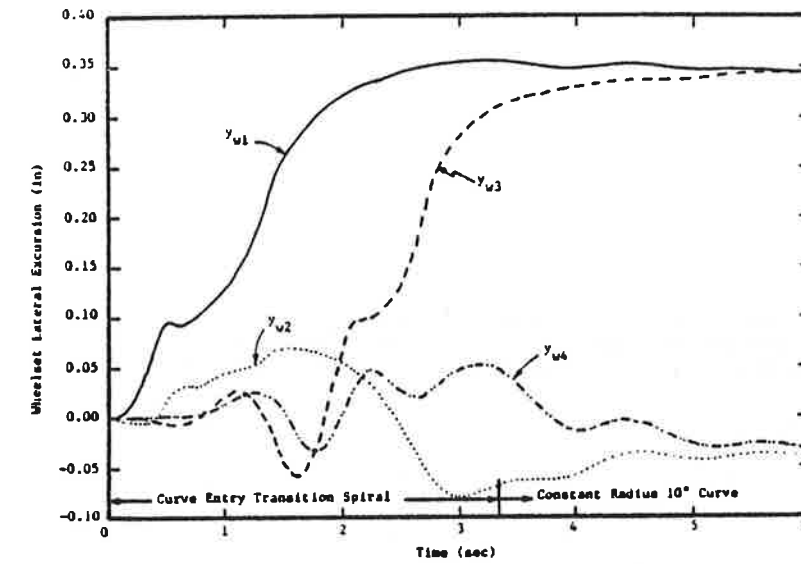
The results of the steady-state studies presented in the Interim report suggest that single-point contact profiles, such as Heumann wheel profiles, offer improved performance in terms of decreased contact work in comparison to two-point contact profiles, such as new AAR wheel profiles. This section addresses the influence of wheel/rail profile on dynamic curving performance.

A curve entry simulation has been conducted to determine the dynamic response of a baseline conventional vehicle with Heumann wheels (for which $k_{px} = 6.50 \times 10^5$ lb/ft) negotiating a 150 ft transition spiral into a 10° curve at a balance speed of 45 ft/sec. The response histories are shown in Figures 3.5 and 3.6. The wheelset lateral excursions and angles of attack as functions of time are shown in Figures 3.5a and b respectively. The leading outer wheel lateral force and contact work as functions of time are shown in Figures 3.6a and b respectively. Since Heumann wheels are employed, single-point contact occurs at the wheels at all times.

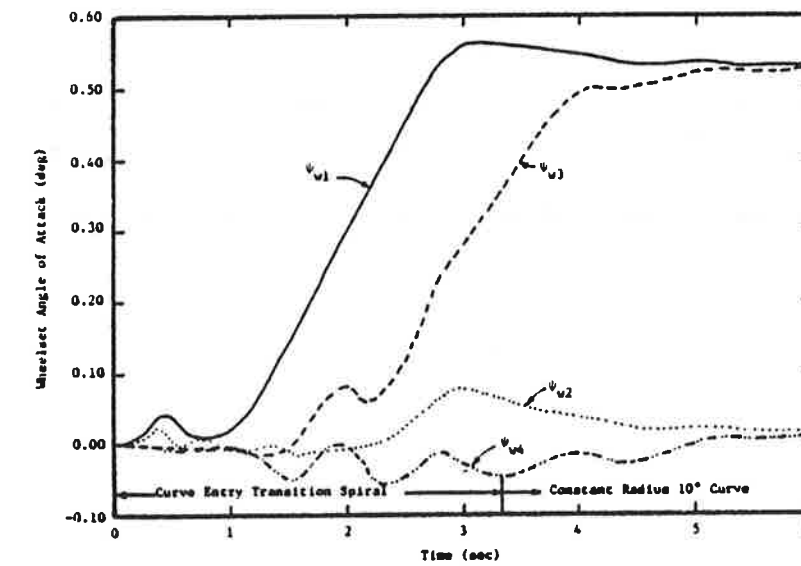
TABLE 3.2

LEADING OUTER WHEEL FORCE AND WORK OF A BASELINE
 CONVENTIONAL VEHICLE WITH NEW WHEELS NEGOTIATING
 A 150 FT CURVE ENTRY SPIRAL INTO A 2.5°, 5°, AND 10° CURVE

DEGREE CURVE (deg)	LEADING OUTER WHEEL LATERAL FORCE (lb)			LEADING OUTER WHEEL WORK (ft-lb/ft)		
	Steady- State	Peak	% Increase	Steady- State	Peak	% Increase
2.5°	340	1660	388%	1	2	100%
5°	2060	2650	29%	36	41	14%
10°	4520	5270	17%	87	93	7%

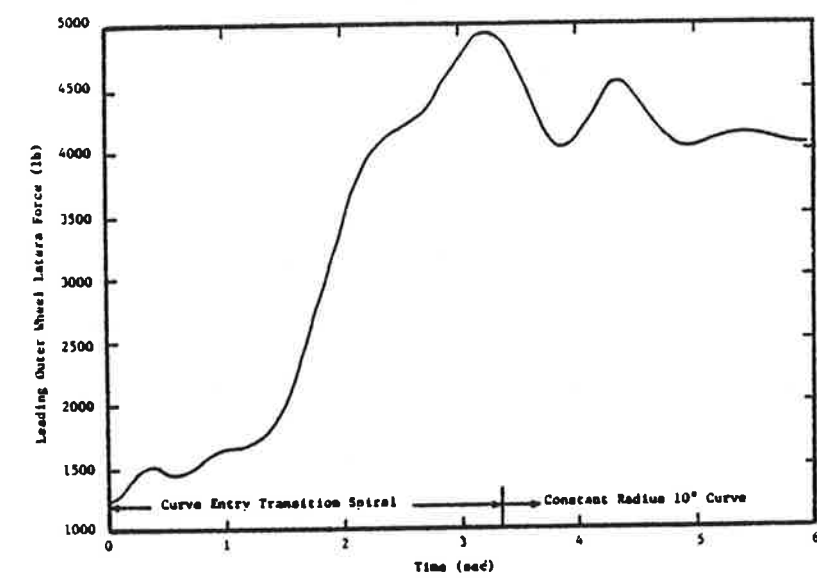


(a)

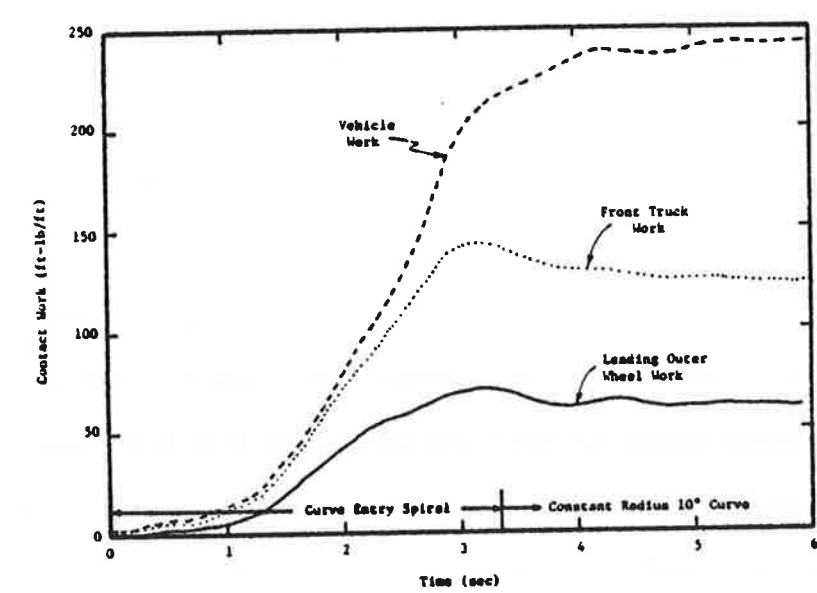


(b)

Figure 3.5 History of (a) Wheelset Lateral Excursions and (b) Angles of Attack of a Baseline Conventional Vehicle with Heumann Wheels Negotiating a 150 ft Curve Entry Spiral into a 10° Curve at a Balance Speed of 45 ft/sec.



(a)



(b)

Figure 3.6 History of (a) Leading Outer (i.e., Flanging) Wheel Lateral Force and (b) Contact Work of a Baseline Conventional Vehicle with Heumann Wheels Negotiating a 150 ft Curve Entry Spiral into a 10° Curve at a Balance Speed of 45 ft/sec.

As the vehicle enters the curve, the leading wheelset of the front truck displaces laterally toward the outer rail, as shown in Figure 3.5a. The leading outer wheel gradually rides up into the flange and stays in flange root contact. The trailing wheelset displacement of the front truck increases and then decreases slightly, always staying near the centered position. The leading wheelset of the rear truck oscillates about the centered position and then smoothly displaces toward the outer rail. The trailing wheelset of the rear truck also oscillates about the centered position. The steady-state excursions are ~ 0.346 in for the leading wheelsets of the two trucks and ~ 0.034 in for the trailing wheelsets.

The angle of attack histories, shown in Figure 3.5b show that the trailing wheelsets of both trucks remain near radial alignment during the simulation. For the leading wheelsets, the angles of attack increase and approach a constant as the vehicle negotiates the curve. The steady-state angles of attack are ~ 0.529 deg. and ~ 0.013 deg. for the leading and trailing wheelsets of the two trucks, respectively.

The leading outer wheel lateral force shown in Figure 3.6a increases as the vehicle enters the curve. It reaches a maximum of 4950 lb when the leading outer wheel rides up into the flange at $t = 3.250$ sec (i.e., 146 ft into the spiral curve). The force decreases in the constant radius section to a steady value of 4050 lb which is 22% less than the peak value.

Figure 3.6b shows the contact work for the leading outer wheel, the front truck, and the vehicle as a function of time. The contact work functions increase as the vehicle enters the curve and approach constant values. The maximum leading outer wheel work is 72 ft-lb/ft versus

62 ft-lb/ft for steady-state and occurs at $t = 3.250$ sec (i.e., 146 ft into the spiral). For the front truck and vehicle the maximum work is 144 and 243 ft-lb/ft, respectively. In contrast, the steady-state values are 121 and 242 ft-lb/ft, respectively. Dynamic effects have little influence on the contact work functions.

3.2.3 Effect of Spiral Length on Curve Entry Performance of a Conventional Vehicle

A study of the effect of spiral length on the peak flanging wheel lateral force of a conventional vehicle with new wheels has been conducted. In the study, the vehicle negotiates a transition spiral of varying length into a 10° curve at a balance speed of 45 ft/sec. The peak flanging force as a function of spiral length is shown in Figure 3.7. Reducing the spiral length increases the peak lateral force resulting from the initial flange contact. For short spiral lengths less than 75 ft, the peak force significantly exceeds the steady-state force. As the spiral length increases, the peak lateral force decreases rapidly and approaches the steady-state flange force. For very long spiral lengths (i.e., greater than the maximum value of 200 ft plotted in Figure 3.7) the peak and steady-state forces coincide implying that the steady-state force represents the maximum lateral force.

3.3 Curve Entry Performance of a Self-Steered Radial Vehicle

A baseline self-steered vehicle with new wheels (for which $k_{px} = 1.20 \times 10^5$ lb/ft, $k_{b2} = 1.0 \times 10^3$ ft-lb/rad, $k_{s2} = 1.0 \times 10^6$ lb/ft) has been simulated passing through a 150 ft transition spiral curve into a 10° curve at a balance speed of 45 ft/sec. Response histories of wheelset lateral excursions and angles of attack are shown in Figures 3.8a and b respectively. Histories of flanging wheel force and contact work are

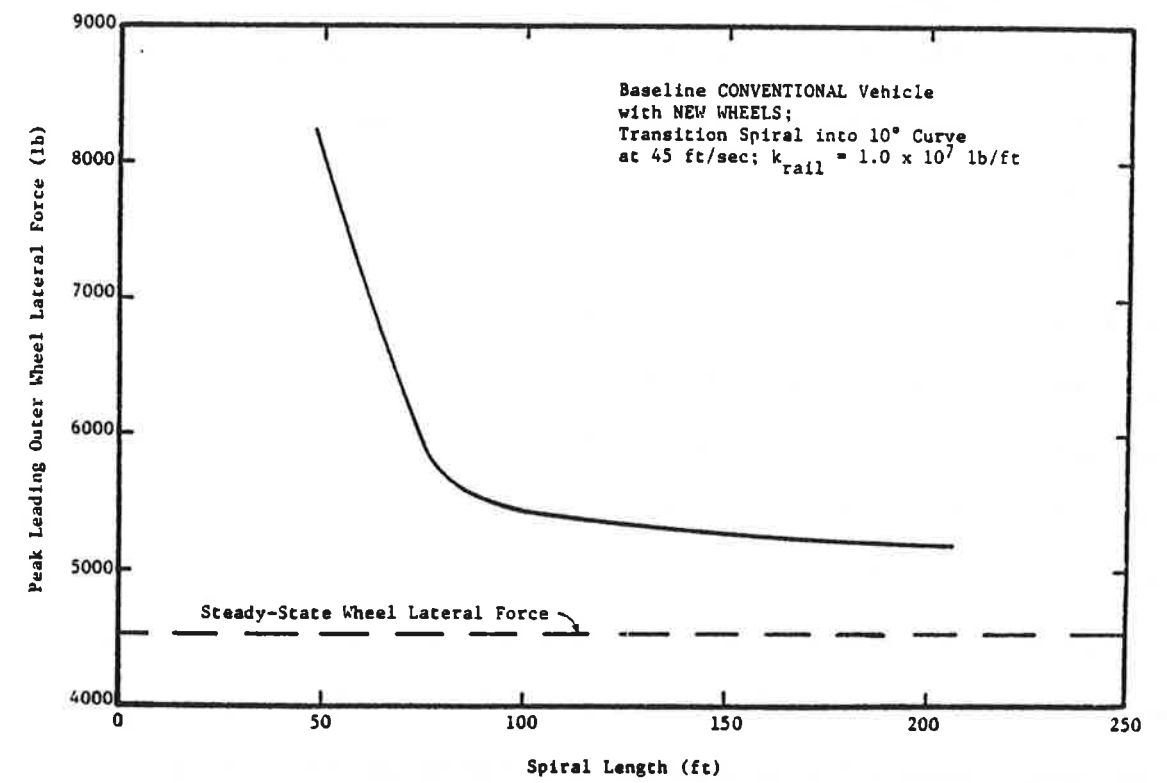
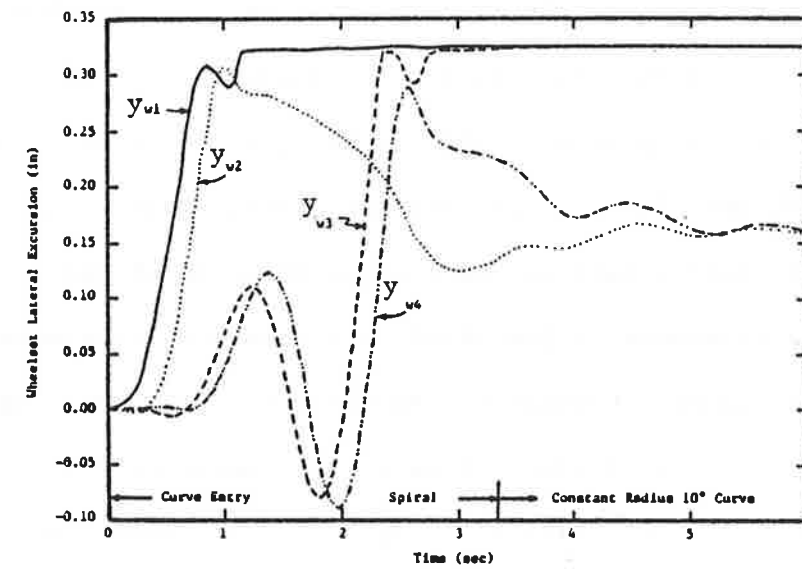
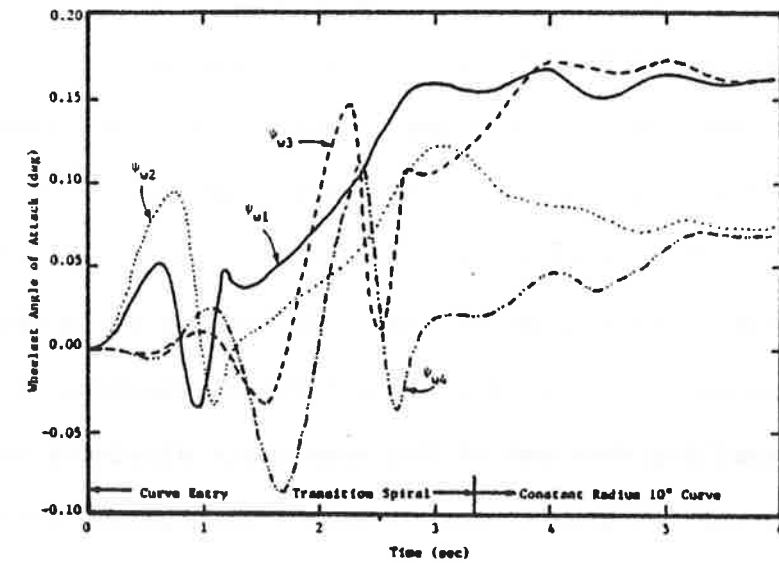


Figure 3.7 Effect of Curve Entry Spiral Length on the Peak Lateral Wheel Force of a Baseline Conventional Vehicle with New Wheels Entering a 10° Curve at a Balance Speed of 45 ft/sec.



(a)



(b)

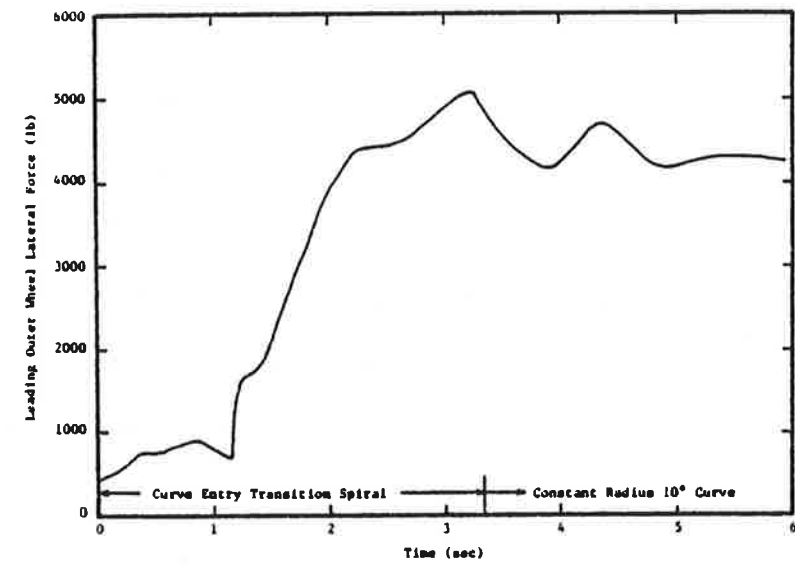
Figure 3.8 History of (a) Wheelset Lateral Excursions and (b) Angles of Attack of a Self-Steered Radial Vehicle with New Wheels Negotiating a 150 ft Curve Entry Spiral into a 10° Curve at a Balance Speed of 45 ft/sec.

shown in Figures 3.9a and b respectively.

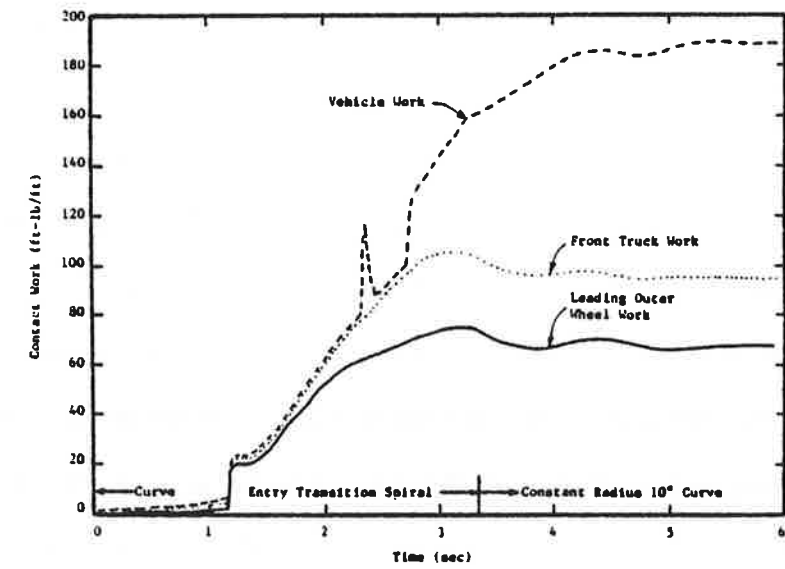
As the front truck enters the spiral curve, the leading wheelset rapidly displaces toward the outer rail. The leading outer wheel approaches the flange, displaces inward slightly, and then hits the flange at $t = 1.200$ sec (i.e., 54 ft into the spiral curve). Two-point tread and flange contact occurs at the leading outer wheel and is maintained for the remainder of the simulation. The trailing wheelset of the front truck displaces laterally toward the outer rail but does not impact the flange and then displaces inward. Single-point tread contact occurs at both wheels of the trailing wheelset of the front truck during the simulation.

Once in the curve, the leading and trailing wheelsets of the rear truck both displace out and in and then approach the outer rail. The leading outer wheel of the rear truck hits the flange at $t = 2.375$ sec (i.e., 107 ft into the spiral curve) and two-point tread and flange contact occurs. It then bounces in, and single-point tread contact is restored until $t = 2.750$ sec (i.e., 124 ft into the spiral curve) at which time two-point contact again occurs. The leading outer wheel of the rear truck remains in two-point contact for the remainder of the simulation. The trailing wheelset of the rear truck displaces toward the outer rail and then returns slightly, always maintaining single-point tread contact at its wheels.

In steady-state, the leading wheelsets of the front and rear truck displace to 0.325 in; the trailing wheelsets of the two trucks displace to 0.162 in. In comparison to the conventional vehicle response of Figure 3.1 the trailing wheelsets of the front and rear self-steered trucks do not displace to the flange clearance in steady-state.



(a)



(b)

Figure 3.9 History of (a) Leading Outer (i.e., Flanging Wheel Lateral Force and (b) Contact Work of a Self-Steered Radial Vehicle with New Wheels Negotiating a 150 ft Curve Entry Spiral into a 10° Curve at a Balance Speed of 45 ft/sec.

The wheelset angles of attack as a function of time are shown in Figure 3.8b. As the vehicle negotiates the spiral curve, the angles of attack of all the wheelsets oscillate, increasing and decreasing rapidly especially when two-point contact occurs. In the constant radius curve section, the oscillations decrease and steady-state conditions are achieved. The steady-state angles of attack are: 0.162 deg for the leading wheelsets and 0.072 deg for the trailing wheelsets of the two trucks.

Figure 3.9a shows the leading outer wheel lateral force as a function of time. The force increases as the vehicle enters the spiral curve and jumps at $t = 1.200$ sec when the leading outer wheel impacts the flange and two-point contact occurs. The force continues to rise, peaking at 5090 lb at 3.250 sec (i.e., 146 ft into the spiral curve) and then settles to its steady-state value of 4260 lb. The peak force exceeds the steady-state force by 20%.

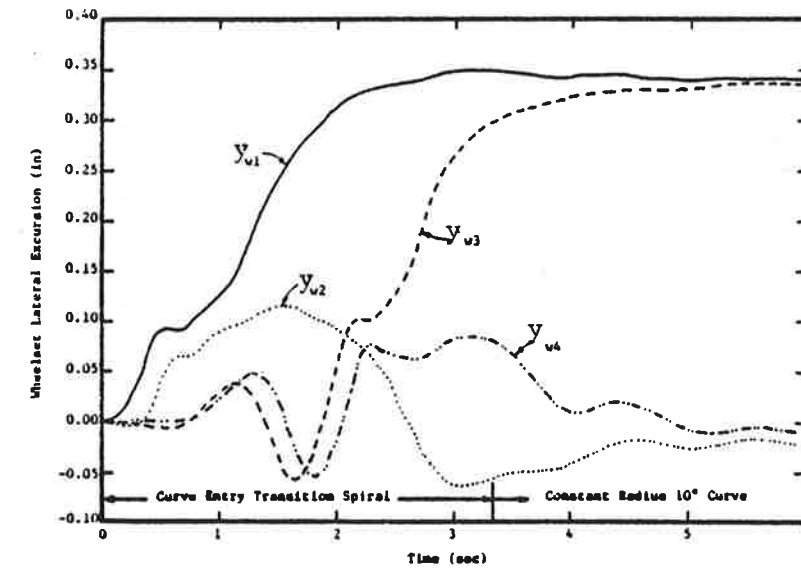
Figure 3.9b shows the leading outer wheel, front truck, and vehicle work as a function of time. The work increases as the vehicle negotiates the curve, increasing significantly at $t = 1.200$ sec when the leading outer wheel of the front truck bangs into the flange and two-point contact occurs. The vehicle work increases significantly at $t = 2.375$ sec when the leading outer wheel of the rear truck impacts the flange and two-point contact occurs. The vehicle work then decreases, and increases again at $t = 2.750$ sec when flanging conditions are restored at the leading outer wheel of the rear truck. The work for the leading outer wheel, front truck, and vehicle continues to rise as the vehicle negotiates the curve. The leading outer wheel and front truck work reach maximum values of 75 and 106 ft-lb/ft, respectively, at $t = 3.250$ sec. The

maximum work for the vehicle coincides with the steady-state work. Steady state conditions are achieved as the vehicle enters the constant radius curve. The steady-state work at the leading outer wheel, front truck, and vehicle is 67, 95, 190 ft-lb/ft, respectively.

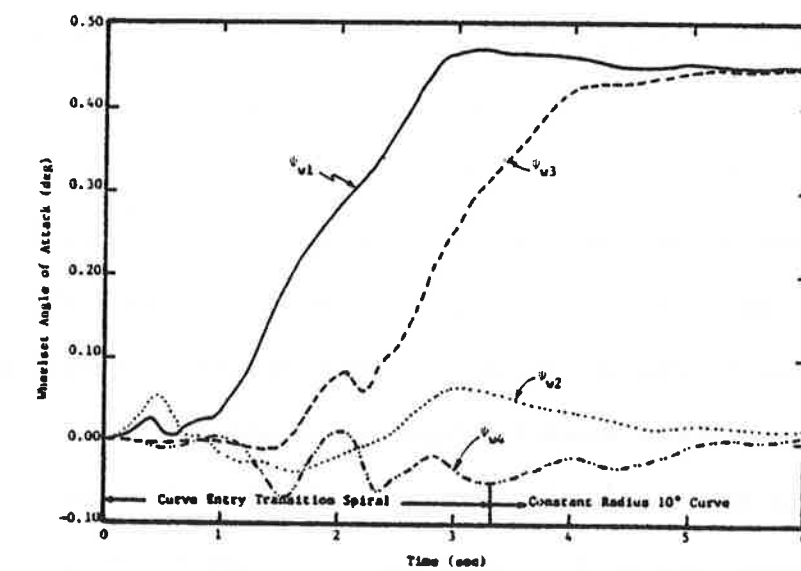
3.3.1 Effect of Wheel/Rail Profile on the Curve Entry Performance Of A Self-Steered Radial Vehicle

This section discusses the influence of wheel/rail profile on the dynamic curving performance of a self-steered radial vehicle. A baseline self-steered vehicle with Heumann wheels (for which $k_{px} = 5.0 \times 10^5$ lb/ft, $k_{b2} = 1.0 \times 10^3$ ft-lb/rad, $k_{s2} = 1.0 \times 10^6$ lb/ft) was simulated traversing a 150 ft curve entry spiral into a 10° curve at a balance speed of 45 ft/ft/sec. The response histories are shown in Figures 3.10 and 3.11. The wheelset lateral excursions and angles of attack as functions of time are shown in Figures 3.10a and b respectively. The leading outer wheel lateral force and contact work as functions of time are shown in Figures 3.11a and b respectively. For the simulation, single-point wheel/rail contact occurs since Heumann wheels are employed. The dynamic response histories for the baseline self-steered vehicle with Heumann wheels are similar in character to the histories for the baseline conventional vehicle with Heumann wheels shown in Figures 3.5 and 3.6.

As the vehicle negotiates the curve, the leading wheelset of the front truck displaces towards the outer rail and flange contact occurs. The leading outer wheel stays in flange contact for the remainder of the simulation. The trailing wheelset of the front truck stays near the centered position, increasing and decreasing slightly before reaching a steady value. The leading wheelset of the rear truck oscillates about the centered position and then displaces towards the outer rail. The

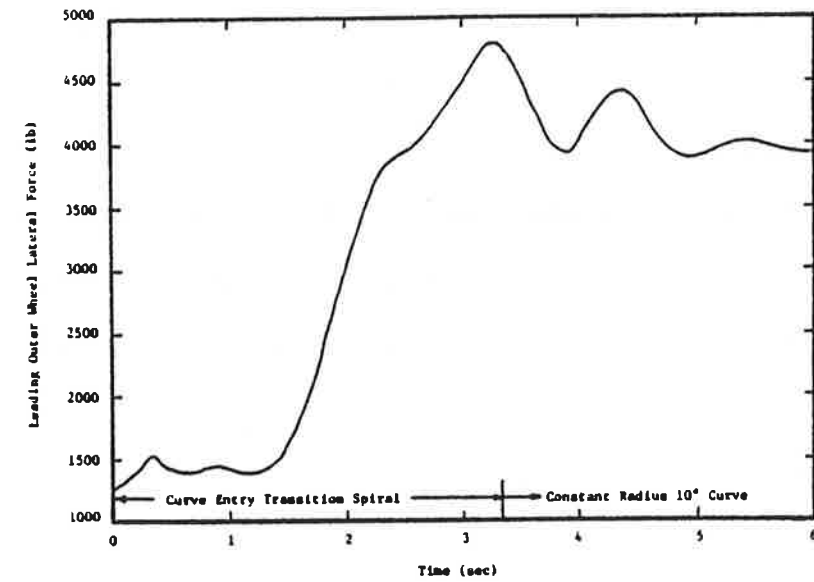


(a)

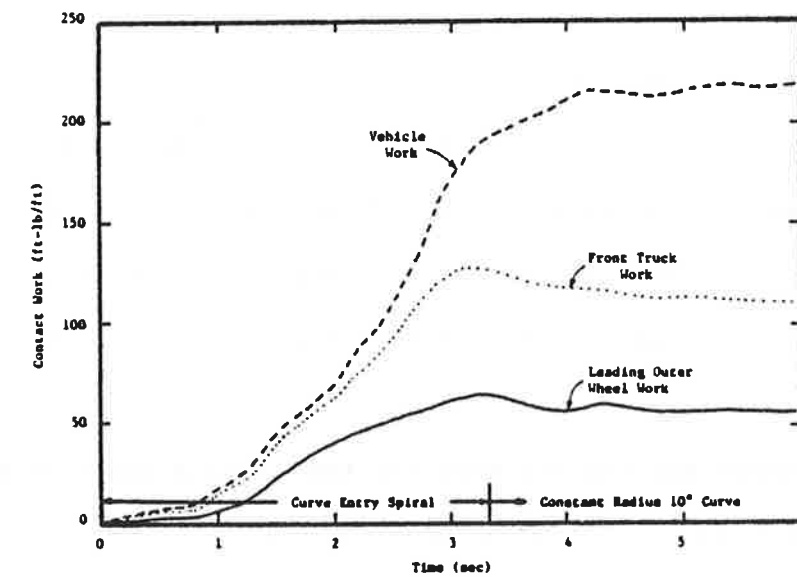


(b)

Figure 3.10 History of (a) Wheelset Lateral Excursions and (b) Angles of Attack of a Self-Steered Radial Vehicle with Heumann Wheels Negotiating a 150 ft Curve Entry Spiral into a 10° Curve at a Balance Speed of 45 ft/sec.



(a)



(b)

Figure 3.11 History of (a) Leading Outer (i.e., Flanging) Wheel Lateral Force and (b) Contact Work of a Self-Steered Radial Vehicle with Heumann Wheels Negotiating a 150 ft Curve Entry Spiral into a 10° Curve at a Balance Speed of 45 ft/sec.

trailing wheelset of the rear truck oscillates about the centered position and then settles to a steady value. The steady-value excursions are ~ 0.341 in for the leading wheelsets of the two trucks and ~ -0.013 in for the trailing wheelsets.

Figure 3.10b shows the wheelset angle of attack histories. The leading wheelsets of both trucks develop positive angles of attack as the vehicle negotiates the curve. The maximum deviation is 0.470 deg at $t = 3.200$ sec (i.e., 144 ft into the spiral curve) for the leading wheelset of the front trucks. The angles of attack of the trailing wheelsets oscillate about radially aligned positions. For the leading and trailing wheelsets of the two trucks, the steady-state angles of attack are 0.446 deg and 0.010 deg, respectively.

The leading outer wheel lateral force, shown in Figure 3.11a increases as the vehicle negotiates the curve. The force increases significantly as the leading outer wheel displaces laterally and flange contact occurs. The maximum lateral force is 4800 lb and occurs at $t = 3.200$ sec (i.e., 144 ft into the spiral curve). The force oscillates and then reaches a steady-state value of 3940 lb, which is 18% less than the peak value.

Figure 3.11b shows the contact work for the leading outer wheel, the front truck, and the vehicle as a function of time. The contact work functions increase as the vehicle enters the curve and approach constant values. The maximum leading outer wheel and front truck work is 64 and 128 ft-lb/ft, respectively, and occurs at $t = 3.200$ sec. The maximum vehicle work is 218 ft-lb/ft and occurs in steady-state conditions. For the leading outer wheel and front truck, the steady-state work is 56 and

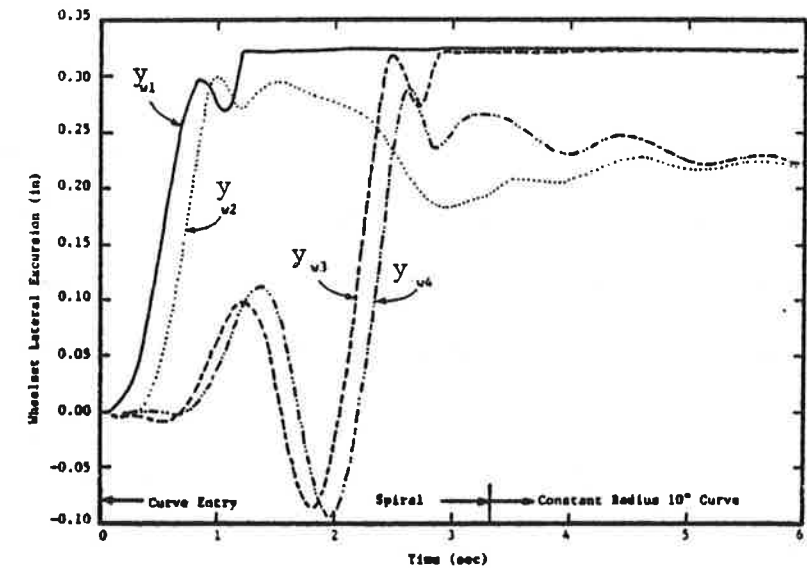
109 ft-lb/ft, respectively. Dynamic effects have little influence on the contact work histories.

3.4 Curve Entry Performance of a Forced-Steered Radial Vehicle

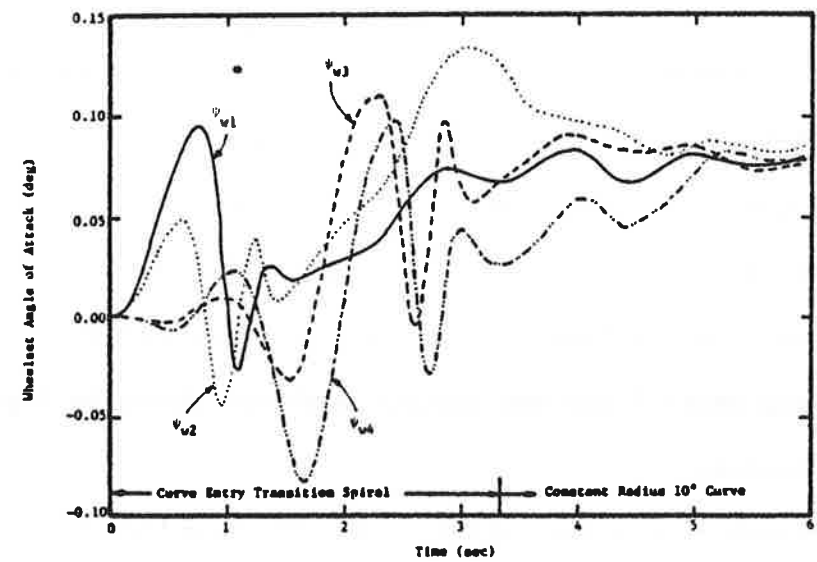
Steady-state curving results indicate that forced-steered radial vehicles potentially offer significant performance benefits (in terms of decreased contact work) in comparison to conventional vehicle performance. This section addresses the dynamic curving performance of a forced-steered radial vehicle. An L-type [1] forced-steered vehicle has been selected for study for consistency with the earlier steady-state curving studies. The curvature steering gain is set to the pure rolling line gain. The study focuses on the performance of the FSR I forced-steered radial design, which has a soft primary longitudinal stiffness of $k_{px} = 7.0 \times 10^4$ lb/ft.

A baseline FSR I forced-steered vehicle with new wheels (for which $k_{b2} = 1.68 \times 10^5$ ft-lb/rad, $k_{s2} = 1.0 \times 10^6$ lb/ft) was simulated passing through a 150 ft transition spiral into a 10° curve at a balance speed of 45 ft/sec. Response histories of wheelset lateral excursions and angles of attack are shown in Figures 3.12a and b, respectively. Histories of flanging wheel force and contact work are shown in Figures 3.13a and b, respectively.

As the front truck enters the spiral curve, the leading wheelset rapidly displaces toward the outer rail. The leading outer wheel approaches the flange, displaces inward slightly, and then moves out impacting the flange, at $t = 1.200$ sec (i.e., 54 ft into the spiral curve). Two-point tread and flange contact occurs at the leading outer wheel and is maintained during negotiation of the remaining

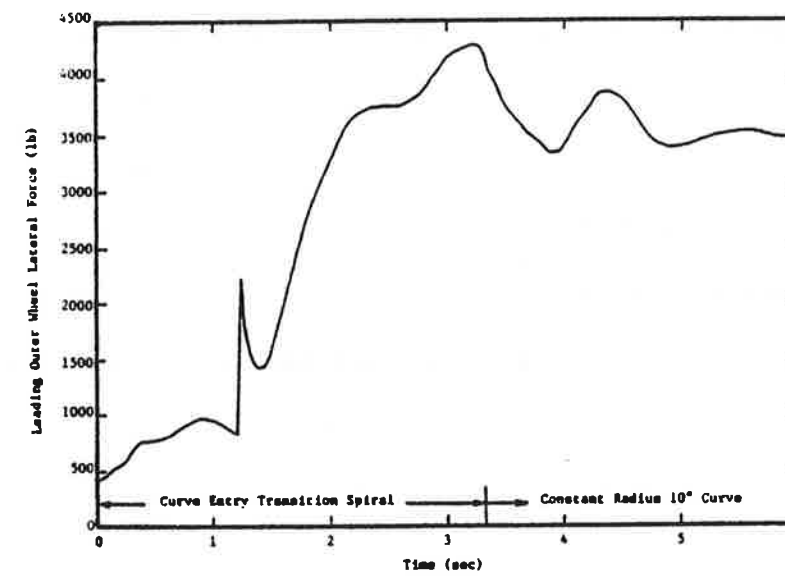


(a)

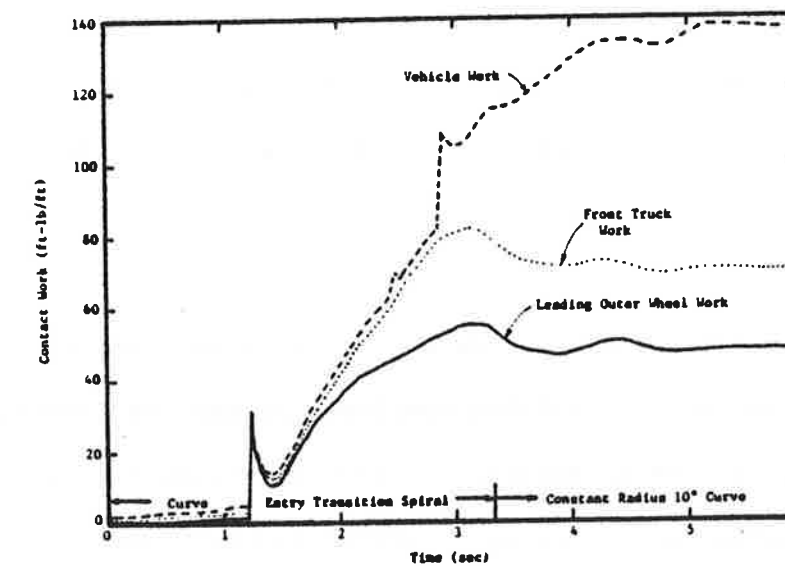


(b)

Figure 3.12 History of (a) Wheelset Lateral Excursions and (b) Angles of Attack of a FSR I Forced-Steered Radial Vehicle with New Wheels Negotiating a 150 ft Curve Entry Spiral into a 10° Curve at a Balance Speed of 45 ft/sec.



(a)



(b)

Figure 3.13 History of (a) Leading Outer (i.e., Flanging) Wheel Lateral Force and (b) Contact Work of a FSR I Forced-Steered Radial Vehicle with New Wheels Negotiating a 150 ft Curve Entry Spiral into a 10° Curve at a Balance Speed of 45 ft/sec.

spiral section and constant radius curve. The trailing wheelset of the front truck displaces laterally toward the outer rail, but the outer wheel does not impact the flange. The trailing wheelset then displaces inward. Single-point tread contact occurs at both wheels of the trailing wheelset of the front truck during the simulation.

As the rear truck enters the spiral curve, the leading and trailing wheelsets both displace out and in and then approach the outer rail. The leading outer wheel of the rear truck impacts the flange at $t = 2.500$ sec (i.e., 112 ft into the spiral) and two-point tread and flange contact occurs. The wheel rebounds back to single-point tread contact and maintains single-point contact until $t = 2.875$ sec (i.e., 129 ft into the spiral). The leading outer wheel of the rear truck then develops two-point tread and flange contact and maintains this condition for the remainder of the simulation. The trailing wheelset of the rear truck displaces toward the outer rail and then returns slightly. Single-point tread contact is maintained at the wheels of the trailing wheelset of the rear truck.

The steady-state lateral excursions are 0.324 in for the leading wheelsets and 0.223 in for the trailing wheelsets of the two trucks. The history of wheelset lateral excursions shown in Figure 3.12 for the FSR I forced-steered vehicle is very similar to the history of excursions shown in Figure 3.8 for the self-steered radial vehicle.

Figure 3.12b shows the wheelset angles of attack as a function of time. The angles of attack oscillate as the vehicle enters the curve. In the constant radius curve the oscillations dampen out and the angles of all wheelsets approach the same steady-state value of

0.079 deg. Ideally, the forced-steering action should position the wheelsets radially (i.e., yielding zero angles of attack). However, the pure rolling line steering gain slightly understeers the wheelsets, and thus the wheelsets develop slightly positive angles of attack in steady-state. In comparison to the angles of attack of the self-steered vehicle (shown in Figure 3.8b), the leading and trailing wheelsets of the forced-steered vehicle adopt identical angles in steady-state.

The flanging wheel lateral force as a function of time is shown in Figure 3.13a. The force increases significantly at $t = 1.200$ sec (i.e., 54 ft into the spiral) when the leading outer wheel impacts the flange and two-point contact occurs. As the vehicle negotiates the curve, the force continues to increase. At $t = 3.200$ sec (i.e., 144 ft into the spiral curve) the maximum force of 4310 lb develops. The maximum force exceeds the steady-state force of 3480 lb by 24%.

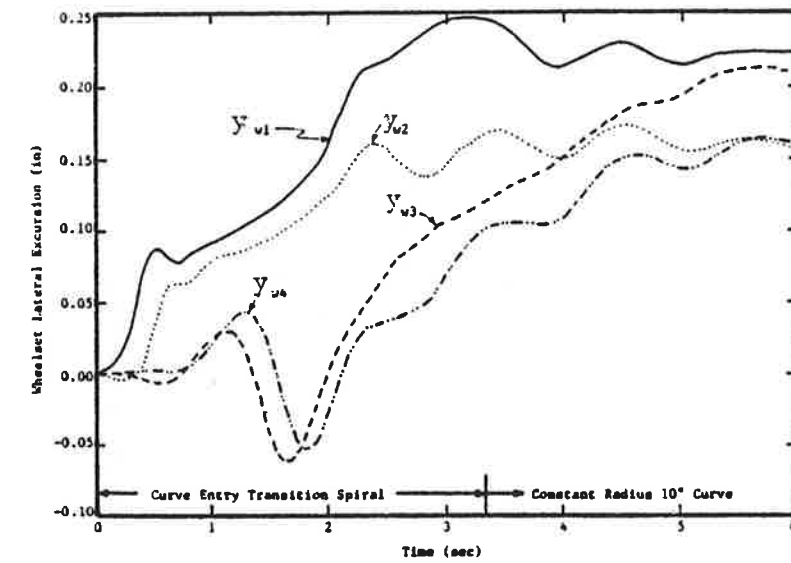
The work expended at the leading outer wheel, the front truck, and the vehicle as a function of time is shown in Figure 3.13b. When the leading outer wheel impacts the flange at $t = 1.200$ sec, the work increases significantly. Following impact, the work decreases and then continues to rise. The work at the leading outer wheel and front truck reaches a maximum of 55 and 82 ft-lb/ft, respectively, at $t = 3.200$ sec. The vehicle work increases significantly at $t = 2.875$ sec when two-point contact develops at the leading outer wheel of the rear truck. The maximum vehicle work is 138 ft-lb/ft and occurs in steady-state conditions. The steady-state work at the leading outer wheel and front truck is 48 and 69 ft-lb/ft, respectively.

3.4.1 Effect of Wheel/Rail Profile on the Curve Entry Performance of a Forced-Steered Radial Vehicle

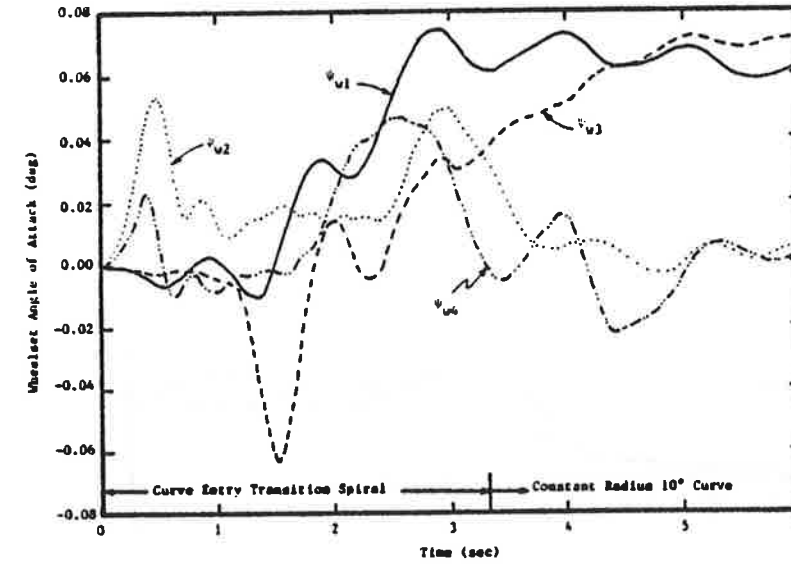
In this section, the influence of wheel/rail profile on the dynamic curving performance of a forced-steered radial vehicle is discussed. A dynamic simulation was conducted to determine the curve entry performance of a baseline FSR I forced-steered vehicle with Heumann wheels (for which $k_{b2} = 1.66 \times 10^6$ ft-lb/ft, $k_{s2} = 1.0 \times 10^6$ lb/ft) negotiating a 150 ft spiral into a 10° curve at a balance speed of 45 ft/sec. Response histories of wheelset lateral excursions and angles of attack are shown in Figures 3.14a and b, respectively. Histories of flanging wheel force and contact work are shown in Figures 3.15a and b, respectively.

As the vehicle enters the curve, the leading and trailing wheelsets of the front truck displace toward the outer rail, but maintain tread contact. The maximum lateral excursion occurs for the leading wheelset at $t = 3.250$ sec (i.e., 146 ft into the spiral curve) and is 0.248 in. The leading and trailing wheelsets of the rear truck increase and decrease slightly and then develop positive excursions. The steady-state excursions are ~ 0.158 in for the trailing wheelsets of the two trucks.

Figure 3.14a shows the wheelset angles of attack as a function of time. Very small angles of attack develop during the simulation. The largest magnitude is 0.073 deg, which occurs for the leading wheelset of the front truck at $t = 2.875$ sec (i.e., 129 ft into the spiral curve). In the curve entry spiral, the angles of attack of all wheelsets oscillate about near radial positions. In the constant radius curve, the leading wheelsets of the front and rear trucks develop positive angles of attack; the trailing wheelsets approach perfect radial alignment. The steady-state angles are ~ 0.002 deg for the trailing wheelsets of the two trucks.

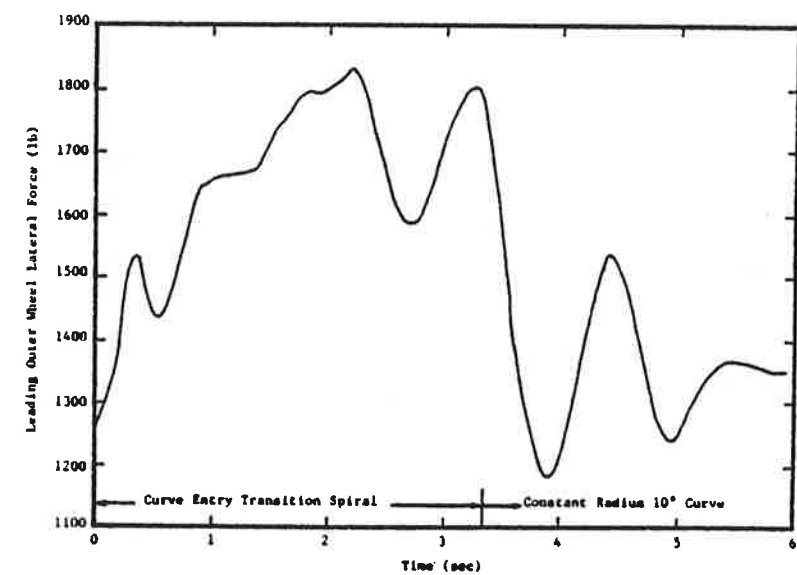


(a)

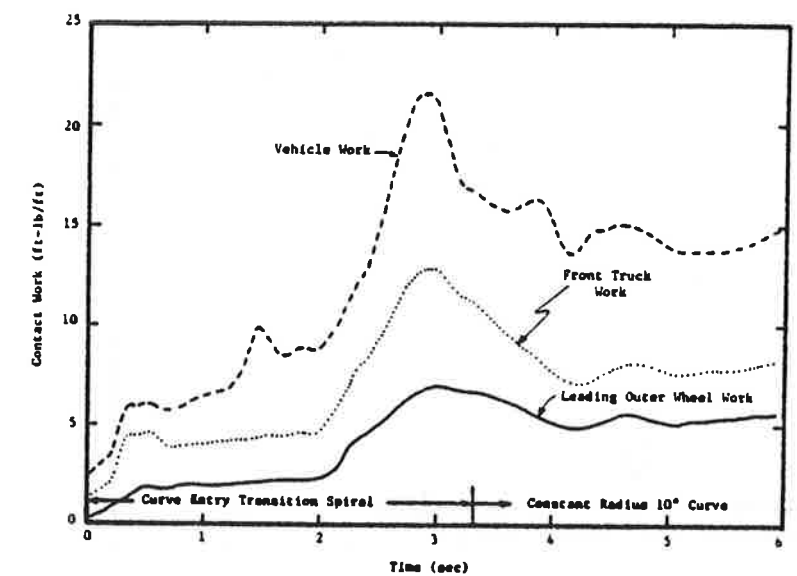


(b)

Figure 3.14 History of (a) Wheelset Lateral Excursions and (b) Angles of Attack of a FSR I Forced-Steered Radial Vehicle with Heumann Wheels Negotiating a 150 ft Curve Entry Spiral into a 10° Curve at a Balance Speed of 45 ft/sec.



(a)



(b)

Figure 3.15 History of (a) Leading Outer (i.e., Flanging) Wheel Lateral Force and (b) Contact Work of a FSR I Forced-Steered Radial Vehicle with Heumann Wheels Negotiating a 150 ft Curve Entry Spiral into a 10° Curve at a Balance Speed of 45 ft/sec.

The forced-steering action successfully positions the trailing wheelsets radially (since minimal flange forces act on the trailing wheelsets)..

The leading outer wheel lateral force is shown in Figure 3.15a. The force is characterized by significant oscillations. The force increases to a maximum of 1820 lb at $t = 2.250$ sec (i.e., 101 ft into the spiral curve). As the vehicle enters the constant radius curve, the force decreases and reaches a steady-state value of 1350 lb. The peak force exceeds the steady-state force by 35%.

The work at the leading outer wheel, the front truck, and the vehicle is shown in Figure 3.15b. In comparison to the work expended by the other vehicles in previous simulations, the work for the forced-steered vehicle with Heumann wheels is very small. The maximum work is 7, 13, and 22 ft-lb/ft for the leading outer wheel, front truck, and total vehicle, respectively. The work in steady-state is 6, 7, and 14 ft-lb/ft, respectively. In this case, dynamic effects influence the contact work histories.

3.5 Comparative Curve Entry Performance of Conventional, Self-Steered, and Forced-Steered Radial Vehicles

The previous sections have examined the dynamic curve entry performance of conventional, self-steered, and forced-steered radial vehicles with new and Heumann wheels. Baseline vehicles have been studied to ensure that the vehicles have identical linear critical speeds. This section compares the transient curving performance of the different vehicles.

The steady-state and peak values of the leading outer wheel lateral force and contact work are summarized in Tables 3.3 and 3.4 for vehicles with new and Heumann wheels, respectively. The tables show that the

TABLE 3.3

DYNAMIC CURVE ENTRY PERFORMANCE IN TERMS OF FLANGING WHEEL LATERAL FORCE AND CONTACT WORK FOR BASELINE VEHICLES WITH NEW WHEELS NEGOTIATING A 150 FT SPIRAL INTO A 10° CURVE AT A BALANCE SPEED OF 45 FT/SEC.

	NEW WHEELS								
	CONVENTIONAL			SELF-STEERED RADIAL			FORCED-STEERED RADIAL (FSR I)		
	Steady-State	Peak	% Increase	Steady-State	Peak	% Increase	Steady-State	Peak	% Increase
Flanging Wheel Lateral Force (lb)	4520	5270	17	4260	5090	20	3480	4310	24
Flanging Wheel Work (ft-lb/ft)	87	93	7	67	75	12	48	55	15

TABLE 3.4

DYNAMIC CURVE ENTRY PERFORMANCE IN TERMS OF FLANGING WHEEL LATERAL FORCE AND CONTACT WORK FOR BASELINE VEHICLES WITH HEUMANN WHEELS NEGOTIATING A 150 FT SPIRAL INTO A 10° CURVE AT A BALANCE SPEED OF 45 FT/SEC.

	HEUMANN WHEELS								
	CONVENTIONAL			SELF-STEERED RADIAL			FORCED-STEERED RADIAL (FSR I)		
	Steady-State	Peak	% Increase	Steady-State	Peak	% Increase	Steady-State	Peak	% Increase
Flanging Wheel Lateral Force (lb)	4050	4950	22	3940	4800	22	1350	1820	35
Flanging Wheel Work (ft-lb/ft)	62	72	16	56	64	14	6	7	17

FSR I forced-steered vehicle offers improved performance in terms of decreased steady-state and peak forces and work in comparison to the conventional and self-steered vehicles. For example, the peak work is 55 ft-lb/ft for the forced-steered vehicle with new wheels in comparison to 93 and 75 ft-lb/ft for the conventional and self-steered vehicles, respectively. The tables also show that the peak/steady-state force and work ratios are highest for the forced-steered vehicle (in terms of percent increase). For example, for vehicles with new wheels, the peak work exceeds the steady-state work by 15% for the forced-steered vehicle and by 7 and 12% for the conventional and self-steered vehicles, respectively. Table 3.4 shows that the greatest improvement in performance is obtained with the forced-steered vehicle with Heumann wheels. The steady-state and peak work is 6 and 7 ft-lb/ft, respectively. However, this vehicle experiences the largest dynamic overshoot in terms of percent. For instance, the peak work exceeds the steady-state work by 17%. The peak lateral force exceeds the steady-state force by 35%.

In summary, the data of Tables 3.3 and 3.4 suggest that significant performance improvements can be achieved by using forced-steered vehicles with Heumann wheels. Forced-steered vehicles experience a higher ratio of dynamic to steady-state force in curve entry than conventional and self-steered vehicles. However, the magnitudes of the transient characteristics of the forced-steered vehicles are smaller than those which develop for conventional and self-steered vehicles.

3.6 Dynamic and Steady-State Model Comparisons

This chapter has explored the dynamic curving performance of conventional, self-steered, and forced-steered radial vehicles with new

and Heumann wheels. The dynamic curving analysis used for the study incorporates a simple model of the secondary yaw suspension system. The model assumes that a coulomb damper element which saturates at the breakaway torque and has a linear viscous band acts between each truck and carbody. In steady-state conditions, the truck and carbody yaw rates vanish and thus no secondary yaw torques develop. The steady-state curving analysis described in the Interim Report [1] assumes that breakaway has occurred at each truck centerpin, and thus includes constant secondary yaw breakaway torques. Due to the different treatment of the secondary yaw torque, the dynamic model does not converge to a condition which is identical to the steady-state model. The differences in force and work predicted by the dynamic and steady-state models are summarized in Table 3.5. The data in the table show that the steady-state analysis which includes finite yaw torque between the track and carbody predicts larger lateral wheel forces than the dynamic analysis which in steady-state curve negotiation has zero yaw torque between the truck and carbody. For the simulations with trucks employing new wheels, the dynamic analysis converges to forces which are within 13% of the steady-state analysis values for all three truck designs and for trucks with Heumann wheels, the two simulations agree within 12% for conventional and radial trucks and within 20% for the low forces predicted for the forced steered truck.

The contact work for all the cases predicted by the dynamic analysis is within 10% of the values predicted by the steady-state analysis except for the forced steering vehicle with Heumann wheels where a 1.0 ft-lb/ft difference exists which is within the accuracy bounds of the computation.

TABLE 3.5

FLANGING WHEEL LATERAL FORCE AND CONTACT WORK
FOR BASELINE VEHICLES RUNNING AT BALANCE SPEED
IN A CONSTANT RADIUS 10° CURVE

	Wheel Lateral Force lb			Contact Work ft-lb/ft		
	Dynamic *	Steady-State **	Percent Difference	Dynamic *	Steady-State **	Percent Difference
New Wheels						
Conventional	4520	5100	11	87	90	3
Radial	4260	4900	13	67	72	7
Forced Steered	3480	4000	13	48	51	6
Heumann Wheels						
Conventional	4050	4500	10	62	69	10
Radial	3940	4480	12	56	61	8
Forced Steered	1350	1700	20	6	7	14

* Quantities are predicted by dynamic model as transients decay to reach steady-state values

** Quantities are predicted directly by steady-state analysis

The differences in representation of the yaw torque restraint between the track and carbody do not result in significant differences in prediction of contact wear or lateral force.

3.7 Review of Field Test Data

Limited field test data for dynamic curving forces is available. Field tests were conducted during the Fall of 1981 on the Washington Metropolitan Area Transit Authority (WMATA) [27]. The program investigated the influence of wheel profiles and suspension modifications on high speed stability and assessed the feasibility of a retrofit to the truck to improve curving performance.

Figures 3.16 and 3.17 present results from the WMATA test. Figure 3.16 shows measured steady state lateral flange forces on curve #37 while Figure 3.17 shows measured peak high rail flange forces. For example at approximately 40 mph and 4° cant deficiency the figures show a 4000 lb steady state flange force and a 7800 lb peak force, i.e., a nearly 2:1 ratio of peak to steady state high rail flange forces for the 1:20 wheel in a standard bushing.

The experimental data show that both wheel profile and suspension stiffness have an influence on steady-state and peak dynamic forces. As the bushing stiffness is reduced, the steady-state lateral force decreases from 4000 to 1800 lbs for the 1:20 wheels and from 5400 to 3800 lbs for the cylindrical wheels at balance speed. The 1:20 wheel profiles have reduced forces in comparison to the cylindrical wheels. Similar trends exist in the dynamic data.

The dynamic data at balance speed for both cylindrical and 1:20 wheels have a magnitude which is between 1.8 and 2.0 times the equivalent

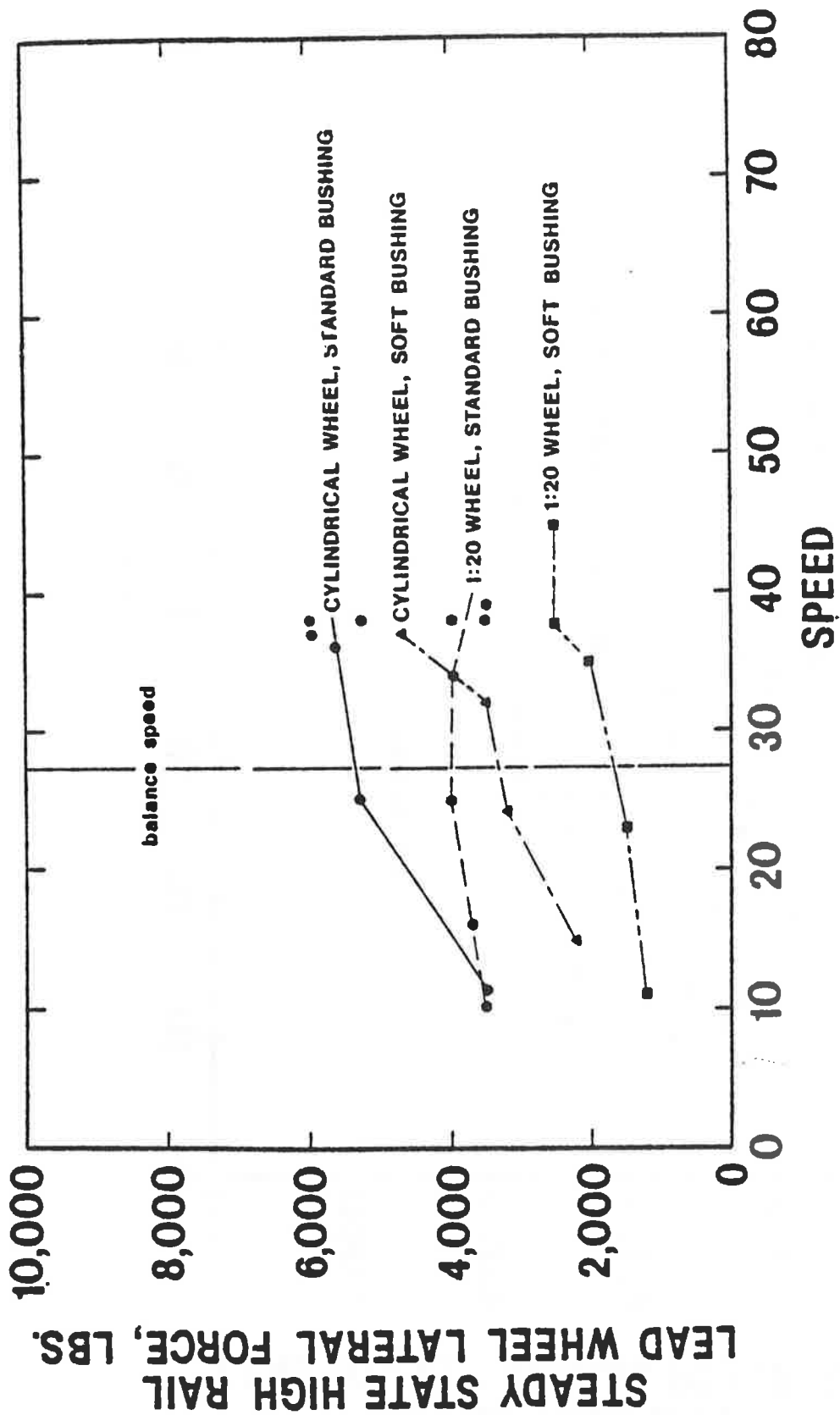


Figure 3.16 CURVE 37 STEADY STATE LATERAL WHEEL FORCES
(Adopted from [27])

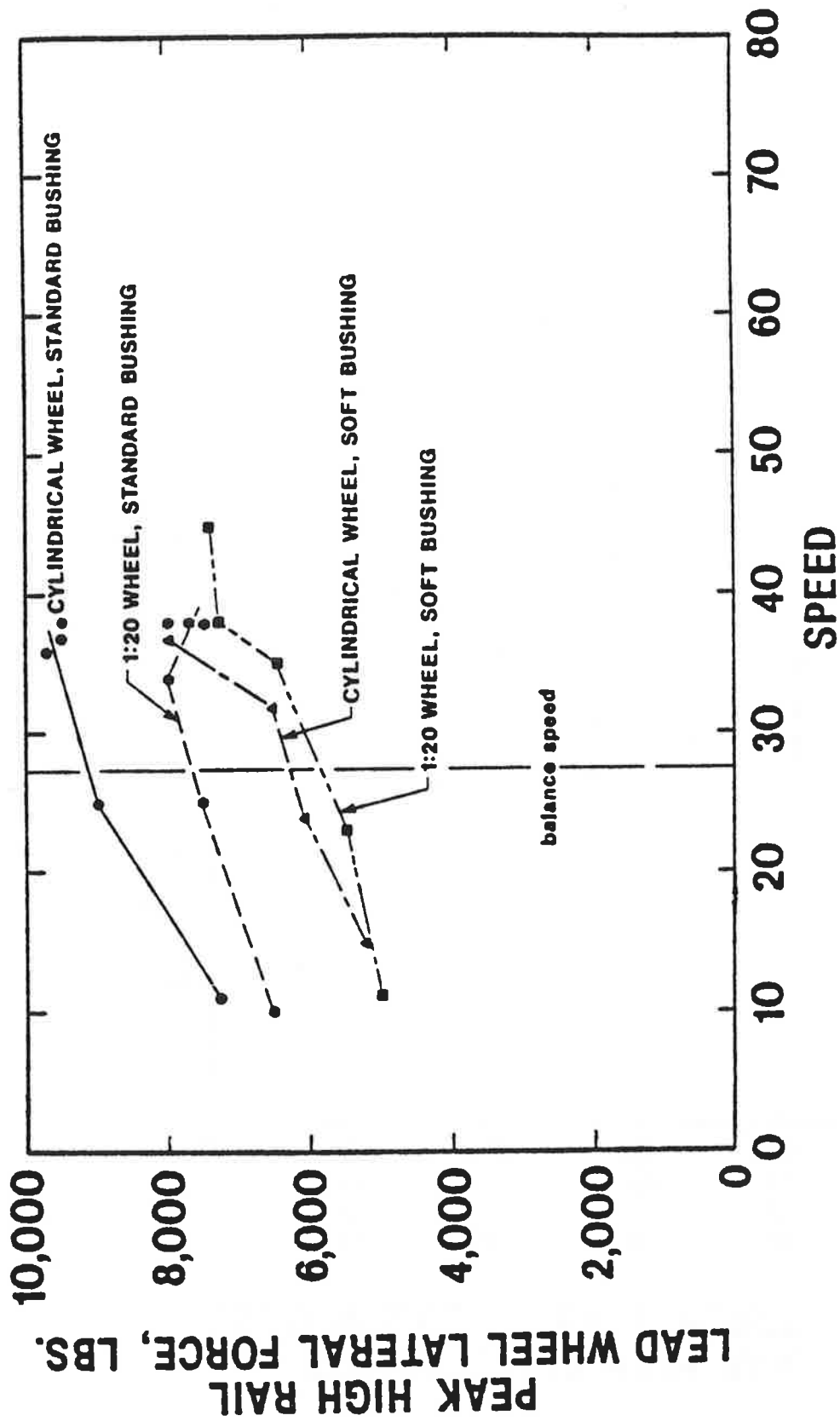


Figure 3.17 CURVE 37 PEAK LATERAL WHEEL FORCES
(Adopted from [27])

steady-state data. For the soft bushing suspension, the peak forces for the cylindrical and 1:20 wheel are both approximately 6250 lbs while equivalent steady-state data are respectively 3800 lbs and 1800 lbs.

In order to provide a preliminary evaluation of the dynamic curving model, the baseline conventional vehicle was simulated passing through 150 ft transition spiral to a 7.8° curve with a 4° cant angle to represent curve #37 at WAMATA. The baseline vehicle primary suspension was increased to 1.38×10^6 lb/ft to approximate a conventional truck equipped with a standard bushing. The results of the simulation for operation at balance speed with the AAR 1:20 profile are shown in Figure 3.18. The simulation data shows a peak force of 6500 lb and steady-state force of 5600 lbs in comparison to the experimental data showing 8000 lb peak force and 4000 lb steady-state force. These data are not in good agreement. Both the experimental data and the simulation studies cited in previous sections have shown that wheel-track profile, geometry and track suspension parameters have strong influences on peak and steady-state forces, thus detailed knowledge of track and vehicle parameters is required to provide a comparison between the analytical model and experimental data.

To provide an indication of these influences, a simulation has been made with all parameters identical to those of Figure 3.18 except the wheel profile has been modified to a Heumann profile. With the Heumann profile, the peak force in curve #37 is reduced to 3700 lb and the steady-state force to 3100 lb. The detailed wheel-track profile geometry has a strong influence on curving forces. A final simulation was run to illustrate the influence of local track conditions on peak curving forces.

Data for this case in which the vehicle in the constant radius section of curve #37 was assumed to have its wheelsets in a state corresponding to the track centerline and allowed to respond in a transient fashion reaching the steady-state condition after a response lasting 2.5 seconds. These simulation results are shown in Figure 3.20. In this case, the peak response force reaches 7200 lbs and then settles to a steady-state of 3100 lbs. This ratio of greater than 2:1 occurs because of an initial state which could be achieved through the response to local track conditions. Large peak force ratios in constant radius curve sections can be generated by local irregularities. Thus, knowledge of local track geometry is required to predict peak forces.

In summary, the review of field test data for dynamic curving and initial comparison with simulation results has identified the need for further effort. Detailed characterization of vehicle and track parameters is required. It is recommended that effort be directed to a coupled analytical/experimental program to develop an experimentally verified dynamic curving model.

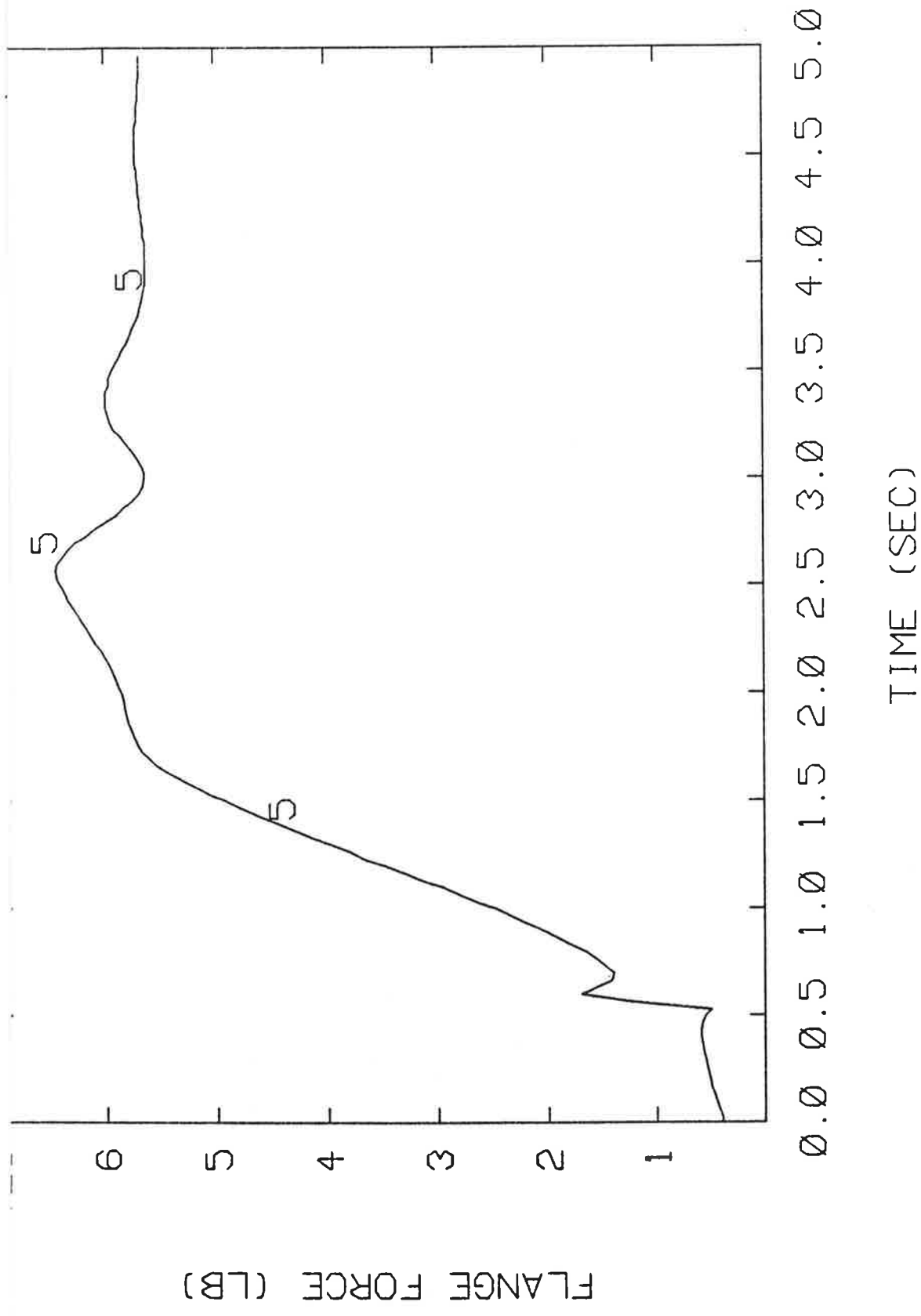
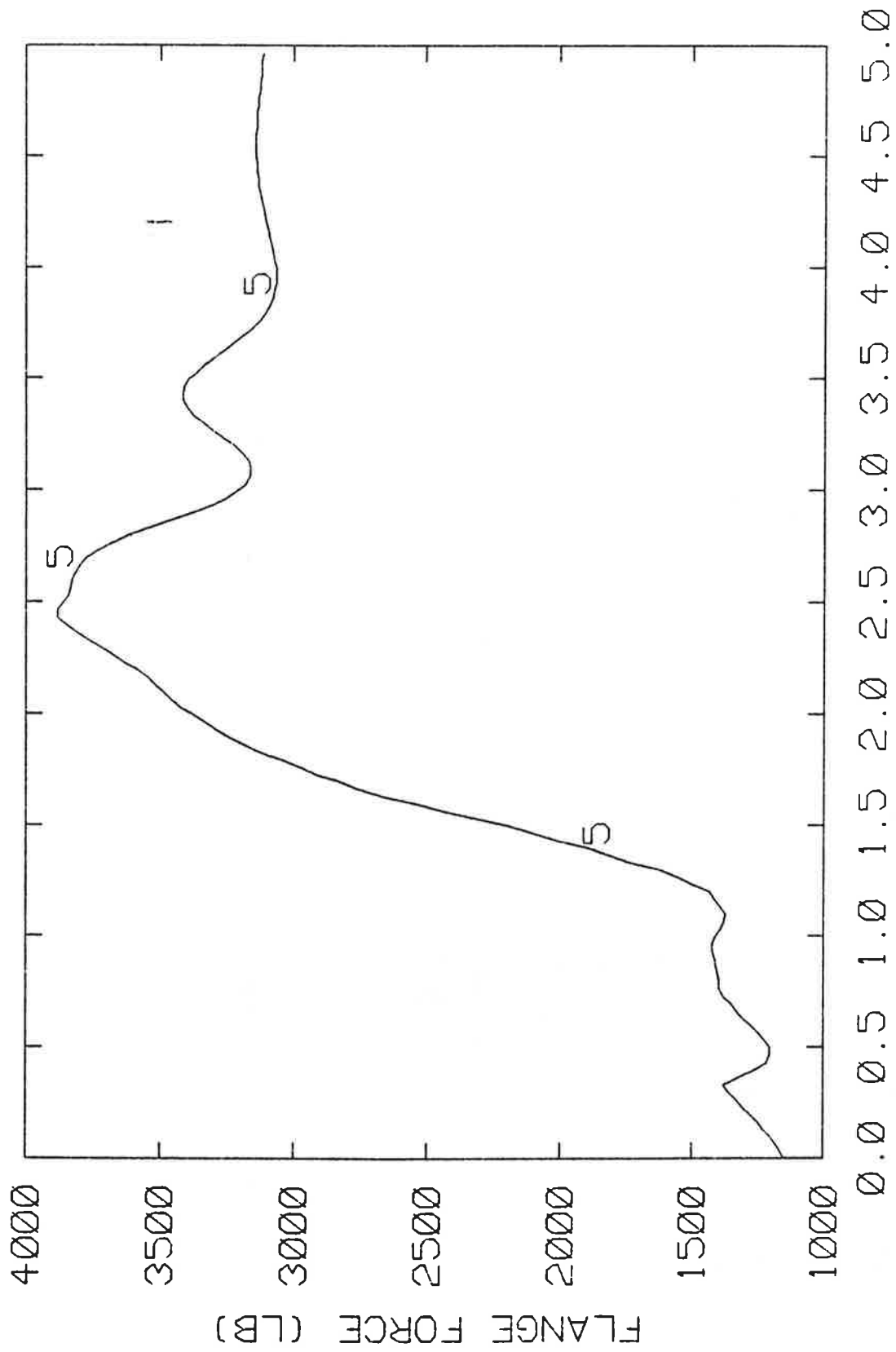


Figure 3.18 Simulation of Curve 37 (7.6° curve, 4° c.d., 40 mph, new wheel, spiral entry)



TIME (SEC)

Figure 3.19 Simulation of curve 37 (7.6° curve, 4° c.d., 40 mph, Heumann wheel, spiral entry)

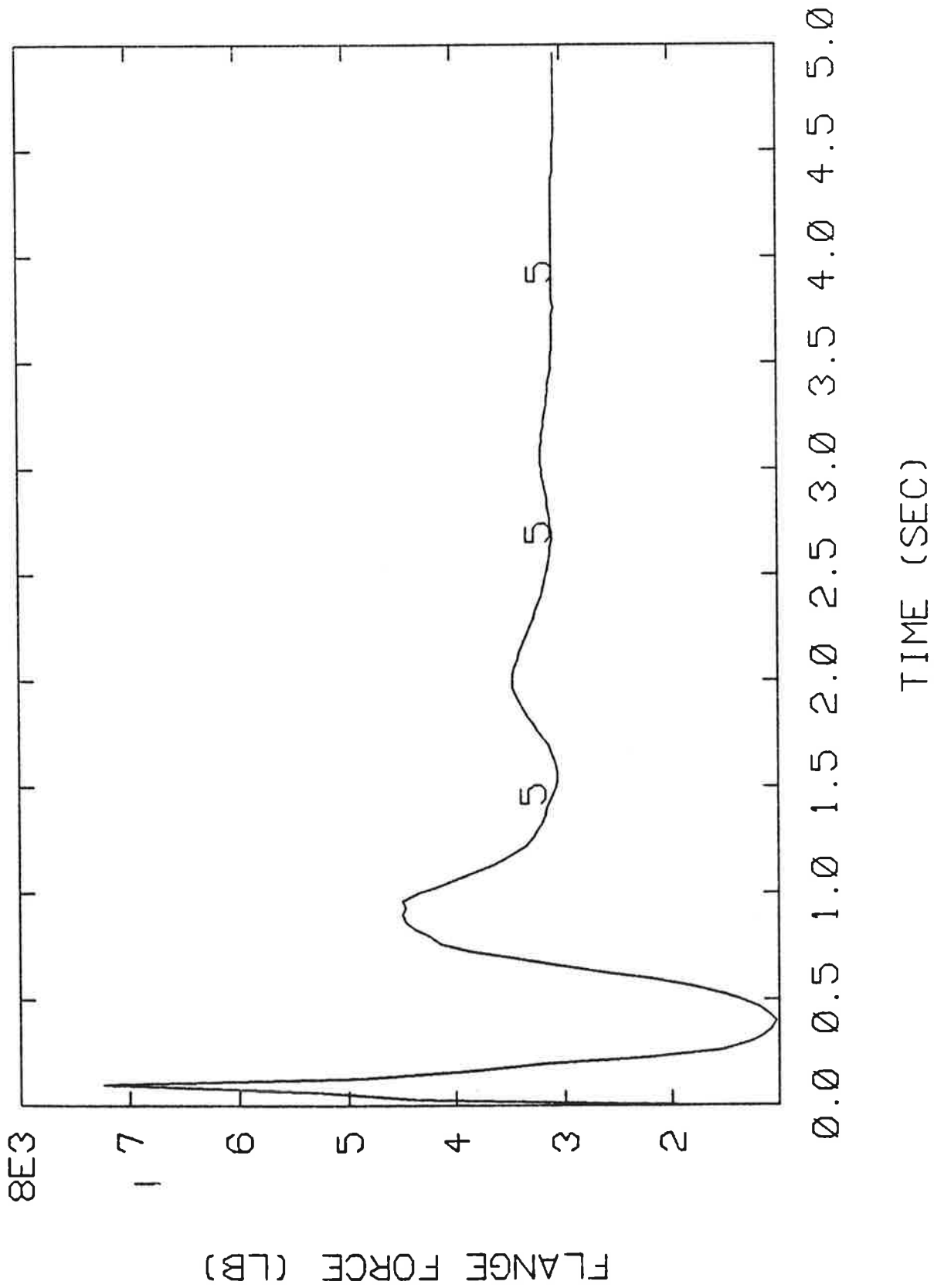


Figure 3.20 Simulation of Curve 37 (7.6°, 4° c.d., 40 mph, Heumann Wheel, no spiral entry)

4.0 SUMMARY AND CONCLUSIONS

A simulation model has been developed to compute the dynamic forces and motions as a rail vehicle enters, transverses and exits curves. The model includes the effects of nonlinear, multipoint wheel-rail contact geometry and is applicable to conventional, self-steered radial and forced steered truck configurations. The track is represented as a smooth space curve and has lateral flexibility. Extension of the track representation to include effects of irregularities is straight forward.

Illustrative simulations of curve entry through a 150 ft spiral transition to 2.5° - 10° constant radius curves have been performed for baseline conventional, radial and forced-steered truck designs operating with new AAR and Heumann wheel profiles. The parametric studies have been conducted for vehicles running at balance speed.

Data for the conventional truck design has shown that dynamic wheel-rail forces occurring during negotiation of a 150 spiral transition to 2.5° , 5° and 10° constant radius curves increase respectively from 1660 lbs, to 2650 lbs and to 5270 lbs. These peak dynamic forces represent increases from steady-state values respectively of 388%, 29% and 17% as curve radius decreases. Thus, dynamic forces are significantly greater than steady-state forces for large radius curves where the overall force levels are small. For 5° curves and greater the dynamic peak forces are within 30% of the steady-state forces and for smaller radius curves, initial flange contact occurs early in the transition and is maintained throughout the curve.

Studies in which the transition spiral entry length was varied for the conventional truck with new wheels entering a 10° curve indicate

that as spiral length is reduced from 150 ft to 100 ft and then to 75 ft, the peak dynamic forces increase from 5270 lb to 5450 lb to 6250 lbs. Thus, as spiral transition length is decreased, peak dynamic forces increase with the 75 ft length having almost a 20% increase in peak forces compared with the 150 ft spiral. For short spiral lengths of 50 ft or less entering 10° curves, peak forces 1.8 times steady-state forces are reached, and short length transitions can lead to significant ratios of peak to steady-state forces for high degree curves.

Data comparing the dynamic curving forces for conventional, radial and forced steering trucks traversing a 150 ft spiral transition to a 10° curve have shown that significant decreases in both steady-state and peak dynamic forces may be achieved using forced steered trucks with Heumann wheel profiles. For all three truck designs both steady-state and peak forces are smaller with a Heumann than a new AAR wheel profile with peak force reductions of 5-6% for the baseline conventional and self-steered radial trucks and of 58% for the forced steered baseline design. For the cases considered, the Heumann wheel profile has a significant influence on peak forces for the forced steered design and relatively modest influences for the conventional and radial baseline track designs.

In the simulation cases, the peak dynamic curving forces for the three trucks with Heumann wheel profiles are 4950 lb for the conventional, 4800 lb for the radial and 1820 lb for the forced steered truck. In these cases, the forced steered truck has peak forces less than half of the forces for the other two baseline designs. The forced steered truck peak force is 35% greater than the steady-state force while the conventional and radial vehicles have peak forces 22% above steady-state forces. While

the forced steered vehicle has a higher dynamic to steady-state force ratio than the other two baseline designs, its maximum dynamic force is less than one half the forces with conventional and radial baseline designs.

An additional set of simulations have been conducted for a conventional truck with increased primary suspension stiffnesses on a 7.6° curve. The increased stiffness corresponds to the stiffness of a Washington Metropolitan Area Transit Authority (WMATA) vehicle. Simulation results run for the curve with 150 ft transition spiral indicated that peak and steady-state forces of 6500 lb and 5600 lb occurred. Test data taken at WMATA have indicated a nearly 2:1 ratio of peak to steady-state force for these track geometries during negotiation by a conventional vehicle with new AAR wheels. Additional simulation data have indicated that the ratio of peak to steady-state forces is strongly influenced by the initial conditions of the vehicle entering the curve. Thus, the prediction of specific dynamic forces requires a detailed knowledge of local track parameters and vehicle parameters. Further effort is required to resolve the differences between field test data results and the simulation.

In summary this report has provided a simulation model for evaluating dynamic forces generated during rail transit vehicle curve negotiation. Further effort is recommended to provide an experimentally verified dynamic curving model. Such an effort should include a detailed characterization of the local track conditions in the test section as well as the vehicle parameters.

5.0 REFERENCES

1. Wormley, D. N., Hedrick, J. K., and Nagurka, M. L., "Stability and Curving Performance of Conventional and Advanced Rail Transit Vehicles," DTRS-57-80C-00152, Transportation Systems Center, U.S.D.O.T., November, 1982.
2. Marcotte, P. P., Mathewson, K. J., and Caldewell, W. N., "Improved Wheel Tread Profiles for Heavy Freight Vehicles," J. of Engineering for Industry, Vol. 102, August, 1980, pp. 263-271.
3. Elkins, J. A., and Weinstock, H., "The Effects of Two-Point Contact on the Curving Behavior of Railroad Vehicles," presented at the 1982 A.S.M.E. Winter Annual Meeting, Phoenix, Arizona, November, 1982.
4. Mueller, C. Th., "Dynamics of Railway Vehicles on Curved Track," Interaction Between Vehicle and Track, The Institution of Mechanical Engineering Proceedings, Vol. 180, Part 3F, 1965 - 1966, pp. 45 - 57.
5. Smith, K., "Curve Entry and Curve Negotiation Characteristics of Two-Axle Trucks," M.S. Thesis, Illinois Institute of Technology, December, 1975.
6. Cooperrider, N. K., and Law, E. H., "The Nonlinear Dynamics of Rail Vehicles in Curve Entry and Negotiation," presented at the 7th IAVSD-IUTAM Symposium on the Dynamics of Vehicles on Roads and Tracks, Cambridge, U.K., September 7-11, 1981.
7. Law, E. H., and Cooperrider, N. K., "Nonlinear Dynamic and Steady-State Curving of Rail Vehicles," presented at the 1980 A.S.M.E. Winter Annual Meeting, San Francisco, CA, December, 1978.
8. Clark, R. A., Eickhoff, B. M., and Hunt, G. A., "Prediction of the Dynamic Response of Vehicles to Lateral Track Irregularities," presented at the 7th IAVSD-IUTAM Symposium on the Dynamics of Vehicles on Roads and Tracks, Cambridge, U.K., September 7-11, 1981.
9. Duffek, W., and Jaschinski, A., "Efficient Implementation of Wheel-Rail Contact Mechanics in Dynamic Curving," presented at the 7th IAVSD-IUTAM Symposium on the Dynamics of Vehicles on Roads and Tracks, Cambridge, U.K., September 7-11, 1981.
10. Krolewski, S. M., "Model Development for Freight Car Dynamic Curving Simulation," S.M. Thesis, Department of Mechanical Engineering, M.I.T., June, 1982.
11. Bolton, P., "Wear of BS11 Rail Steels in Rolling/Sliding Contact with Class "D" Tyep Steel," British Railways Technical Note TNMET21, February, 1980.
12. Kumar, S., Prasanna Rao, D. L., and Rajkuma, B. R., "A Wheel-Rail Wear Study for Railroad Transit Systems," I.I.T. Report IIT-TRANS-80-1, August, 1980.

13. Bolton, P. J., Clayton, P., and McEwen, I. J., "Wear of Rail and Tyre Steels Under Rolling/Sliding Conditions," British Rail Research, presented at the ASME/ASNE Conference, August, 1980.
14. Elkins, J. A., and Allen, R. A., "Testing a Transit Vehicle for Wheel and Rail Wear," A.S.M.E. Transactions, Paper 81-WA/DSC-19, 1981.
15. Ahlbeck, D. R., "The Effects of Track Modulus on Vehicle-Track Dynamic Interaction," IEEE/ASME Joint Railroad Conference, Erie, PA, April, 1982.
16. Kalker, J. J., "Survey of Wheel-Rail Rolling Contact Theory," Vehicle System Dynamics, Vol. 5, 1979, pp. 317 - 358.
17. List, H. A., Caldwell, W. N., and Marcotte, P., "Proposed Solutions to the Freight Car Truck Problems of Flange Wear and Truck Hunting," ASME Paper No. 75-WA-RT-8, 1976.
18. Scheffel, H., "The Hunting Stability and Curving Ability of Railway Vehicles," Rail International, No. 2., February, 1974, pp. 154-177.
19. Horak, D., Bell, C. E., and Hedrick, J. K., "A Comparison of the Stability and Curving Performance of Radial and Conventional Rail Vehicle Trucks," J. of Dynamic Systems, Measurement and Control, Vol. 103, September, 1981, pp. 191-200.
20. Scales, B. T., "Behavior of Bogies on Curves," Railway Engineering Journal, July, 1972, pp. 19-24.
21. Smith, R. E., "Steering Conversion of CTA 2400 Rapid Transit Truck, Volume I: Design Feasibility Study," Project Memorandum, U.S.D.O.T. Report No. DOT-TSC-UM104-PM-80-48, December, 1980.
22. Bell, C. E., and Hedrick, J. K., "Forced Steering of Rail Vehicles: Stability and Curving Mechanics," Vehicle System Dynamics, Vol. 10, pp. 357-386, 1981.
23. Cooperrider, N. K., and Law, E. H., "Data Book: Wheel/Rail Geometry for Five Wheel Profiles and Three Rail Profiles," Report No. ERC-R-75015, Department of Mechanical Engineering, Arizona State University, Tempe, Arizona 85281.
24. Cooperrider, N. K., and Wirth, J. L., "Wheel Tread Profile as a Rail Vehicle Design Parameter," A.S.M.E. Technical Report 82-WA/DSC-3, 1982.
25. Mekosh, G., "Technical Analysis for Modifying an Existing Heavy Rapid Rail Truck to a Steerable Configuration," Report for Contract No. DOT-TSC-1740, May, 1980.

26. Elkins, J. A., and Eickhoff, B. M., "Advances in Non-Linear Wheel/Rail Force Prediction Methods and Their Validation," Journal of Dynamic Systems, Measurement and Control, Vol. 104, No. 2, June, 1982, pp. 133-142.
27. Boyd, P. J., Zaiko, J. P, and Jordan, W. L., "Wheel/Rail Force Measurement at the Washington Metropolitan Area Transit Authority - Phase II, Volume II, Test Report," UMTA-MA-06-0025-83-2, June, 1983.
28. Gilchrist, A. O., and Brickle, B. V., "A Re-Examination of the Proneness to Derailment of a Railway Wheelset," J. of Mechanical Engineering Science, Vol. 18, No. 3, 1976, pp. 131 - 141.

APPENDIX A

DYNAMIC CURVING EQUATIONS OF MOTION OF A WHEELSET

A.1 Introduction

The basic element of the rail vehicle steering and support system is the wheelset. The contact and friction mechanisms which develop at the wheel/rail interfaces have a dominant effect on vehicle curving behavior. The curving performance of a vehicle is a direct function of the ability of its wheelsets to negotiate a curve.

The majority of previous steady-state and dynamic curving studies have assumed that each wheel of the vehicle contacts the rails at a single point. This is an acceptable approximation of tread contact, but for some wheel/rail profiles this represents a simplistic view of flange contact. For profiles with steep flanges including many U.S. profiles, two points of contact can occur simultaneously at the flanging wheel.

In this Appendix, an analytic model is developed to predict the dynamic curving performance of a rail vehicle wheelset. The model represents single-point and two-point wheel/rail contact at the flanging wheel and accounts for nonlinearities due to wheel/rail profile geometry and friction (creep) force saturation. The derivation assumes that (1) the wheelset maintains continuous wheel/rail contact as it traverses smooth, laterally flexible, right-handed curved track, and (2) the forward speed of the wheelset as well as the track curvature and super-elevation (or bank) angle are known functions of the distance along the track. Wheelset and rail equations are derived by application of

Newtonian mechanics, resulting in force and moment dynamic equilibrium equations. By appropriate manipulation, a set of coupled scalar differential equations are generated which characterize the dynamic curving behavior of a wheelset in single-point or two-point contact at the flanging wheel. The governing equations represent a system of 5 states for the wheelset and 2 states for the rails. The wheelset has 2 states (i.e., 1 degree of freedom) to describe its lateral and yaw motions as well as a state to represent its spin speed. Each rail has a state to describe its lateral motion. When two-point contact occurs, the state of the rail at the flanging wheel is known due to a constraint relation which exists between the wheelset and rail lateral motions. Finally, an appropriate numerical solution procedure involving digital integration of the equations of motion is described.

A.2 Coordinate Systems

Six coordinate systems are established, each consisting of mutually-perpendicular right-handed axes x, y, z with corresponding unit vectors $\hat{i}, \hat{j}, \hat{k}$. The $x, y,$ and z axes denote the longitudinal, lateral, and vertical directions, respectively, of each system. The coordinate systems are:

I	Inertial	}	Track-Related
H	Horizontal		
T	Track		

- | | | | |
|---|---|---|----------------------|
| 1 | Yaws with wheelset | } | Wheelset-
Related |
| 2 | Yaws and rolls with wheelset | | |
| 3 | Wheelset (i.e., yaws, rolls, and pitches with wheelset) | | |

The first three systems are used to define the orientation of the track (which has variable geometry). The latter three systems are used to define the orientation of the wheelset.

Figure A.1 shows the inertial ("I"), horizontal ("H"), track ("T"), and wheelset ("W") coordinate systems. The inertial system, "I", is fixed in inertial space. The track system, "T", with origin O_T moves along the track centerline with tangential speed V and is superelevated relative to the horizontal system, "H". The x_T and y_T axes lie in the track plane (x_T points in the longitudinal direction and y_T points radially outward); the z_T axis is oriented normal to the track plane and points up. The "W" coordinate system has axes aligned with the principal directions of the wheelset (i.e., fixed in the directions of the three principal mass moments of inertia), with its origin at the wheelset's center of mass, W^* .

Relative to the inertial system, the track system is rotated due to curvature and superelevation angle. The orientation of the wheelset is specified relative to the track system by a yaw, roll, and pitch angle. Wheelset axes initially aligned with track axes are rotated successively through the following sequence: (1) yaw (ψ_w) about the z_T axis, (2) roll (ϕ_w) about the rotated x_T axis, and (3) pitch (θ_w) about the rotated y_T axis. Figure A.2 defines the different coordinate system rotations and

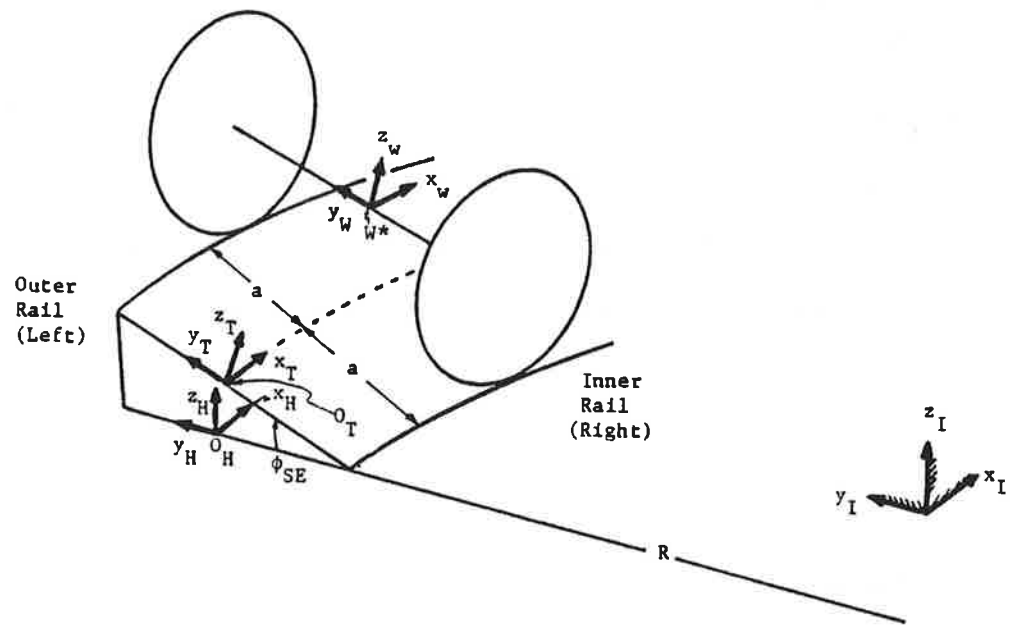


Figure A.1 Wheelset and Track Coordinate Systems

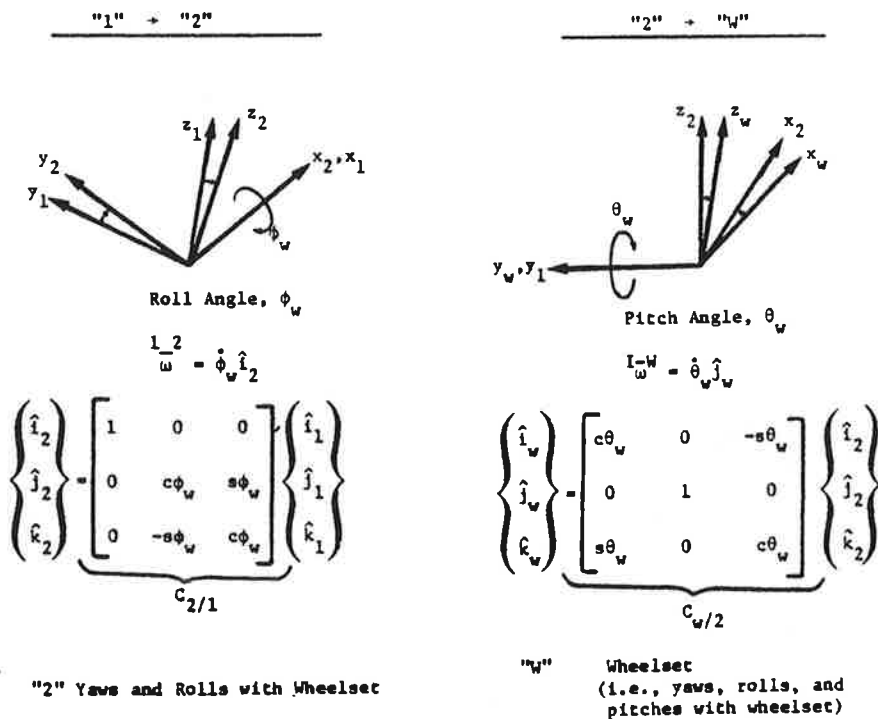
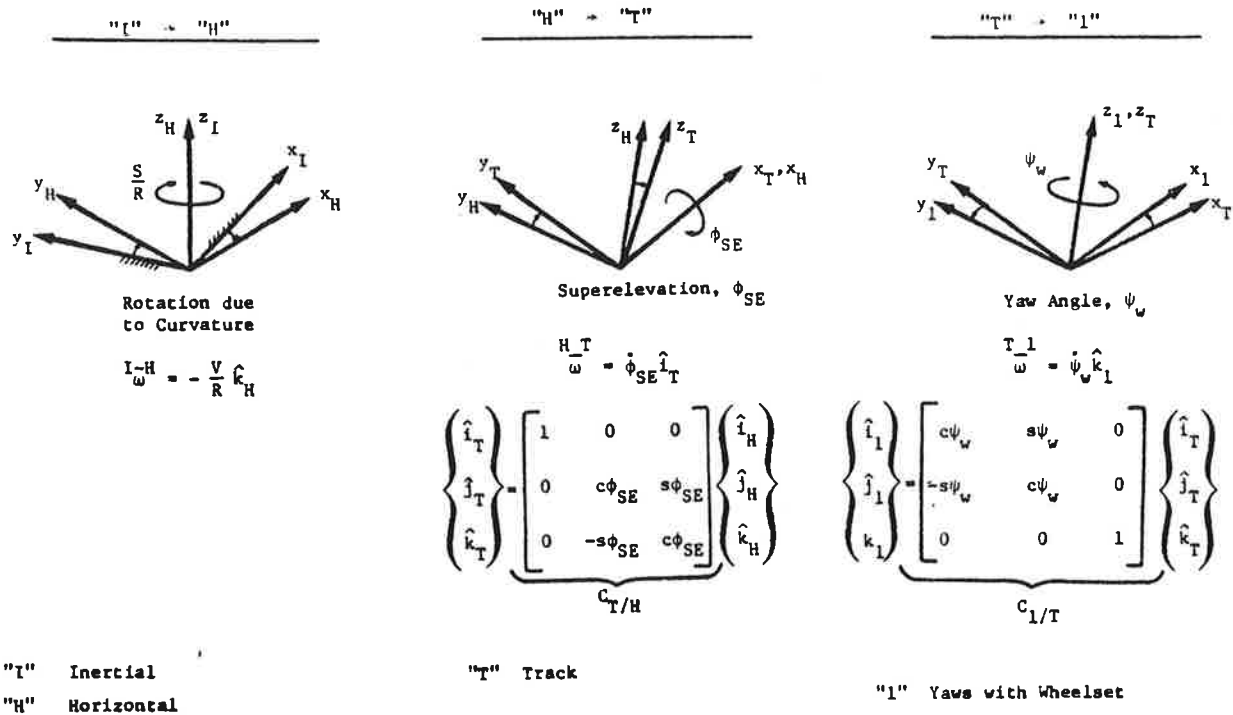


Figure A.2 Definition of Wheelset and Track Coordinate System Orientations (Rotations Only)
 [The following notation is used: $s\alpha = \sin(\alpha)$, $c\alpha = \cos(\alpha)$]

corresponding transformation relations. The transformation relation for multiple rotations is obtained by matrix multiplication. For instance, the relation between the wheelset and track systems is:

$$\begin{Bmatrix} \hat{i}_W \\ \hat{j}_W \\ \hat{k}_W \end{Bmatrix} = [C_{W/T}] \begin{Bmatrix} \hat{i}_T \\ \hat{j}_T \\ \hat{k}_T \end{Bmatrix} \quad (A-1)$$

where the coordinate transformation matrix $[C_{W/T}]$ is found from matrix multiplication as follows:

$$[C_{W/T}] = [C_{W/2}][C_{2/1}][C_{1/T}] \quad (A-2)$$

Assuming small yaw, roll, and pitch angles, this coordinate transformation matrix is:

$$[C_{W/T}] = \begin{bmatrix} 1 & \psi_W & -\theta_W \\ -\psi_W & 1 & \phi_W \\ \theta_W & -\phi_W & 1 \end{bmatrix} \quad (A-3)$$

Finally, an important simplification occurs since the transformation matrices are orthogonal. As a result, matrix inversion is equivalent to the simpler transpose operation. Thus, the inverse relation:

$$\begin{Bmatrix} \hat{i}_T \\ \hat{j}_T \\ \hat{k}_T \end{Bmatrix} = [C_{T/W}] \begin{Bmatrix} \hat{i}_W \\ \hat{j}_W \\ \hat{k}_W \end{Bmatrix} \quad (A-4)$$

is easily obtained since:

$$[C_{T/W}] = [C_{W/T}]^{-1} = [C_{W/T}]^t \quad (A-5)$$

(where superscript t implies transpose).

In this Appendix, equations are developed to describe the dynamic behavior of a wheelset traversing right-handed curved track. For a wheelset moving along right-handed curved track, as shown in Figure A.1, positive lateral excursions, y_W , are associated with displacements toward the left rail (i.e., the outer or high rail). Thus, as the wheelset displaces laterally in the positive sense, flange contact occurs at the left wheel.

A.3 Acceleration of Wheelset Center of Mass

The inertial acceleration of the center of mass of the wheelset, $\underline{I} \underline{W}^* \underline{a}$, is:

$$\begin{aligned} \underline{I} \underline{W}^* \underline{a} = & \underline{I} \underline{O}_T \underline{a} + \underline{r} \underline{W}^* / \underline{O}_T + \underline{r} \underline{W}^* / \underline{O}_T + \underline{I} \cdot \underline{T} \underline{W}^* / \underline{O}_T \\ & + \underline{I} \underline{T} \underline{W}^* / \underline{O}_T + 2 \underline{I} \underline{T} \underline{W}^* / \underline{O}_T \end{aligned} \quad (A-6)$$

where $\underline{I} \underline{O}_T \underline{a}$ is the inertial acceleration of point O_T (the origin of the "T" system), $\underline{I} \underline{T} \underline{\omega}$ and $\underline{I} \underline{T} \underline{\dot{\omega}}$ are the angular velocity and angular acceleration, respectively, of the "T" system relative to the "I" system, $\underline{r} \underline{W}^* / \underline{O}_T$ is

the position vector from O_T to W^* (the center of mass of the wheelset "W"), and $\frac{T \cdot W^*}{r} / O_T$ and $\frac{T \cdot W^*}{r} / O_T$ are the first and second derivatives, respectively, taken in the "T" system of the position vector from O_T to W^* . Assuming small superelevation angle, the inertial acceleration of O_T is:

$$\frac{I}{a} O_T = \dot{V} \hat{i}_T - \frac{V^2}{R} \hat{j}_T + (a \ddot{\phi}_{SE} + \frac{V^2}{R} \phi_{SE}) \hat{k}_T. \quad (A-7)$$

In equation (A-7), a represents half the rail gage. The angular velocity of the "T" system with respect to the "I" system is:

$$\frac{I}{\omega} T = \dot{\phi}_{SE} \hat{i}_T - \frac{V}{R} \phi_{SE} \hat{j}_T - \frac{V}{R} \hat{k}_T. \quad (A-8)$$

The displacement of W^* from O_T is:

$$\frac{W^*}{r} / O_T = x_W \hat{i}_T + y_W \hat{j}_T + (z_W + r_o) \hat{k}_T \quad (A-9)$$

where x_W , y_W , and z_W represent small longitudinal, lateral, and vertical displacements, respectively, of the wheelset center of mass. Substituting equations (A-7) - (A-9) into (A-6) yields the inertial acceleration of the center of mass of the wheelset:

$$\begin{aligned} \frac{I}{a} W^* &= [\ddot{x}_W + \dot{V}] \hat{i}_T + [\ddot{y}_W - r_o \ddot{\phi}_{SE} - \frac{V^2}{R}] \hat{j}_T \\ &+ [\ddot{z}_W + a \ddot{\phi}_{SE} + \frac{V^2}{R} \phi_{SE}] \hat{k}_T. \end{aligned} \quad (A-10)$$

A.4 Rate of Angular Momentum of Wheelset

From Figure A.2, the angular velocity of the wheelset or "W" system relative to the "I" system is:

$$\frac{I}{\omega} \dot{W} = -\frac{V}{R} \hat{k}_H + \dot{\phi}_{SE} \hat{i}_T + \dot{\psi}_W \hat{k}_1 + \dot{\phi}_W \hat{i}_2 + \dot{\theta}_W \hat{j}_W . \quad (A-11)$$

Assuming small angles, equation (A-11) simplifies to:

$$\frac{I}{\omega} \dot{W} = \omega_{WX} \hat{i}_2 + \omega_{WY} \hat{j}_2 + \omega_{WZ} \hat{k}_2 \quad (A-12)$$

where the components are:

$$\begin{aligned} \omega_{WX} &= \dot{\phi}_{SE} + \dot{\phi}_W \\ \omega_{WY} &= \dot{\theta}_W \end{aligned} \quad (A-13)$$

$$\omega_{WZ} = \dot{\psi}_W - \frac{V}{R} .$$

Since the "2" system is aligned with the principal directions of the wheelset, the angular momentum of the wheelset about its center of mass is given by:

$$\frac{I}{H} \dot{W/W^*} = I_{WX} \omega_{WX} \hat{i}_2 + I_{WY} \omega_{WY} \hat{j}_2 + I_{WX} \omega_{WZ} \hat{k}_2 \quad (A-14)$$

where I_{WX} and I_{WY} are the roll and pitch principal mass moments of inertia of the wheelset, respectively. In equation (A-14), the yaw and roll moments of inertia are assumed identical due to symmetry.

The time rate of change of angular momentum is expressed by:

$$\frac{I \cdot W/W^*}{H} = \frac{2 \cdot W/W^*}{H} + \frac{I}{\omega} \times \frac{W/W^*}{H} \quad (A-15)$$

where $\frac{I \cdot W/W^*}{H}$ and $\frac{2 \cdot W/W^*}{H}$ are the first derivatives of the angular momen-

tum in the "1" and "2" systems, respectively, and where $\overset{1}{\omega}^2$ is the angular velocity of the "2" system relative to the "1" system. Since the "2" coordinate system does not spin (pitch) with the wheelset, its angular velocity with respect to the "1" system is:

$$\overset{1}{\omega}^2 = \omega_{WX} \hat{i}_2 + \omega_{WZ} \hat{k}_2 \quad (\text{A-16})$$

where ω_{WX} and ω_{WY} are defined in equation (A-13). Substituting equations (A-13), (A-14), and (A-16) into (A-15) and neglecting smaller order terms gives the inertial time rate of change of angular momentum:

$$\begin{aligned} \frac{I \cdot W/W^*}{H} &= [I_{WX}(\ddot{\phi}_{SE} + \ddot{\phi}_W) - I_{WY}\dot{\theta}_W(\dot{\psi}_W - \frac{V}{R})] \hat{i}_2 \\ &+ [I_{WY}\ddot{\theta}_W] \hat{j}_2 \\ &+ [I_{WX}(\ddot{\psi}_W - \frac{\dot{V}}{R} - V(\frac{\dot{i}}{R})) + I_{WY}\dot{\theta}_W(\dot{\phi}_{SE} + \dot{\phi}_W)] \hat{k}_2. \end{aligned} \quad (\text{A-17})$$

A.5 Wheelset Forces and Moments

As a wheelset negotiates a curve, partial slip or creepage occurs at the wheel/rail contact patches. Due to normal loads acting on the slipping wheelset, friction-type forces known as creep forces are generated. The creep forces depend upon the amounts of pure-roll and pure-slip at each contact patch. In addition to creep forces, normal (or reaction) forces act at each contact patch to equilibrate wheelset loads.

Other external forces and moments acting on the wheelset are:

- Body forces including wheelset weight and other loads carried by the wheelset from the truck, carbody above.
- Suspension forces and moments which depend upon the truck configuration (e.g., conventional transit, radial, etc.)
- Thrust forces and traction (driving/braking) moments which depend upon the truck type (e.g., powered truck)

In the following sections, normal forces and creep forces/moments are discussed.

A.5.1 Normal Forces

Normal forces act at each wheel/rail contact patch. The left and right normal forces, F_{NL} and F_{NR} , respectively, are shown in Figure A.3 for a wheelset in single-point contact. Also shown in Figure A.3 are the left and right contact angles (δ_L, δ_R), the left and right rolling radii (r_L, r_R), and the wheelset roll angle relative to the track plane (ϕ_W).

Each normal force acts perpendicular to the contact patch plane and can be resolved into lateral and vertical components in the track plane. For single-point wheel/rail contact at the left and right wheels, the resolved normal force components are:

$$\begin{aligned}
 F_{NYL} &= -F_{NL} \sin(\delta_L + \phi_W) \\
 F_{NZL} &= F_{NL} \cos(\delta_L + \phi_W) \\
 F_{NYR} &= F_{NR} \sin(\delta_R - \phi_W) \\
 F_{NZR} &= F_{NR} \cos(\delta_R - \phi_W)
 \end{aligned}
 \tag{A-18}$$

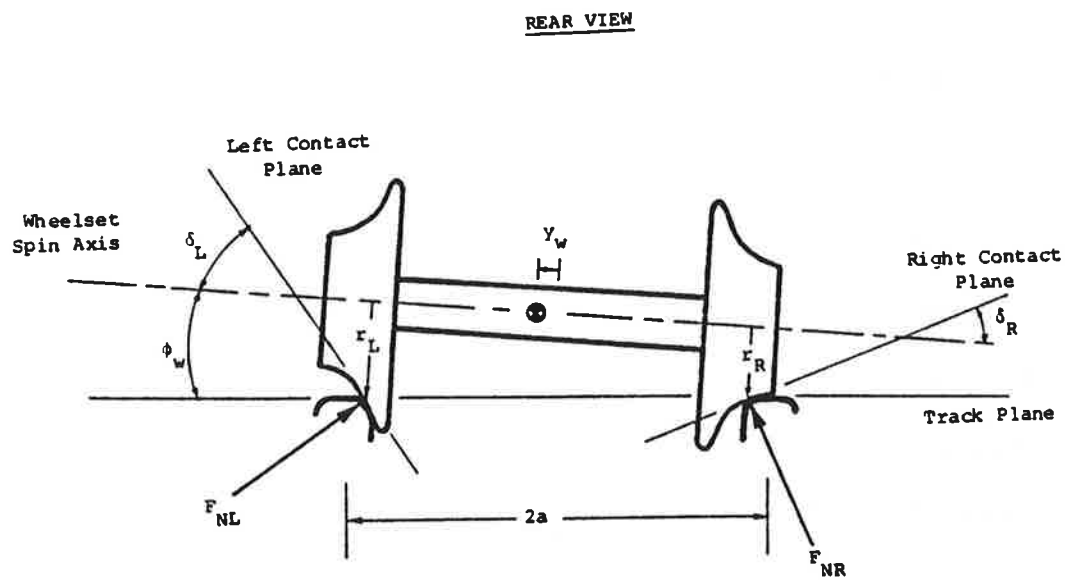


Figure A.3 Wheel/Rail Geometry and Normal Forces Assuming Single-Point Contact

where F_{NYL}, F_{NYR} = left, right normal force in lateral "track" direction

F_{NZL}, F_{NZR} = left, right normal force in vertical "track" direction

The sum of the lateral components of the normal forces is sometimes referred to as the "gravitational stiffness force".

A.5.2 Creep Forces and Moments

In general, rolling/sliding contact theories predict longitudinal and lateral components of creep force in the plane of the contact patch and a creep moment normal to the patch. Contact patch coordinate systems as well as the transformation relations between the contact patch and track axes are defined in Figure A.4. The creep forces and moments at the left, right contact patches are:

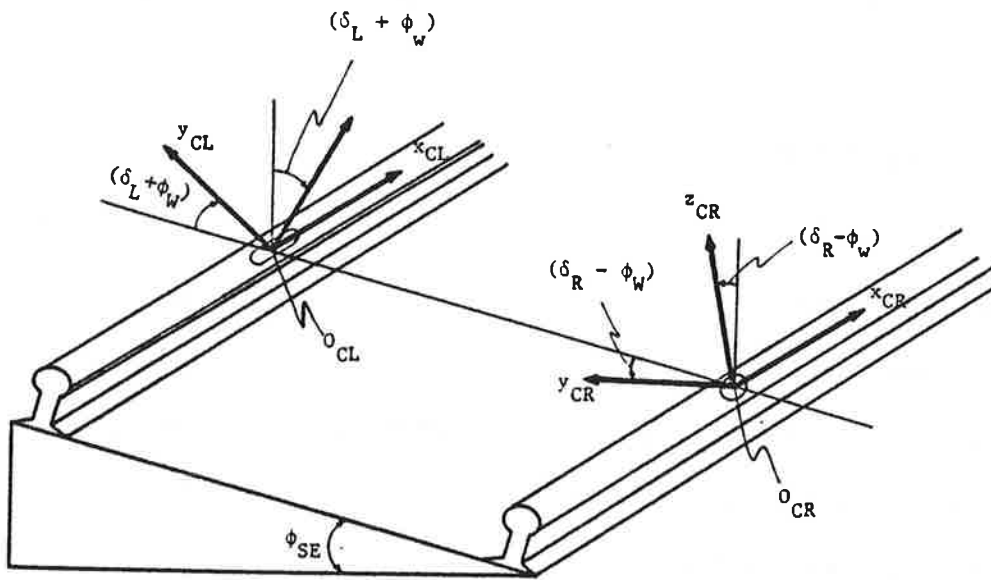
$$\begin{aligned}\bar{F}_{CL} &= F_{CPXL} \hat{i}_{CL} + F_{CPYL} \hat{j}_{CL} \\ \bar{F}_{CR} &= F_{CPXR} \hat{i}_{CR} + F_{CPYR} \hat{j}_{CR} \\ \bar{M}_{CL} &= M_{CPZL} \hat{k}_{CL} \\ \bar{M}_{CR} &= M_{CPZR} \hat{k}_{CR}\end{aligned}\tag{A-19}$$

where F_{CPXL}, F_{CPXR} = left, right creep force in longitudinal contact patch direction

F_{CPYL}, F_{CPYR} = left, right creep force in lateral contact patch direction

M_{CPZL}, M_{CPZR} = left, right creep moment normal to contact patch

and where $\hat{i}_{CL}, \hat{j}_{CL}, \hat{k}_{CL}$ and $\hat{i}_{CR}, \hat{j}_{CR}, \hat{k}_{CR}$ are unit vectors along the left and right contact patch coordinate systems, respectively.



$$\begin{Bmatrix} \hat{i}_{CL} \\ \hat{j}_{CL} \\ \hat{k}_{CL} \end{Bmatrix} \begin{bmatrix} 1 & 0 & 0 \\ 0 & c(\delta_L + \phi_w) & s(\delta_L + \phi_w) \\ 0 & -s(\delta_L + \phi_w) & c(\delta_L + \phi_w) \end{bmatrix} \begin{Bmatrix} \hat{i}_J \\ \hat{j}_T \\ \hat{k}_T \end{Bmatrix} ; \begin{Bmatrix} \hat{i}_{CR} \\ \hat{j}_{CR} \\ \hat{k}_{CR} \end{Bmatrix} = \begin{bmatrix} 1 & 0 & 0 \\ 0 & c(\delta_R - \phi_w) & s(\delta_R - \phi_w) \\ 0 & s(\delta_R - \phi_w) & c(\delta_R - \phi_w) \end{bmatrix} \begin{Bmatrix} \hat{i}_T \\ \hat{j}_T \\ \hat{k}_T \end{Bmatrix}$$

Figure A.4 Contact Patch Coordinate Systems

Performing the coordinate transformations gives the creep forces and moments resolved in the track system as follows:

Left Contact Patch:

$$\begin{aligned}
 F_{CXL} &= F_{CPXL} \\
 F_{CYL} &= F_{CPYL} \cos(\delta_L + \phi_W) \\
 F_{CZL} &= F_{CPYL} \sin(\delta_L + \phi_W) \\
 M_{CXL} &= 0 \\
 M_{CYL} &= -M_{CPZL} \sin(\delta_L + \phi_W) \\
 M_{CZL} &= M_{CPZL} \cos(\delta_L + \phi_W)
 \end{aligned}
 \tag{A-20}$$

Right Contact Patch:

$$\begin{aligned}
 F_{CXR} &= F_{CPXR} \\
 F_{CYR} &= F_{CPYR} \cos(\delta_R - \phi_W) \\
 F_{CZR} &= -F_{CPYR} \sin(\delta_R - \phi_W) \\
 M_{CXR} &= 0 \\
 M_{CYR} &= M_{CPZR} \sin(\delta_R - \phi_W) \\
 M_{CZR} &= M_{CPZR} \cos(\delta_R - \phi_W)
 \end{aligned}
 \tag{A-21}$$

A.5.2.1 Heuristic Creep Model

A heuristic nonlinear creep force model is adopted in this analysis. The creep forces and moments are initially using Kalker's linear theory [16]. At each wheel/rail interface, the longitudinal and

lateral contact patch components of creep force are:

$$\begin{aligned} F'_{CPX} &= -f_{33}\xi_x \\ F'_{CPY} &= -f_{11}\xi_y - f_{12}\xi_{sp} \end{aligned} \tag{A-22}$$

and the spin creep moment acting normal to the contact patch is:

$$M'_{CPZ} = f_{12}\xi_y - f_{22}\xi_{sp} \tag{A-23}$$

where f_{11} , f_{12} , f_{22} , and f_{33} are the lateral, lateral/spin, spin, and longitudinal creep coefficients, respectively, and ξ_x , ξ_y , and ξ_{sp} are the longitudinal, lateral, and spin contact patch creepages, respectively. The creepages are the relative wheel/rail velocities at the contact patch normalized by the nominal forward velocity. They are derived in the following section (A.5.2.2).

The creep coefficients f_{11} , f_{12} , f_{22} , and f_{33} are functions of the wheel/rail geometry, material properties, and normal load. They are computed according to Kalker's linear theory [16], which assumes that the shape and dimensions of the contact area (as well as the distribution of the normal stress) are given by the Hertz solution for two elastic bodies in contact. In this solution, the contact patch is elliptical. The creep coefficients are then typically reduced by 50% to account for discrepancies between field and laboratory test data due to contaminated rail conditions in the field.

The creep coefficients depend on the normal load, F_N , in the following way:

$$f_{11} = \left(\frac{F_N}{F_N^*} \right)^{2/3} f_{11}^*$$

$$f_{12} = \left(\frac{F_N}{F_N^*} \right) f_{12}^*$$

$$f_{22} = \left(\frac{F_N}{F_N^*} \right)^{4/3} f_{22}^*$$

$$f_{33} = \left(\frac{F_N}{F_N^*} \right) f_{33}^*$$

(A-24)

In equation (A-24), f_{ij}^* are nominal creep coefficients computed for the nominal normal load F_N^* ; f_{ij} are creep coefficients for normal load F_N .

The magnitude of the resultant creep force cannot exceed the amount of available adhesion, μF_N , at the wheel/rail contact interface. Accordingly, the resultant creep force is saturated using a modified Vermeulen-Johnson model [8] which includes the effect of spin creepage. A saturation coefficient, ϵ , is calculated by:

$$\epsilon = \begin{cases} \frac{1}{\beta} \left[\beta - \frac{1}{3}\beta^2 + \frac{1}{27}\beta^3 \right] \dots \text{For } \beta < 3 \\ \frac{1}{\beta} \dots \dots \dots \text{For } \beta \geq 3 \end{cases} \quad \text{(A-25)}$$

where β is the normalized unlimited resultant creep force:

$$\beta = \frac{1}{\mu F_N} \sqrt{(F'_{CPX})^2 + (F'_{CPY})^2} . \quad (A-26)$$

The saturated contact patch creep forces and moment are then:

$$\left. \begin{aligned} F_{CPX} &= \epsilon F'_{CPX} \\ F_{CPY} &= \epsilon F'_{CPY} \\ M_{CPZ} &= \epsilon M'_{CPZ} . \end{aligned} \right\} \quad (A-27)$$

These equations predict a resultant creep force which agrees with linear Kalker Theory for small creepages and which saturates to the adhesion limit for larger creepages, as shown in Figure A.5.

A.5.2.2 Derivation of Creepages for Dynamic Curving

The creepages are the relative velocities of the wheel and rail at the contact patch normalized with respect to the nominal forward velocity. The longitudinal and lateral components of creepage at the left contact patch, ξ_{XL} and ξ_{YL} , respectively, are:

$$\left. \begin{aligned} \xi_{XL} &= \frac{1}{V} (\bar{v}_{rel}^{0_{CL}} \cdot \hat{i}_{CL}) \\ \xi_{YL} &= \frac{1}{V} (\bar{v}_{rel}^{0_{CL}} \cdot \hat{j}_{CL}) \end{aligned} \right\} \quad (A-28)$$

where $\bar{v}_{rel}^{0_{CL}}$ is the relative wheel/rail velocity at the left contact patch*, i.e., the velocity of 0_{CL} on the wheel with respect to the rail.

* 0_{CL} is the origin of the left contact patch coordinate system.

Resultant
Creep Force

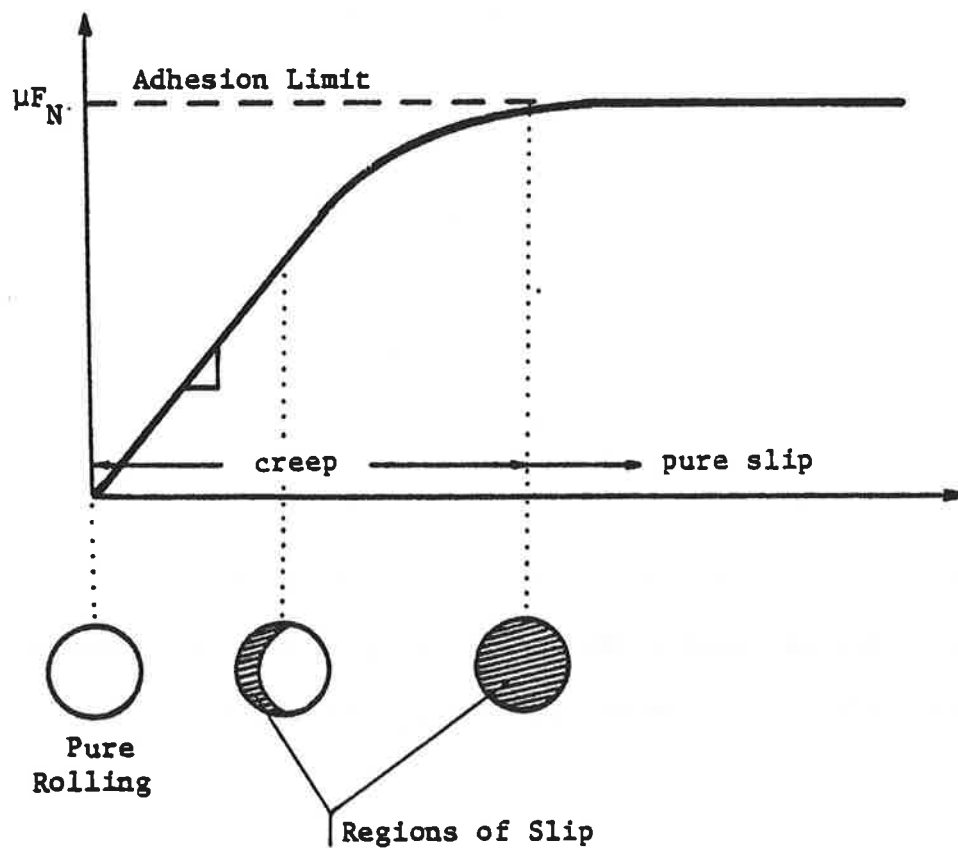


Figure A.5 Contact Patch Creep Force vs. Creepage Relation

For small wheelset roll and yaw angles,

$$\begin{aligned}
 \bar{V}_{rel}^0{}_{CL} &= [\dot{x}_W + V(1 + \frac{a}{R}) - r_L \dot{\theta}_W - a\dot{\psi}_W] \hat{i}_T \\
 &+ [\dot{y}_W + r_L(\dot{\phi}_W - \dot{\theta}_W \psi_W) - \dot{y}_{rail_L}] \hat{j}_T \\
 &+ [\dot{z}_W + a\dot{\phi}_W - \Delta_{XL} \dot{\theta}_W] \hat{k}_T .
 \end{aligned} \tag{A-29}$$

In equation (A-29), \dot{y}_{rail_L} is the left rail lateral velocity. Also, Δ_{XL} is the longitudinal displacement of the contact patch from under the wheelset centerline due to yaw.* For a positive wheelset yaw angle, the left contact patch displaces forward a distance Δ_{XL} and the right contact patch displaces backward a distance Δ_{XR} , as shown in Figure A.6. Transforming equation (A-29) to contact patch coordinates and assuming no relative velocity normal to the contact patch implies the following constraint relation obtained by setting the coefficient of \hat{k}_{CL} to zero.

$$\dot{z}_W + a\dot{\phi}_W - \Delta_{XL} \dot{\theta}_W = [\dot{y}_W + r_L(\dot{\phi}_W - \dot{\theta}_W \psi_W) - \dot{y}_{rail_L}] \tan(\delta_L + \phi_W) \tag{A-30}$$

Using this constraint in equation (A-29) and evaluating equation (A-28) results in the following expressions for the longitudinal and lateral creepages at the left contact patch, ξ_{XL} and ξ_{YL} , respectively:

$$\left. \begin{aligned}
 \xi_{XL} &= \frac{1}{V} [\dot{x}_W + V(1 + \frac{a}{R}) - r_L \dot{\theta}_W - a\dot{\psi}_W] \\
 \xi_{YL} &= \frac{1}{V} [\dot{y}_W + r_L(\dot{\phi}_W - \dot{\theta}_W \psi_W) - \dot{y}_{rail_L}] / \cos(\delta_L + \phi_W)
 \end{aligned} \right\} \tag{A-31}$$

*In [28] the longitudinal shift of the contact patch, Δ_{XL} , was derived for steady-state conditions as: $\Delta_{XL} = r_L \psi_W \tan(\delta_L + \phi_W)$.

PLAN
VIEW:

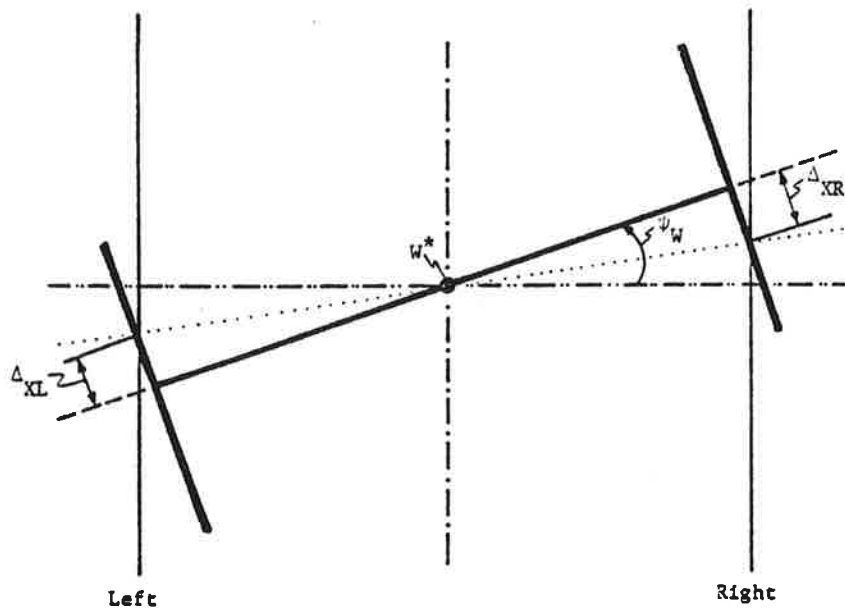


Figure A.6 Longitudinal Displacement of Contact Points
Due to Wheelset Yaw

The spin creepage at the left contact patch, ξ_{SPL} , is:

$$\xi_{SPL} = \frac{1}{V} (\bar{\omega}_{rel} \cdot \hat{k}_{CL}) \quad (A-32)$$

where $\bar{\omega}_{rel}$ is the relative wheel/rail angular velocity given by:

$$\bar{\omega}_{rel} = \dot{\phi}_W \hat{i}_2 + \dot{\theta}_W \hat{j}_2 + (\dot{\psi}_W - \frac{V}{R}) \hat{k}_2 \quad (A-33)$$

The spin creepage is obtained by transforming equation (A-33) to left contact patch coordinates, evaluating equation (A-32), and assuming small wheelset angles.

$$\xi_{SPL} = \frac{1}{V} [-\dot{\theta}_W \sin(\delta_L + \phi_W) + (\dot{\psi}_W - \frac{V}{R} + \phi_W \dot{\theta}_W) \cos(\delta_L + \phi_W)] \quad (A-34)$$

A similar development results in expressions for the creepages at the right contact patch:

$$\left. \begin{aligned} \xi_{XR} &= \frac{1}{V} [\dot{x}_W + V(1 - \frac{a}{R}) - r_R \dot{\theta}_W + a \dot{\psi}_W] \\ \xi_{YR} &= \frac{1}{V} [\dot{y}_W + r_R (\dot{\phi}_W - \dot{\theta}_W \psi_W) - \dot{y}_{rail_R}] / \cos(\delta_R - \phi_W) \\ \xi_{SPR} &= \frac{1}{V} [\dot{\theta}_W \sin(\delta_R - \phi_W) + (\dot{\psi}_W - \frac{V}{R} - \phi_W \dot{\theta}_W) \cos(\delta_R - \phi_W)] \end{aligned} \right\} (A-35)$$

A.5.2.3 Definition of Contact Patch Work

The work expended at the wheel/rail contact patches has been proposed as a curving performance index [13]. The contact patch work is related to wheel and track wear.

Contact patch work is defined as the dot product of the resultant creep force and creepage vectors, as follows:

$$W = F_{CPX}\xi_X + F_{CPY}\xi_Y + M_{CP}\xi_{SP} \quad (A-36)$$

The work index, W, represents the work expended at the contact patch per unit distance along the track. As such, W has units of work per distance or force.

If creepage occurs, work is expended at the contact patch. This is verified by substituting equations (A-22), (A-23), and (A-27) into equation (A-36) yielding:

$$W = - [f_{33}\xi_X^2 + f_{11}\xi_Y^2 + f_{22}\xi_{SP}^2] \quad (A-37)$$

Since the creep coefficients, f_{11} , f_{22} , and f_{33} , and the saturation coefficient, ϵ , are positive numbers, the work index is negative. Thus, work is always expended at the contact patch.

The work, W, is related to the power dissipated at the contact patch as follows:

$$P = VW \quad (A-38)$$

where V is the vehicle speed (assumed constant). Equation (A-38) represents the power dissipated by friction.

A.6 Wheelset Equations of Motion

The wheelset equations of motion are derived by direct application of Newtonian mechanics prescribed by the principles of linear and angular momentum. The principle of linear momentum states that the net

external force acting on the wheelset is equal to the product of the mass of the wheelset, m_W , and the inertial acceleration of the center of mass, \ddot{a} . Thus,

$$\bar{F} = m_W \ddot{a} \quad (\text{A-39})$$

where \bar{F} represents the sum of all external forces acting on the wheelset, including creep and normal forces. The principle of angular momentum states that the net external moment acting about the center of mass of the wheelset is equal to the time rate of change of angular momentum about the center of mass.

$$\bar{M} = \dot{H} \quad (\text{A-40})$$

where \bar{M} is the sum of all external moments acting about the center of mass of the wheelset. Equations (A-39) and (A-40) represent six scalar differential equations of motion for the wheelset.

A simple model of the track is adopted in which each rail is assumed to have lateral freedom only. In this model, overturning motion of the rails is neglected. Figure A.7 shows the mass-spring-viscous damper arrangement used to model each rail. The equation of motion for each rail is:

$$-F_y = m_r \ddot{y}_{\text{rail}} + c_r \dot{y}_{\text{rail}} + k_r y_{\text{rail}} \quad (\text{A-41})$$

where F_y is the net lateral wheel force composed of creep and normal forces; m_r is the effective lateral rail mass, c_r is the effective lateral rail damping, k_r is the effective lateral rail stiffness, and y_{rail} is the lateral rail displacement. Equation (A-38) represents

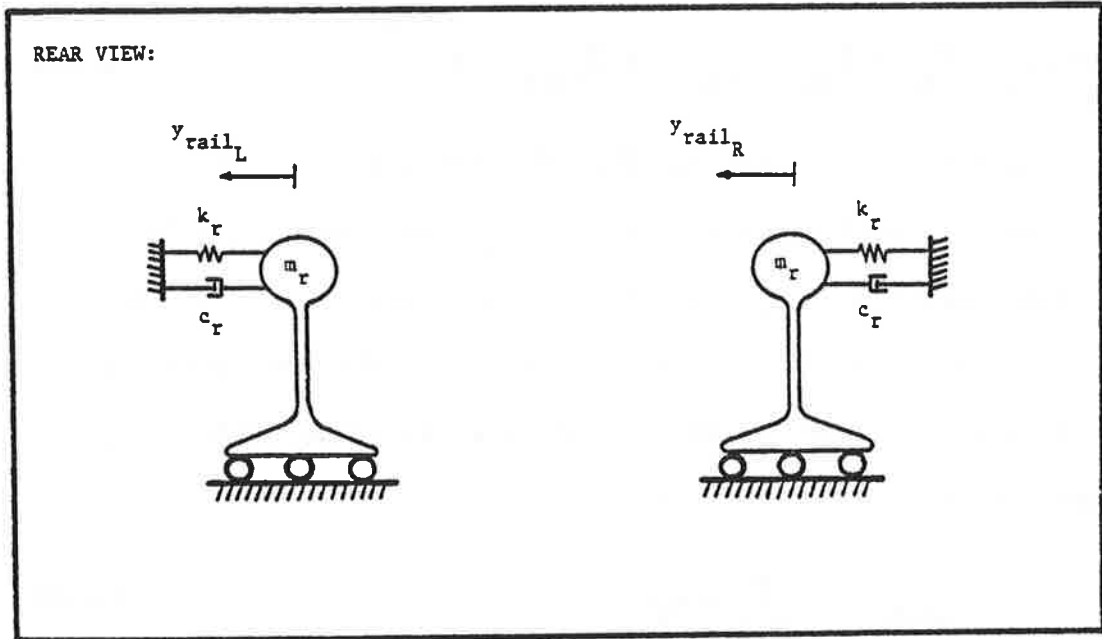


Figure A.7 Lateral Track Model

the scalar differential equations of motion for the left and right rails.

A.6.1 Single-Point Contact

This section develops the dynamic curving equations of motion of a wheelset in single-point contact at the left and right wheels. A free-body diagram is shown in Figure A.8. From equation (A-39), the vector force equation of motion is:

$$\bar{F}_{CL} + \bar{F}_{CR} + \bar{F}_{NL} + \bar{F}_{NR} + \bar{F}_{susp_W} + \bar{F}_{axle} = m_W \bar{a} \quad (A-42)$$

where \bar{F}_{CL} , \bar{F}_{CR} are creep forces and \bar{F}_{NL} , \bar{F}_{NR} are normal forces at the left, right contact points, respectively, \bar{F}_{susp} are suspension forces, \bar{F}_{axle} are axle forces, $m_W = W_w/g$ is the wheelset mass, and \bar{a} is the inertial acceleration of the center of mass of the wheelset given by equation (A-10). The axle forces consist of longitudinal thrust, F_t , and wheelset weight, W_w , as follows:

$$\bar{F}_{axle} = F_t \hat{i}_T - W_w \hat{k}_H \quad (A-43)$$

Assuming small angles, equation (A-42) is equivalent to the following three scalar equations of motion resolved along track coordinates.

Wheelset Longitudinal Equation

$$\frac{W_w}{g} (\ddot{x}_W + \dot{v}) = F_{CXL} + F_{CXR} + F_{susp_{x_W}} + F_t \quad (A-44)$$

Wheelset Lateral Equation

$$\left. \begin{aligned} \frac{W_w}{g} (\ddot{y}_W - r_o \ddot{\phi}_{SE}) &= F_{CYL} + F_{CYR} + F_{NYL} + F_{NYR} + F_{susp_{y_W}} \\ &+ W_w (\phi_d - \phi_W) \end{aligned} \right\} \quad (A-45)$$

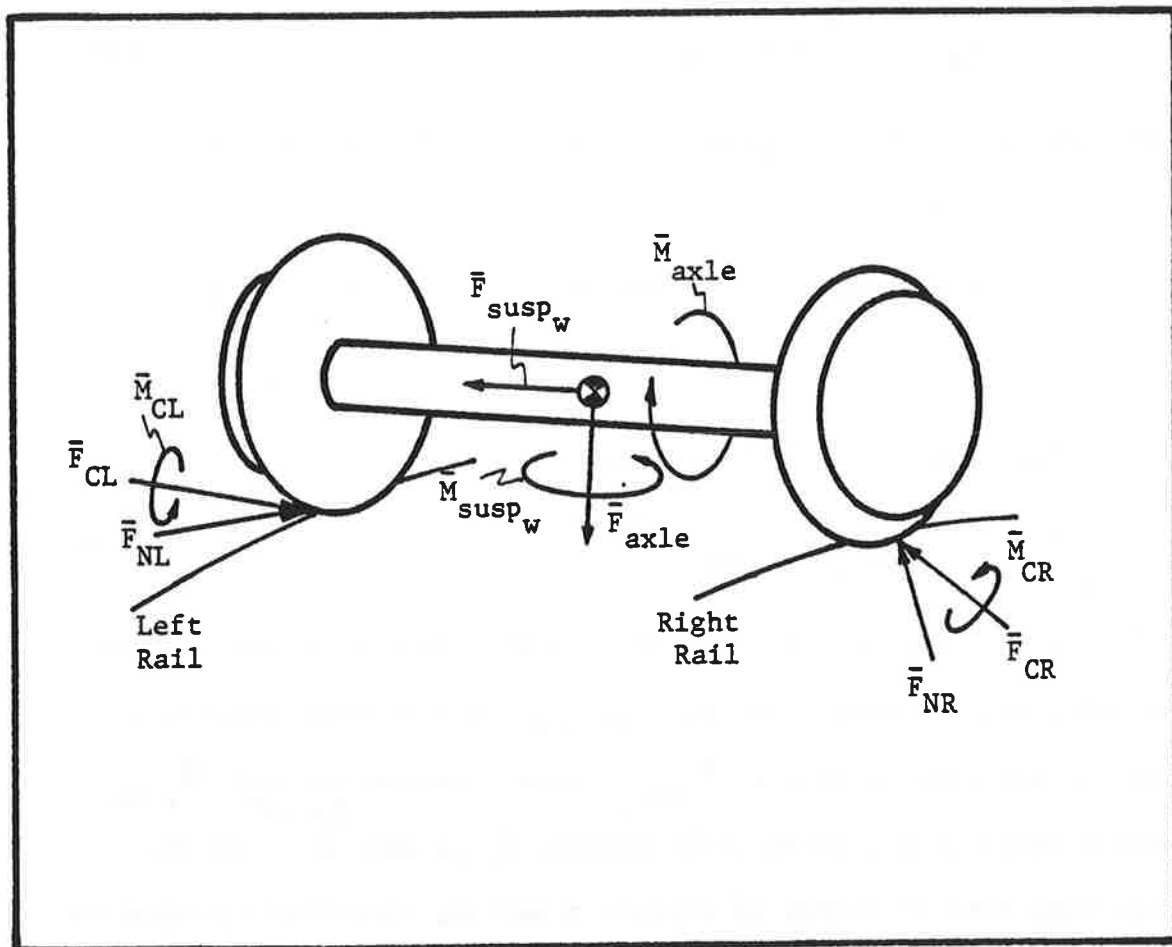


Figure A.8 Free-Body Diagram of Wheelset in Single-Point Contact

Wheelset Vertical Equation

$$\frac{W_w}{g} (\ddot{z}_w + a\ddot{\phi}_{SE}) = F_{CZL} + F_{CZR} + F_{NZL} + F_{NZR} + F_{susp_{z_w}} - W_w \quad (A-46)$$

In equation (A-45), ϕ_d represents the cant deficient, given by

$$\phi_d = \frac{v^2}{Rg} - \phi_{SE} \quad (A-47)$$

The cant deficiency is an angular measure of the lateral unbalance between centrifugal and gravitational forces.

The vector moment equation of motion, equation (A-40), is defined by:

$$\begin{aligned} \bar{R}_L \times (\bar{F}_{CL} + \bar{F}_{NL}) + \bar{R}_R \times (\bar{F}_{CR} + \bar{F}_{NR}) + \bar{M}_{CL} \\ + \bar{M}_{CR} + \bar{M}_{susp_w} + \bar{M}_{axle} = \frac{I \cdot W/W^*}{H} \end{aligned} \quad (A-48)$$

where \bar{R}_L , \bar{R}_R are displacement vectors from the wheelset center of mass to the left, right contact points, \bar{M}_{CL} , \bar{M}_{CR} are the creep moments at the left, right contact points, \bar{M}_{susp_w} are suspension moments, \bar{M}_{axle} are axle moments (e.g., drive/brake torque, $T_d \hat{j}_2$) and $\frac{I \cdot W/W^*}{H}$ is the inertial time rate of change of angular momentum, specified by equation (A-17). The displacement vectors, \bar{R}_L and \bar{R}_R are given by

$$\left. \begin{aligned} \bar{R}_L &= -\{[a-r_L \tan(\delta_L + \phi_w)] \psi_w \hat{i}_T + a \hat{j}_T - r_L \hat{k}_T\} \\ \bar{R}_R &= \{[a-r_R \tan(\delta_R - \phi_w)] \psi_w \hat{i}_T - a \hat{j}_T - r_R \hat{k}_T\} \end{aligned} \right\} \quad (A-49)$$

where small yaw and roll angles have been assumed and the longitudinal

displacements of the contact points with wheelset yaw have been taken into account. Substituting expressions (A-49) into equation (A-48), expanding, and neglecting smaller order terms gives the following three scalar equations resolved along "2" system coordinates.

Wheelset Roll Equation

$$\begin{aligned}
 I_{WX}(\ddot{\phi}_W + \ddot{\phi}_{SE}) &= I_{WY}\dot{\theta}_W(\dot{\psi}_W - \frac{V}{R}) + a(F_{CZL} + F_{NZL}) \\
 &+ r_L(F_{CYL} + F_{NYL} - \psi_W F_{CXL}) - a(F_{CZR} + F_{NZR}) \\
 &+ r_R(F_{CYR} + F_{NYR} - \psi_W F_{CXR}) \\
 &+ M_{susp_x W} + \psi_W(M_{CYL} + M_{CYR})
 \end{aligned} \tag{A-50}$$

Wheelset Spin Equation

$$\begin{aligned}
 I_{WY}\ddot{\theta}_W &= -r_L[F_{CXL} + \psi_W\{F_{CYL} + F_{CZL}\tan(\delta_L + \phi_W)\}] \\
 &- r_R[F_{CXR} + \psi_W\{F_{CYR} - F_{CZR}\tan(\delta_R - \phi_W)\}] \\
 &+ M_{CYL} + M_{CYR} + M_{susp_y W} + \phi_W(M_{CZL} + M_{CZR}) \\
 &+ T_d
 \end{aligned} \tag{A-51}$$

Wheelset Yaw Equation

$$\begin{aligned}
 I_{WX}(\ddot{\psi}_W - \frac{\dot{V}}{R} - V(\frac{\dot{I}}{R})) &= -I_{WY}\dot{\theta}_W(\dot{\phi}_W + \dot{\phi}_{SE}) \\
 &- a(F_{CXL} - F_{CXR}) - \psi_W\{(a - r_L\tan(\delta_L + \phi_W))(F_{CYL} + F_{NYL})
 \end{aligned}$$

$$\begin{aligned}
& -(a-r_R \tan(\delta_R - \phi_W))(F_{CYR} + F_{NYR}) \} + M_{CZL} + M_{CZR} \\
& + M_{susp} - \phi_W(M_{CYL} + M_{CYR})
\end{aligned} \tag{A-52}$$

In these equations, the longitudinal creep moments, M_{CXL} and M_{CXR} , have been set to zero as was shown in equations (A-20) and (A-21). Also, relations (A-18) have been used to simplify the wheelset spin equation, equation (A-51). As expected, normal forces do not (explicitly) appear in this equation.

The dynamics of the rails are approximated using the lateral rail model shown in Figure A.7. The equations of motion of the left and right rails are determined by equation (A-41).

Left Rail Lateral Equation

$$m_r \ddot{y}_{rail_L} + c_r \dot{y}_{rail_L} + k_r y_{rail_L} = -F_{NYL} - F_{CYL} \tag{A-53}$$

Right Rail Lateral Equation

$$m_r \ddot{y}_{rail_R} + c_r \dot{y}_{rail_R} + k_r y_{rail_R} = -F_{NYR} - F_{CYR} \tag{A-54}$$

Equations (A-44) - (A-47) and (A-50) - (A-52) represent six wheelset equations of motion; equations (A-53) and (A-54) represent two rail equations of motion. This system of 8 equations describes the dynamic behavior of a wheelset in single-point contact as it negotiates laterally flexible, curved track. Mathematically, these equations are coupled, nonlinear, scalar, differential equations. They can be solved for the time histories of the following 8 indepen-

dent variables: $x_W, y_W, \dot{\theta}_W, \psi_W, F_{NzL}, F_{NzR}, y_{rail_L}, y_{rail_R}$. This assumes that F_t, T_d , wheelset mass and inertia properties, and suspension forces and moments are known input data. Also, V, R , and ϕ_{SE} are assumed known functions of distance along the track. For continuous wheel/rail contact, the following geometry are known functions of y_W, y_{rail_L} , and y_{rail_R} for a given wheel/rail profile: $z_W, \phi_W, r_L, r_R, \delta_L, \delta_R$. Thus, the wheelset vertical displacement, z_W , and the wheelset roll angle, ϕ_W , can be written in terms of the state variables y_W, y_{rail_L} , and y_{rail_R} . Similarly, the wheelset vertical velocity and roll angle rate are functions of the wheelset and rail lateral velocities.

It is convenient to calculate the normal forces from the wheelset vertical and roll equations. Simultaneous solution of equations (A-46) and (A-50) gives the normal forces at the left and right wheel/rail contact patches as follows:

$$\left. \begin{aligned} F_{NL} &= \frac{v_L}{\Delta_1} \\ F_{NR} &= \frac{v_R}{\Delta_1} \end{aligned} \right\} \quad (A-55)$$

where

$$\begin{aligned} v_L &= F_Z^* \{ a \cos(\delta_R - \phi_W) - r_R \sin(\delta_R - \phi_W) \} + M_\phi^* \cos(\delta_R - \phi_W) \\ v_R &= F_Z^* \{ a \cos(\delta_L + \phi_W) - r_L \sin(\delta_L + \phi_W) \} - M_\phi^* \cos(\delta_L + \phi_W) \end{aligned}$$

and

$$\Delta_L = 2a \cos(\delta_L + \phi_W) \cos(\delta_R - \phi_W) - r_R \cos(\delta_L + \phi_W) \sin(\delta_R - \phi_W) \\ - r_L \sin(\delta_L + \phi_W) \cos(\delta_R - \phi_W)$$

In the expressions for v_L and v_R , F_Z^* is an equivalent vertical force and M_ϕ^* is an equivalent roll moment given by:

$$F_Z^* = -F_{CZL} - F_{CZR} - F_{susp} z_W + \frac{W}{g} (\ddot{z}_W + a \ddot{\phi}_{SE}) + W_w$$

and

$$M_\phi^* = a(F_{CZR} - F_{CZL}) - r_L(F_{CYL} - \psi_W F_{CXL}) \\ - r_R(F_{CYR} - \psi_W F_{CXR}) - \psi_W(M_{CYL} + M_{CYR}) - M_{susp} x_W \\ + I_{WX}(\ddot{\phi}_W + \ddot{\phi}_{SE}) - I_{WY} \dot{\theta}_W (\dot{\psi}_W - \frac{V}{R})$$

The normal forces, F_{NL} and F_{NR} , are resolved into lateral and vertical components according to equations (A-18).

A.6.2 Two-Point Contact

The previous development is appropriate for a wheelset which maintains single-point wheel/rail contact at both wheels for all lateral displacements. This continuous single-point contact approximation is appropriate for some wheel/rail profiles, particularly many European profiles. As the wheelset displaces laterally, the point of contact at the outer wheel shifts smoothly from the tread to the flange, while the inner wheel maintains tread contact. For other profiles with steep flanges, such as many U.S. wheel/rail profiles, two points of contact can develop at the flanging wheel. As before, single-point tread contact occurs at both the inner and outer wheels for a net wheelset ex-

cursion less than the flange clearance. Two-point contact occurs at the flanging wheel and single-point contact occurs at the inner wheel for a wheelset displacement (relative to the flanging wheel rail) equal to the flange clearance. Single-point flange contact occurs at the flanging wheel for net excursions greater than the flange clearance. This represents a dangerous situation conducive to derailment.

For a wheelset negotiating a right-handed curved track, the left wheel represents the outer or flanging wheel. Figure A.9 shows the contact condition at the left wheel as the wheelset displaces laterally. Single-point tread contact (Figure A.9a) and single-point flange contact (Figure A.9c) occur for net excursions less than and greater than the flange clearance, respectively. Two-point contact occurs for a wheelset excursion (with respect to the left rail) equal to the flange clearance. Two-point contact is depicted in Figure A.9b where the rail head is shown to contact simultaneously both the tread and flange of the left wheel.

For a wheelset in two-point contact^{*}, the displacement relative to the left rail is fixed at the flange clearance, y_{fc} , or mathematically,

$$y_W - y_{\text{rail}_L} = y_{fc} \quad (\text{A-56})$$

Equation (A-56) represents a constraint relation which can be used to specify the contact geometry (rolling radius, contact angle) of the

*The terminology assumes that the two points of contact occur at the flanging wheel. "A wheelset in two-point contact" actually has three points of wheel/rail contact, two at the flanging or outer wheel and one at the inner wheel.

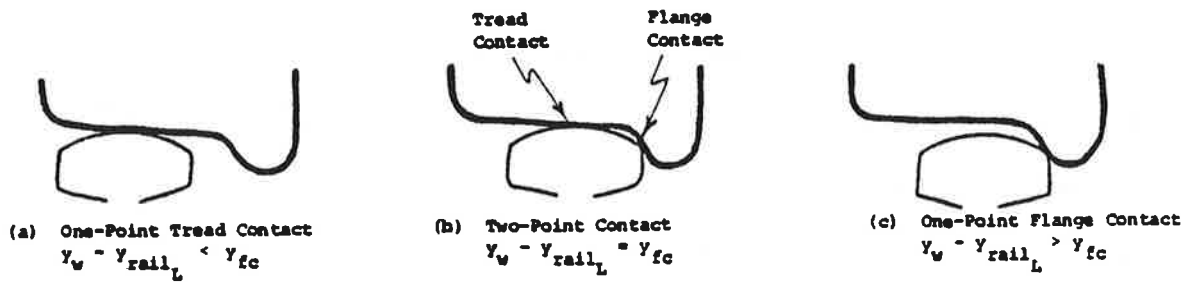


Figure A.9 Left Wheel/Rail Contact

tread and flange contact points of the left wheel. Differentiation of equation (A-56) gives the relation between the wheelset and left rail lateral velocities and accelerations:

$$\left. \begin{aligned} \dot{y}_W &= \dot{y}_{\text{rail}_L} \\ \ddot{y}_W &= \ddot{y}_{\text{rail}_L} \end{aligned} \right\} \quad (\text{A-57})$$

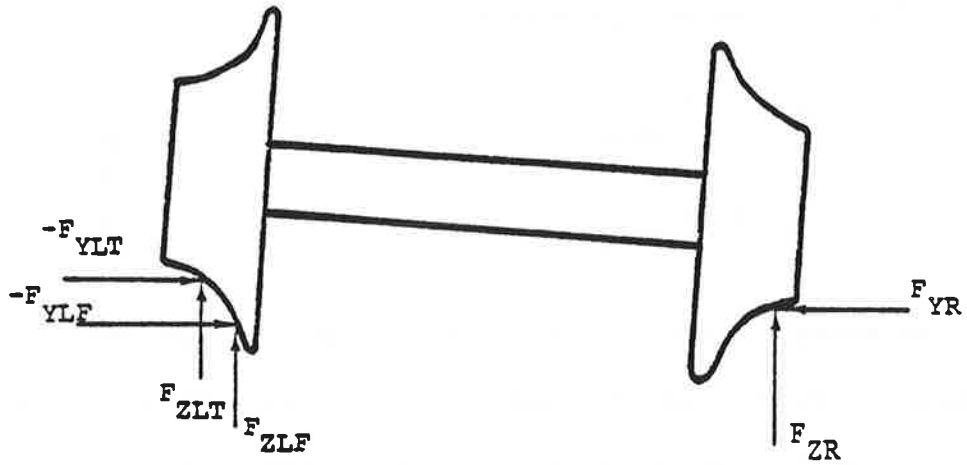
Figure A.10 shows the wheel/rail forces acting on a wheelset in two-point contact. The equations of motion describing a wheelset in two-point contact at the left wheel are similar to the equations derived for a wheelset in single-point contact, with new terms to account for the additional contact patch. The expressions derived for single-point contact at the left, such as the normal force, the creep force and moment, and the creepages at the left, are correct for two-point contact. Now, however, these expressions apply to a left tread and left flange contact patch when the appropriate contact geometry is used. The notation is subscripts LT and LF for left tread and left flange contact patch, respectively, in place of subscript L (for left contact patch) of the single-point contact derivation.

Assuming small yaw and roll angles, the equations of motion of a wheelset in two-point contact at the left wheel are given below.

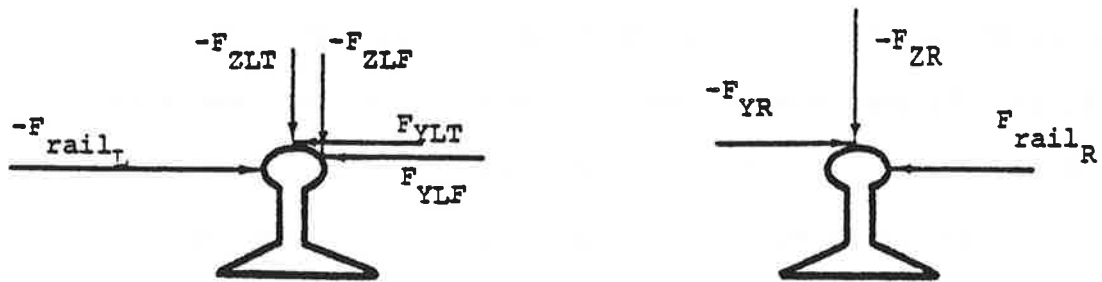
Wheelset Longitudinal Equation

$$\frac{W_W}{g} (\ddot{x}_W + \dot{V}) = F_{\text{CXLT}} + F_{\text{CXLF}} + F_{\text{CXR}} + F_{\text{susp}_{x_W}} + F_t \quad (\text{A-58})$$

REAR VIEW



Wheel Forces



Rail Forces

Figure A.10 Wheel and Rail Forces for Two-Point Contact

Wheelset Lateral Equation

$$\begin{aligned} \frac{W_w}{g} (\ddot{y}_w - r_o \ddot{\phi}_{SE}) &= F_{CYLT} + F_{CYLF} + F_{CYR} + F_{NYLT} \\ &+ F_{NYLF} + F_{NYR} + F_{susp_{y_w}} + W_w(\phi_d - \phi_w) \end{aligned} \quad (A-59)$$

Wheelset Vertical Equation

$$\begin{aligned} \frac{W_w}{g} (\ddot{z}_w + a \ddot{\phi}_{SE}) &= F_{CZLT} + F_{CZLF} + F_{CZR} + F_{NZLT} \\ &+ F_{NZLF} + F_{NZR} + F_{susp_{z_w}} - W_w \end{aligned} \quad (A-60)$$

Wheelset Roll Equation

$$\begin{aligned} I_{WX} (\ddot{\phi}_w + \ddot{\phi}_{SE}) &= I_{WY} \dot{\theta}_w (\dot{\psi}_w - \frac{V}{R}) + a(F_{CZLT} + F_{CZLF} + F_{NZLT} + F_{NZLF}) \\ &+ r_{LT}(F_{CYLT} + F_{NYLT} - \psi_w F_{CXLT}) + r_{LF}(F_{CYLF} + F_{NYLF} - \psi_w F_{CXLF}) \\ &- a(F_{CZR} + F_{NZR}) + r_R(F_{CYR} + F_{NYR} - \psi_w F_{CXR}) \\ &+ M_{susp_{x_w}} + \psi_w(M_{CYLT} + M_{CYLF} + M_{CYR}) \end{aligned} \quad (A-61)$$

Wheelset Spin Equation

$$\begin{aligned} I_{WY} \ddot{\theta}_w &= -r_{LT}[F_{CXLT} + \psi_w \{F_{CYLT} + F_{CZLT} \tan(\delta_{LT} + \phi_w)\}] \\ &- r_{LF}[F_{CXLF} + \psi_w \{F_{CYLF} + F_{CZLF} \tan(\delta_{LF} + \phi_w)\}] \\ &- r_R[F_{CXR} + \psi_w \{F_{CYR} - F_{CZR} \tan(\delta_R - \phi_w)\}] \\ &+ M_{CYLT} + M_{CYLF} + M_{CYR} + M_{susp_{y_w}} \\ &+ \phi_w(M_{CZLT} + M_{CZLF} + M_{CZR}) + T_d \end{aligned} \quad (A-62)$$

Wheelset Yaw Equation

$$\begin{aligned}
 I_{WX} \left[\ddot{\psi}_X - \frac{\dot{V}}{R} - V \left(\frac{\dot{i}}{R} \right) \right] &= -I_{WY} \dot{\theta}_W (\dot{\phi}_W + \dot{\phi}_{SE}) \\
 &- a(F_{CXLT} + F_{CXLF} - F_{CXR}) - \psi_W \{ (a-r_{LT} \tan(\delta_{LT} + \phi_W)) (F_{CYLT} + F_{NYLT}) \\
 &+ (a-r_{LF} \tan(\delta_{LF} + \phi_W)) (F_{CYLF} + F_{NYLF}) - (a-r_R \tan(\delta_R - \phi_W)) (F_{CYR} + F_{NYR}) \} \\
 &+ M_{CZLT} + M_{CZLF} + M_{CZR} + M_{susp} z_W \\
 &+ \phi_W (M_{CYLT} + M_{CYLF} + M_{CYR}) \quad (A-63)
 \end{aligned}$$

Left Rail Lateral Equation

$$m_r \ddot{y}_{rail_L} + c_r \dot{y}_{rail_L} + k_r y_{rail_L} = -F_{NYLT} - F_{NYLF} - F_{CYLT} - F_{CYLF} \quad (A-64)$$

Right Rail Lateral Equation

$$m_r \ddot{y}_{rail_R} + c_r \dot{y}_{rail_R} + k_r y_{rail_R} = -F_{NYR} - F_{CYR} \quad (A-65)$$

Equations (A-58) - (A-65) represent 8 coupled, nonlinear, differential equations of motion. The equations describe the dynamic behavior of a wheelset in two-point contact at the left wheel as it negotiates laterally flexible, right-handed curved track. The equations can be solved for the time histories of the following 8 independent variables: x_W , y_W , $\dot{\theta}_W$, ψ_W , F_{NZLT} , F_{NZLF} , F_{NZR} , y_{rail_R} . The left rail lateral displacement, y_{rail_L} , is a known function of the wheelset lateral excursion, y_W , according to equation (A-56). Similarly, \dot{y}_{rail_L} and \ddot{y}_{rail_L} are given by equations (A-57).

The normal forces are determined by solving simultaneously the wheelset vertical and roll equations, the left rail lateral equation, and the two-point contact constraint relations. By manipulation of equations (A-60), (A-61), and (A-64) with (A-56) and (A-57), the normal forces at the left tread, left flange, and right wheel/rail contact patches, F_{NLT} , F_{NLF} , and F_{NR} , respectively, are:

$$\left. \begin{aligned} F_{NLT} &= \frac{v_{LT}}{\Delta_2} \\ F_{NLF} &= \frac{v_{LF}}{\Delta_2} \\ F_{NR} &= \frac{v_{2R}}{\Delta_2} \end{aligned} \right\} \quad (A-66)$$

where

$$\begin{aligned} v_{LT} &= F_y^{**} \{ 2a \cos(\delta_{LF} + \phi_W) \cos(\delta_R - \phi_W) - r_{LF} \sin(\delta_{LF} + \phi_W) \cos(\delta_R - \phi_W) \\ &\quad - r_R \cos(\delta_{LF} + \phi_W) \sin(\delta_R - \phi_W) \} + F_Z^{**} \{ \sin(\delta_{LF} + \phi_W) [a \cos(\delta_R - \phi_W) \\ &\quad - r_R \sin(\delta_R - \phi_W)] \} + M_\phi^{**} \sin(\delta_{LF} + \phi_W) \cos(\delta_R - \phi_W) \\ v_{LF} &= F_y^{**} \{ -2a \cos(\delta_{LT} + \phi_W) \cos(\delta_R - \phi_W) + r_{LT} \sin(\delta_{LT} + \phi_W) \cos(\delta_R - \phi_W) \\ &\quad + r_R \cos(\delta_{LT} + \phi_W) \sin(\delta_R - \phi_W) \} - F_Z^{**} \{ \sin(\delta_{LT} + \phi_W) [a \cos(\delta_R - \phi_W) \\ &\quad - r_R \sin(\delta_R - \phi_W)] \} - M_\phi^{**} \sin(\delta_{LT} + \phi_W) \cos(\delta_R - \phi_W) \end{aligned}$$

$$\begin{aligned}
v_{2R} = & F_y^{**} \{ r_{LF} \cos(\delta_{LT} + \phi_W) \sin(\delta_{LF} + \phi_W) - r_{LT} \sin(\delta_{LT} + \phi_W) \cos(\delta_{LF} + \phi_W) \} \\
& + F_z^{**} \{ a [\cos(\delta_{LT} + \phi_W) \sin(\delta_{LF} + \phi_W) - \sin(\delta_{LT} + \phi_W) \cos(\delta_{LF} + \phi_W)] \\
& + (r_{LF} - r_{LT}) \sin(\delta_{LT} + \phi_W) \sin(\delta_{LF} + \phi_W) \} - M_\phi^{**} \{ \cos(\delta_{LT} + \phi_W) \sin(\delta_{LF} + \phi_W) \\
& - \sin(\delta_{LT} + \phi_W) \cos(\delta_{LF} + \phi_W) \}
\end{aligned}$$

and

$$\begin{aligned}
\Delta_2 = & [2a \cos(\delta_R - \phi_W) - r_R \sin(\delta_R - \phi_W)] \{ \cos(\delta_{LT} + \phi_W) \sin(\delta_{LF} + \phi_W) \\
& - \sin(\delta_{LT} + \phi_W) \cos(\delta_{LF} + \phi_W) \} + (r_{LF} - r_{LT}) \sin(\delta_{LT} + \phi_W) \sin(\delta_{LF} + \phi_W) \cos(\delta_R - \phi_W)
\end{aligned}$$

In the expressions for δ_{LT} , δ_{LF} , and δ_{2R} , the equivalent lateral force, vertical force, and roll moment, F_y^* , F_z^* , and M_ϕ^* respectively, are:

$$\begin{aligned}
F_y^{**} = & -F_{CYLT} - F_{CYLF} - m_r \ddot{y}_W - c_r \dot{y}_W - k_r (y_W - y_{fc}) \\
F_z^{**} = & -F_{CZLT} - F_{CZLF} - F_{CZR} - F_{susp_{z_W}} + \frac{W_W}{g} (\ddot{z}_W + a \ddot{\phi}_{SE}) + W_W
\end{aligned}$$

and

$$\begin{aligned}
M_\phi^{**} = & -a (F_{CZLT} + F_{CZLF} - F_{CZR}) - r_{LT} (F_{CYLT} - \psi_W F_{CXLT}) \\
& - r_{LF} (F_{CYLF} - \psi_W F_{CXLF}) - r_R (F_{CYR} - \psi_W F_{CXR}) \\
& - \psi_W (M_{CYLT} + M_{CYLF} + M_{CYR}) - M_{susp_{x_W}} + I_{WX} (\ddot{\phi}_W + \ddot{\phi}_{SE}) \\
& - I_{WY} \dot{\theta}_W (\dot{\psi}_W - V/R)
\end{aligned}$$

The normal forces, F_{NLT} , F_{NLF} , and F_{NR} , given by equations (A-66), are resolved into lateral and vertical components by relations similar to equations (A-18) but modified to account for a tread and flange con-

tact patch at the left.

This development assumes that two-point contact occurs at the outer or left wheel. However, two-point contact can occur at the inner or right wheel during violent curve entry and hunting conditions and during negotiation of reverse curves. The derivation of the equations of motion of a wheelset in two-point contact at the right wheel follows directly from the above analysis, and is not presented here.

A.7 Wheelset Numerical Methods

The equations of motion developed in Section A.6 describe the dynamic behavior of a wheelset negotiating flexible, curved track of variable geometry. In this section, a general method for wheelset analysis is presented which accounts for both single-point and two-point wheel/rail contact. In addition, the numerical technique to solve the wheelset equations is discussed.

Due to suspension forces and moments, the wheelset equations of motion are coupled to the vehicle equations of motion. The details of the suspension forces and moments and the vehicle equations are presented in Appendix B.

In a dynamic curving analysis the wheelset lateral dynamics are extremely important since they determine whether or not flanging occurs. The lateral dynamics are virtually decoupled from the longitudinal dynamics. As a result, wheelset longitudinal dynamics are neglected. Thus, by assumption, x_W , \dot{x}_W , and \ddot{x}_W are zero. As an

additional benefit, this assumption eliminates a degree of freedom (for each wheelset), and reduces computer simulation time.

It is also assumed that the effective lateral mass of the rail, m_r , is zero. This is justified since the rail lateral stiffness and viscous damping forces dominate. Further, it is assumed that the influence of lateral rail velocity on lateral creepage is negligible.* British Rail [8] has suggested that this approximation is reasonable since the lateral creep force is generally saturated during flange contact.

A flowchart of a general method for wheelset analysis is shown in Figure A.11. At each time step, the single-point contact wheelset equations are solved and the solution is checked for consistency. The single-point contact solution is consistent if (1) a single-point contact wheel-rail profile is used, or (2) a two-point contact profile is used but the net excursion at the left and right wheels is not equal to the flange clearance. In the latter case, single-point tread contact occurs if the net wheelset excursion is less than the flange clearance; single-point flange contact occurs if the net excursion is greater than the flange clearance. If the solution is inconsistent, the wheelset equations appropriate for two-point contact at the left or right wheel are solved (depending whether the net excursion equals the flange clearance at the left or right wheel). By necessity, the two-point contact solution must be consistent. This implies that

* These assumptions, i.e., neglecting the rail mass and the effect of rail lateral velocity on lateral creepage, simplify the computational aspects of the dynamic curving analysis.

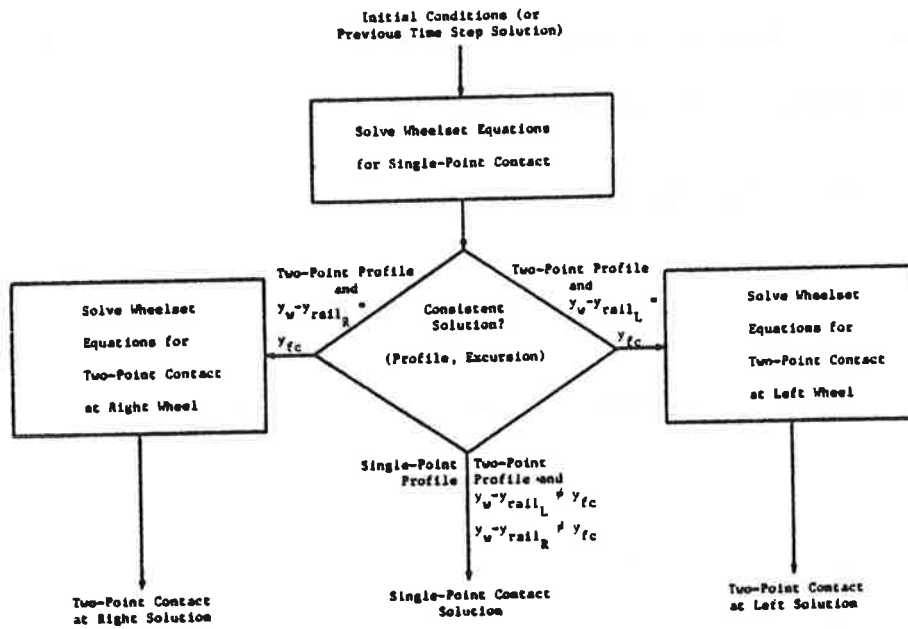


Figure A.11 Wheelset Dynamic Curving Analysis at One Time-Step

- (1) the net wheelset excursion is equal to the flange clearance, and
- (2) two points of contact actually exist (i.e., positive normal forces act at both contact patches of the flanging wheel).

The single-point and two-point contact wheelset equations are solved via a fourth order Runge-Kutta integration algorithm. The method requires that the equations of motion are transformed to a system of first-order differential equations.

A.7.1 Single-Point Contact

For a wheelset in single-point contact, the solution approach is to solve the wheelset lateral, yaw, and spin equations and the left and right rail lateral equations for the following states:

$$\begin{aligned}
 X_1 &= y_W \\
 X_2 &= \psi_W \\
 X_3 &= \dot{\theta}_W \\
 X_4 &= \dot{y}_W \\
 X_5 &= \dot{\psi}_W \\
 X_6 &= y_{\text{rail}_R} \\
 X_7 &= y_{\text{rail}_L}
 \end{aligned}
 \tag{A-67}$$

The seven first order differential equations of motion are:

$$\begin{aligned}
 \dot{X}_1 &= X_4 \\
 \dot{X}_2 &= X_5
 \end{aligned}$$

Wheelset Spin [Equation (A-51)]

$$\dot{X}_3 = f(X_1, X_2, \dots, X_7, \bar{F}_{\text{susp}_W}, \bar{M}_{\text{susp}_W})$$

Wheelset Lateral [Equation (A-45)]

(A-68)

$$\dot{X}_4 = f(X_1, X_2, \dots, X_7, \bar{F}_{\text{susp}_W}, \bar{M}_{\text{susp}_W})$$

Wheelset Yaw [Equation (A-52)]

$$\dot{X}_5 = f(X_1, X_2, \dots, X_7, \bar{F}_{\text{susp}_W}, \bar{M}_{\text{susp}_W})$$

Right Rail Lateral [Equation (A-54)]

$$\dot{X}_6 = f(X_1, X_2, \dots, X_7, \bar{F}_{\text{susp}_W}, \bar{M}_{\text{susp}_W})$$

Left Rail Lateral [Equation (A-53)]

$$\dot{X}_7 = f(X_1, X_2, \dots, \bar{X}_7, \bar{F}_{\text{susp}_W}, \bar{M}_{\text{susp}_W})$$

The normal forces at the left and right contact patches, F_{NL} and F_{NR} , are calculated from the wheelset vertical and roll equations according to equations (A-55). In these equations, the normal forces are given as a function of the creep forces and moments. However, the creep forces and moments depend on the normal forces. Thus, at each time step an iterative scheme is required to solve for the wheel/rail forces and moments, as shown in Figure A.12. In equations (A-55), the normal forces are also a function of the suspension forces and moments. The wheelset suspension force, \bar{F}_{susp_W} , and moment, \bar{M}_{susp_W} , couple equations (A-68) to the vehicle equations of motion and are presented in Appendix B.

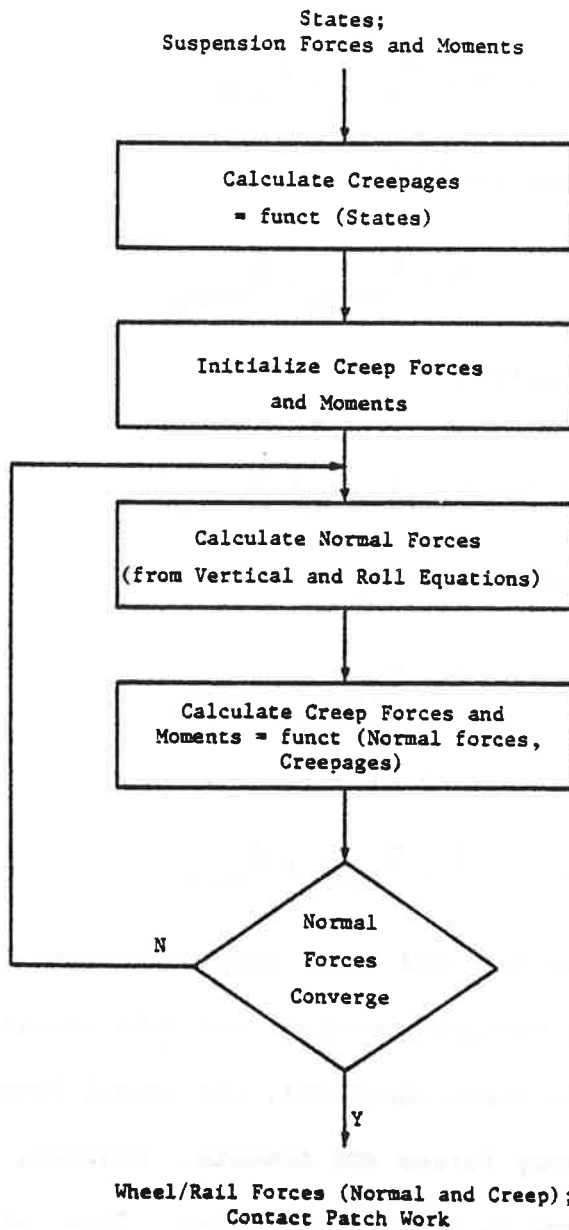


Figure A.12 Wheel/Rail Force Calculation at One Time-Step

A.7.2 Two-Point Contact

For a wheelset in two-point contact at the left wheel, states X_1 and X_7 are dependent due to the contact constraint relation (A-56). The left rail lateral displacement is a known function of the wheelset lateral displacement. In this case, six first order differential equations are written:

$$\dot{X}_1 = X_4$$

$$\dot{X}_2 = X_5$$

Wheelset Spin [Equation (A-62)]

$$\dot{X}_3 = f(X_1, X_2, \dots, X_6, \bar{F}_{susp_W}, \bar{M}_{susp_W})$$

Wheelset Lateral [Equation (A-59)]

$$\dot{X}_4 = f(X_1, X_2, \dots, X_6, \bar{F}_{susp_W}, \bar{M}_{susp_W})$$

Wheelset Yaw [Equation (A-63)]

$$\dot{X}_5 = f(X_1, X_2, \dots, X_6, \bar{F}_{susp_W}, \bar{M}_{susp_W})$$

(A-69)

Right Rail Lateral [Equation (A-65)]

$$\dot{X}_6 = f(X_1, X_2, \dots, X_6, \bar{F}_{susp_W}, \bar{M}_{susp_W})$$

The wheelset vertical and roll equations and the left rail lateral equation are used to calculate the normal force at the left tread, left flange, and right contact patch, F_{NLT} , F_{NLF} , and F_{NR} , respectively, according to equations (A-65). At each time step, an iterative scheme similar to the method shown in Figure A.12 is used. The left rail

lateral displacement, velocity, and acceleration are specified by equations (A-56) and (A-57). Equations (A-69) are coupled to the vehicle equations of motion by the wheelset suspension force and moment, \bar{F}_{susp_W} and \bar{M}_{susp_W} , respectively. These are discussed in Appendix B.

Equations (A-68) are appropriate for a wheelset in single-point contact at the left and right wheels; equations (A-69) are appropriate for a wheelset in two-point contact at the left wheel (and single-point contact at the right wheel). Following a parallel derivation, equations of motion similar to equations (A-69) can be written for a wheelset in two-point contact at the right wheel. In such a case, states X_1 and X_6 are dependent.

Equations (A-68), (A-69), and the equations for a wheelset in two-point contact at the right wheel represent sets of coupled, scalar, first order differential equations which characterize the behavior of a wheelset as it traverses flexible, curved track. These governing equations represent a system of 7 states: 5 states for the wheelset and 2 states for the rails. The wheelset has 2 states (i.e., 1 degree of freedom) to describe its lateral and yaw motions, as well as a state to represent its spin speed. Each rail has a state to describe its lateral deflection. When two-point contact occurs, the state of the rail at the flanging wheel is known due to a constraint relation which exists between the wheelset and rail lateral displacements.

APPENDIX B

DYNAMIC CURVING EQUATIONS OF MOTION OF A RAIL VEHICLE MODEL

B.1 Introduction

In this Appendix, the dynamic curving equations of motion of a rail vehicle model are developed. The vehicle model is shown schematically in Figure B.1. The vehicle model incorporates the nonlinear wheelset model described in Appendix A. In addition, it includes a generic truck model that can represent arbitrary interconnections between the wheelsets, truck frames, bolsters, and carbody. Thus, conventional, self-steered radial, and forced-steered radial truck configurations can be modelled. In addition to the wheel/rail nonlinearities of the wheelset model, nonlinear suspension effects are included in the vehicle model.

B.2 Coordinate Systems

The front and rear truck frames, the front and rear bolsters, and the carbody are assumed to be rigid bodies. For each rigid body, a "body-fixed" coordinate system is established, consisting of mutually-perpendicular, right-handed axes x , y , z with corresponding unit vectors \hat{i} , \hat{j} , \hat{k} . The x , y , and z axes denote the longitudinal, lateral, and vertical directions, respectively. The axes of each coordinate system are aligned with the principal directions (i.e., in the directions of the principal mass moments of inertia) and the origin of each system is located at the center of mass.

Figure B.2 shows the following "body-fixed" coordinate systems: "F1" and "F2" for the front and rear truck frames, respectively; "B1"

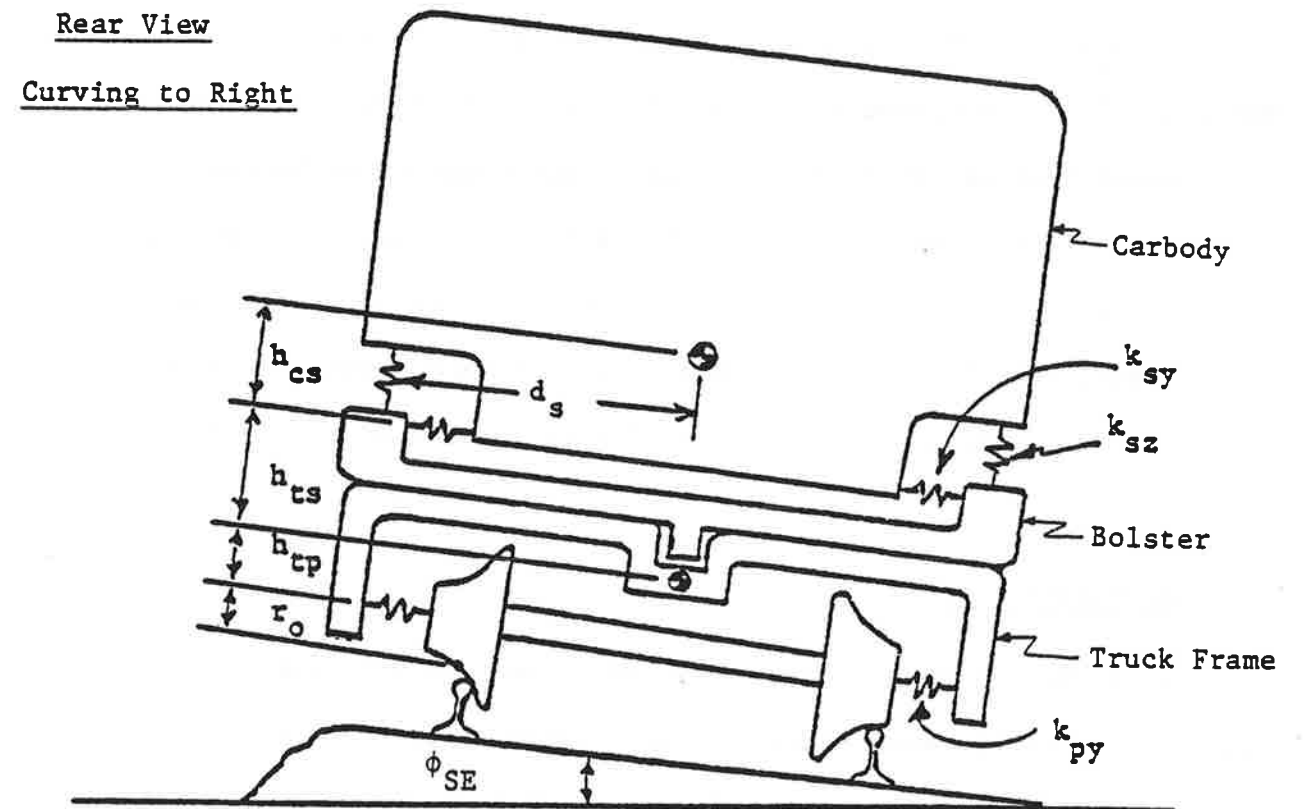


Figure B.1 Rail Vehicle Model During Curving,
Rear View

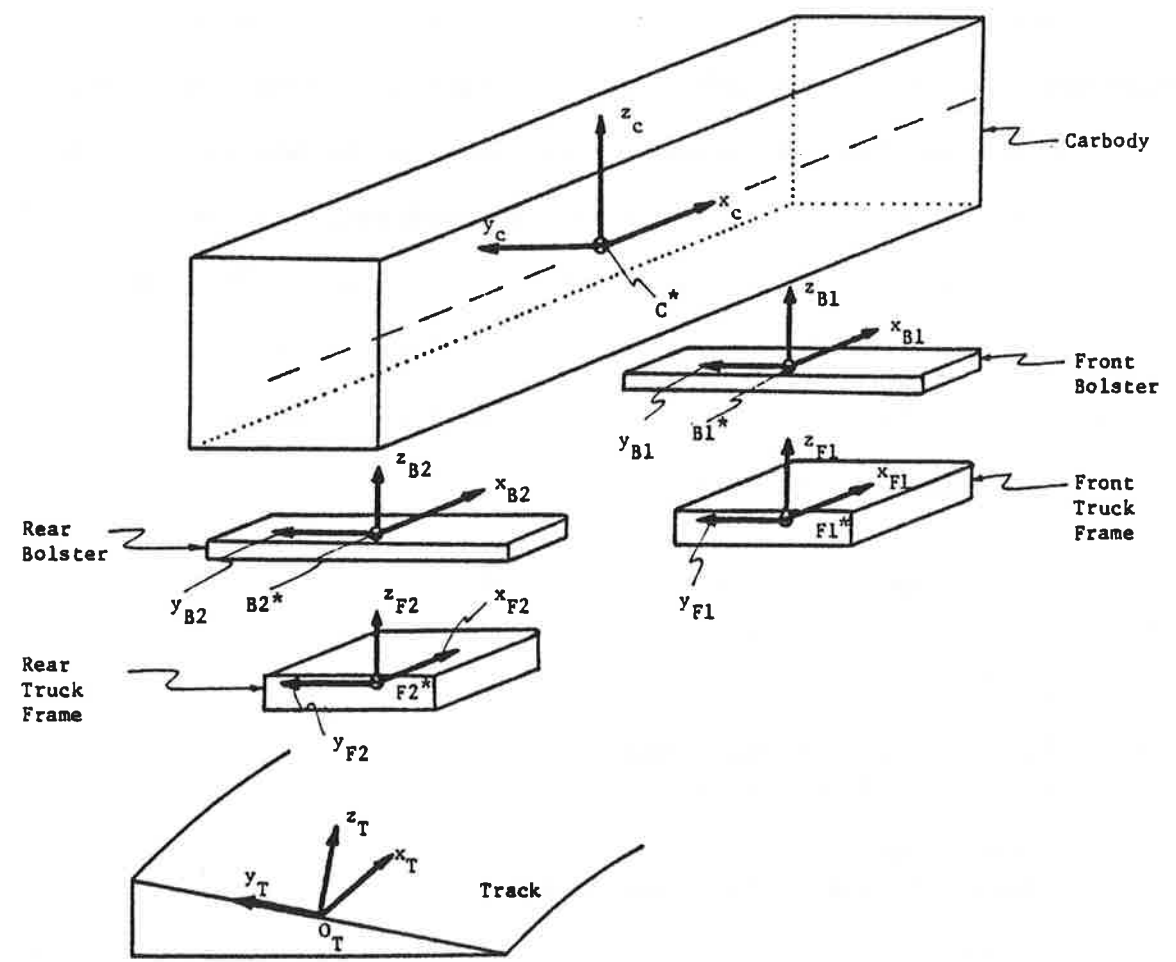


Figure B.2 Rail Vehicle Model Coordinate Systems

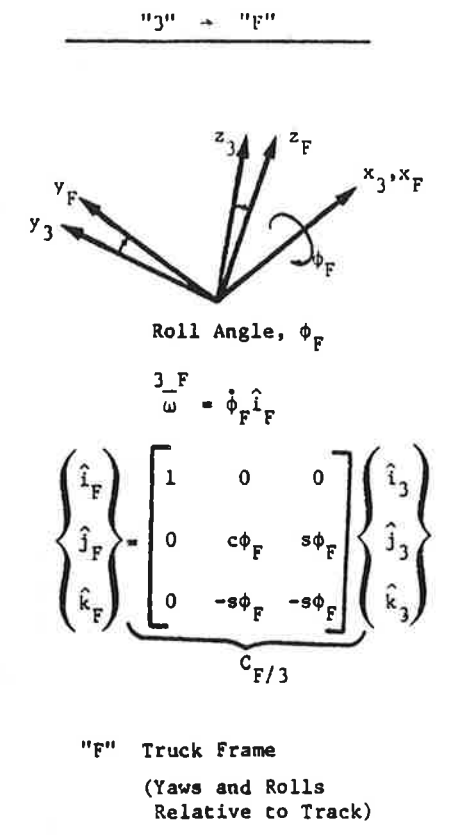
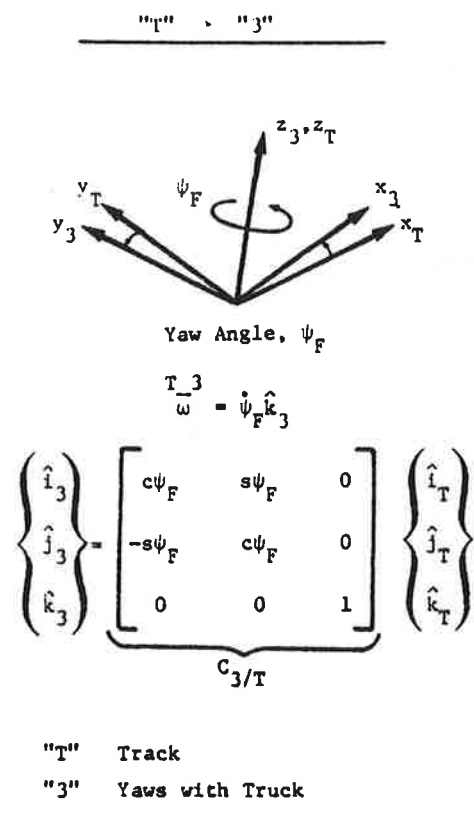
and "B2" for the front and rear bolsters, respectively; and "C" for the carbody. The centers of mass are denoted with asterisks. Figure B.2 also shows the track coordinate system, "T". This system moves along the superelevated track centerline with tangential speed V , as described in Appendix A (Section A.2).

In addition to "body-fixed" coordinate systems, intermediate coordinate systems are used to define the orientation of each rigid body. Table B.1 summarizes the coordinate systems used in the analysis. (For simplicity, the table does not list separate coordinate systems for the front and rear trucks and bolsters. System "F" represents "F1" for the front truck and "F2" for the rear truck, etc.) Coordinate systems "3" and "4" are intermediate systems used to define the orientation of the truck frame and carbody, respectively.

TABLE B.1 COORDINATE SYSTEMS

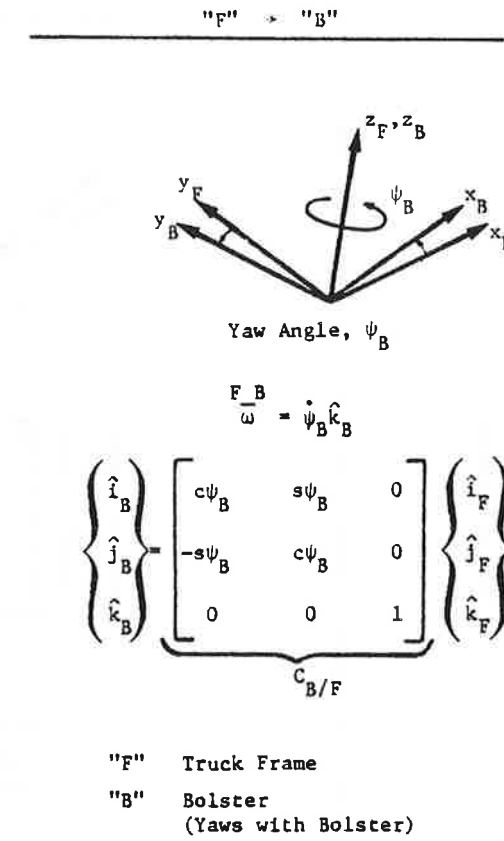
T	Track
3	"Intermediate" Truck Frame (Yaws with Truck Frame)
F	Truck Frame (Yaws and Rolls with Truck Frame)
B	Bolster (Yaws with Bolster)
4	"Intermediate" Carbody (Yaws with Carbody)
C	Carbody (Yaws and Rolls with Carbody)

Figures B.3, B.4, and B.5 show the coordinate system rotations and the corresponding transformation relations used to define the



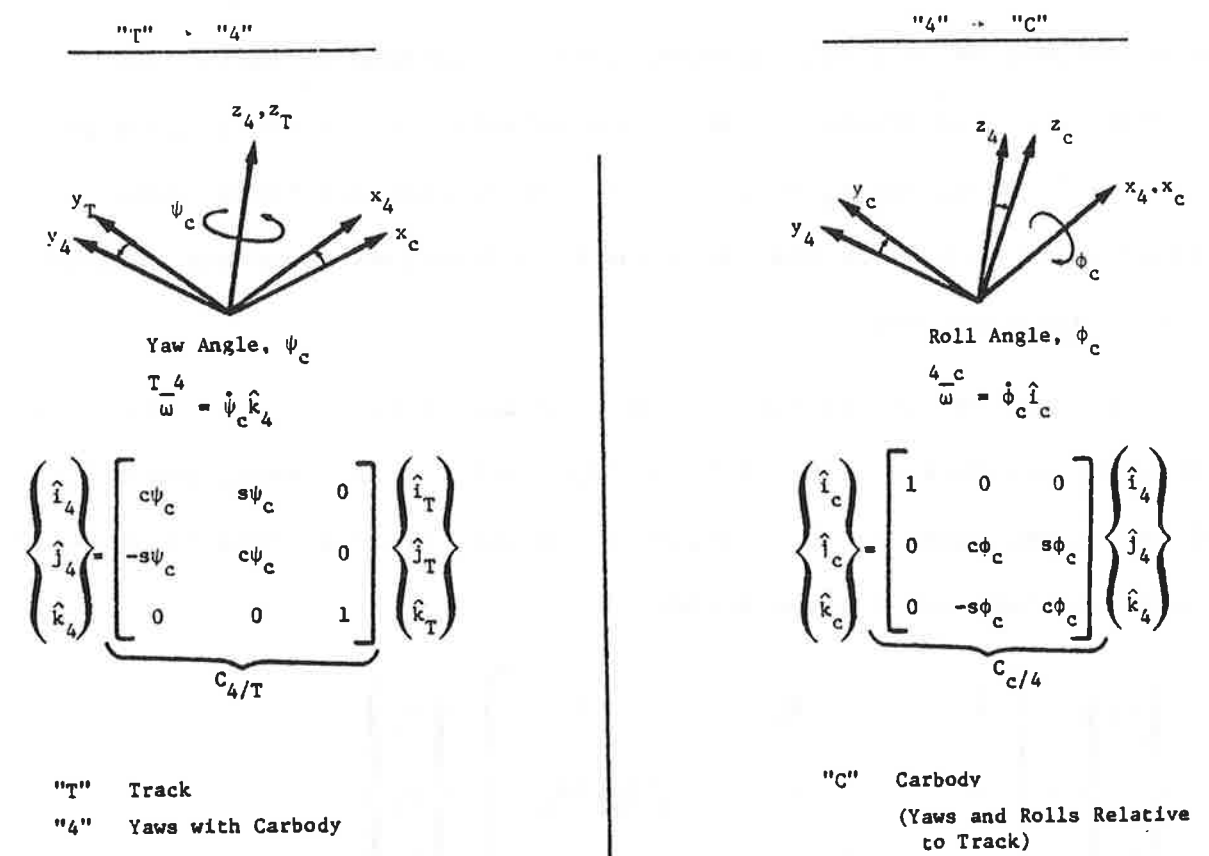
The following notation is used: sa = sin(a), ca = cos(a)

Figure B.3 Definition of Truck Frame Orientation (Rotation Only)



The following notation is used: $s\alpha = \sin(\alpha)$, $c\alpha = \cos(\alpha)$

Figure B.4 Definition of Bolster Orientation (Rotation Only)



The following notation is used: $sa = \sin(\alpha)$, $ca = \cos(\alpha)$

Figure B.5 Definition of Carbody Orientation (Rotation Only)

orientation of the truck frame, bolster, and carbody, respectively. The orientation of the truck frame and carbody is specified relative to the track coordinate system by yaw and roll angles. The sequence of rotations for the truck frame and carbody is yaw displacement about the z_T axis followed by roll displacement about the rotated x_T axis. The orientation of the bolster is specified relative to the truck frame by a yaw angle about the z_F axis. It is assumed that the truck frame, bolster, and carbody do not pitch and thus rotations about the rotated y_T axis are neglected.

As discussed in Section A.2, transformation relations for multiple rotations are obtained by matrix multiplication. Performing the multiplication and assuming small angles gives the following relation between the truck frame and track systems.

$$\begin{Bmatrix} \hat{i}_F \\ \hat{j}_F \\ \hat{k}_F \end{Bmatrix} = \begin{bmatrix} 1 & \psi_F & 0 \\ -\psi_F & 1 & \frac{1}{2}(\phi_{W1} + \phi_{W2}) \\ 0 & -\frac{1}{2}(\phi_{W1} + \phi_{W2}) & 1 \end{bmatrix} \begin{Bmatrix} \hat{i}_T \\ \hat{j}_T \\ \hat{k}_T \end{Bmatrix} \quad (B-1)$$

where the truck frame roll angle is assumed to be the average of the leading and trailing wheelset roll angles, ϕ_{W1} and ϕ_{W2} . (For analysis of the rear truck, angles ϕ_{W1} and ϕ_{W2} correspond to ϕ_{W3} and ϕ_{W4} , respectively.) Similarly, the relation between the bolster and track systems is:

$$\begin{Bmatrix} \hat{i}_B \\ \hat{j}_B \\ \hat{k}_B \end{Bmatrix} = \begin{bmatrix} 1 & \psi_B & 0 \\ -\psi_B & 1 & \frac{1}{2}(\phi_{W1} + \phi_{W2}) \\ 0 & -\frac{1}{2}(\phi_{W1} + \phi_{W2}) & 1 \end{bmatrix} \begin{Bmatrix} \hat{i}_T \\ \hat{j}_T \\ \hat{k}_T \end{Bmatrix} \quad (B-2)$$

since the bolster rolls with the truck frame. The transformation relation between the carbody and track systems for small yaw and roll angles is:

$$\begin{Bmatrix} \hat{i}_C \\ \hat{j}_C \\ \hat{k}_C \end{Bmatrix} = \begin{bmatrix} 1 & \psi_C & 0 \\ -\psi_C & 1 & \phi_C \\ 0 & -\phi_C & 1 \end{bmatrix} \begin{Bmatrix} \hat{i}_T \\ \hat{j}_T \\ \hat{k}_T \end{Bmatrix} \quad (B-3)$$

B.3 Acceleration of Center of Mass

The inertial acceleration of the center of mass of the truck, bolster, carbody, or any rigid body Q with center of mass Q* moving along the track is defined by:

$$\begin{aligned} \frac{I_{Q^*}}{a} &= \frac{I_{O_T}}{a} + \frac{T \cdot Q^* / O_T}{r} + \frac{I \cdot T}{\omega} \times \frac{Q^* / O_T}{r} \\ &+ \frac{I \cdot T}{\omega} \times \left(\frac{I \cdot T}{\omega} \times \frac{Q^* / O_T}{r} \right) + 2 \frac{I \cdot T}{\omega} \times \frac{T \cdot Q^* / O_T}{r} \end{aligned} \quad (B-4)$$

where $\frac{I_{O_T}}{a}$ is the inertial acceleration of point O_T given by equation (A-7), $\frac{I \cdot T}{\omega}$ is the angular velocity of the "T" system relative to the "I" system given by equation (A-8), and $\frac{Q^* / O_T}{r}$ is the displacement vector from O_T to Q^* .

B.3.1 Acceleration of Truck Frame/Bolster Center of Mass

The displacement of the center of mass of the truck frame, F^* , relative to point O_T is \bar{r}^{F^*/O_T} given by:

$$\bar{r}^{F^*/O_T} = x_F \hat{i}_T + y_F \hat{j}_T + (z_F + r_o + h_{tp}) \hat{k}_T \quad (B-5)$$

where x_F , y_F , and z_F represent small longitudinal, lateral, and vertical displacements, respectively, of the truck frame center of mass. Substituting equation (B-5) into (B-4) and setting $Q^* = F^*$ gives the acceleration of the center of mass of the truck frame:

$$\begin{aligned} \overset{I}{\bar{a}}^{F^*} &= [\ddot{x}_F + \dot{V}] \hat{i}_T + [\ddot{y}_F - (r_o + h_{tp}) \ddot{\phi}_{SE} - \frac{V^2}{R}] \hat{j}_T \\ &+ [\ddot{z}_F + a \ddot{\phi}_{SE} + \frac{V^2}{R} \phi_{SE}] \hat{k}_T \end{aligned} \quad (B-6)$$

It is assumed that the only relative displacement between the truck frame and bolster is yaw rotation. In translation, the truck frame and bolster execute the same motions. Thus, the acceleration of the center of mass of the bolster is given by equation (B-6). (This assumes that the vertical distance between the centers of mass of the truck frame and bolster is small relative to $(r_o + h_{tp})$).

B.3.2 Acceleration of Carbody Center of Mass

The displacement of the center of mass of the carbody, C^* , from point O_T , denoted by \bar{r}^{C^*/O_T} , is

$$\bar{r}^{C^*/O_T} = x_C \hat{i}_T + y_C \hat{j}_T + (z_C + r_o + h_{tp} + h_{ts} + h_{cs}) \hat{k}_T \quad (B-7)$$

where x_C , y_C , and z_C represent small longitudinal, lateral, and verti-

cal carbody displacements, respectively. Substituting into equation (B-4) with $Q^* = C^*$ yields the acceleration of the center of mass of the carbody:

$$\begin{aligned} \frac{I_{C^*}}{a} = & [\ddot{x}_C + \dot{V}] \hat{i}_T + [\ddot{y}_C - (r_o + h_{tp} + h_{ts} + h_{cs}) \ddot{\phi}_{SE} - \frac{V^2}{R}] \hat{j}_T \\ & + [\ddot{z}_C + a \ddot{\phi}_{SE} + \frac{V^2}{R} \phi_{SE}] \hat{k}_T \end{aligned} \quad (B-8)$$

B.4 Rate of Angular Momentum

B.4.1 Rate of Angular Momentum of Truck Frame and Bolster

The angular velocity of the truck frame, "F", in inertial space "I" is:

$$\frac{I_{F}}{\omega} = -\frac{V}{R} \hat{k}_H + \dot{\phi}_{SE} \hat{i}_T + \dot{\psi}_F \hat{k}_3 + \frac{1}{2}(\dot{\phi}_{W1} + \dot{\phi}_{W2}) \hat{i}_F \quad (B-9)$$

Assuming small angles, equation (B-9) is equivalent to

$$\frac{I_{F}}{\omega} = \omega_{FX} \hat{i}_F + \omega_{FZ} \hat{k}_F \quad (B-10)$$

by transformation where the components are

$$\left. \begin{aligned} \omega_{FX} &= \dot{\phi}_{SE} + \frac{1}{2}(\dot{\phi}_{W1} + \dot{\phi}_{W2}) \\ \omega_{FZ} &= \dot{\psi}_F - \frac{V}{R} \end{aligned} \right\} \quad (B-11)$$

The angular momentum of the truck frame about its center of mass is given by

$$\bar{H}_{F/F^*} = I_{FX} \omega_{FX} \hat{i}_F + I_{FZ} \omega_{FZ} \hat{k}_F \quad (B-12)$$

where I_{FX} and I_{FZ} are the roll and yaw principal mass moments of inertia of the truck frame, respectively.

The inertial time rate of change of angular momentum is expressed by:

$$\frac{I \cdot F / F^*}{H} = \frac{F \cdot F / F^*}{H} + \frac{I_F}{\omega} \times \frac{F / F^*}{H} \quad (B-13)$$

where $\frac{I \cdot F / F^*}{H}$ and $\frac{F \cdot F / F^*}{H}$ are the time rates of change (i.e., first derivatives) of the angular momentum in the "I" and "F" systems, respectively. Substituting equations (B-10), (B-11), and (B-12) into (B-13) and neglecting smaller order terms gives the inertial time rate of change of angular momentum of the truck frame:

$$\begin{aligned} \frac{I \cdot F / F^*}{H} &= [I_{FX} \{\ddot{\phi}_{SE} + \frac{1}{2}(\ddot{\phi}_{W1} + \ddot{\phi}_{W2})\}] \hat{i}_F \\ &+ [I_{FZ} \{\ddot{\psi}_F - \frac{\dot{V}}{R} - V(1/R)\}] \hat{k}_F \end{aligned} \quad (B-14)$$

By parallel arguments, the inertial time rate of change of angular momentum of the bolster is:

$$\begin{aligned} \frac{I \cdot B / B^*}{H} &= [I_{BX} \{\ddot{\phi}_{SE} + \frac{1}{2}(\ddot{\phi}_{W1} + \ddot{\phi}_{W2})\}] \hat{i}_B \\ &+ [I_{BZ} \{\ddot{\psi}_B - \frac{\dot{V}}{R} - V(1/R)\}] \hat{k}_B \end{aligned} \quad (B-15)$$

where small angles have been assumed and smaller order terms have been neglected.

B.4.2 Rate of Angular Momentum of Carbody

The angular velocity of the carbody "C" with respect to inertial space "I" is:

$$\frac{I_C}{\omega} = -\frac{V}{R} \hat{k}_H + \dot{\phi}_{SE} \hat{i}_T + \dot{\psi}_C \hat{k}_4 + \dot{\phi}_C \hat{k}_C \quad (B-16)$$

In carbody coordinates, equation (B-16) is equivalent to:

$$\frac{I_C}{\omega} = (\dot{\phi}_{SE} + \dot{\phi}_C)\hat{i}_C + (\dot{\psi}_C - \frac{V}{R})\hat{k}_C \quad (B-17)$$

where smaller order terms have been neglected. The inertial times rate of change of angular momentum of the carbody is derived by following a development similar to the derivation in Section B.4.1 for the truck frame. The result is:

$$\begin{aligned} \frac{I_C}{H} \dot{C}^* &= [I_{CX}(\ddot{\phi}_{SE} + \ddot{\phi}_C)]\hat{i}_C \\ &+ [I_{CZ}\{\ddot{\psi}_C - \dot{V}/R - V(1/R)\}]\hat{k}_C \end{aligned} \quad (B-18)$$

where I_{CX} and I_{CZ} are the roll and yaw principal mass moments of inertia of the carbody, respectively. In deriving equation (B-16), small angles have been assumed and smaller order terms have been neglected.

B.5 Forces and Moments

This section focuses on the internal suspension forces and moments acting on the wheelsets, trucks, bolsters, and carbody of the rail vehicle model shown in Figure B.1. The vehicle model incorporates a generic truck model capable of representing conventional, self-steered radial, and several forced-steered radial truck designs.

A schematic of the generic truck model is shown in Figure B.6. The geometric offsets, $\Delta\psi_1$, $\Delta\psi_2$, Δy_1 , Δy_2 , represent the effects of forced-steering linkages and are given by the following steering relations.

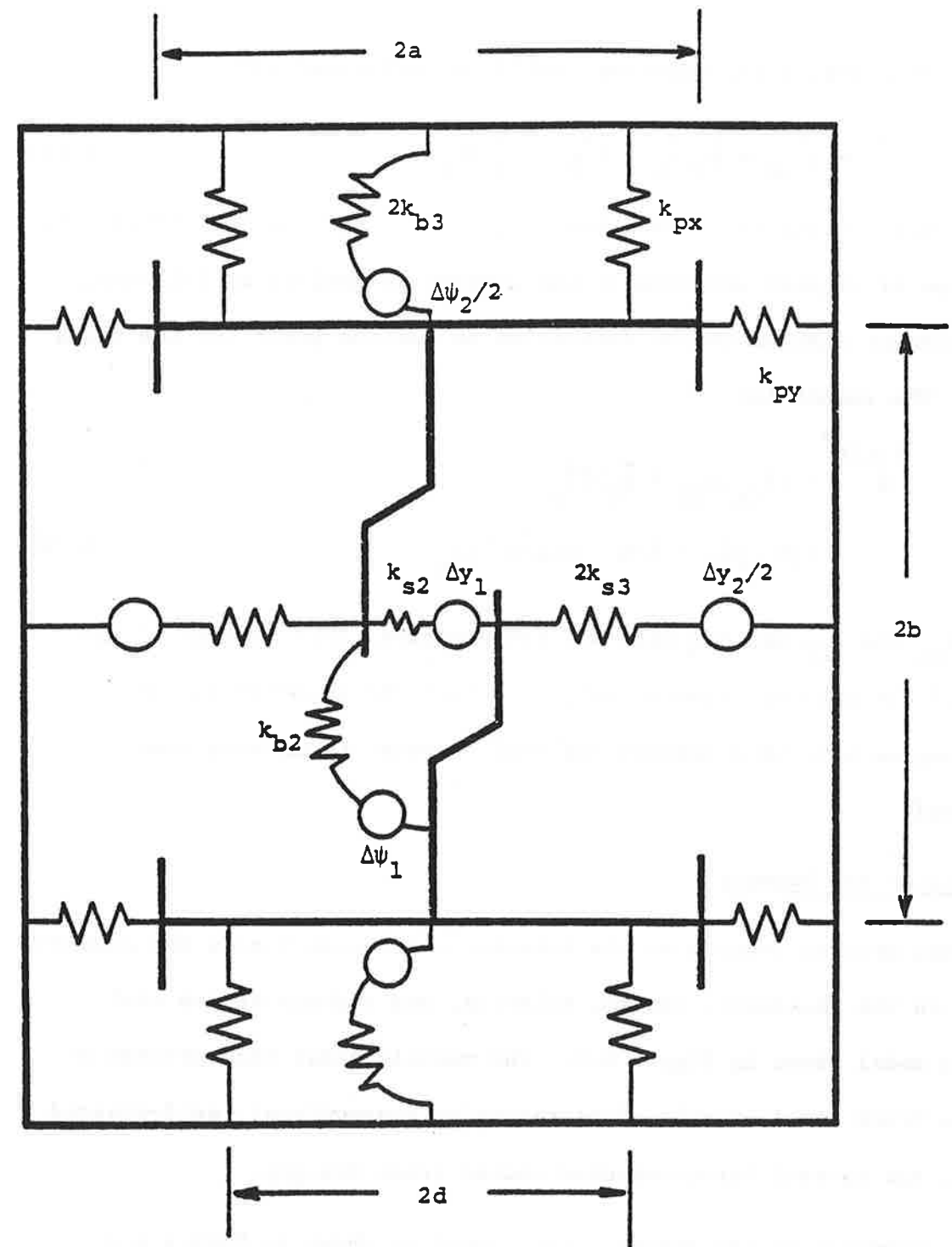


Figure B.6 Generic Truck Model

Yaw Offset Relation

$$\begin{aligned}\Delta\psi_1 = \Delta\psi_2 = & \pm 2G_1 \left(\frac{\psi_{W1} + \psi_{W2}}{2} - \psi_B \right) \pm 2G_2 \left(\frac{y_{W1} - y_{W2}}{2b} - \psi_B \right) \\ & \pm 2G_3 \left(\frac{y_{W1} + y_{W2}}{2} - y_F \right) \pm 2G_4 (\psi_F - \psi_B) \\ & \pm 2G_5 \left(\frac{\psi_{W1} + \psi_{W2}}{2} - \psi_F \right) \pm 2G_6 \left(\frac{y_{W1} - y_{W2}}{2b} - \psi_F \right) \quad (B-19)\end{aligned}$$

Lateral Offset Relation

$$\Delta y_1 = \Delta y_2 = 2H_1 \left(\frac{y_{W1} + y_{W2}}{2} - y_C \right) + 2H_2 (y_F - y_C) + 2H_3 \left(\frac{y_{W1} + y_{W2}}{2} - y_F \right) \quad (B-20)$$

The G_i 's in equation (B-19) are curvature steering gains and the H_i 's in equation (B-20) are cant deficient steering gains. The suspension system of the generic truck model produces suspension forces and moments which act on the wheelsets, truck frame, bolster, and carbody. Expressions for the suspension forces and moments due to the steering linkages are derived in [1].

B.5.1 Wheelset Suspension Forces and Moments

Suspension forces and moments act on each wheelset due to primary longitudinal and lateral suspension elements, self-steered and forced-steered linkages, and loads carried from above. Figure B.7 shows the lateral and vertical suspension forces, $F_{susp_{wi}^y}$ and $F_{susp_{wi}^z}$, and the equivalent roll and yaw suspension moments, $M_{susp_{wi}^x}$ and $M_{susp_{wi}^z}$, respectively, acting on wheelset i . In this analysis, the longitudinal suspension force, $F_{susp_{wi}^x}$, is zero since the analysis neglects the wheelset longitudinal degree of freedom. The spin sus-

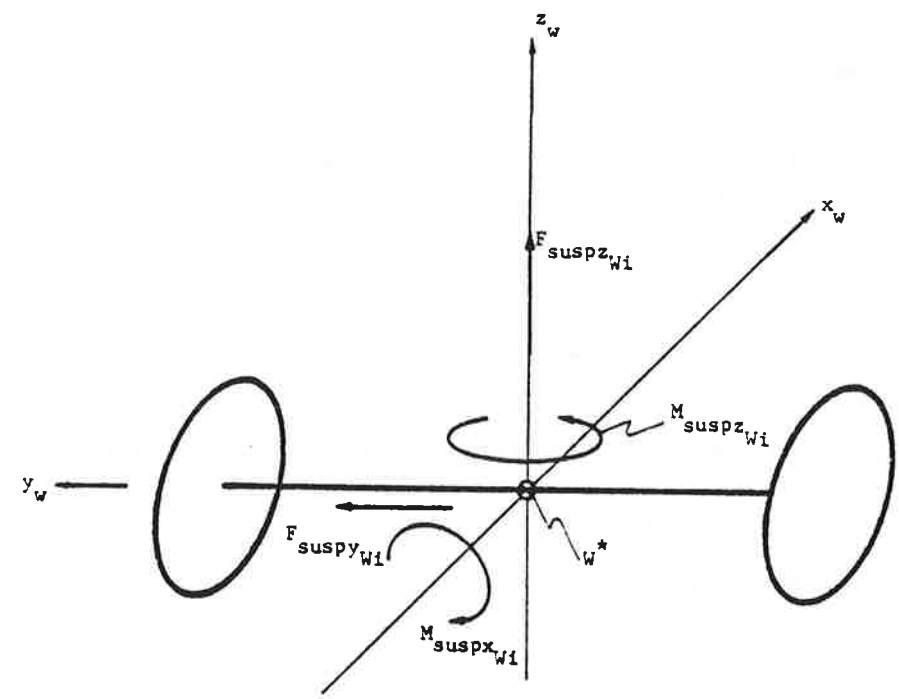


Figure B.7 Suspension Forces and Moments Acting on Wheelset i

pension moment, $M_{susp_{wi}}$, is also zero since no moments develop about the spin axis due to suspension components.

The lateral suspension force, $F_{susp_{wi}}$, and yaw suspension moment, $M_{susp_{wi}}$, acting on the leading wheelset of the front and rear trucks are given by the expressions below.

Leading Wheelset Lateral (i = 1 Front Truck;
i = 3 Rear Truck)

$$\begin{aligned}
 F_{susp_{wi}} = & [-2k_{py} - \{G_3 + (\frac{G_2 + G_6}{b})\}^2 (k_{b2} + k_{b3}) - (H_1 - H_3 + 1)^2 (k_{s2} + k_{s3}) - k_{s3}] y_{w1} \\
 & + [\{G_3 + (\frac{G_2 + G_6}{b})\} \{1 + (G_1 + G_5)\} (k_{b2} + k_{b3}) + b(H_1 + H_3 + 1)(k_{s2} + k_{s3}) \\
 & + bk_{s3}] (\psi_{w1} - \frac{b}{R}) \\
 & + [-\{G_3 - (\frac{G_2 + G_6}{b})\}^2 (k_{b2} + k_{b3}) - \{H_1 + H_3\}^2 - 1\} (k_{s2} + k_{s3}) - k_{s3}] y_{w2} \\
 & + [\{-G_3 + (\frac{G_2 + G_6}{b})\} \{1 + (G_1 + G_5)\} (k_{b2} + k_{b3}) + b(H_1 + H_3 + 1)(k_{s2} + k_{s3}) \\
 & - bk_{s3}] (\psi_{w2} + \frac{b}{R}) \\
 & + [2k_{py} + 2G_3 \{G_3 + (\frac{G_2 + G_6}{b})\} (k_{b2} + k_{b3}) - 2(H_2 - H_3)(H_1 + H_3 + 1)(k_{s2} + k_{s3}) \\
 & + 2k_{s3}] y_F \\
 & + [2bk_{py} + 2(G_4 - G_5 - G_6) \{-G_3 - (\frac{G_2 + G_6}{b})\} (k_{b2} + k_{b3})] \psi_F \\
 & + [2(G_1 + G_2 + G_4) \{+G_3 + (\frac{G_2 + G_6}{b})\} (k_{b2} + k_{b3})] \psi_B
 \end{aligned}$$

$$\begin{aligned}
& + [2(H_1+H_2)(H_1+H_3+1)(k_{s2}+k_{s3})]y_c \\
& + [-2C_{py} - (C_{s2}+2C_{s3})]2\dot{y}_{w1} + [b(C_{s2}+2C_{s3})](\dot{\psi}_{w1} - b(1/R)) \\
& + [C_{s2}]\dot{y}_{w2} + [bC_{s2}](\dot{\psi}_{w2} + b(1/R)) \\
& + [2C_{py}+2C_{s3}]\dot{y}_F + [2bC_{py}]\dot{\psi}_F
\end{aligned} \tag{B-21}$$

Leading Wheelset Yaw (i = 1 Front Truck;
i = 3 Rear Truck)

$$\begin{aligned}
M_{suspz_{wi}} & = [\{G_3 \pm (\frac{G_2+G_6}{b})\} \{1 \mp (G_1+G_5)\} (k_{b2}+k_{b3}) \\
& + b(H_1+H_3+1)(k_{s2}+k_{s3})+bk_{s3}]y_{w1} \\
& + [-2d_p^2 k_{px} - (G_1+G_5 \mp 1)^2 (k_{b2}+k_{b3}) - b^2 (k_{s2}+k_{s3}) \\
& - k_{b3} - b^2 k_{s3}] (\psi_{w1} - \frac{b}{R}) \\
& + [\{G_3 \mp (\frac{G_2+G_6}{b})\} \{1 \mp (G_1+G_5)\} (k_{b2}+k_{b3}) \\
& + b(H_1+H_3-1)(k_{s2}+k_{s3})+bk_{s3}]y_{w2} \\
& + [\{1 - (G_1+G_5)\}^2 (k_{b2}+k_{b3}) - b^2 (k_{s2}+k_{s3}) \\
& - k_{b3} + b^2 k_{s3}] (\psi_{w2} + \frac{b}{R}) \\
& + [2G_3 \{-1 \pm (G_1+G_5)\} (k_{b2}+k_{b3}) + 2b(H_2-H_3)(k_{s2}+k_{s3}) - 2bk_{s3}]y_F \\
& + [2d_p^2 k_{px} + 2(G_4-G_5-G_6) \{ \pm 1 - (G_1+G_5) \} (k_{b2}+k_{b3}) + 2k_{b3}] \psi_F
\end{aligned}$$

$$\begin{aligned}
& + [2(G_1 + G_2 + G_4)(G_1 + G_5 + 1)(k_{b2} + k_{b3})] \psi_B \\
& + [-2b(H_1 + H_2)(k_{s2} + k_{s3})] y_c \\
& + [b(C_{s2} + 2C_{s3})] \dot{y}_{w1} + [-2d_p^2 C_{px} - C_{b2} - 2C_{b3} - b^2(C_{s2} + 2C_{s3})] (\dot{\psi}_{w1} - b(1/R)) \\
& + [-bC_{s2}] \dot{y}_{w2} + [C_{b2} - b^2 C_{s2}] (\dot{\psi}_{w2} + b(1/R)) \\
& + [-2bC_{s3}] \dot{y}_F + [2d_p^2 C_{px} + 2C_{b3}] \dot{\psi}_F
\end{aligned} \tag{B-22}$$

In these equations, as well as the equations that follow, the notation \pm implies + for the front truck and - for the rear truck. Also, y_{w1} and y_{w2} represent the lateral excursions of the leading and trailing wheelsets of the truck, respectively, ψ_{w1} and ψ_{w2} denote the yaw angles of the leading and trailing wheelsets, respectively. For analysis of the rear truck, y_{w1} , y_{w2} , ψ_{w1} , and ψ_{w2} correspond to y_{w3} , y_{w4} , ψ_{w3} , and ψ_{w4} , respectively.

Due to the suspension arrangement, a lateral force, $F_{susp_{wi}}$, and a yaw moment, $M_{susp_{wi}}$, act on the trailing wheelsets of the front and rear trucks.

Trailing Wheelset Lateral (i = 2 Front Truck;
i = 4 Rear Truck)

$$\begin{aligned}
F_{susp_{wi}} = & [-\{G_3^2 - (\frac{G_2 + G_6}{b})^2\} (k_{b2} + k_{b3}) - \{(H_1 + H_3)^2 - 1\} (k_{s2} + k_{s3}) - k_{s3}] y_{w1} \\
& + [\{G_3 + (\frac{G_2 + G_6}{b})\} \{1 + (G_1 + G_5)\} (k_{b2} + k_{b3})]
\end{aligned}$$

$$\begin{aligned}
& +b(H_1+H_3-1)(k_{s2}+k_{s3})+bk_{s3}](\psi_{w1} - \frac{b}{R}) \\
& +[-2k_{py} - \left\{G_3 \mp \left(\frac{G_2+G_6}{b}\right)\right\}^2 (k_{b2}+k_{b3}) - (H_1+H_3-1)^2 (k_{s2}+k_{s3}) - k_{s3}]y_{w2} \\
& + \left\{ -G_3 \pm \left(\frac{G_2+G_6}{b}\right)\right\} \left\{ 1 \pm (G_1+G_5)\right\} (k_{b2}+k_{b3}) \\
& +b(H_1+H_3-1)(k_{s2}+k_{s3})-bk_{s3}](\psi_{w2} + \frac{b}{R}) \\
& +[2k_{py} + 2G_3 \left\{G_3 \mp \left(\frac{G_2+G_6}{b}\right)\right\} (k_{b2}+k_{b3}) \\
& -2(H_2-H_3)(H_1+H_3-1)(k_{s2}+k_{s3})+2k_{s3}]y_F \\
& +[-2k_{py}b + 2(G_4-G_5-G_6)\left\{\mp G_3 + \left(\frac{G_2+G_6}{b}\right)\right\} (k_{b2}+k_{b3})]\psi_F \\
& +[2(G_1+G_2+G_4)\left\{\pm G_3 - \left(\frac{G_2+G_6}{b}\right)\right\} (k_{b2}+k_{b3})]\psi_B \\
& +[2(H_1+H_2)(H_1+H_3-1)(k_{s2}+k_{s3})]y_c \\
& +[C_{s2}]\dot{y}_{w1} \quad \quad \quad +[-bC_{s2}](\dot{\psi}_{w1} - b(1/R)) \\
& +[-2C_{py} - (C_{s2}+2C_{s3})]\dot{y}_{w2} + [-b(C_{s2}+2C_{s3})](\dot{\psi}_{w2} + b(1/R)) \\
& +[2C_{py} + 2C_{s3}]\dot{y}_F \quad \quad \quad + [-2bC_{py}]\dot{\psi}_F
\end{aligned} \tag{B-23}$$

Trailing Wheelset Yaw (i = 2 Front Truck;
i = 4 Rear Truck)

$$M_{\text{susp}z_{wi}} = \left[\left\{ -G_3 \mp \left(\frac{G_2+G_6}{b}\right)\right\} \left\{ 1 \pm (G_1+G_5)\right\} (k_{b2}+k_{b3}) \right]$$

$$\begin{aligned}
& +b(H_1+H_3+1)(k_{s2}+k_{s3})-bk_{s3}]y_{w1} \\
& +\left\{1-(G_1+G_5)^2\right\}(k_{b2}+k_{b3})-b^2(k_{s2}+k_{s3})-k_{b3}-b^2k_{s3}\left](\psi_{w1}-\frac{b}{R})\right. \\
& +\left\{-G_3+\left(\frac{G_2+G_6}{b}\right)\right\}\left\{1+(G_1+G_5)\right\}(k_{b2}+k_{b3}) \\
& +b(H_1+H_3-1)(k_{s2}+k_{s3})-bk_{s3}]y_{w2} \\
& +\left[-2d_p^2k_{px}-\left\{1+(G_1+G_5)\right\}^2(k_{b2}+k_{b3})-b^2(k_{s2}+k_{s3})\right. \\
& \left.-k_{b3}-b^2k_{s3}\right](\psi_{w2}+\frac{b}{R}) \\
& +\left[2G_3\left\{1+(G_1+G_5)\right\}(k_{b2}+k_{b3})+2b(H_2-H_3)(k_{s2}+k_{s3})+2bk_{s3}\right]y_F \\
& +\left[2d_p^2k_{px}+2(G_4-G_5-G_6)\left\{1-(G_1+G_5)\right\}(k_{b2}+k_{b3})+2k_{b3}\right]\psi_F \\
& +\left[2(G_1+G_2+G_4)(G_1+G_5+1)(k_{b2}+k_{b3})\right]\psi_B \\
& +\left[-2b(H_1+H_2)(k_{s2}+k_{s3})\right]y_c \\
& +\left[bC_{s2}\right]\dot{y}_{w1} \quad +\left[C_{b2}-b^2C_{s2}\right](\dot{\psi}_{w1}-b(1/R)) \\
& +\left[-b(C_{s2}+2C_{s3})\right]\dot{y}_{w2}+\left[-2d_p^2C_{px}-\left\{C_{b2}+2C_{b3}+b^2(C_{s2}+2C_{s3})\right\}\right](\dot{\psi}_{w2}+b(1/R)) \\
& +\left[2bC_{s3}\right]\dot{y}_F + \left[2d_p^2C_{px} + 2C_{b3}\right]\dot{\psi}_F \tag{B-24}
\end{aligned}$$

The vertical suspension force, $F_{susp_{wi}}$, is equal to the load carried vertically by the leading and trailing wheelsets, i.e.,

$$F_{\text{suspz}_{wi}} = -\left[\frac{1}{2}(W_F + W_B) + \frac{1}{4} W_C \right], \quad i = 1, 2, 3, 4. \quad (\text{B-25})$$

The roll suspension moment, $M_{\text{suspx}_{wi}}$, is due to the truck frame, bolster, and carbody weights as follows.

$$\begin{aligned} M_{\text{suspx}_{wi}} = & -\frac{1}{2}(W_F + W_B)[\phi_d = \frac{1}{2}(\phi_{w1} + \phi_{w2})]h_{tp} \\ & - \frac{1}{4} W_C [\phi_d - \phi_c](h_{cs} + h_{ts} + h_{tp}) \\ & - \frac{1}{2}(W_F + W_B)\left[y_F + \frac{b^2}{R} - y_{wi}\right] \\ & - \frac{1}{4} W_C \left(y_c + \frac{l^2}{R} - y_{wi}\right), \quad i = 1, 2, 3, 4. \quad (\text{B-26}) \end{aligned}$$

In equation (B-25) and (B-26), $i = 1, 2$ for the leading, trailing wheelsets of the front truck, and $i = 3, 4$ for the leading, trailing wheelsets of the rear truck. For analysis of the rear truck, ϕ_{w1} and ϕ_{w2} in equation (B-26) correspond to ϕ_{w3} and ϕ_{w4} , respectively.

B.5.2 Truck Frame and Bolster Suspension Forces and Moments

In this section, expressions for the suspension forces and moments acting on the truck frame and bolster are presented. In a conventional rail vehicle, suspension forces and moments act due to the primary and secondary suspension systems. In an advanced design vehicle with steerable trucks, the steering linkages exert additional forces and moments on the trucks and bolsters.

The secondary suspension system acting between the truck, bolster, and carbody is modelled as follows. The carbody is coupled to the bolster via parallel spring/viscous damper elements in the lateral and vertical directions and a torsional spring/viscous damper combination in the yaw direction. The bolster is connected to the truck frame by a torsional coulomb damper which saturates at the breakaway torque. The damper allows yaw motion between the truck frame and bolster. In all directions except yaw the bolster and truck frame follow identical motions. In forced-steered vehicle designs, the steering linkages are physically connected to the bolster.

Due to the suspension system, an equivalent lateral force and yaw moment act at the center of mass of each truck frame. The lateral suspension force, $F_{suspy_{Fi}}$, and yaw suspension moment, $M_{suspz_{Fi}}$, acting on truck frame i ($i = 1$ for front truck; $i = 2$ for rear truck) are shown in Figure B.8 and are given by the following equations.

Truck Frame Lateral ($i = 1$ Front Truck;
 $i = 2$ Rear Truck)

$$\begin{aligned}
 F_{suspy_{Fi}} = & [2k_{py} + 2G_3 \left\{ G_3 + \left(-\frac{G_2 + G_6}{b} \right) \right\} (k_{b2} + k_{b3}) \\
 & - 2(H_2 - H_3)(H_1 + H_3 + 1)(k_{s2} + k_{s3}) + 2k_{s3}] y_{w1} \\
 & + [2G_3 \left\{ -1 + (G_1 + G_5) \right\} (k_{b2} + k_{b3}) + 2b(H_2 - H_3)(k_{s2} + k_{s3}) - 2bk_{s3}] \left(\psi_{w1} - \frac{b}{R} \right) \\
 & + [2k_{py} + 2H_3 \left\{ G_3 + \left(-\frac{G_2 + G_6}{b} \right) \right\} (k_{b2} + k_{b3}) \\
 & - 2(H_2 - H_3)(H_1 + H_3 - 1)(k_{s2} + k_{s3}) + 2k_{s3}] y_{w2}
 \end{aligned}$$

Plan
View:

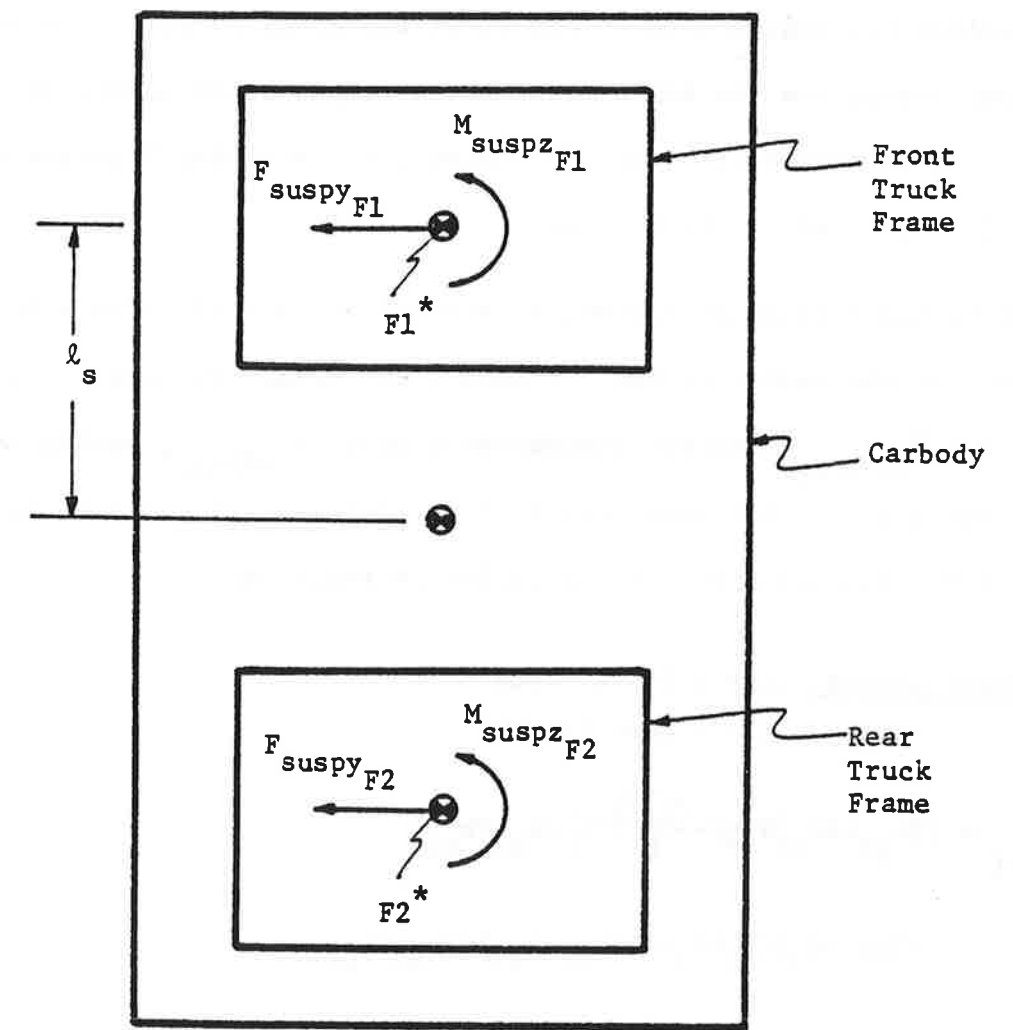
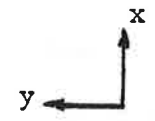


Figure B.8 Lateral Suspension Forces and Yaw Suspension Moments Acting on Truck Frame

$$\begin{aligned}
& + [2G_3 \left\{ 1 + (G_1 + G_5) \right\} (k_{b2} + k_{b3}) + 2b(H_2 - H_3)(k_{s2} + k_{s3}) + 2bk_{s3}] (\psi_{w2} + \frac{b}{R}) \\
& + [-4k_{py} - 2k_{sy} - 4G_3^2(k_{b2} + k_{b3}) - 4(H_2 - H_3)^2(k_{s2} + k_{s3}) - 4k_{s3}] y_F \\
& + [+4G_3(G_4 - G_5 - G_6)(k_{b2} + k_{b3})] \psi_F \\
& + [+4G_3(G_1 + G_2 + G_4)(k_{b2} + k_{b3})] \psi_B \\
& + [2k_{sy} + 4(H_1 + H_2)(H_2 - H_3)(k_{s2} + k_{s3})] y_c \\
& + [+2k_{sy} \ell_s] (\psi_c \pm \frac{\ell_s}{R}) \\
& + [2C_{py} + 2C_{s3}] \dot{y}_{w1} \qquad \qquad \qquad + [-2bc_{s3}] (\dot{\psi}_{w1} - b(1/R)) \\
& + [2C_{py} + 2C_{s3}] \dot{y}_{w2} \qquad \qquad \qquad + [+2bc_{s3}] (\dot{\psi}_{w2} + b(1/R)) \\
& + [-4C_{py} - 2C_{sy} - 4C_{s3}] \dot{y}_F + [2C_{sy}] \dot{y}_c \\
& + [+2C_{sy} \ell_s] (\dot{\psi}_c \pm \ell_s(1/R)) \qquad \qquad \qquad (B-27)
\end{aligned}$$

Truck Frame Yaw (i = 1 Front Truck; i = 2 Rear Truck)

$$\begin{aligned}
M_{suspz_{Fi}} & = [2bk_{py} + 2 \left\{ \mp G_3 - \left(\frac{G_2 + G_6}{b} \right) \right\} (G_4 - G_5 - G_6)(k_{b2} + k_{b3})] y_{w1} \\
& + [2d_p^2 k_{px} + 2(G_4 - G_5 - G_6) \left\{ \mp 1 - (G_1 + G_5) \right\} (k_{b2} + k_{b3}) + 2k_{b3}] (\psi_{w1} - \frac{b}{R}) \\
& + [-2bk_{py} + 2 \left\{ \mp G_3 + \left(\frac{G_2 + G_6}{b} \right) \right\} (G_4 - G_5 - G_6)(k_{b2} + k_{b3})] y_{w2}
\end{aligned}$$

$$\begin{aligned}
& + [2d_p^2 k_{px} + 2(G_4 - G_5 - G_6) \{ \bar{1} - (G_1 + G_5) \} (k_{b2} + k_{b3}) + 2k_{b3}] (\psi_{w2} + \frac{b}{R}) \\
& + [4G_3 (G_4 - G_5 - G_6) (k_{b2} + k_{b3})] y_F \\
& + [-4d_p^2 k_{px} - 4b^2 k_{py} - 4(G_4 - G_5 - G_6)^2 (k_{b2} + k_{b3}) - 4k_{b3}] \psi_F \\
& + [4(G_4 - G_5 - G_6) (G_1 + G_2 + G_4) (k_{b2} + k_{b3})] \psi_B \\
& + [2bc_{py}] \dot{y}_{w1} + [2d_p^2 c_{px} + 2c_{b3}] (\dot{\psi}_{w1} - b(1/R)) \\
& + [-2bc_{py}] \dot{y}_{w2} + [2d_p^2 c_{px} + 2c_{b3}] (\dot{\psi}_{w2} + b(1/R)) \\
& + [-4d_p^2 c_{px} - 4b^2 c_{py} - 4c_{b3}] \dot{\psi}_F - T_{coul} \tag{B-28}
\end{aligned}$$

In equation (B-28), T_{coul} represents the coulomb friction yaw moment acting on the truck frame due to interaction with the bolster. For numerical purposes, the model of coulomb friction is modified to include a linear viscous band at the origin, as follows:

$$T_{coul} = \begin{cases} T_o & \dots \dots \dots \text{for } (\dot{\psi}_F - \dot{\psi}_B) \geq T_o/k_o \\ k_o (\dot{\psi}_F - \dot{\psi}_B) & \dots \dots \dots \text{for } -T_o/k_o < (\dot{\psi}_F - \dot{\psi}_B) < T_o/k_o \\ -T_o & \dots \dots \dots \text{for } (\dot{\psi}_F - \dot{\psi}_B) \leq -T_o/k_o \end{cases} \tag{B-29}$$

At low relative yaw rates between the bolster and truck frame, the model assumes viscous damping occurs. At higher relative yaw rates, the model assumes coulomb damping occurs with the frictional torque saturating at the centerplate breakaway value. The coulomb friction

characteristic of equation (B-29) is shown in Figure B.9. This method approximates the frictional torque levels below $|T_o|$ (during "stopped conditions"). The selection of the width of the linear viscous band is important. Too wide a band will produce viscous damping results. However, if the band is too narrow, it will be missed during "stopped conditions" by discrete integration.

A net yaw moment acts on the bolster due to the coulomb friction element and due to the steering linkages of forced-steered vehicle designs. The yaw suspension moment, $M_{susp_{Bi}}$, acting on bolster i ($i = 1$ for front bolster; $i = 2$ for rear bolster) is shown in Figure B.10 and is given by equation (B-30).

Bolster Yaw ($i = 1$ Front Bolster; $i = 2$ Rear Bolster)

$$\begin{aligned}
 M_{susp_{Bi}} = & [2(G_1+G_2+G_4)(+G_3+\frac{G_2+G_6}{b})(k_{b2}+k_{b3})]y_{w1} \\
 & + [2(G_1+G_2+G_4)(G_1+G_5+1)(k_{b2}+k_{b3})](\psi_{w1}-\frac{b}{R}) \\
 & + [+2(G_1+G_2+G_4)(G_3+\frac{G_2+G_6}{b})(k_{b2}+k_{b3})]y_{w2} \\
 & + [2(G_1+G_2+G_4)(G_1+G_5+1)(k_{b2}+k_{b3})](\psi_{w2}+\frac{b}{R}) \\
 & + [+4G_3(G_1+G_2+G_4)(k_{b2}+k_{b3})]y_F \\
 & + [4(G_1+G_2+G_4)(G_4-G_5-G_6)(k_{b2}+k_{b3})]\psi_F \\
 & + [-k_{s\psi}-4(G_1+G_2+G_4)^2(k_{b2}+k_{b3})]\psi_B
 \end{aligned}$$

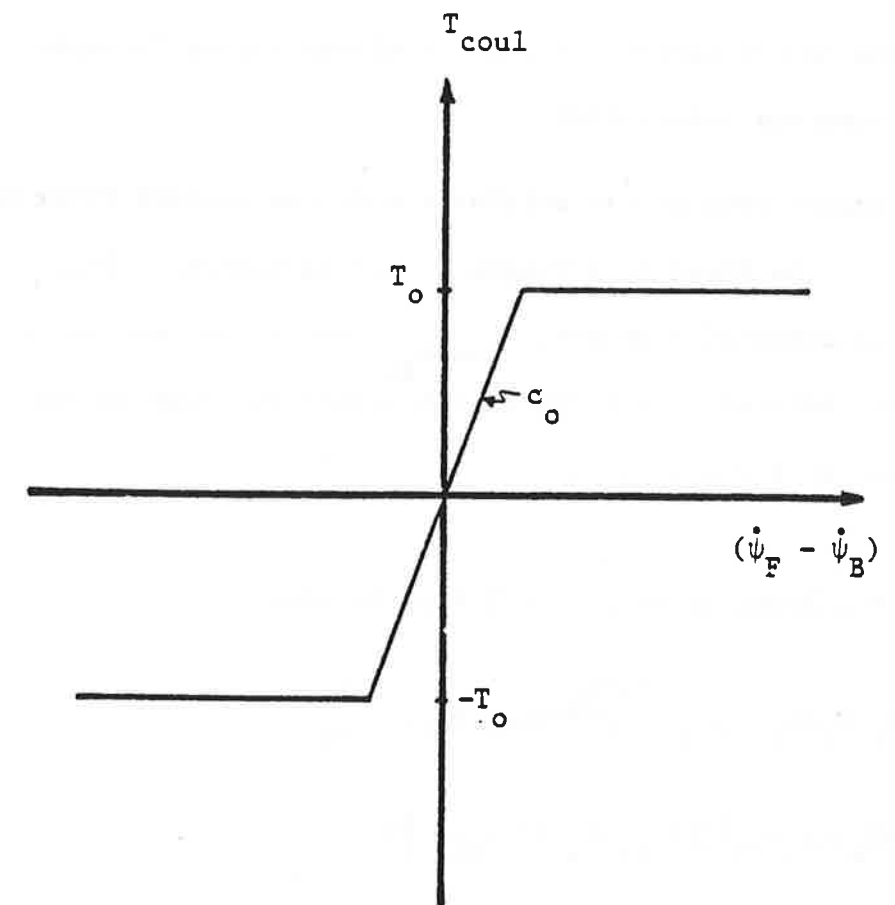


Figure B.9 Truck Frame/Bolster Yaw Suspension Characteristic

Plan
View:

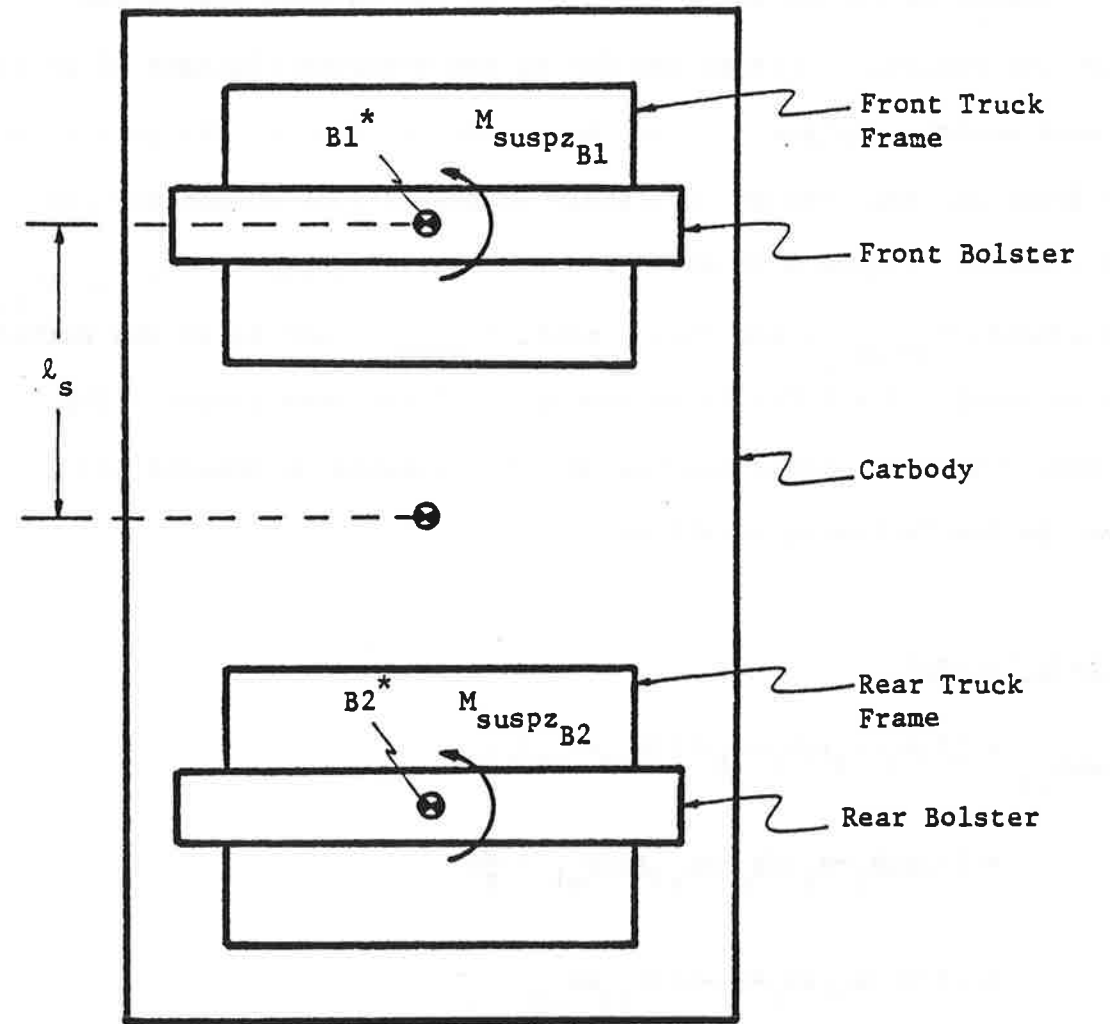
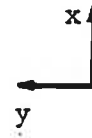


Figure B.10 Yaw Suspension Moments Acting on Bolsters

$$+[k_{s\psi}](\psi_c \pm \frac{l_s}{R})$$

$$+[-C_{s\psi}]\dot{\psi}_B + [C_{s\psi}](\dot{\psi}_c \pm l_s(1/R)) + T_{coul}$$

(B-30)

B.5.3 Carbody Suspension Forces and Moments

Suspension forces and moments act on the carbody due to the secondary suspension system and due to the steering linkages of forced-steered vehicle designs. It is convenient to consider the influence of the front and rear trucks separately on the carbody suspension forces and moments. Figure B.11 shows the effective lateral force, $F_{suspy_{Ci}}$, yaw moment, $M_{suspz_{Ci}}$, and roll moment, $M_{suspX_{Ci}}$, acting on the carbody due to truck i ($i = 1$ for front truck; $i = 2$ for rear truck). The lateral suspension force and yaw and roll suspension moments are given by the following equations.

Carbody Lateral

$$F_{suspy_{Ci}} = [2(H_1+H_2)(H_1+H_3+1)(k_{s2}+k_{s3})]y_{w1}$$

$$+ [-2b(H_1+H_2)(k_{s2}+k_{s3})](\psi_{w1} - \frac{b}{R})$$

$$+ [2(H_1+H_2)(H_1+H_3-1)(k_{s2}+k_{s3})]y_{w2}$$

$$+ [-2b(H_1+H_2)(k_{s2}+k_{s3})](\psi_{w2} + \frac{b}{R})$$

$$+ [2k_{sy} + 4(H_1+H_2)(H_2-H_3)(k_{s2}+k_{s3})]y_F$$

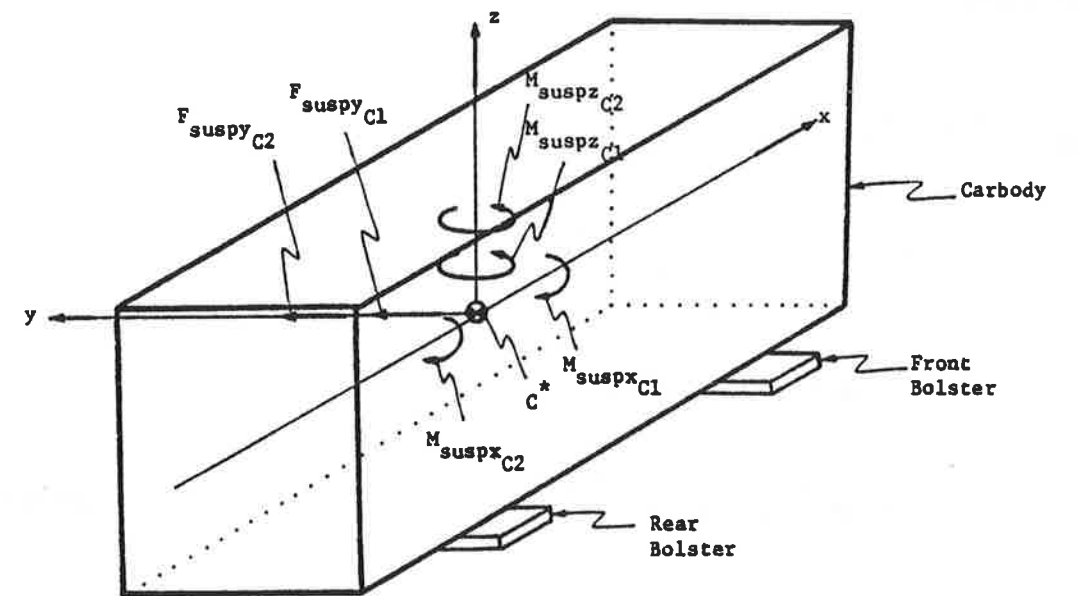


Figure B.11 Suspension Forces and Moments Acting on Carbody

$$\begin{aligned}
& +[-2k_{sy} - 4(H_1 + H_2)^2(k_{s2} + k_{s3})]y_c \\
& + [2C_{sy}] \dot{y}_B + [-2C_{sy}] \dot{y}_c \\
& + [-2h_{cs} k_{sy}] \dot{\phi}_c + [-2h_{cs} C_{sy}] \dot{\phi}_c
\end{aligned} \tag{B-31}$$

Carbody Yaw

$$\begin{aligned}
M_{suspz_{Ci}} & = [+2\ell_s k_{sy}] y_F + [k_{s\psi}] \psi_B \\
& + [-2\ell_s^2 k_{sy} - k_{s\psi}] (\psi_c \pm \frac{\ell_s}{R}) \\
& + [+2\ell_s C_{sy}] \dot{y}_F + [C_{s\psi}] \dot{\psi}_B \\
& + [-2\ell_s^2 C_{sy} - C_{s\psi}] (\dot{\psi}_c + \ell_s (1/R))
\end{aligned} \tag{B-32}$$

Carbody Roll

$$\begin{aligned}
M_{susp_{Ci}} & = [-2k_{sy} h_{cs}^2 - 2k_{sz} d_s^2] \phi_c \\
& + [-2C_{sy} h_{cs}^2 - 2C_{sz} d_s^2] \dot{\phi}_c
\end{aligned} \tag{B-33}$$

The dynamics of the front and rear trucks (and bolsters) are coupled due to connection via the carbody. In steady-state curving conditions, the effect of coupling between the trucks is negligible (for typical secondary suspension parameters). The suspension forces

and moments from the carbody acting on the front and rear trucks are equal and opposite. In dynamic curving situations, such as curve entry and exit, the forces and moments acting on the front and rear trucks are not equal and opposite. The trucks do not behave independently and, thus, a full vehicle model is required.

In the next section, the equations of motion are developed for a full vehicle model.

B.6 Equations of Motion

The wheelsets, trucks, bolsters, and carbody are assumed to be rigid bodies. The equations of motion are derived by direct application of Newtonian mechanics. As discussed in Appendix A (Section A.6), the principles of linear and angular momentum give six scalar differential equations for each rigid body. The equations represent three dynamic force equilibrium equations and three dynamic moment equilibrium equations.

B.6.1 Wheelset Equations of Motion

The equations of motion of a wheelset in single-point and two-point contact at the flanging wheel are developed in Appendix A. For a wheelset in single-point contact, the first order differential equations of motion are given in equations (A-68). For a wheelset in two-point contact at the flanging wheel, the equations are given in equations (A-70). The wheelset suspension forces and moments are presented in Section B.5.1. The lateral suspension force and yaw suspension moment acting on the wheelsets are listed in equations (B-21) -

(B-24); the vertical suspension force and roll suspension moment are given in equations (B-25) and (B-26).

B.6.2 Truck Frame and Bolster Equations of Motion

In this section, the lateral and yaw equations of motion of the truck frame and bolster are presented. The lateral equation is obtained by applying the principle of linear momentum in the lateral direction. Taking into account the lateral components of truck frame and bolster weight (since the truck frame and bolster move together laterally) and assuming small angles, the lateral equation of motion is:

TRUCK FRAME/BOLSTER LATERAL EQUATION

$$\frac{(W_F + W_B)}{g} [\ddot{y}_F - (r_o + h_{tp})\ddot{\phi}_{SE}] = (W_F + W_B) [\phi_d - \frac{1}{2}(\phi_{w1} + \phi_{w2})] + F_{suspy_F} \quad (B-34)$$

The truck frame yaw equation is obtained by applying the principle of angular momentum in the yaw direction. Assuming small angles, the truck frame yaw equation of motion is:

TRUCK FRAME YAW EQUATION

$$I_{FZ} [\ddot{\psi}_F - \frac{\dot{V}}{R} - V(1/R)] = M_{suspz_F} \quad (B-35)$$

Similarly, the bolster yaw equation of motion is:

BOLSTER YAW EQUATION

$$I_{BZ} [\ddot{\psi}_B - \frac{\dot{V}}{R} - V(1/R)] = M_{suspz_B} \quad (B-36)$$

The truck frame lateral suspension force, F_{suspy_F} , in equation (B-34), the truck frame yaw suspension moment, M_{suspz_F} , in equation (B-35), and the bolster yaw suspension moment, M_{suspz_B} , in equation (B-36) are defined in equations (B-27), (B-28), and (B-30), respectively.

B.6.3 Carbody Equations of Motion

The lateral and yaw equations of motion of the carbody are presented in this section. The lateral equation of motion is derived by applying the principle of linear momentum in the lateral direction and accounting for the contributions of the lateral suspension forces from the front and rear trucks. The equation is:

CARBODY LATERAL EQUATION

$$\frac{W_c}{g} [\ddot{y}_c - (r_o + h_{tp} + h_{ts} + h_{cs}) \ddot{\phi}_{SE}] = W_c (\phi_d - \phi_c) + F_{\text{suspy}_{C1}} + F_{\text{suspy}_{C2}} \quad (\text{B-37})$$

where the lateral component of the carbody weight is included and small angles are assumed.

The yaw equation of motion is obtained by invoking the principle of angular momentum in the yaw direction and including the influence of the yaw suspension moments from the front and rear trucks. Assuming small angles, the carbody yaw equation is:

CARBODY YAW EQUATION

$$I_{cz} \left[\ddot{\psi}_c - \frac{\dot{V}}{R} - V(1/R) \right] = M_{suspz_{C1}} + M_{suspz_{C2}} \quad (B-38)$$

Similarly, the carbody roll equation of motion is derived by applying the principle of angular momentum in the roll direction.

CARBODY ROLL EQUATION

$$I_{cx} [\ddot{\phi}_c + \ddot{\phi}_{SE}] = M_{susp_{C1}} + M_{susp_{C2}} \quad (B-39)$$

The carbody roll angle, ϕ_c , is the angular displacement about a longitudinal axis passing through the carbody center of mass. When $\phi_c = 0$, the carbody is parallel to the track plane.

The carbody lateral suspension forces, $F_{suspy_{Ci}}$, in equation (B-37), the yaw suspension moments, $M_{suspz_{Ci}}$, in equation (B-38), and the roll suspension moments, $M_{susp_{Ci}}$, in equation (B-39) are defined in equations (B-31), (B-32), and (B-33), respectively.

B.6.4 Modified Carbody Yaw Equation of Motion

In the development above, a detailed model of truck frame-bolster-carbody interaction has been assumed which includes a degree of freedom for bolster yaw motions. In the model, the carbody is connected to each bolster by yaw suspension stiffness and damping elements. Physically, the stiffness and damping are provided by anchor rods which offer large torsional resistance. The model also includes a (modified)

coulomb friction element between the bolster and truck frame to represent the effect of the friction pads at the truck centerplate. The truck frame-bolster yaw suspension characteristic is shown in Figure B.12.

Since the secondary yaw stiffness between the carbody and bolster is very large,* it is reasonable to model the bolster as rigidly coupled to the carbody in yaw. This simplifies the analysis by eliminating a degree of freedom for bolster yaw. In the following, it is assumed that each bolster yaws with the carbody, but displaces laterally and rolls with the truck frame. For forced-steered vehicles, this implies that the steering linkages are effectively connected to the carbody.

Since each bolster yaws with the carbody, the bolster yaw angle, ψ_B , is a function of the carbody yaw angle, ψ_C , given by

$$\psi_B = \psi_C \pm \frac{l_s}{R} \quad (B-40)$$

Substituting equation (B-40) into the bolster and carbody yaw equations of motion and combining terms results in the following equation for carbody/bolster yaw:

*In addition to large secondary yaw stiffness ($>5.0 \times 10^6$ ft-lb/rad), the bolster weight (~1500 lb) is small (relative to truck frame and carbody weights). Thus, the natural frequency of yaw oscillation of the bolster (~15 Hz) is large relative to the truck frame and carbody natural frequencies.

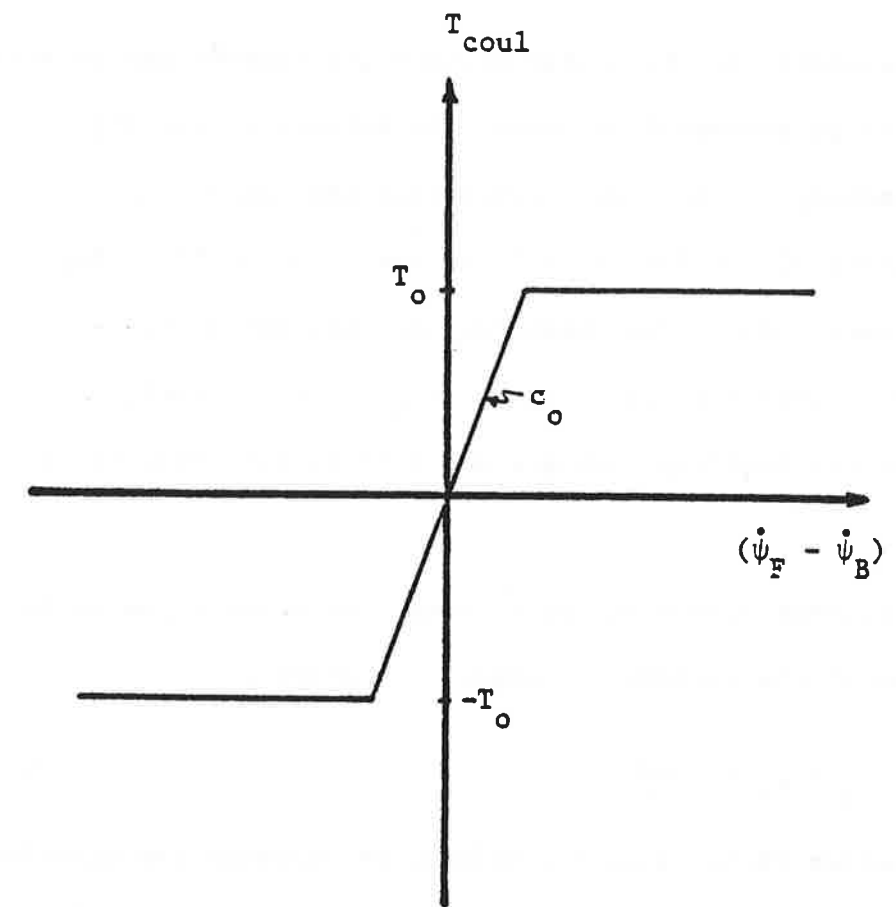


Figure B.12: Truck Frame/Bolster Yaw Suspension Characteristic

CARBODY/BOLSTER YAW EQUATION

$$I_{CZ}^* \left[\ddot{\psi}_c - \frac{\dot{V}}{R} - V(1/R) \right] = M_{suspZ_{C1}}^* + M_{suspZ_{C2}}^* \quad (B-41)$$

where I_{CZ}^* is the yaw moment of inertia of the carbody and front and rear bolsters (about a vertical axis through the carbody center of mass) and $M_{suspZ_{Ci}}^*$ is the suspension yaw moment acting on the carbody and bolster due to interaction with truck i. The expression for the suspension yaw moment, $M_{suspZ_{Ci}}^*$, is obtained by summing the suspension yaw moments on the carbody and bolster, i.e.,

CARBODY/BOLSTER YAW

$$\begin{aligned} M_{suspZ_{Ci}}^* = & [2(G_1+G_2+G_4)(\pm G_3 + \frac{G_2+G_6}{b})(k_{b2}+k_{b3})]y_{w1} \\ & + [2(G_1+G_2+G_4)(G_1+G_5\mp 1)(k_{b2}+k_{b3})](\psi_{w1} - \frac{b}{R}) \\ & + [+2(G_1+G_2+G_4)(G_3\mp \frac{G_2+G_6}{b})(k_{b2}+k_{b3})]y_{w2} \\ & + [2(G_1+G_2+G_4)(G_1+G_5\pm 1)(k_{b2}+k_{b3})](\psi_{w2} + \frac{b}{R}) \\ & + [+2l_s k_{sy} \mp 4G_3(G_1+G_2+G_4)(k_{b2}+k_{b3})]y_F \\ & + [4(G_1+G_2+G_4)(G_4-G_5-G_6)(k_{b2}+k_{b3})]\psi_F \\ & + [-2l_s^2 k_{sy} - 4(G_1+G_2+G_4)^2(k_{b2}+k_{b3})](\psi_c \pm \frac{l_s}{R}) \end{aligned}$$

$$+[\pm 2\ell_s C_{sy}] \dot{y}_F + [-2\ell_s^2 C_{sy}] (\dot{\psi}_c \pm \ell_s (1/R))$$

$$+T_{\text{coul}}$$

(B-42)

B.7 Numerical Methods

The equations of motion presented in Section B.6 describe the dynamic behavior of the wheelsets, trucks, bolsters, and carbody of a rail vehicle model as it traverses flexible, curved track. The equations of motion are solved by digital integration using a fourth-order Runge-Kutta scheme, which requires that the equations be in first order form. In this section, the equations of motion of the full vehicle model are cast in a form convenient for computer manipulation. In a sense, this section represents a continuation of Section A.7 of Appendix A which presented the first order differential equations of motion of a wheelset.

The full vehicle model is represented by 42 states: 20 states for the 4 wheelsets, 8 states for the 2 trucks, 6 states for the carbody, and 8 states for the rails. These states are listed in Table B.2. Each wheelset has 2 states (1 degree of freedom) to describe lateral motions (y_{Wi}, \dot{y}_{Wi}) 2 states to describe yaw motions $(\psi_{Wi}, \dot{\psi}_{Wi})$, and a state to represent spin speed $(\dot{\theta}_{Wi})$. In addition, the rails in contact with each wheelset have 2 states to describe lateral deflections $(y_{\text{rail}_{Ri}}, y_{\text{rail}_{Li}})$. Each truck frame is characterized by 2 states for lateral motions (y_{Fi}, \dot{y}_{Fi}) and 2 states for yaw motions $(\psi_{Fi}, \dot{\psi}_{Fi})$. The carbody has 2 states for lateral motions (y_C, \dot{y}_C) , 2 states for yaw

motions $(\psi_c, \dot{\psi}_c)$, and 2 states for roll motions $(\phi_c, \dot{\phi}_c)$.

Assuming that single-point contact occurs at all wheels of the vehicle, the first order differential equations of motion are given by the following equations.

SINGLE-POINT CONTACT VEHICLE EQUATIONS

$$\begin{aligned}\dot{x}_1 &= x_4 \\ \dot{x}_2 &= x_5 \\ \dot{x}_8 &= x_{11} \\ \dot{x}_9 &= x_{12} \\ \dot{x}_{15} &= x_{17} \\ \dot{x}_{16} &= x_{18} \\ \dot{x}_{19} &= x_{22} \\ \dot{x}_{20} &= x_{23} \\ \dot{x}_{26} &= x_{29} \\ \dot{x}_{27} &= x_{30} \\ \dot{x}_{33} &= x_{35} \\ \dot{x}_{34} &= x_{36} \\ \dot{x}_{37} &= x_{40} \\ \dot{x}_{38} &= x_{41} \\ \dot{x}_{39} &= x_{42}\end{aligned}$$

(B-43)

WHEELSET SPIN [EQUATION (A-51)]

$$\dot{X}_3 = f(X_1, X_2, \dots, X_{42})$$

$$\dot{X}_{10} = f(X_1, X_2, \dots, X_{42})$$

$$\dot{X}_{21} = f(X_1, X_2, \dots, X_{42})$$

$$\dot{X}_{28} = f(X_1, X_2, \dots, X_{42})$$

WHEELSET LATERAL [EQUATION (A-45)]

$$\dot{X}_4 = f(X_1, X_2, \dots, X_{42})$$

$$\dot{X}_{11} = f(X_1, X_2, \dots, X_{42})$$

$$\dot{X}_{22} = f(X_1, X_2, \dots, X_{42})$$

$$\dot{X}_{29} = f(X_1, X_2, \dots, X_{42})$$

(B-43)
Continued

WHEELSET YAW [EQUATION (A-52)]

$$\dot{X}_5 = f(X_1, X_2, \dots, X_{42})$$

$$\dot{X}_{12} = f(X_1, X_2, \dots, X_{42})$$

$$\dot{X}_{23} = f(X_1, X_2, \dots, X_{42})$$

$$\dot{X}_{30} = f(X_1, X_2, \dots, X_{42})$$

RIGHT RAIL LATERAL [EQUATION (A-54)]

$$\dot{X}_6 = f(X_1, X_2, \dots, X_{42})$$

$$\dot{X}_{13} = f(X_1, X_2, \dots, X_{42})$$

$$\dot{X}_{24} = f(X_1, X_2, \dots, X_{42})$$

$$\dot{X}_{31} = f(X_1, X_2, \dots, X_{42})$$

LEFT RAIL LATERAL [EQUATION (A-53)]

$$\dot{X}_7 = f(X_1, X_2, \dots, X_{42})$$

$$\dot{X}_{14} = f(X_1, X_2, \dots, X_{42})$$

$$\dot{X}_{25} = f(X_1, X_2, \dots, X_{42})$$

$$\dot{X}_{32} = f(X_1, X_2, \dots, X_{42})$$

TRUCK FRAME/BOLSTER LATERAL [EQUATION (B-34)]

$$\dot{X}_{17} = f(X_1, X_2, \dots, X_{42})$$

$$\dot{X}_{35} = f(X_1, X_2, \dots, X_{42})$$

TRUCK FRAME YAW [EQUATION (B-35)]

$$\dot{X}_{18} = f(X_1, X_2, \dots, X_{42})$$

$$\dot{X}_{36} = f(X_1, X_2, \dots, X_{42})$$

CARBODY LATERAL [EQUATION (B-36)]

$$\dot{X}_{40} = f(X_1, X_2, \dots, X_{42})$$

CARBODY/BOLSTER YAW [EQUATION (B-41)]

$$\dot{X}_{41} = f(X_1, X_2, \dots, X_{42})$$

CARBODY ROLL [EQUATION (B-39)]

$$\dot{X}_{42} = f(X_1, X_2, \dots, X_{42})$$

(B-43)
Continued

The first order equations of motion listed in equations (B-43) apply if single-point contact occurs at all wheels. If two-point contact occurs at a wheel (or wheels), these equations must be modified. For instance, if two-point contact occurs at the left wheel of the leading wheelset, the following modifications are introduced in equations (B-43).

LEADING WHEELSET SPIN [EQUATION (A-62)]

$$\dot{X}_3 = f(X_1, X_2, \dots, X_{42})$$

LEADING WHEELSET LATERAL [EQUATION (A-59)]

$$\dot{X}_4 = f(X_1, X_2, \dots, X_{42})$$

LEADING WHEELSET YAW [EQUATION (A-63)]

(B-44)

$$\dot{X}_5 = f(X_1, X_2, \dots, X_{42})$$

LEADING RIGHT RAIL LATERAL [EQUATION (A-65)]

$$\dot{X}_6 = f(X_1, X_2, \dots, X_{42})$$

Also, the equation for the leading left rail lateral displacement, X_7 , is eliminated. State X_7 is a known function of X_1 due to the contact constraint relation (A-56). Equations (B-43) are correct except for these modifications. If two-point contact occurs at other wheels, similar replacements are made.

TABLE B.2: STATES OF THE RAIL VEHICLE MODEL

FRONT TRUCK, LEADING WHEELSET

$$\begin{aligned} x_1 &= y_{w1} \\ x_2 &= \psi_{w1} \\ x_3 &= \dot{\theta}_{w1} \\ x_4 &= \dot{y}_{w1} \\ x_5 &= \dot{\psi}_{w1} \\ x_6 &= y_{\text{rail}_{R1}} \\ x_7 &= y_{\text{rail}_{L1}} \end{aligned}$$

FRONT TRUCK, TRAILING WHEELSET

$$\begin{aligned} x_8 &= y_{w2} \\ x_9 &= \psi_{w2} \\ x_{10} &= \dot{\theta}_{w2} \\ x_{11} &= \dot{y}_{w2} \\ x_{12} &= \dot{\psi}_{w2} \\ x_{13} &= y_{\text{rail}_{R2}} \\ x_{14} &= y_{\text{rail}_{L2}} \end{aligned}$$

FRONT TRUCK

$$\begin{aligned} x_{15} &= y_{F1} \\ x_{16} &= \psi_{F1} \\ x_{17} &= \dot{y}_{F1} \\ x_{18} &= \dot{\psi}_{F1} \end{aligned}$$

REAR TRUCK, LEADING WHEELSET

$$\begin{aligned} X_{19} &= y_{w3} \\ X_{20} &= \psi_{w3} \\ X_{21} &= \dot{\theta}_{w3} \\ X_{22} &= \dot{y}_{w3} \\ X_{23} &= \dot{\psi}_{w3} \\ X_{24} &= y_{\text{rail}_{R3}} \\ X_{25} &= y_{\text{rail}_{L3}} \end{aligned}$$

REAR TRUCK

$$\begin{aligned} X_{33} &= y_{F2} \\ X_{34} &= \psi_{F2} \\ X_{35} &= \dot{y}_{F2} \\ X_{36} &= \dot{\psi}_{F2} \end{aligned}$$

REAR TRUCK, TRAILING WHEELSET

$$\begin{aligned} X_{26} &= y_{w4} \\ X_{27} &= \psi_{w4} \\ X_{28} &= \dot{\theta}_{w4} \\ X_{29} &= \dot{y}_{w4} \\ X_{30} &= \dot{\psi}_{w4} \\ X_{31} &= y_{\text{rail}_{R4}} \\ X_{32} &= y_{\text{rail}_{L4}} \end{aligned}$$

CARBODY

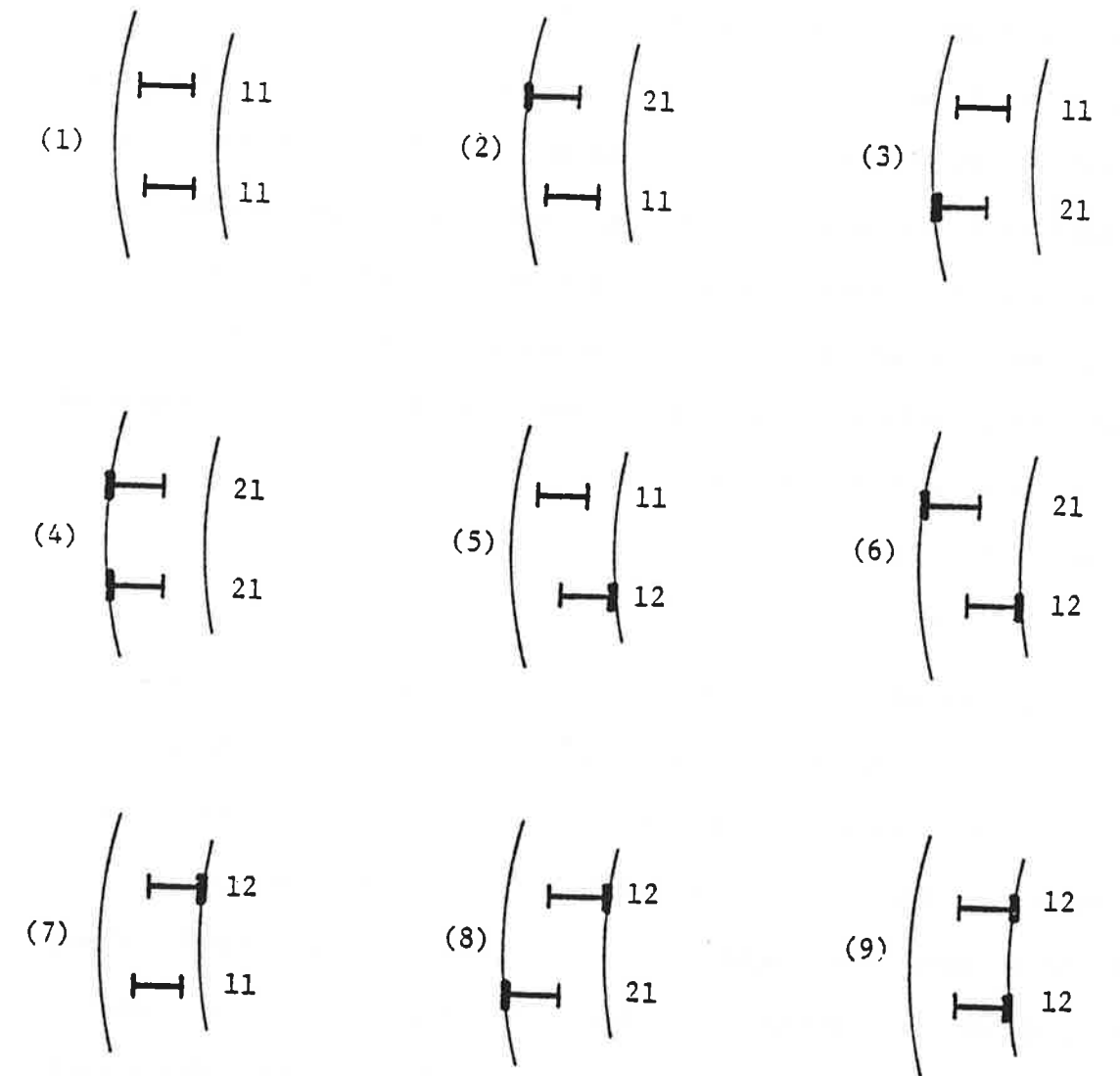
$$\begin{aligned} X_{37} &= y_c \\ X_{38} &= \psi_c \\ X_{39} &= \phi_c \\ X_{40} &= \dot{y}_c \\ X_{41} &= \dot{\psi}_c \\ X_{42} &= \dot{\phi}_c \end{aligned}$$

In typical steady-state curving conditions, flanging occurs at the leading outer wheel of the vehicle (for practical vehicle suspension parameters and for negotiation of curves $>2.5^\circ$). Thus, for wheel/rail profiles with steep flanges, such as new AAR 1 in 20 wheels, two-point contact develops at the leading outer wheel. Single-point contact occurs at all other wheels. In dynamic curving situations, flanging can occur at any wheel or combination of wheels. For a vehicle with new wheel profiles, two-point contact can develop at the outer or inner wheels of any of the wheelsets, especially during violent curve entry and exit, during negotiation of reverse curves, and during hunting.

For each wheelset of the vehicle, 3 distinct possibilities of wheel/rail contact exist. The possibilities are: (1) single-point contact at both wheels, (2) two-point contact at the outer wheel and single-point contact at the inner wheel, or (3) two-point contact at the inner wheel and single-point contact at the outer wheel. Thus, for a truck with 2 wheelsets, a total of 9 wheel/rail contact possibilities can be identified, as illustrated in Figure B.13. For a full vehicle with front and rear trucks, 81 contact combinations are possible. A separate set of vehicle equations of motion exists for each combination.

B.7.1 Dynamic Curving Program

The nonlinear vehicle equations of motion are numerically integrated to provide time histories of (1) all the state variables, (2) the wheel/rail contact forces, and (3) the contact patch work. A






Key:  11 Single-Point Contact Outer and Inner Wheels.
 21 Two-Point Contact Outer Wheel; Single-Point Contact Inner Wheel.
 12 Single-Point Contact Outer Wheel; Two-Point Contact Inner Wheel.

Figure B.13 Wheel/Rail Contact Possibilities for Wheelsets of a Truck with New Wheels.

variable time-step, fourth order Runge-Kutta algorithm is employed for the integration. The dynamic curving analysis is coded in a FORTRAN program, entitled DYCURV (DYnamic CURVing). A flowchart of the program, the layout of the "equation" subroutines, and appropriate descriptions of the subroutines appear in Figures B.14, B.15, and Table B.3, respectively. Program DYCURV automatically determines the wheel/rail contact condition at each wheel. The program solves the single-point contact vehicle equations and evaluates whether or not a correct solution has been obtained. If a two-point contact wheel/rail profile is being used and the net wheelset lateral excursion at any wheel equals the flange clearance, the solution is not correct. Then, without incrementing the time-step, a different (appropriate) set of vehicle equations is solved and, again, checked for consistency. A consistent (i.e., correct) two-point contact solution is obtained if positive normal forces are predicted at the two contact points at each flanging wheel.

Program DYCURV requires a very small time-step generally for numerical stability. Previous dynamic curving analyses [7, 10] have suggested a time-step of 0.00075 sec. This value is used in program DYCURV when tread contact occurs at all wheel/rail interfaces. When flange contact occurs at any wheel the program automatically reduces the time-step to 0.0005 sec. Thus, for a 1 second simulation in which flange contact occurs, 2,000 time-step iterations are required. The computer time required on a DEC VAX 1178 is about 1 CPU minute for a 1 second simulation, at a cost of \$3.75/CPU minute at high priority.

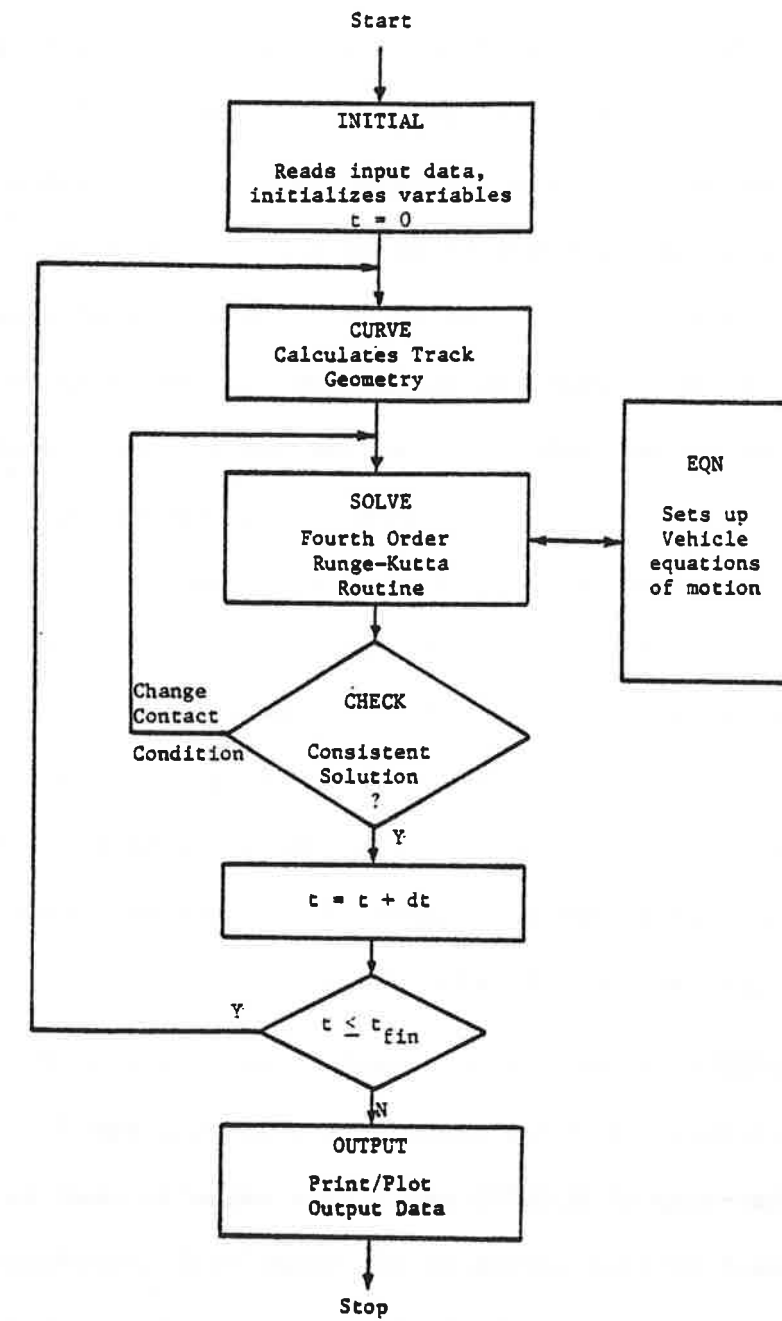
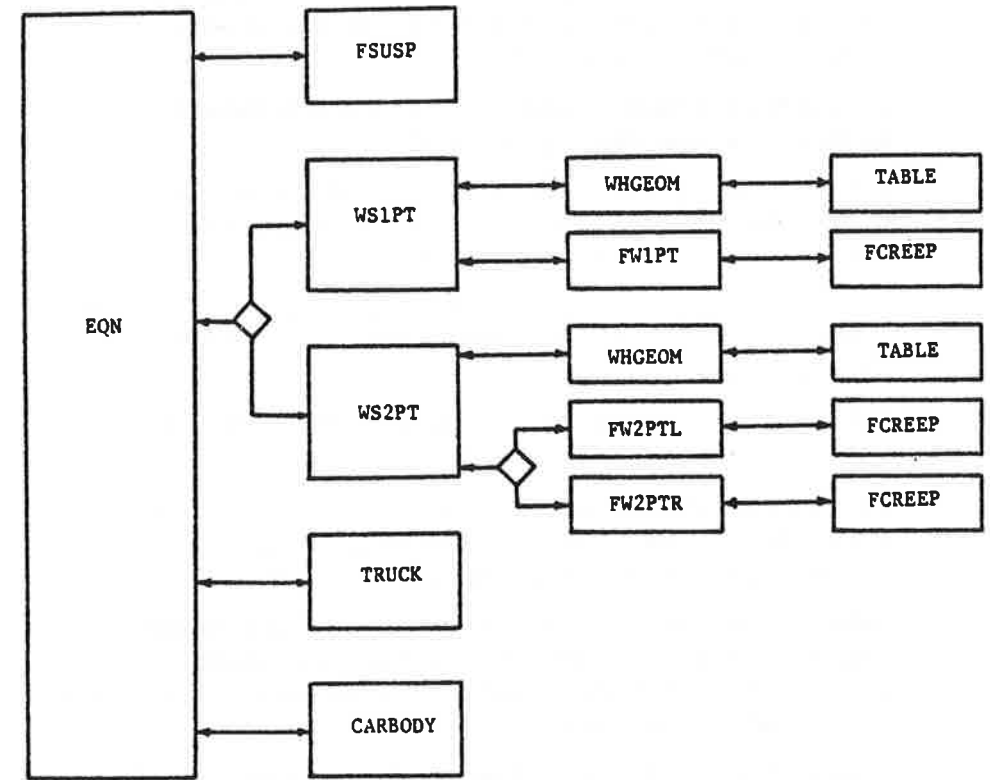


Figure B.14 Flowchart of Dynamic Curving Program



B.15 Layout of Equation Subroutines

TABLE B.3 SUBROUTINE DESCRIPTIONS FOR DYNAMIC CURVING PROGRAM

CARBODY	Sets up first order differential equations of motion of carbody.
CHECK	Checks consistency of solution (i.e., checks wheelset lateral excursions and signs of forces to determine if single-point or two-point contact occur at each wheel); if inconsistent, changes contact condition.
CURVE	Calculates track geometry: track curvature, superelevation angle, and rates.
EQN	Sets up appropriate first order differential equations of motion of vehicle (depending on contact conditions at wheels).
FCREEP	Determines creep forces and moment using "heuristic" scheme (Linear Kalker with Vermeulen-Johnson saturation).
FSUSP	Calculates suspension forces and moments acting on wheelsets, trucks, and carbody.
FW1PT	Calculates wheel/rail forces (creep and normal) using iterative approach assuming single-point contact occurs at both wheels.
FW2PTL	Calculates wheel/rail forces (creep and normal) using iterative approach assuming two-point contact occurs at left wheel and single-point contact occurs at right wheel.
FW2PTR	Calculates wheel/rail forces (creep and normal) using iterative approach assuming two-point contact occurs at right wheel and single-point contact occurs at left wheel.
INITIAL	Reads input data: system parameters, initial conditions, and wheel/rail geometry.
OUTPUT	Prints/plots output data: states, wheel/rail forces, contact work.
SOLVE	Standard fourth order Runge-Kutta integration routine.
TABLE	Interpolates wheel/rail contact geometry data from table.
TRUCK	Sets up first order differential equations of motion of truck.
WHGEOM	Determines wheel/rail contact geometry for net lateral excursion.

TABLE B.3 Continued

WS1PT	Sets up wheelset and rail equations of motion assuming single-point contact occurs at both wheels.
WS2PT	Sets up wheelset and rail equations of motion assuming two-point contact occurs at one wheel and single-point contact occurs at other wheel.

If the program is to be used for extensive parametric studies, optimal on-flange and off-flange time-steps should be determined. These values will be a function of the "stiffness" of the system of equations being integrated.

